PONTIFÍCIA UNIVERSIDADE CATÓLICA
DO RIO DE JANEIRO

Marcelo de Alencastro Pasqualette

Optimization of the interfacial shear stress and assessment of closure relations for horizontal viscous oil-gas flows in the stratified and slug regimes

Dissertação de Mestrado

Dissertation presented to the Programa de Pós-Graduação em Engenharia Mecânica of PUC-Rio in partial fulfillment of the requirements for the degree of Mestre em Engenharia Mecânica.

Advisor: Profª Angela Ourivio Nieckele
Co-Advisor: Dr. João Neuenschwander Escosteguy Carneiro

Rio de Janeiro
August 2017

Pontifícia Universidade Católica
do Rio de Janeiro

Marcelo de Alencastro Pasqualette

Optimization of the interfacial shear stress and assessment of closure relations for horizontal viscous oil-gas flows in the stratified and slug regimes

Dissertation presented to the Programa de Pós-Graduação em Engenharia Mecânica of PUC-Rio in partial fulfillment of the requirements for the degree of Mestre em Engenharia Mecânica. Approved by the undersigned Examination Committee

Profa. Angela Ourivio Nieckele
Advisor
Departamento de Engenharia Mecânica – PUC-Rio

Dr. João Neuenschwander Escosteguy Carneiro
Co-Advisor
Instituto SINTEF do Brasil

Prof. Eugênio Spanó Rosa
UNICAMP

Dr. José Roberto Fagundes Netto
Pesquisador Autônomo

Prof. Márcio da Silveira Carvalho
Vice Dean of Graduate Studies
Centro Técnico Científico – PUC-Rio

Rio de Janeiro, August 11th, 2017

Marcelo de Alencastro Pasqualette

The author graduated in Mechanical Engineering from the Federal University of Rio de Janeiro in 2015 with the *cum* laude honor. In the former, the author received a PIBIC-CNPq scholarship for two years and an ANP PRH-37 scholarship for other two years. He has been working at the SINTEF Institute of Brazil for four years in the areas of multiphase flow, thermodynamics and flow assurance. He has eight complete papers published at conferences and two peer-reviewed articles published at journals.

Ficha Catalográfica

Pasqualette, Marcelo de Alencastro

Optimization of the interfacial shear stress and assessment of closure relations for horizontal viscous oil-gas flows in the stratified and slug regimes / Marcelo de Alencastro Pasqualette ; advisor: Angela Ourivio Nieckele ; co-advisor: João Neuenschwander Escosteguy Carneiro. – 2017.
199 f. : il. color. ; 30 cm

Dissertação (mestrado)–Pontifícia Universidade Católica do Rio de Janeiro, Departamento de Engenharia Mecânica, 2017.
Inclui bibliografia

1. Engenharia Mecânica – Teses. 2. Modelo 1D de dois fluidos. 3. Escoamento óleo viscoso-gás. 4. Metodologia de captura de regime. 5. Tensão cisalhante interfacial. 6. Modelos de fechamento. I. Nieckele, Angela Ourivio. II. Carneiro, João Neuenschwander Escosteguy. III. Pontifícia Universidade Católica do Rio de Janeiro. Departamento de Engenharia Mecânica. IV. Título.

CDD: 621

Acknowledgements

I would like to thank, firstly, to my advisor Prof^{a} Angela Nieckele for her guidance and wisdom during these years working on my dissertation.

I enormously thank my co-advisor João Carneiro for the friendship, counselling and leadership not only during the construction of the present work, but since I joined SINTEF Brazil four years ago.

I gladly thank the friends and colleges that have worked with me (and still do) in SINTEF Brazil, especially Milena, Gabriel, Mariana, Alessandra and Bárbara. Thanks for the laughs!

I highly appreciate the company of my long-term friends, especially Luiz Helt and Thadeu Arlens. Thank you for the friendship, the beers and the laughs during all of those years!

I joyfully thank my friends Daniel Gurjão and César Pacheco for the pleasant and fun conversations and for showing that Saint Thomas Aquinas was right when he stated about friendship: *idem velle idem nolle*. Long live to our joint projects!

I thank my whole family for their support and love during my life, but especially for the years in which I have been working on my dissertation. My grandmother, my uncles, my aunts, my cousins, my godfather, my godmother and many others. Nevertheless, I do mostly thank my loving father, mother and brother for just being you they are. I owe them who I am and this work would not exist if it were not for them.

Finally, I thank God for his grace and love, which has been changing my life and my worldview since I recently turned my eyes to Him.

Abstract

Pasqualette, Marcelo de Alencastro; Nieckele, Angela Ourivio (Advisor); Carneiro, João Neuenschwander Escosteguy (Co-Advisor). **Optimization of the interfacial shear stress and assessment of closure relations for horizontal viscous oil-gas flows in the stratified and slug regimes.** Rio de Janeiro, 2017. 199p. Dissertação de mestrado - Departamento de Engenharia Mecânica, Pontifícia Universidade Católica do Rio de Janeiro.

The current depletion of traditional oil fields is increasing the demand for the production and transport of unconventional oils, which might possess a high dynamic viscosity. In this context, the study of the simultaneous flow of gas and viscous oils in pipelines is of paramount importance for the Oil & Gas industry. One-dimensional numerical simulations play a key role in such studies, especially the ones based on the 1D Two-Fluid Model, whose numerical solution in fine meshes consists in the Regime Capturing Methodology. The purpose of this work is to use this approach for reproducing the experimental data of isothermal slug and stratified wavy viscous oil-gas flows in a horizontal laboratory-scale pipe. For improving the results of the methodology, experimental data were used together with an optimization procedure and a simplified version of the 1D Two-Fluid Model for successfully creating two new expressions for the interfacial friction factor, which showed better efficiency than standard literature correlations. The effect of introducing a dynamic pressure, axial momentum diffusion and dynamic interfacial shear in the 1D Two-Fluid Model was examined. Results of pressure gradient and liquid holdup (histograms, mean values and transient profiles) were compared against experimental data. It was seen, with the aid of well-posedness analyses, that the dynamic pressure and the new expressions for the interfacial shear stress provided satisfactory results.

Keywords

1D Two-Fluid Model; Viscous-Oil Gas Flow; Regime Capturing Methodology; Interfacial Shear Stress; Closure Models.

Resumo

Pasqualette, Marcelo de Alencastro; Nieckele, Angela Ourivio; Carneiro, João Neuenschwander Escosteguy. **Otimização da tensão cisalhante interfacial e avaliação das relações de fechamento para escoamentos horizontais de óleo viscoso-gás nos regimes estratificado e golfadas.** Rio de Janeiro, 2017. 199p. Dissertação de mestrado - Departamento de Engenharia Mecânica, Pontifícia Universidade Católica do Rio de Janeiro.

O atual esgotamento de campos de petróleo tradicionais tem aumentado a demanda pela produção e transporte óleos não convencionais, que podem possuir uma alta viscosidade dinâmica. Neste contexto, o estudo do escoamento simultâneo de gás e óleos viscosos em tubulações é de grande importância para a indústria de Óleo & Gás. Simulações numéricas uni-dimensionais desempenham um papel essencial nestes estudos, especialmente aquelas baseadas no Modelos de Dois-Fluidos 1D, cuja solução numérica em malhas refinadas consiste na Metodologia de Captura de Regimes. O propósito deste trabalho é utilizar esta abordagem para reproduzir dados experimentais de escoamentos óleo viscoso-gás em golfadas e estratificado ondulado em um duto horizontal em escala laboratorial. Para aprimorar os resultados desta metodologia, dados experimentais foram usados conjuntamente com um procedimento de otimização e uma versão simplificada do Modelos de Dois-Fluidos 1D para criar duas novas expressões para o fator de atrito interfacial, as quais mostraram maior eficiência que correlações padrão da literatura. O efeito da introdução da pressão dinâmica, difusão axial de quantidade de movimento e tensão interfacial dinâmica no Modelo de Dois-Fluidos 1D foi analisado. Resultados de gradiente de pressão e de fração volumétrica de líquido (histogramas, valores médios e perfis transientes) foram comparados com dados experimentais. Observou-se, com o auxílio de análises de boa-colocação, que a pressão dinâmica e as novas expressões para o fator de atrito interfacial fornecem resultados satisfatórios.

Palavras-chave

Modelo 1D de Dois-Fluidos; Escoamento Óleo Viscoso - Gás; Metodologia de Captura de Regime; Tensão Cisalhante Interfacial; Modelos de Fechamento.

Table of Contents

List of Tables

List of Figures

List of Symbols

a	Coefficients of the discretized equations
A	Pipe cross sectional area
A_K	Pipe cross sectional area of phase K
$\mathbf{A}$	Coefficient matrix of the general first-order quasi-linear system of Eq. (3.108)
b	Source terms of the discretized equations
$\mathscr{b}_j$	Auxiliary variables defined in Eqs. (3.122)-(3.127)
$\mathcal{B}_{\mathcal{D},UK}$	Dynamic pressure contribution to $s_{c,UK}$
$\mathcal{B}_{\mathcal{G},UK}$	Gravitational contribution to $s_{c,UK}$
$\mathcal{B}_{\mathcal{H},UK}$	Hydrodynamic pressure contribution to $s_{c,UK}$
$\mathcal{B}_{i,UK}$	Interfacial shear stress contribution to $s_{c,UK}$
$\mathcal{B}_{\sigma,UK}$	Surface tension contribution to $s_{c,UK}$
$\mathbf{B}$	Coefficient matrix of the general first-order quasi-linear system of Eq. (3.108)
$\mathbf{c}$	Source vector of the general first-order quasi-linear system of Eq. (3.108)
c_i^*	Influence function of Biberg (1999c)
Ca_i	Interfacial Capillary number
Ca_{sG}	Superficial gas Capillary number
C_0	Parameter of Eq. (2.1)
C_h	Memory coefficient
$\mathcal{C}_1$	Curve in the (x, t) plane in which every state of $\mathbf{\Phi}$ is defined
$\mathcal{C}_{mK}$	Momentum distribution parameter of phase K
CFL	Courant-Friedrichs-Levy number
dx	Length of an infinitesimal pipe element
d_K	Variable defined in Eq. (3.83) for phase K
$\mathscr{d}$	Coefficients in the denominator of Eq. (4.27)
D	Pipe internal diameter
D_{hK}	Hydraulic diameter related to phase K

D^*_{hL}	Modified hydraulic diameter related of the liquid phase
$\mathbf{D}_c$	Matrix that contains the derivatives of each element of $\mathbf{c}$ in relation to each element of $\mathbf{\Phi}$
$\mathcal{DF}_K$	Drag force due to a dispersed field in phase K
e	Root-mean-squared error that combines the Point-Model relative errors $e_{\alpha L}$ and $e_{dP/dx}$
e_{RMS}	Root-mean-squared error related to the Regime Capturing Methodology results, Eq. (5.1)
$e_{\alpha L}$	Relative error of the Point-Model results for liquid holdup in relation to the experiments
$e_{dP/dx}$	Relative error of the Point-Model results for pressure gradient in relation to the experiments
$\mathbb{e}$	Mathematical constant of Euler, $\mathbb{e} = 2.71828\ldots$
f_{G0}	Gas wall Fanning friction factor considering a null pipe wall roughness
f_i	Interfacial Fanning friction factor
f_{i0}	Smooth interfacial Fanning friction factor
f_K	Wall Fanning friction factor of phase K
$\mathcal{F}^I_{\mathrm{obj}}$	First formulation of the objective function for the optimization problem
$\mathcal{F}^{II}_{\mathrm{obj}}$	Second formulation of the objective function for the optimization problem
F_K	Flux of phase K
F^*_K	Pseudo-flux of phase K
Fr_{i0}	Smooth interfacial Froude number
Fr_K	Froude number of phase K
Fr_{hL}	Liquid height Froude number
g	Gravitational acceleration
$\mathbf{gb}$	Global best sample in the PSO algorithm
$\mathcal{G}$	Function whose zero must be found in the Point-Model, Eq. (4.4)
h_K	Height of phase K
$\mathcal{H}_\mathcal{D}$	Auxiliary variable, Eq.
$\mathbb{i}$	Imaginary unit, $\mathbb{i} = \sqrt{-1}$
$\mathbf{ib}$	Individual best sample in the PSO algorithm
it	Iteration number
j	General counter

jc	Case number of the cases used in the optimization procedures
js	Sample number of the PSO algorithm
$\mathcal{J}_i$	Coefficient of the liquid height axial derivative in Eq. (3.47)
k	Wavenumber of perturbations or interfacial waves
L	Total pipe length
L_b	Long (Taylor) bubble length
L_S	Slug length
$\mathscr{m}$	Exponent in Eq. (3.52)
n	Coordinate normal to curve $\mathcal{C}_1$ (Figure 3.9)
$\mathscr{n}$	Coefficients in the numerator of Eq. (4.27)
N_c	Number of cases selected for use in the optimization procedures outlined in Figure 4.6
N_L	Number of nodal points on the spatial mesh
N_Φ	Number of variables in the first-order quasi-linear system of Eq. (3.108) and in $\mathbf{\Phi}$
$\mathbf{p}$	Population of samples in the PSO algorithm
p_K	Local pressure in phase K
P	Single-pressure of the 1D Two-Fluid Model (equal to P_{iG})
P_{iK}	Pressure at the interface in the side of phase K
P_K	Bulk pressure in phase K
r_κ	Interfacial curvature radius
$\mathbf{r}_j$	Random number variables of uniform distribution between 0 and 1, $j \in \{1,2\}$
res	Residue of a discretized conservation equation
$\mathcal{R}_G$	Gas constant
Re_i	Interfacial Reynolds number
Re_K	Reynolds number of phase K
$\mathrm{Re}_{\mathrm{lam}}$	Laminar-limit value for the Reynolds number
Re_{sK}	Superficial Reynolds number of phase K
$\mathrm{Re}_{\mathrm{turb}}$	Turbulent-limit value for the Reynolds number
s	Coordinate tangential to curve $\mathcal{C}_1$ (Figure 3.9)
$s_{c,UK}$	Source term linear coefficient of the momentum conservation equation of the 1D Two-Fluid Model for phase K
$s_{\mathscr{p},UK}$	Source term angular coefficient of the momentum conservation

	equation of the 1D Two-Fluid Model for phase K
S_i	Interfacial perimeter
S_K	Wetted perimeter of phase K
t	Temporal variable
tol	Convergence tolerance
T	Fluid temperature
$\mathcal{T}_K$	Momentum axial diffusion of phase K
U_b	Long (Taylor) bubble translational velocity
U_d	Drift velocity
U_i	Reference interfacial velocity
U_{iK}	Interfacial velocity in the side of phase K
U_K	Bulk (or absolute) velocity of phase K
U_M	Mixture velocity
U_{sK}	Superficial velocity of phase K
U_t	Slug translational velocity
$\hat{U}_K$	Pseudo-velocity of phase K
$\mathbf{v}$	Update vector of the PSO algorithm
$\mathcal{V}$	Generic parameter in Eq. (4.27)
w_t	Interpolation function
x	Axial pipe (spatial) coordinate
x_j	Position of the j-th nodal point of the spatial mesh
x_j^u	Position of the j-th face of the spatial mesh
X_i	Adimentional interfacial shear stress, Eq. (4.10)
X_L	Adimentional liquid wall shear stress, Eq. (4.9)
$X_{\mathcal{W}}$	Adimentional gravitational force per area, Eq. (4.11)
y	Cross sectional pipe (spatial) coordinate
z_t	Interpolation function for the laminar and turbulent friction factors

Greek Symbols

α_K	Holdup (volume fraction) of phase K
α_{wK}	Holdup (volume fraction) of phase K next to the pipe wall
β_1	Constant of the individuality term of the update equation of the PSO algorithm

β_2	Constant of the sociability term of the update equation of the PSO algorithm
β_ω	Constant of the inertia term of the update equation of the PSO algorithm
γ_K^*	Weight of phase K for evaluating through a harmonic mean the mixture viscosity μ_M of Biberg (1999b)
Γ_K	Mass transfer rate to phase K from the other phase due to phase change
δ	Half of the liquid wetted angle
δx_j	Distance between the j-th and $(j+1)$-th nodal points of the mesh
$\Delta P_{\mathcal{D},K}$	Dynamic pressure contribution to the interfacial-bulk pressure difference
$\Delta P_{\mathcal{H},K}$	Hydrostatic pressure contribution to the interfacial-bulk pressure difference
Δt	Time step
Δx	Key spatial mesh distance
Δx_j	Distance between the j-th and $(j+1)$-th face of the mesh
ε	Internal pipe wall absolute roughness
ε_G	Corrected gas wall roughness, Eq. (4.24)
ϵ_K^*	Modified phase K holdup of Biberg (1999b)
η	Coefficients of the new interfacial friction factor correlations
$\eta_{\mathcal{D}}$	Coefficient for the dynamic pressure of Bestion (1990)
η_μ	Coefficient for the phasic effective dynamic viscosity of Fullmer *et al*. (2011)
$\eta_{\mu t}$	Coefficient for the turbulent dynamic viscosity, Eq. (3.35)
$\boldsymbol{\eta}$	Vector containing the coefficients of each new interfacial friction factor correlation
θ	Pipe inclination angle (positive when flow is upward and negative otherwise)
κ	Interfacial curvature
λ	Characteristics of the general first-order quasi-linear system of Eq. (3.108)
Λ_K	Source term for the phase K 1D Two-Fluid Model momentum conservation equation
μ_K	Dynamic viscosity of phase K
μ_K^{eff}	Effective viscosity of Fullmer *et al.* (2011) of phase K
μ_K^t	Turbulent viscosity of phase K

ν_S	Slug frequency
ξ	Generic variable in Eq. (4.27)
π	Geometrical constant, $\pi = 3.14159\ldots$
$\rho_{\mathcal{D}}$	Type of weighted average density for the dynamic pressure of Bestion (1990)
ρ_K	Density of phase K
σ	Interfacial (surface) tension
ς	Sub-relaxation factor
τ_i	Interfacial shear stress
τ_i^*	Effective interfacial shear stress
τ_{i0}	Smooth interfacial shear stress
τ_{wK}	Wall shear stress of phase K
$\boldsymbol{\phi}$	Vector of perturbations added to $\boldsymbol{\Phi}_0$
$\boldsymbol{\phi}_{\mathcal{A}}$	Vector of amplitudes of the perturbation $\boldsymbol{\phi}$
Φ_j	Each variable in $\boldsymbol{\Phi}$, $j \in \{1, \ldots, N\}$
$\boldsymbol{\Phi}$	State vector that contains the variables of the general first-order quasi-linear system of Eq. (3.108).
$\boldsymbol{\Phi}_0$	Base steady, in time and spatially, state vector
ψ	General/example variable
Ψ_K	Parameters of phase K defined in Eqs. (3.27) and (3.28)
ω	Angular frequency of perturbations or interfacial waves

Subscripts

$\mathscr{a}$	Generic subscript
crit	Related to the appearance of interfacial waves
exp	Related to the experimental/measured value
e	Related to the face e of the mesh
E	Related to the nodal point $\mathbf{E}$ of the mesh
ee	Related to the face ee of the mesh
EE	Related to the nodal point $\mathbf{EE}$ of the mesh
$\mathscr{f}$	Generic subscript
G	Related to the gas phase
i	Related to the interface

in	Related to the inlet section conditions of the pipe
K	Related to the gas or liquid phase, $K \in \{G, L\}$
lam	Related to the laminar regime
L	Related to the liquid phase
M	Related to the mixture
max	Related to a maximum value
min	Related to a minimum value
out	Related to the outlet section conditions of the pipe
pm	Related to calculations by the Point Model
P	Related to the nodal point **P** of the mesh
ref	Related to reference variables
$\mathscr{S}$	Related to an air-water system at 1atm and 20°C
SF	Single-phase monitor variable
$SF_{\mathscr{sp}}$	Single-phase monitor variable critical value
t2D	Related to the appearance of two-dimensional waves at the interface, according to Tzotzi & Andritsos (2013)
tKH	Related to the appearance of Kelvin-Helmholtz waves at the interface, according to Tzotzi & Andritsos (2013)
turb	Related to the turbulent regime
w	Related to the face w of the mesh
W	Related to the nodal point **W** of the mesh
ww	Related to the face ww of the mesh
WW	Related to the nodal point **WW** of the mesh

Superscripts

0	Related to a previous time step
it	Related to the iteration it
$\mathscr{pi}$	Related to the previous iteration

Operators

σ_ψ	Standard deviation of ψ
$\tilde{\psi}$	Variable calculated through the upwind scheme
$\check{\psi}$	Variable calculated as an arithmetic mean

$\langle\psi\rangle$	Mean value of ψ
$\bar{\psi}^A$	Area-average of ψ
$\overline{\psi_K}^{\alpha}$	Volumetric-fraction-weighted mean of ψ for phase K

"Two roads diverged in a wood, and I –
I took the one less traveled by,
And that has made all the difference."
(Robert Frost)

" - Por que renuncias à luta?
- Perdi as esperanças.
- Pois luta sem esperanças!
- Mas, se perdi a fé?
- Luta sem fé!
- Mas se me abandonaram?
- Persiste sozinho. Faze de teu coração uma lança, de teu peito um escudo, segue
o impulso do teu braço, e fere o último esforço do teu desespero. "
(Mário Ferreira dos Santos)

"(...) mas dispusestes tudo com medida, quantidade e peso"
(Sb 11,20)

1. INTRODUCTION

In the oil & gas industry, both acquired data and projections show that the rate of increase of the conventional oil sources (crude oil and natural gas liquids) production has being diminishing at least for a decade, due to the depletion of traditional petroleum fields (I.A.E., 2015). This is the case, for example, of the Norwegian conventional crude oil production, which fell from 1.80×10^{8} Sm^3, in 2001, to 0.94×10^{8} Sm^3 in 2016 (Norsk Petroleum, 2017), as it can be seen in Figure 1.1.

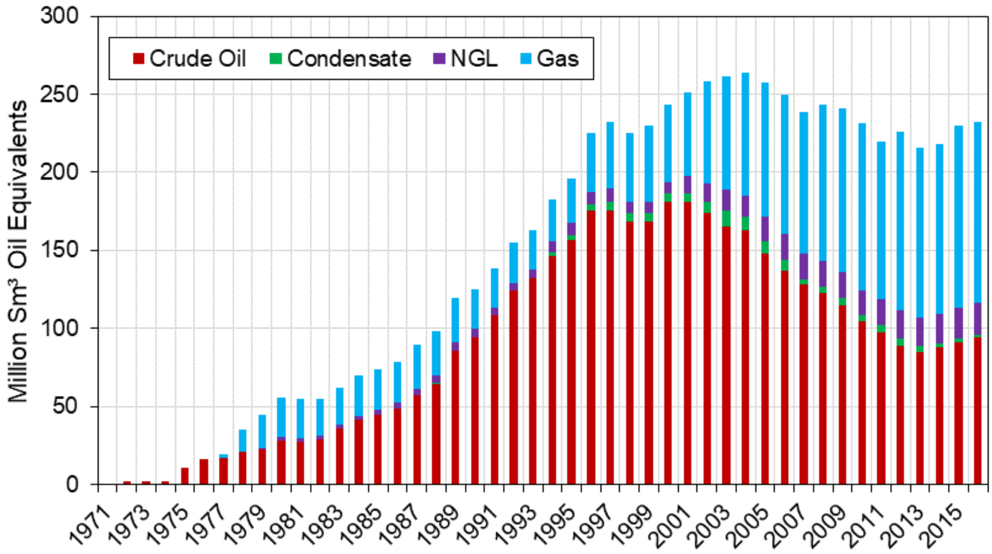

Figure 1.1 – Norwegian annual crude oil, condensate, NGL (Natural Gas Liquid) and gas production from 1971 to 2016. Data extracted from Norsk Petroleum (2017).

At the same time, there has been a significant increase in the demand for the exploitation of unconventional oils, which tends to continue according to projections made for several scenarios, as shown in Figure 1.2, according to the *World Energy Outlook 2014* (I.A.E., 2015).

The *Schlumberger Oilfield Glossary* (Schlumberger, 2017) defines an unconventional oil as a umbrella term (also applied to gases) that covers oil resources "whose porosity, permeability, fluid trapping mechanism, or other characteristics differ from conventional sandstone and carbonate reservoirs". That is why Zee Ma & Holditch (2016) go further and define unconventional oils as "subsurface hydrocarbon resources that are tight and must be developed using large hydraulic fracture treatments or methods", i.e., non-standard techniques. Among unconventional oils, besides tar sands and shale and tights oils, heavy oils (specific gravity lower than 22.3°API) are a notable example of unconventional oils (Zee Ma & Holditch, 2016; Schlumberger, 2017). Usually, such oils also have a dynamic viscosity (henceforth referred to as just "viscosity") much higher than the 1cp, which is, the viscosity of water, and it has the same order of magnitude than the viscosity of most conventional oils in standard conditions. For this reason, the study of the thermo-hydrodynamic features of flows in production lines containing viscous oils is a subject that has been attracting many researches and engineers in the oil & gas industry. Improving the efficiency and costs of such enterprise is always a desirable goal, even in periods of time in which the oil barrel price is low (Figure 1.3).

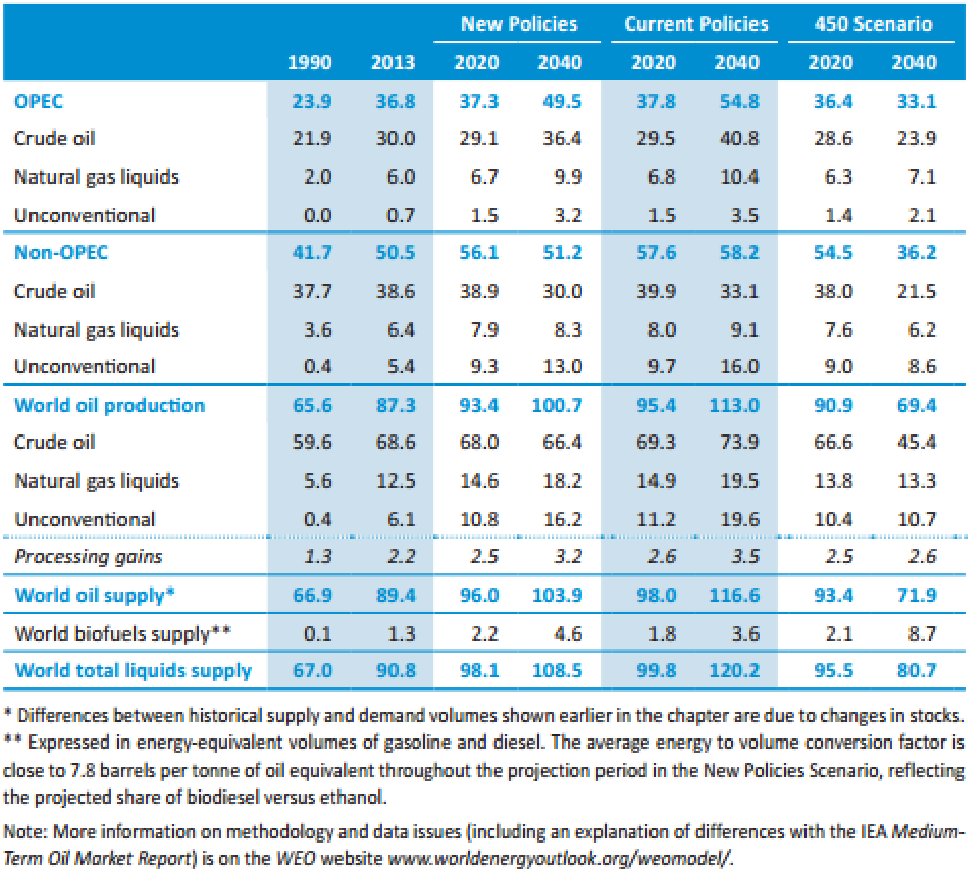

			New Policies		Current Policies		450 Scenario	
	1990	2013	2020	2040	2020	2040	2020	2040
OPEC	**23.9**	**36.8**	**37.3**	**49.5**	**37.8**	**54.8**	**36.4**	**33.1**
Crude oil	21.9	30.0	29.1	36.4	29.5	40.8	28.6	23.9
Natural gas liquids	2.0	6.0	6.7	9.9	6.8	10.4	6.3	7.1
Unconventional	0.0	0.7	1.5	3.2	1.5	3.5	1.4	2.1
Non-OPEC	**41.7**	**50.5**	**56.1**	**51.2**	**57.6**	**58.2**	**54.5**	**36.2**
Crude oil	37.7	38.6	38.9	30.0	39.9	33.1	38.0	21.5
Natural gas liquids	3.6	6.4	7.9	8.3	8.0	9.1	7.6	6.2
Unconventional	0.4	5.4	9.3	13.0	9.7	16.0	9.0	8.6
World oil production	**65.6**	**87.3**	**93.4**	**100.7**	**95.4**	**113.0**	**90.9**	**69.4**
Crude oil	59.6	68.6	68.0	66.4	69.3	73.9	66.6	45.4
Natural gas liquids	5.6	12.5	14.6	18.2	14.9	19.5	13.8	13.3
Unconventional	0.4	6.1	10.8	16.2	11.2	19.6	10.4	10.7
Processing gains	*1.3*	*2.2*	*2.5*	*3.2*	*2.6*	*3.5*	*2.5*	*2.6*
World oil supply*	**66.9**	**89.4**	**96.0**	**103.9**	**98.0**	**116.6**	**93.4**	**71.9**
World biofuels supply**	0.1	1.3	2.2	4.6	1.8	3.6	2.1	8.7
World total liquids supply	**67.0**	**90.8**	**98.1**	**108.5**	**99.8**	**120.2**	**95.5**	**80.7**

* Differences between historical supply and demand volumes shown earlier in the chapter are due to changes in stocks.
** Expressed in energy-equivalent volumes of gasoline and diesel. The average energy to volume conversion factor is close to 7.8 barrels per tonne of oil equivalent throughout the projection period in the New Policies Scenario, reflecting the projected share of biodiesel versus ethanol.

Note: More information on methodology and data issues (including an explanation of differences with the IEA *Medium-Term Oil Market Report*) is on the *WEO* website *www.worldenergyoutlook.org/weomodel/*.

Figure 1.2 – Projections for oil demands in three different scenarios. Extracted from the *World Energy Outlook 2014* (I.E.A., 2015).

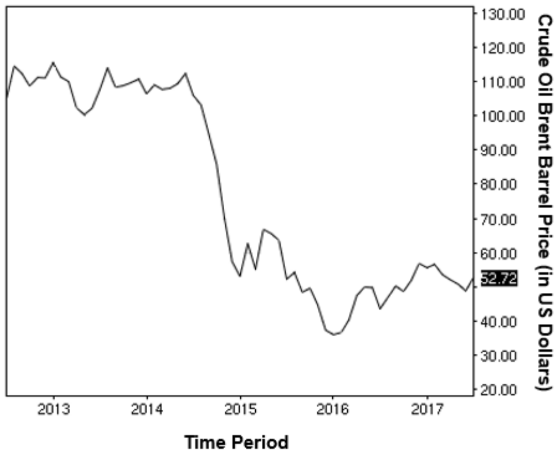

Figure 1.3 – Crude Oil Brent in a five years time period with the current price highlighted. Adapted from NASDAQ (2017).

In flows of oils (not just the viscous ones) in petroleum production lines often more than one phase is present due to the common co-existence, with the liquid oil, of natural gas, water, sand, gravel and flow assurance solids (hydrates, scales, waxes, asphaltenes, among others), which characterizes a multiphase flow.

The use of numerical tools for investigating, making predictions and assisting in the design of pipelines in which such flows shall take place is of paramount importance. The one-dimensional (1D) simulations play an important role in these activities for the fact that the geometries involved in oil production are usually pipelines that span kilometers, so that, two- (2D) or three-dimensional (3D) models are excessively costly in a computational perspective. This is especially seen in the vast use of the 1D commercial multiphase flow simulators such as Olga (Bendiksen *et al.*, 1991) and LedaFlow (Danielson *et al.*, 2005) by the oil & gas industry.

The three most important 1D approaches for simulating gas-liquid flows are the Unit-Cell Model (Dukler & Hubbard, 1975), the Slug Tracking Methodology (Nydal & Banerjee, 1996) and the Regime Capturing Methodology (also known as Slug Capturing Methodology) (Issa & Kempf, 2003; Nieckele & Carneiro, 2017). The Unit-Cell Model is the most used from the three, for having a low computational cost and a satisfactory robustness. Nevertheless, it is highly dependent on empirical and semi-empirical correlations directly related to the flow pattern, and their accuracy always decays for conditions outside the ones for which they were created. Although it is also not computationally costly, the Slug Tracking Methodology, likewise, suffers from excessive dependency on empirical expressions for the slug features, especially from the one that defines their presence.

Although demanding more CPU time than the other approaches and having to deal with the stability-hyperbolicity problem (Prosperetti & Tryggvason, 2007), the solution of the 1D Two-Fluid Model (Ishii, 1975) in fine meshes, that is, the Regime Capturing Methodology, is much less dependent on empirical expressions than both the Unit-Cell Model and the Slug Tracking Methodology. This is justified for the interfacial dynamics (growth of instabilities, slugs appearance, among others) being a natural product of the methodology as well as the flow pattern. With this methodology, the same set of correlations can be used for all the flow patterns, which is in great contrast with the other two approaches. Nevertheless, although very promising and satisfactorily validated for air-water flows (Carneiro *et al.*, 2011; Nieckele *et al.*, 2013; Han & Guo, 2015; Ferrari *et al.*, 2017), this methodology has, with few exceptions, not being much explored for performing 1D simulations of different fluid combinations, especially for viscous oil-gas flows.

One of the greatest challenges in the use of 1D gas-liquid models is the adequate modelling of the interfacial shear stress, for being a parameter in which complex phenomena (interfacial waves, relation between them and the turbulence of the phases, among others) are included (Hanratty, 2013; Ayati *et al.*, 2016; André & Bardet, 2017). For viscous oil-gas flows, an added difficulty is related to the high oil viscosity, which induces several effects on the interfacial dynamics that directly impacts the interfacial shear stress (Andritsos & Hanratty, 1987b; Newton *et al.*, 1999; Matsubara & Naito, 2011). Furthermore, most of the literature correlations for such variable were empirically created based on air-water flows experimental data. This automatically originates uncertainties on the effectiveness of these correlations when applied to viscous oil-gas flows, which may be problematic due to the great influence it has on the 1D simulation results (Ottens *et al.*, 1999; Pasqualette *et al.*, 2015). Adequate expressions for the interfacial shear stress for viscous oil-gas flows is still a gap in the literature and new correlations for it still need to be built.

1.1. Objectives of the Dissertation

With all of this in mind, the main objective of this work is to extend and test the Regime Capturing Methodology for viscous oil-gas flows by addressing the stability-hyperbolicity problem and by the use of two newly proposed correlations for the interfacial shear stress. Simulations with this methodology are performed with the purpose of reproducing the Eskerud Smith *et al.* (2011) experiments, in which the liquid phase is a viscous (viscosity approximately one hundred times the one of the water) mineral oil and the gas is sulfur hexafluoride (SF_6). They flow isothermally in a laboratory-scale horizontal pipe in the stratified wavy and slug flow patterns. Well-posedness analyses are performed for assisting the management of the stability-hyperbolicity problem. An optimization procedure is proposed and used, together with a simplified, steady-state version of the 1D Two-Fluid Model, for the development of the two aforementioned new expressions for the interfacial shear stress. Then, the new correlations are tested in a transient Two-Fluid Model for various mesh spacings, in a Regime Capturing Methodology fashion. Different closure models related to the dynamic pressure, axial diffusion and dynamic interfacial shear are tested along with the different interfacial friction expressions, in order to investigate the stabilizing/destabilizing effects on the transient interfacial dynamics.

1.2. Structure of the Dissertation

Primarily, a vast literature review and a theoretical background is provided to the reader on key themes for illustrating much that was previously mentioned and for more precisely defining the gaps in literature. Afterwards, the Regime Capturing Methodology is fully presented in its modelling (the 1D Two-Fluid Model) and numerical aspects (the numerical method), together with the formulation of the well-posedness (characteristic) analysis for the model. Then, the optimization procedure proposed for conceiving the two new expressions for the interfacial shear stress is detailed. In the following chapter, the results of the well-posedness analyses and of the Regime Capturing Methodology simulations for the selected Eskerud Smith *et al.* (2011) database cases in the stratified wavy and slug flow patterns are presented, compared to the measurements and discussed. Focus is dedicated to the performance of the two new expressions for the interfacial shear stress in the methodology and to the effect of different terms of the 1D Two-Fluid Model on the interfacial dynamics. Finally, concluding remarks are presented, together with suggestions for future works.

2. LITERATURE REVIEW AND THEORETICAL BACKGROUND

In this chapter of the work, the literature review considered important for this work is presented together with some theoretical background. It is worth to highlight that a basic knowledge of the reader on multiphase flow is assumed, in which we include subjects often present in the initial pages of textbooks of the area (Brennen, 2005; Hanratty, 2013). These are, mostly, the flow pattern classification (annular, stratified smooth, stratified wavy, roll waves, slug, churn, among others) and elementary terminology, that is, the labelling of key parameters in gas-liquid flows. The topics covered in this literature review and theoretical background are important for understanding the contribution of this work and how it is inserted in the ongoing development of the technology chosen as theme of the former, reason why several observations and statements made in this chapter are invoked in the following ones.

The first theme discussed is the influence of the liquid viscosity on essential features of gas-liquid horizontal flows, such as how the transitions between flow patterns change, always considering air-water flow as reference. Afterwards, an overview of the state-of-art 1D modelling of gas-liquid flows is given, in which it is discussed the most used mathematical models and approaches. Special attention is dedicated to vital literature works that used the Regime Capturing Methodology to simulate gas-liquid flows, one of the 1D modelling strategies reviewed, which are presented and discussed. The third theme chosen is the stability-hyperbolicity problem of the 1D Two-Fluid Model of Ishii (1975), which is one of the most important mathematical models in literature for performing 1D simulations of two-phase flows and which often faces the issue of ill-posedness in the Hadamard (1902) sense, described in Drew & Passman (1999) and in Prosperetti & Tryggvason (2007). The fourth and last topic introduces the main strategies and expressions for representing the interfacial shear stress in the 1D Two-Fluid Model as a closure relation for gas-liquid horizontal stratified flows. It is highlighted how such parameter is affected by the presence of interfacial waves.

The first and third topics are presented primarily to provide the reader the findings of key works in a chronological order and, then, a summary of what can be concluded from them. In the other topics, however, important points are used as guidelines for the presentation, rather than the key works found in literature and referenced herein. A summary is also provided for these other topics, though.

2.1. Influence of the Liquid Viscosity on Gas-Liquid Horizontal Flows

Taitel & Dukler (1976) were the first authors to systematically address the transitions from stratified flow to other flow patterns. In Figure 2.1 (U_{sL} and U_{sG} are the superficial velocities of the liquid and gas, respectively), the flow pattern map of Taitel & Dukler (1976) (extracted from the same work) is compared to the one of Mandhane *et al.* (1974) for a horizontal air-water flow in a 2.5cm ID at 25°C and 1atm. Although the semi-theoretical model of Taitel & Dukler (1976) does account indirectly for the influence of fluid properties, important underlying assumptions do not hold for stratified viscous-oil and gas flows.

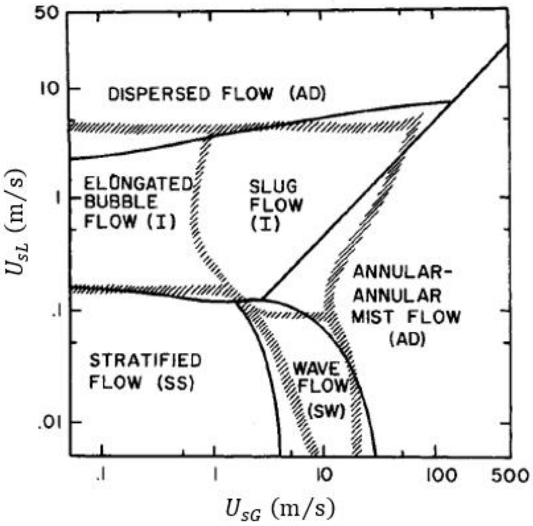

Figure 2.1 – Flow pattern map of Taitel & Dukler (1976) for a 25°C, 1 atm air-water horizontal flow in a 2.5cm I.D. pipe compared against the map of Mandhane *et al.* (1974). Figure adapted from Taitel & Dukler (1976).

The description of key works that concern the influence of the liquid viscosity on gas-liquid horizontal flows begins with the paper of Weisman *et al.* (1979). They were one of the first groups of researchers to address, in a systematic experimental investigation, the impact of important flow parameters, such as the liquid viscosity, on the flow pattern maps. They performed experiments in a 2-inch internal diameter 6.1m long pipe with air and two different solutions of water and glycerol: one with 75cp and the other with 150cp of liquid viscosity. They constructed flow pattern maps, using the mass flow rate as variable, for these two pairs of fluids and noticed little change with the increase in the liquid viscosity regarding the major flow patterns, i.e., separated, intermittent and dispersed. Among these little variations, it can be highlighted that the transition to slug flow was shifted to lower liquid mass flow rates (particularly at high gas mass flow rates) and that the transition to annular flow was shifted to slightly higher gas mass flow rates. In addition, it can be mentioned that much of the plug flow (similar to slug flow, but with no slug aeration) region in the map became slug flow.

Almost a decade after the work of Weisman *et al.* (1979), Andritsos & Hanratty (1987a) published a research paper in which they looked into the interfacial waves characteristics in gas-liquid horizontal flows and the transition from stratified smooth to stratified wavy flow. Their work was mainly experimental, but they also used a linear stability analysis in which a perturbation is added to the liquid phase height. With the latter, they discovered that the increase in the liquid viscosity makes it more difficult to predict the transition from stratified smooth to stratified wavy flow with two-dimensional (2D) waves. Besides, they uncovered that the initiation of waves for high-viscosity liquids is governed by the Kelvin-Helmholtz mechanism. Andritsos & Hanratty (1987a) performed experiments with air and four solutions of water and glycerol in 2.52cm and 9.53cm internal diameter pipes. The viscosity of the referred solutions are of 4.5cp, 12cp, 70cp and 80cp. They observed that the superficial velocities range in which 2D waves in the stratified wavy flow exist is insignificant for the liquids with high viscosities. Mostly, the waves are three-dimensional (3D) and irregular, which they label as Kelvin-Helmholtz waves. However, Andritsos & Hanratty (1987a) also verified that the interfaces appear to be less rough when waves are present for the liquids with higher viscosities. Nevertheless, they state that the interfacial shear stress should have a significant increase due to the presence of waves at the interface.

The work of Andritsos *et al.* (1989) used the same experimental setup and fluids of Andritsos & Hanratty (1987a) to analyze the transition between horizontal stratified and slug flows, by revisiting the findings of Lin & Hanratty (1986). The latter observed that an increase in the liquid viscosity stabilizes the flow and consequently diminishes the initiation of slugs. This was confirmed by the new experiments of Andritsos *et al.* (1989). Lin & Hanratty (1986) also remarked that the transition to slugs occur through the growth of long wavelength interfacial instabilities with the increase of gas superficial velocities. However, Andritsos *et al.* (1989) confirmed this phenomenon only for low-viscosity liquids, while, for the high-viscosity liquids, small wavelength instabilities appear primarily. They might grow and bridge the pipe section, forming slugs, or might coalesce and give birth to long wavelength waves, which might develop into slugs. For this reason, Andritsos *et al.* (1989) confirmed that the inviscid stability analysis of Lin & Hanratty (1986) could only predict the transition from stratified to slug flow for air-water experiments, and it did not manage to capture the same phenomenon for liquids with higher viscosities.

Nädler & Mewes (1995) performed an experimental investigation on the effect of liquid viscosity on the phase distribution in gas-liquid slug horizontal flow. Air was used as the gas phase and, as the liquid phase, two oils (one with 14cp of viscosity and other with 37cp) and water were used. The measurements were conducted in a 59mm internal diameter pipe with a total length of 12m. The main finding of Nädler & Mewes (1995) was that, by increasing the liquid viscosity, the liquid holdup of the slugs barely changes. Besides, they verified that the mean liquid holdup of the flow also increases with the liquid viscosity.

Newton *et al.* (1999) performed experiments in gas-liquid horizontal flows for assessing the effectiveness of commonly used interfacial shear stress correlations for liquids with higher viscosities. The necessity of such work originated from the fact that most of such correlations were elaborated and validated for air-water experimental databases. This creates uncertainty when they are used for viscous liquids, especially when waves are present at the interface, which cause effects on the flow whose understanding is far for being complete even for low-viscosity liquids. Newton *et al.* (1999) used a 12m long 50mm internal diameter pipe for performing their measurements, with air as the gas phase and they switched between tap water (1cp of liquid viscosity), kerosene (2cp) and a light machine oil (46cp) to serve as liquid phase. Their analysis showed that the commonly used correlations for the interfacial shear stress are inadequate for liquids whose viscosity is higher than its value for water. Newton *et al.* (1999) also proposed new correlations for the interfacial shear stress.

Aiming to identify effects of very high-viscosity oils on the flow, Gokcal (2008) measured the slug characteristics (length, holdup, frequency, among others) for horizontal and slightly inclined flows of air and an oil of that nature. The viscosity of the chosen oil was approximately 650cp at 20°C and he used an experimental setup composed by an 18.9m long 50.8mm internal diameter pipe. Using the relation for the slug translational velocity U_t, which can be calculated through Eq. (2.1) (C_o is a coefficient, U_M is the mixture velocity and U_d is the drift velocity), Gokcal (2008) verified that increasing the liquid viscosity also increases the values of the drift velocity, thus, classical correlations cease to be valid for such conditions.

$$U_t = C_o U_M + U_d \tag{2.1}$$

In addition, he confirmed the value of approximately 2.0 for C_o in the case of laminar flow within the slugs (Wallis, 1969), which is significantly different from usual values found for turbulent flows, i.e., in the range of 1-1.2 (Hanratty, 2013). Gokcal (2008), furthermore, assessed that the slug length and frequency decrease and increase, respectively, as the liquid becomes more viscous.

Foletti *et al.* (2011) elaborated a flow pattern map for air and a highly viscous oil (approximately 900cp of liquid viscosity) with a series of experiments performed in a 9m long 22mm internal diameter pipe. They obtained a very poor agreement between their experimental map and the ones obtained through classical methodologies. In addition, they verified that, while in air-water flows the slug flow can be described by the alternate passage of dispersed (liquid slug) and stratified flow (liquid film region), for high-viscosity liquids it is better characterized as an alternation between dispersed and an eccentric annular flow, due to the constant presence of liquid in the pipe walls. It is important to remind that Eq. (2.1) is also valid for the translational velocity U_b of long bubbles in slug flow and that it is approximately equal to the translational velocity of slugs for a fully-developed flow in dynamic equilibrium. Foletti *et al.* (2011) found a value of 2.14 for C_o. Furthermore, the authors tested standard mechanistic models for evaluating the pressure gradient and the long bubbles length for the slug flows and, they obtained unsatisfactory agreement with the experimental data.

Matsubara & Naito (2011) investigated the influence of the liquid viscosity on flow pattern maps, in order to verify the findings of Weisman *et al.* (1979), which, as previously mentioned, stated that such maps do not change much with the increase in the referred property. They performed experiments in a 19m long 22mm internal diameter pipe using air as the gas phase. For the liquid, they considered water and some aqueous solution of polysaccharide thickener, whose viscosity had values of 100cp, 250cp, 2500cp, 7500cp and 11000cp. Matsubara & Naito (2011) found out that increasing the liquid viscosity makes the flow pattern maps differ significantly from those produced through the Taitel & Dukler (1976) method. Therefore, they verified that the liquid viscosity does play a significant role in the flow pattern maps, which is the contrary of what was observed by Weisman *et al.* (1979). This is seen mainly through the displacement in the maps, for increasing liquid viscosities, of the stratified and roll wave regions for intermittent and annular flows, respectively. In addition, Matsubara & Naito (2011) observed that the predictions of the Taitel & Dukler (1976) flow map for high-viscosity oils improve if one considers that the interfacial friction factor is various orders of magnitude higher than the gas friction factor.

In the paper of Eskerud Smith *et al.* (2011), whose experimental database is going to be used in this work and whose main features were already previously described, the prediction of the point-model of the Olga flow simulator (Bendiksen *et al.*, 1991) were compared against the measurements of pressure drop and liquid holdup and the observed flow patterns. For the low-viscosity oil data, the Olga point-model predictions agreed well with the experimental data, which was not the case for the measurements regarding the highly viscous oil. The use of the Slug Tracking module of Olga for performing dynamic simulations managed to improve the results for such oil, but not in a significant manner. Eskerud Smith *et al.* (2011) also tested several literature correlations for the interfacial friction factor and compared their evaluations with the values calculated from the experimental data, but none of the expressions had a positive overall performance. This will be explored later more thoroughly.

For investigating the effects of the high liquid viscosity on the characteristics of gas-liquid horizontal flows, Zhao *et al.* (2013) conducted a series of experiments in a 5.5m long 26mm internal diameter pipe. They used air as the gas phase and several types of oils as the liquid phase, with viscosities ranging from 1000cp to

7500cp. Regarding the flow patterns observed, Zhao *et al.* (2013) obtained in their experiments slug, plug, annular and blow-through-slug (a transitional pattern between slug and annular) flow. The most present flow pattern was slug flow, followed by plug flow, which indicates that intermittent flow dominates the flow pattern map for these fluids and setup. In the slug flow, a thin oil film was observed above the long bubbles and stratified flow was not observed for any flow rates covered in their measurements. Zhao *et al.* (2013) measured the liquid slug holdup and found no significant impact of liquid viscosity on such parameter. They observed that both the mean liquid holdup of the flow and its pressure gradient increase with the liquid viscosity. In addition, they used mechanistic models for predicting these parameters of the flows. Good agreement against the experiments was obtained only for cases with smaller viscosity, as well as low liquid velocity.

Using air and a high-viscosity oil (900cp), Farsetti *et al.* (2014) performed experimental tests of gas-liquid flow in a nearly horizontal 9m long 22.8mm internal diameter pipe. They focused their work on the intermittent flow patterns and assessed the pressure gradient, the bubble translational velocity, the slug frequencies, the slug lengths, the bubble lengths and the mean slug liquid holdup. The measured values are compared to predictions made by widely used simple models and correlations that were validated mostly against low-viscosity liquid experimental data. The poor agreement obtained led to the conclusion that the models and correlations tested cannot be extrapolated to gas-liquid flows in which the liquid is highly viscous.

2.1.1. Summary

In summary, one can list the following effects of the increase of liquid viscosity in gas-liquid horizontal flows:

- The liquid phase tends to become laminar;
- Both the pressure gradient and the mean liquid holdup tend to increase;
- The predictability of mechanistic models, correlations and expressions elaborated and validated against experimental data of low-viscosity liquids usually become unsatisfactory;
- Increase of the intermittent (slug flow, plug flow, among others) and

annular flow regions with simultaneous decrease of the stratified and roll waves flow regions is observed in flow pattern maps;

- Regarding the stratified flow, the occurrence of smooth interfaces becomes rare and, therefore, wavy interfaces appear more often, especially with short wavelengths and are governed by the Kelvin-Helmholtz mechanism;
- Slug flow is often better described as an alternation between dispersed flow and an eccentric annular flow, due to the constant presence of a thin liquid film which wets the pipe wall;
- When the flow pattern is slug (or plug) flow, the average slug length diminishes, the slug frequency increases and the coefficient C_0 increases from 1.2 to 2.0 as the liquid becomes laminar. The tendency of the slug liquid holdup is to barely change;
- The interfacial friction factor tends to increase when compared to flows with lower viscosity liquids at similar conditions

2.2. Overview of the 1D Modelling of Gas-Liquid Flows

In the first chapter of this work, the importance of 1D models of gas-liquid flows for the industry in general and especially for the oil and gas industry was explained. It is also important to highlight that the focus of this overview is in the hydrodynamics of the flow, which is represented, primarily, by the mass and momentum conservation equations.

The 1D models of gas-liquid flows can be divided according to the mathematical formulation chosen for representing the flow, i.e., the set of conservation equations (Nydal, 2012). While "Multi-Fluid" approaches deal with sets of conservation equations for each phase, "One-Fluid" approaches treat all phases as a single mixture (Prosperatti & Tryggvason, 2007). This is often directly dependent on the degree of coupling between the phases, which varies, for example, depending on the flow patterns (Ishii & Hibiki, 2011). If the gas and liquid phase momenta are treated as two different fields, for which separate balance equations are formulated, and similarly for mass and energy, the mathematical model for representing the gas-liquid thermo-fluid-dynamics is known as the 1D Two-Fluid Model (Ishii, 1975). Gas and liquid phase mass, momentum and energy equations are coupled through source terms representing interfacial interactions. Otherwise, if a single field formulation is chosen, Mixture Models (Nydal, 2012) can be formulated from the more general Multi-Fluid equations. In this approach, the bulk velocities of each phase are calculated for example from the mixture velocity through some drift relations (Zuber & Findley, 1965), reason why such approach is often labeled as 1D Drift-Flux Model. The latter is widely used in the literature, such as in the works of Malekzadeh *et al.* (2012) and Santim *et al*. (2017). In the former, a drift-flux model was used for performing 1D simulations of severe slugging in a pipeline-riser system. In Santim *et al.* (2017), the authors simulated gas-liquid slug flow, analyzing pressure and void waves propagation with a 1D drift-flux model and compared it with other methodologies. If no-slip is assumed between phases, the so-called 1D Homogeneous Model (Coelho *et al*., 2016) is a special case of the 1D Drift-Flux approach.

The 1D Two-Fluid Model is the main interest of this work and its formulations, intrinsic hypotheses and more particular features are going to be detailed later. This model has two main issues: one related to the stability-hyperbolicity property, which may lead to an ill-posed problem; and the other related to the selection of closure models. In fact, the choice of closure models also affects the stability and hyperbolicity of the Two-Fluid Model. Both aspects will be thoroughly explored in the present work.

The ill-posedness issue is widely known in the literature and usually manifests in fine mesh resolutions. Nevertheless, the 1D Two-Fluid Model is widely used and the most common strategy is the use of coarse spatial and temporal meshes, for avoiding an excessively high computational cost. This is specially the case of standard engineering simulations of long pipelines. One example may be taken from Figueiredo *et al.* (2016), who analyzed horizontal gas-liquid stratified flow in gas pipelines.

In order to capture "small-scale" instabilities at the gas-liquid interface, one needs to employ very fine grid resolution, often of the order of the pipe diameter or less (Nydal, 2012; Nieckele & Carneiro, 2017). The definition of "large-scale" and "small-scale" is of course dependent on the problem requirements. Alves *et al.* (2016), for example, numerically investigated annular and churn vertical gas-liquid flows by solving a hyperbolic 1D two-fluid model. The grid sizes were sufficiently fine to capture "large-scale" instabilities associated to the annular-churn transition, but local instabilities (such as large amplitude waves in annular flows, for example) were not resolved.

When coarse meshes are employed to solve the 1D Two-Fluid Model one must consider two important factors, which may affect the quality of predictions: possibility of truncation errors due to the discretization process and the inadequate representation of sub-mesh phenomena. This issue is particularly critical, because some small-scale events are too complex to be correctly accounted for with simple and standard closure relations. The different concepts that are commonly employed for representing the small-scale effects in the 1D Two-Fluid Model are listed below (Nydal, 2012):

- The transient Unit-Cell Model;
- The Regime-Capturing Methodology;
- The Hybrid Tracking-Capturing Methodology.

Originally, the Unit-Cell Model (Dukler & Hubbard, 1975) was first developed for performing steady-state 1D gas-liquid flow simulations in which simple mass, momentum and, when necessary, energy balance equations are written for a unit-cell, which is the basic configuration of the model and consists in a liquid slug body and a long bubble with a liquid film region. After forming a system of algebraic equations, adopting the necessary closure relations, it is solved for evaluating the global flow parameters. In spite of its strong dependence on correlations, the Unit-Cell Model is interesting, because, besides its low computational cost, it considers the slug flow as the standard flow pattern, which, through the calculated values of slug body length and liquid film region, may also implicitly incorporate dispersed or separated (annular or stratified) flow. If the slug body length is null, the flow pattern is considered separated flow, while dispersed bubbly flow occurs if the film region disappears. Orell (2005) used the Unit-Cell Model by performing 1D simulations of several air-water and air-oil flows for various pipe configurations and obtained good agreement against experimental data. The Unit-Cell Model was then combined with the 1D Two-Fluid Model, providing information for the closure relations (or sub-mesh model) for evaluating the source terms of the momentum equation, in an approach often labeled as "transient Unit-Cell Model". This approach is formulated for example in Bendiksen *et al.* (1996) and has been used by several investigators such as in Cazarez-Candia *et al.* (2011), in which the flow in an oil well was simulated. The transient Unit-Cell Model is the basic framework of commercial multiphase flow 1D simulators of the oil and gas industry, such as Olga and LedaFlow (Danielson *et al.*, 2005), for its versatility and the possibility of using coarse meshes.

A different approach with the 1D Two-Fluid Model is simply to use finer meshes for numerically solving it, with different closure relations for representing small-scale effects. Issa & Kempf (2003) proved that, for an isothermal gas-liquid horizontal pipe flow initially with a stratified flow configuration, it is possible through such procedure to capture the initiation and dynamics (growth, decay, coalescence, among others) of interfacial instabilities and their development into hydrodynamic slugs in a successful way. Consequently, this methodology was originally labeled as “Slug Capturing Methodology”, although some authors simply refer to it as “Capturing Methodology” (Nydal, 2012). In this work, this approach is labeled as “Regime Capturing Methodology” (Nieckele & Carneiro, 2017), because it will also be employed to capture interfacial waves in stratified flow. In fact, Nieckele & Carneiro (2017) have demonstrated the possibility of capturing several flow regimes as a natural outcome of the solution of the 1D Two-Fluid Model in fine meshes.

The transient Unit-Cell Model provides good results for some integral parameters of the flow (mean liquid holdup, pressure gradient, among others) and it is computationally cheap, but the Regime Capturing Methodology depends less on correlations and provides more detailed information. Nevertheless, it comes with the cost of a substantially higher computational cost when compared to the one of the transient Unit-Cell Model. These two methodologies may also be used in a complementary way, with the transient Unit-Cell Model for analyzing the majority of the flow domain and the Regime Capturing Methodology employed in certain sections of interest of the pipeline geometry. The capability is available, for example, in the commercial simulator LedaFlow (Danielson *et al.*, 2005).

A third approach is the Hybrid Tracking-Capturing Methodology of Renault (2007). It combines the best features of the Regime Capturing Methodology and of the Slug Tracking Methodology, which is a 1D Lagrangian scheme that tracks the advancement of the slug fronts and tails throughout the pipelines. In spite of being originally elaborated for simulating hydrodynamic and terrain slugs by Nydal & Banerjee (1996), it has been extended to track roll waves (De Leebeeck & Nydal, 2010). The Slug Tracking Methodology, or just Tracking Methodology (Nydal, 2012) has the advantage of being computationally cheap when compared to the Regime Capturing Methodology, also with less grid dependency. Eskerud Smith & Nydal (2016), for example, successfully used this methodology for simulating nitrogen-naphtha severe slugging cases in a 1km long pipeline pressurized at 25 bar. Nevertheless, the major drawback of this approach is being dependent on user input for slug initiation and some empirical correlations imposing slug flow parameters. With this in mind, Renault (2007) proposed a hybrid procedure in which the simulations start as a Regime Capturing Methodology and, if it detects that a slug was formed, it switches to the Slug Tracking Methodology, originating, then, the Hybrid Tracking-Capturing Methodology.

2.2.1. The Regime Capturing Methodology for Gas-Liquid Flows

Before beginning to describe the features of key literature works that have used the Regime Capturing Methodology, it is important to mention that it is not the purpose of this review to reproduce neither the exact mathematical model nor the numerical methodology used in each work. Solely their main aspects will be characterized, since the complete formulation of the methodology will be detailed later in this work.

Having said that, the work of Issa & Kempf (2003) was the first to show that, under certain conditions, the solution in fine meshes of the 1D Two-Fluid Model was capable to capture the appearance of slugs starting from a stratified flow pattern. The used model consisted in two sets of mass and momentum equations, for gas and liquid phases. They validated the methodology using experimental data from an air-water slug flow in a 36m long pipe with a 78mm internal diameter for two configurations: one horizontal and or downwardly inclined by 1.5°. Issa & Kempf (2003) also used air-water experimental data for a V-section composed by a downhill pipe of 14m and an uphill pipe of 23m, both with 78mm of internal diameter and inclinations of 1.5°. Through a simplified analysis and mesh convergence tests, Issa & Kempf (2003) found that the simulated cases were well-posed.

Bonizzi & Issa (2003) expanded the work of Issa & Kempf (2003) by adding the possibility of mechanical gas entrainment and disengagement into the liquid phase. The process of gas entrainment (or aeration phenomenon) in slug flow mainly takes place at the slug front. The liquid slug usually moves faster than the film ahead of it, creating a highly turbulent zone at the bubble rear. The gas deposition (or disengagement, or reabsorption of the bubbles by the gas phase) happens at the slug tail because of the slip between the bubbles, which move slower, and the liquid slug body. Bonizzi & Issa (2003) rewrote the mass and momentum equations for the liquid phase for representing the mixture of liquid and bubbles and added to the system of governing equations a mass conservation equation of the gas bubbles. Bonizzi & Issa (2003) observed an improvement on the predictions of the Regime Capturing Methodology by considering the aeration of the slugs, using the same experimental database employed by Issa & Kempf (2003).

The work of Bonizzi *et al.* (2009) expanded even more the concept adopted by Bonizzi & Issa (2003) by accounting for the possibility of entrainment and deposition of liquid droplets in the gas phase and their dynamics for isothermal horizontal gas-liquid flows. The entrainment of droplets in the gas phase can be caused by their impact on the liquid phase, wave undercut, rupture of bubbles located near the interface and, the most important of them, the atomization of the crest of large-amplitude interfacial waves (Ishii & Grolmes, 1975). The deposition of droplets occurs due to the trajectory mechanism, but, mostly, due to the turbulent fluctuations of the droplets in the gas phase and the gravitational effects (Mito & Hanratty, 2007). This topic is out of the scope of this work. In their formulation, Bonizzi *et al.* (2009) defined the “fields” as continuous liquid, continuous gas, dispersed liquid (droplets) and dispersed gas (bubbles), the “layers” (or mixtures) as the combinations of bubbles and continuous liquid and of droplets and continuous gas. They used a mass conservation equation for each field and a momentum equation for the two layers. Their model was validated against several experimental data and they showed that it can satisfactory predict the transition of an initially stratified air-water horizontal flow to slug, annular and bubbly flow. The possibility of ill-posedness was discarded by Bonizzi *et al.* (2009) after performing a few mesh convergence tests.

Carneiro *et al.* (2011) used a Regime Capturing Methodology similar to the one of Issa & Kempf (2003) for simulating isothermal air-water slug flow cases in a horizontal 10m long 24mm internal diameter pipeline. The obtained values of the slug and long bubble statistics (slug frequency, long bubble length, slug length, long bubble translational velocity and slug translational velocity) were compared to experimental data and a good agreement was obtained.

In their work, Nieckele *et al.* (2013) used the same model as Carneiro *et al.* (2011) for performing a more detailed statistical analysis of the slug and bubble lengths, obtaining excellent results and convergence with the experimental data.

Emamzadeh & Issa (2013a; 2013b) used a version of the Regime Capturing Methodology that can be seen as an adaptation of the one developed in Bonizzi & Issa (2003) or a simplification of the one registered in Bonizzi *et al.* (2009). In their mathematical model, for considering the dynamics of droplets in the gas and the mass transfer between the dispersed and continuous liquid fields (entrainment and deposition), they used a mass conservation equation for the droplets along with sets of mass and momentum equations for liquid and mixture of gas and dispersed drops. Emamzadeh & Issa (2013a) used this model for simulating isothermal air-water annular flow in several vertical and horizontal pipes whose internal diameters ranged between 1 and 10cm. By comparing the numerical results of droplet concentration, droplet entrainment rate, liquid film height and pressure gradient, the authors found a satisfactory agreement with measurements. Emamzadeh & Issa (2013b) used the same version of the Regime Capturing Methodology, except for some differences in the closure relations, for testing its ability to predict the transition from an air-water horizontal stratified flow to annular flow. The model was successfully validated against an experimental flow pattern map of literature. In neither of their works, Emamzadeh & Issa (2013a; 2013b) addressed the possibility of ill-posedness of the mathematical model.

Simões *et al.* (2014) used a Regime Capturing Methodology for simulating a non-boiling gas-liquid horizontal flow including heat transfer. Simões *et al.* (2014) considered two sets of mass, momentum and energy equations and neglected the possibility of the presence of dispersed phases. They compared their most important numerical results for a stratified flow in a 20m long 52mm internal diameter pipe against values evaluated with well-established correlations, with good agreement. Further, the model results were compared against an experimental database for slug flow in a pipe with 52mm of internal diameter and 23.81m of total length, also showing very good agreement. The well-posedness of the model was shown by a mesh convergence test performed for the main parameters of the slug flows simulated.

For numerically investigating the severe slugging phenomenon, Han & Guo (2015) used a Regime Capturing Methodology for simulating the isothermal air-water severe slugging phenomenon in a pipeline-riser system. A 114m horizontal pipe was considered, followed by a -2° downward inclined pipe, by a 15.3m vertical riser and a 2m horizontal outlet. The internal diameter was considered constant and equal to 50.8mm. In their model, two sets of mass and momentum equations were used, disregarding any dispersed field, entrainment or deposition process. A simplified hyperbolicity analysis revealed that the model would have issues of ill-posedness in the vertical riser, which was dealt with by adding a dynamic (or interfacial) pressure model to the Regime Capturing Methodology. After validating it for a standard literature test case whose analytical solution is available, Han & Guo (2015) obtained numerical results with excellent agreement with the measurements.

With an almost equal formulation of the Regime Capturing Methodology of Issa & Kempf (2003), Issa & Galleni (2015) performed simulations of vertical isothermal slug flow of air and a liquid with a density of 913.39 kg/m³ and viscosity of 5cp in a 6m long 67mm pipe. They obtained results with a good agreement against experimental data and demonstrated, by mesh convergence tests, that their model does not suffer from ill-posedness.

In their work, Pasqualette *et al.* (2015) used the same Regime Capturing Methodology as Nieckele *et al.* (2013) for simulating isothermal horizontal viscous oil-gas flows. The purpose was to correctly capture the flow pattern transition caused by an increase in the superficial gas velocity for a constant liquid flow rate, starting from a slug flow to stratified wavy flows with large and small interfacial waves. Several literature correlations were tested for the interfacial shear stress, but none managed to adequately capture the aforementioned transition. Pasqualette *et al.* (2017) extended the work of Pasqualette *et al.* (2015), by testing newly made interfacial shear stress correlations.

Fontalvo *et al.* (2016) used an isothermal 1D Two-Fluid Model in the Regime Capturing Methodology framework for simulating interfacial waves in a vertical gas-liquid annular flow. For guaranteeing the hyperbolicity of their model, Fontalvo *et al.* (2016) used and compared three different formulations for a dynamic pressure term added to the momentum balance equations. Their model was validated against air-water flows in a 2m long 1.4-inch pipe using the spectral characteristics (e.g.

dominant frequencies) of the liquid holdup numerical signals.

For simulating the hydrodynamics and heat transfer phenomenon of horizontal annular gas-liquid flows, Silva & Nieckele (2016) employed the Regime Capturing Methodology, using a non-adiabatic 1D Two-Fluid Model similar to the one of Simões *et al.* (2014). They validated their methodology using the experimental data of an air-water flow, for which satisfactory results were obtained. Investigative simulations were also performed for a gas condensate mixture flowing in a 200m long 6-inch internal diameter submitted to a pressure of 350bar. The gas properties were modelled with the ideal gas assumption and with the Peng & Robinson (1976) equation of state, whose distinct results were compared and discussed.

Ferrari *et al.* (2017) implemented a Regime Capturing Methodology for simulating gas-liquid isothermal horizontal flows in which, besides the two sets of mass and momentum equations for each phase (entrainment and deposition phenomena were neglected), a fifth transport equation was used in the model with a pressure relaxation term, in which its main function is to hyperbolize the mathematical model. Primarily, standard literature tests of air-water flows were used for validating the model and, then, Ferrari *et al.* (2017) simulated some isothermal air-water horizontal slug flow cases from the same database used by Issa & Kempf (2003). A satisfactory convergence against the experimental data and well-established correlations was obtained and the hyperbolicity of the model was demonstrated by a characteristic analysis and by mesh convergence tests. Ferrari *et al.* (2016) also performed tests in a similar model concept for horizontal flows of air and high-viscosity oils, but they were inconclusive due to the low number of presented results.

2.2.2. Summary

From the literature works previously described, the following four remarks regarding the employment of the Regime-Capturing Methodology can be made:

- It has been used mostly so far for simulating isothermal flows;
- Most works only use two sets of mass and momentum equations;
- It has been mostly used for numerically investigating slug flows and, in a

much lower degree, annular flows;

- With just a few exceptions, such as Ferrari *et al.* (2016), Silva & Nieckele (2016) and (Pasqualette *et al.*, 2015; Pasqualette *et al.*, 2017), the methodology has been almost exclusively used for simulating air-water flows;

Especially from the two last remarks, one can see the clear gap in the Regime Capturing Methodology literature in relation to its use for simulating isothermal horizontal flows of gas and a high-viscosity liquid in the slug and stratified flow patterns.

2.3. The Stability-Hyperbolicity Problem of the 1D Two-Fluid Model

It is well known that the numerical solution of a mathematical model must be independent of the mesh, for sufficiently refined grid levels. This is in consonance with the definition of Hadamard (1902) of well-posedness, which states that a well-posed mathematical problem must fulfill the following conditions, otherwise it would be ill-posed:

- The solution must exist;
- The solution must be unique;
- The solution must vary in a continuous and smooth manner with changes in the initial conditions of the problem.

It has been mathematically proven in literature (Dinh *et al.*, 2003) that the above requirements for the problem to be considered well-posed in the sense of Hadamard (1902) coincide with the features of an initial value problem with a strong hyperbolicity. In time, the 1D Two-Fluid Model poses an initial value problem, while, in space, it consists in a boundary value problem. In other words, from an initial spatial state, the solution will advance in time with the recurrent solution of a boundary value problem.

The degree of hyperbolicity of a system of partial differential equations is given by the values of its characteristics, which are mathematical quantities associated with the speed in which the information travels throughout the domain. They are also associated with the number of boundary conditions required in each of the boundaries of the domain (Figueiredo *et al.*, 2016). According to Drew &

Passman (1999) and Prosperetti & Tryggvason (2007), if all the characteristics of a system of equations are real than it is hyperbolic and well-posed, and if one of them is complex than the system is elliptic and ill-posed. In case that all the characteristics are real and distinct, then the system is strongly hyperbolic and, if they are not, than it is weakly hyperbolic (Dinh *et al.*, 2003). Another way to obtain the same rule of correspondence between the values of the characteristics and the hyperbolicity of the quasi-linear system of conservation equations is through the third requirement of Hadamard (1902) for well-posedness. Mathematically, it means that the insertion of a small perturbation on a certain initial condition should not lead to the inexistence of a result, but solely a continuously different one.

However, the relation between well-posedness, stability and hyperbolicity is an overly complex matter and, for this reason, a more basic and practical discussion is frequently adopted. In hyperbolic (real characteristics) mathematical models, when small wavelength perturbations appear in the domain, either from a non-standard initial condition or from some instability mechanism intrinsic to the physical phenomenon represented, they can have their growth rate limited, i.e., they become completely stable or decay. Such feature makes the model always tend to the same unique solution. However, in elliptic (complex characteristics) systems, small wavelength perturbations grow unphysically. This particularity of ill-posed and non-hyperbolic systems makes their numerical solution strongly dependent on the mesh size used. Very distinct results will be obtained, depending on the amount of small instabilities that are captured by the mesh, since their growth is uncontrolled. Furthermore, one of the consequences of the explosive instability of the small wavelength perturbations is that instabilities of longer wavelengths will also grow spuriously, as posed by the stability-hyperbolicity theorem (Prosperetti & Tryggvason, 2007).

The stability-hyperbolicity problem of the 1D Two-Fluid Model has been discussed in literature since it has been shown that it might possess complex characteristics and, therefore, lose hyperbolicity (Lyczkowski *et al.*, 1975). Not every formulation of the 1D Two-Fluid Model is ill-posed and it also depends on the conditions of the flow to be simulated. For testing the hyperbolicity of the 1D Two-Fluid Model, the most basic test is to perform the analysis of its characteristics, as performed by Issa & Kempf (2003). An alternative manner is through a linear stability analysis, particularly by calculating the growth rate of small wavelength instabilities, as done by Fullmer *et al.* (2014). This option is especially advantageous for analyzing the effects of higher-order terms, because reducing the system of equations to first-order for performing its characteristics analysis might lead to issues, as shown by Montini (2011). However, due to the importance and influence of the mesh size and the discretization schemes for the numerical solution of the 1D Two-Fluid Model, a more rigorous approach is to perform a linear stability analysis in the discretized equations of the model. This methodology, labeled von Neumann analysis, has been recently used in literature (Liao *et al.*, 2008; Issa & Galleni, 2015; Sanderse *et al.*, 2017). Nevertheless, due to nonlinear effects and to the intricacies of the numerical methodologies that are often used, the ultimate test of hyperbolicity (and, of course, well-posedness) is to perform the classical mesh convergence test for key parameters of the solution of the 1D Two-Fluid Model.

There are several methods to regularize, that is, to recover hyperbolicity of the 1D Two-Fluid Model, such as through a model for the dynamic pressure (Bestion, 1990), by artificially increasing the numerical and/or physical momentum diffusion of the model (Fullmer *et al.*, 2014), or by adding the volume fraction conservation equation and using two pressures as variables together with pressure relaxation effects (Baer & Nunziato, 1986; Saurel & Abgrall, 1999; Flatten & Lund, 2011; Ferrari *et al.*, 2017). Pasqualette *et al.* (2017) showed that increasing interfacial shear stress is also capable of stabilizing (and regularize) the 1D Two-Fluid Model in the Regime Capturing Methodology framework. Other traditional regularization methods are: adding artificial axial diffusion to the mass conservation equations (Fullmer *et al.*, 2014) and correctly modelling the momentum distribution parameters (Song, 2003). More details on the regularizing methods just cited will be provided in a later chapter of this work.

2.3.1. Summary

The importance of always addressing the stability-hyperbolicity problem of the isothermal 1D Two-Fluid Model was shown in this topic. If not adequately taken care of, such issue might invalidate the results of the numerical simulations (e.g. of the Regime Capturing Methodology), since they would not be well-posed in the Hadamard (1902) sense and neither would their results converge with the spatial mesh used for the discretization of the governing equations.

2.4. Interfacial Shear Stress Modelling in the 1D Two-Fluid Model for Gas-Liquid Horizontal Stratified Flows

The adequate modelling of the interfacial shear stress is one of the most challenging tasks when developing and using the 1D Two-Fluid Model. That is due to the lack of knowledge and still ongoing debate of which phenomena should be accounted for in the evaluation of the interfacial shear stress. The mesh chosen for the numerical solution of the 1D Two-Fluid Model can also be a source of problem for the modelling of the interfacial shear stress. The reason behind it is that one phenomena, which is sub-mesh for coarse grids might not be for finer ones, as it was discussed by Pasqualette *et al.* (2017) and will be further detailed later in this topic. The set of closures usually developed for coarse grid models (such as Unit Cell or Point Models) might not be adequate for Regime Capturing Methodology applications.

The main phenomenon that the interfacial shear stress must take into account is the interfacial waves. Although, it is known (Andritsos & Hanratty, 1987a; Andreussi & Persen, 1987) that the presence of interfacial waves should increase the interfacial shear stress when compared to a smooth interface, the exact physical mechanisms embedded in this relation are not yet fully understood. That is because of the complex relation between the turbulent structures of the phases with the interfacial dynamics (Ayati *et al.*, 2016) and the way it affects the cross sectional velocity profile in each phase (Belcher & Hunt, 1993). In addition, how the different components (tangential and normal to the interface) of the interfacial shear stress should be accounted for and the questions regarding the consideration of its viscous and pressure contributions increase even more the challenge of modelling the referred parameter (André & Bardet, 2017). As it was aforementioned, when coarse meshes are used for the numerical solution of the 1D Two-Fluid Model, all the effects of large and small-scale interfacial waves should be included in the interfacial shear stress model. However, when finer meshes are used, as in the Regime Capturing Methodology, it is mostly the effects of small-scale interfacial instabilities that should be accounted for in the selected interfacial shear stress model. Therefore, ideally, it is recommended either to use a very robust model that could include in it the correct physics for each mesh size or to use different interfacial shear stress models depending on the spatial grid. The most common approach is neither one of these, but it is to use the same simple interfacial shear stress models for all the meshes, as it will be clearer later. As it has been shown in a previous topic, this relation between the interfacial dynamics and the interfacial shear stress also represents an intrinsic relation of the latter with the liquid viscosity, because it affects deeply the characteristics of the interfacial waves (Andritsos & Hanratty, 1987a).

The influence of the wall shear stress is another phenomenon that should be taken into account by an ideal model for the interfacial shear stress. This is due to the former affecting the cross sectional velocity profile, which changes the latter (Náraigh *et al.*, 2011). Once an expression representing the relation between the shear stresses is used, the question of which shear stress should be modelled is raised. In that case, it is of common practice to model the wall shear stress (Andritsos & Hanratty, 1987b), although the other option has been used by some works, like Biberg (1998).

The most common strategy in the interfacial shear stress modeling is, firstly, to write the interfacial shear stress with the same Darcy or Fanning non-dimensional expressions from single-phase flow theory (Hanratty, 2013). In Eq. (2.2), a Fanning expression is written, in which τ_i is the interfacial shear stress, f_i is the Fanning interfacial friction factor (henceforth only referred to as "interfacial friction factor"), ρ_G is the density of the gas phase and U_i is a reference velocity for the interface.

$$\tau_i = \frac{1}{2} f_i \rho_G |U_i| U_i \qquad (2.2)$$

With Eq. (2.2), therefore, the problem changes from modelling τ_i to finding an expression for f_i. The referred equation for τ_i is written in relation to the gas phase (by using its density) for the possibility of interpreting τ_i with the same role as a wall shear stress for such phase. This perfectly matches with widely adopted understanding of the gas phase flowing as if it was a single-phase flow, in which the liquid phase, i.e., the interface, is part of the pipe walls (Ng *et al.*, 2004). The velocity U_i is usually defined as the relative bulk velocity between the phases, although it might also be calculated as an average between them or as the difference between the gas phase bulk velocity and an interfacial wave velocity (Hanratty, 2013).

Often, to simplify the formulation, it is considered that the interfacial friction factor is equal to the gas wall friction factor, when the pipe wall roughness is neglected (Hanratty, 2013). This, however, is only a good approximation when the interface is smooth, that is, when there are no waves (Andritsos & Hanratty, 1987b). In literature, there are a number of expressions for f_i that try to account for the effects of interfacial waves, as reviewed by Ottens *et al.* (2001). One of the most important expressions was elaborated by Andritsos & Hanratty (1987b) and has been improved in several works (Newton *et al.*, 1999; Calgaro, 2012; Tzotzi & Andritsos, 2013; Zhao *et al.*, 2015). The correlation of Andreussi & Persen (1987) is widely used as well as several modifications, which have been proposed in literature (Calgaro, 2012; Khaledi *et al.*, 2014). The expression of Spedding & Hand (1997), although not much used, also deserved to be highlighted.

These above mentioned three correlations and their modifications share a framework that considers f_i equal to a reference friction factor (when there are no waves at the interface), which increases when waves appear. Andreussi & Persen (1987) use a critical Froude number to monitor the surging of interfacial waves and Andritsos & Hanratty (1987b) and Spedding & Hand (1997) use a transition gas superficial velocity. More than one expression for f_i might be used in the same correlation, when different types of interfacial waves are separately addressed (Tzotzi & Andritsos, 2013). The three correlations have also in common the fact that the effects of the interfacial waves is compressed in the expression for the interfacial friction factor

Nevertheless, there are other models for the interfacial shear stress that do not use Eq. (2.2). Ullmann & Brauner (2006), for instance, modified the referred equation by adding to it parameters originated from the analytical solution of a laminar-laminar stratified flow. However, the most notorious example is the model of Biberg (2007), which does not use the concept of interfacial friction factor. For the special case of stratified flows in which both phases are turbulent, Biberg (2007) formulated a complex implicit model, which evaluates not only the interfacial shear stress but also the wall shear stresses. The model was obtained after a pre-integration of the cross sectional velocity profile in each phase expressed through an analytical model for the turbulent viscosity. In spite of being one of the most precise and robust model for the shear stresses in stratified flow, being overly complex, implicit and depending on fully empirical correlations for the turbulent intensity on each side of the interface makes the advantages limited.

By revisiting the derivation of the 1D Two-Fluid Model and considering that the interface is wavy according to a known function, Liné & Lopez (1997) managed to separate in two terms the interfacial shear stress for a smooth interface and the one solely due to the presence of the interfacial waves. However, Liné & Lopez (1997) did not manage to find an expression for the interfacial shear stress due to the waves that depends only on local parameters of the flow, as it is the ideal for the 1D Two-Fluid Model. A model for τ_i with this feature has been proposed by Brauner & Maron (1993; 1994). They elaborated a dynamic interfacial shear stress model in which the influence of the waves is separated from the smooth interface contribution and an expression including the derivative of the liquid phase height in relation to the axial coordinate. The advantage of using such variant is that, by using local variables, the steepness of the interfacial wave is captured by the solution of the 1D Two-Fluid Model. Hence, the wave shape evolution is directly related to the interfacial shear stress (Maron & Brauner, 1987). A model incorporating the liquid height derivative was also employed by Holmas (2010), who modified the expressions for the turbulent intensity on each side of the interface within the model of Biberg (2007). Nevertheless, a more detailed description of the dynamic model of Brauner & Maron (1993; 1994) will be provided later in this work.

2.4.1. Summary

In this topic, the importance of correctly modelling the interfacial shear stress and its intrinsic difficulties were described. That is why one of the purpose of this work is to create new expressions for the interfacial friction factor with the Eskerud Smith *et al.* (2011) experimental database, as it will be detailed in another chapter.

2.5. Final Comments

In this presentation of the literature review and the theoretical background of this work, several gaps in the literature regarding the themes discussed could be identified. Among them, the lack of use of the Regime Capturing Methodology for viscous-oils gas flows, such as the Eskerud Smith *et al.* (2011) database, can be highlighted. This is especially true for an adequate prediction of the complex interfacial dynamics, resultant mainly from the high oil viscosity, in the isothermal horizontal slug and stratified wavy viscous oil–gas flows. Besides, a systematic treatment of the stability-hyperbolicity problem, reflected in the Regime Capturing Methodology results convergence (or non-convergence) with the spatial mesh of the numerical method, for such types of flows is also an analysis missing in literature. Finding good models for the interfacial shear stress for viscous oil-gas flows is challenge as well and which has not being accomplished, due to the complex interfacial phenomena involved (e.g. relation between waves and turbulence).

This work aims to advance the filling of the previous mentioned literature gaps, although it is not its intention to exhaust the themes. As it will be seen, several good and interesting analyzes, discussions and investigations are here performed with the purpose of attacking such gaps.

3. THE REGIME CAPTURING METHODOLOGY

In order to be able to determine the flow field of a stratified or slug flow, as well as the transition from one flow pattern to another, the Regime Capturing Methodology was selected. In this chapter, this methodology is properly described and detailed. The presentation is divided in the two main aspects of the methodology: the 1D Two-Fluid Model and its numerical solution. At the last part of the chapter a discussion regarding the stability-hyperbolicity problem of the 1D Two-Fluid Model is addressed.

3.1. The 1D Two-Fluid Model

The basic and general definition of the 1D Two-Fluid Model was already provided in this work, but it is here repeated for its paramount importance.

The 1D Two-Fluid Model consists in two sets of mass, momentum and energy conservation equations formulated separately for each phase and that contain interfacial transfer source terms for representing the interaction between the phases. Its rigorous mathematical derivation, originally performed by Ishii (1975), starts from the local instantaneous balance equations of mass, momentum and energy for two phases, together with interfacial jump conditions for the three conserved quantities. For making such complex formulations more useful, two analogous paths might be taken. In the first one, adopted by Drew & Passman (1999), averages are performed in the equations after adding to them a phase indicator function, while in the second one, followed by Ishii & Hibiki (2011), ensemble averages are applied in the expressions. After using the definition of macroscopic variables in the resulting set of equations for making its physical representativeness clearer, the three-dimensional (3D) Two-Fluid Model, or just Two-Fluid Model, is obtained. Finally, its one-dimensional version, the 1D Two-Fluid Model, is acquired by performing a pipe cross section area average in the former, which guarantees that the only spatial variable is the axial one.

Traditionally, simplified approximations are employed in the mathematical procedure just described, leading to a simplified version of the 1D Two-Fluid Model, which may not be applicable to more complex situations. For example, as mentioned by Liné & Lopez (1997), it is fundamental to consider effects of the waviness of the interface in the formulation.

In the following pages, a version of the isothermal 1D Two-Fluid Model is presented, which will be used in the Regime Capturing Methodology, with the particular assumptions made in this work. As a starting point, the classical mass and momentum conservation equations of the model for a phase $K \in \{G, L\}$ (G represents the gas and L the liquid) are depicted in Eqs. (3.1) and (3.2), respectively, in a manner similar to the formulation of Ishii & Hibiki (2011).

$$\frac{\partial\left(\overline{A_K}^A\overline{\rho_K}^\alpha\right)}{\partial t}+\frac{\partial\left(\overline{A_K}^A\overline{\rho_K}^\alpha\overline{U_K}^\alpha\right)}{\partial x}=\overline{\Gamma_K}^A \tag{3.1}$$

$$\begin{aligned}\frac{\partial\left(\overline{A_K}^A\overline{\rho_K}^\alpha\overline{U_K}^\alpha\right)}{\partial t}&+\frac{\partial\left[\mathcal{C}_{mK}\overline{A_K}^A\overline{\rho_K}^\alpha\left(\overline{U_K}^\alpha\right)^2\right]}{\partial x}\\ &=-\overline{A_K}^A\frac{\partial\overline{P_K}^\alpha}{\partial x}+\overline{\left[\left(P_{\iota K}-P_K\right)\frac{\partial A_K}{\partial x}\right]}^A+\frac{\partial\left(\overline{A_K}^A\overline{\mathcal{T}_K}^\alpha\right)}{\partial x}\\ &\quad-\overline{A_K}^A\overline{\rho_K}^\alpha g\sin\theta-\frac{4\alpha_{wK}\tau_{wK}A}{D_{hK}}-\overline{\mathcal{DF}_K}^A\\ &\quad-\left(\overline{\boldsymbol{\nabla}A_K\cdot\tau_\iota^*}^A\right)_x+\overline{\Gamma_K}^A\overline{U_{\iota K}}^\alpha\end{aligned} \tag{3.2}$$

In the referred equations, A_K is the cross section area occupied by phase $K \in \{G, L\}$ and $A = A_G + A_L$ is the pipe total cross section area. The temporal variable is represented by t and x symbolizes the pipe axial spatial component. Besides, ρ_K is the phase K density; U_K the (bulk) phase velocity and P_K the phase pressure. Furthermore, Γ_K is the mass transfer rate to phase K from the other phase due to phase change; $\mathcal{C}_{mK}$ is the momentum distribution parameter of phase K; $\mathcal{T}_K$ is the axial momentum diffusion; α_{wK} is the phase K holdup next to the pipe wall; τ_{wK} is the phase K shear stress at the wall; $\mathcal{DF}_K$ is the drag force due to a dispersed phase; τ_ι^* is an effective interfacial shear stress; and U_{iK} and P_{iK} are, respectively, the interfacial velocity and interface pressure in the side of phase K. The acceleration of gravity is represented by g, and θ is the pipeline angle with the horizontal plane (positive when the flow is upward and negative otherwise). Finally, $D_{hK} = 4A_K/S_K$ is the classical definition of hydraulic diameter for phase $K \in \{G, L\}$, where S_K is the phase wetted perimeter. It is worth mentioning that only the vector component in the x-direction is being considered in the seventh term of the Right-Hand-Side (RHS) of Eq. (3.2).

The ratio of the phase K cross section area to the pipeline area is represented by α_K and given by Eq. (3.3). Note that for 1D situations it is equivalent to the volumetric ratio, assuming the same infinitesimal axial length dx, thus, this variable is frequently called as volume fraction, or holdup.

$$\alpha_K = \frac{A_K}{A} \tag{3.3}$$

From the definition of holdup in Eq. (3.3), a relation between α_G and α_L can be easily obtained and it is shown in Eq. (3.4).

$$\alpha_G + \alpha_L = 1 \tag{3.4}$$

The operators $\bar{\psi}^A$ and $\overline{\psi_K}^{\alpha}$, for the general variable ψ, represent, respectively, the area-average operation, Eq. (3.5), and the volumetric-fraction-weighted mean for phase K, Eq. (3.6).

$$\bar{\psi}^A = \frac{1}{A}\int_A \psi \, dA \tag{3.5}$$

$$\overline{\psi_K}^{\alpha} = \frac{\overline{\alpha_K \psi_K}^A}{\overline{\alpha_K}^A} \tag{3.6}$$

Examining Eqs. (3.1) and (3.2) of the 1D Two-Fluid Model, it is clear that several parameters still need to be modelled and that further hypotheses still need to be made. These equations can be further simplified by adding the following assumptions (Issa & Kempf, 2003; Ishii & Hibiki, 2011):

- The pipe cross sectional area A is considered constant, i.e., it does not vary in time nor in space;
- The presence of dispersed phases (bubbles and droplets) is neglected, therefore: $\overline{\mathcal{DF}_K}^A = 0$;
- Phase change, such as boiling and condensation, due to pressure changes is completely neglected: $\overline{\Gamma_K}^A = 0$;
- The parameter α_{wK} is considered to be approximately equal to α_K.

The first two terms on the RHS of Eqs. (3.2) can be rewritten in order to obtain the bulk pressure $\overline{P_K}^{\alpha}$ present in just one of the terms, as it can be seen in Eq. (3.7) (Issa & Kempf, 2003; Carneiro *et al.*, 2011), where the area-average and the volumetric-fraction-weighted-mean operators were dropped.

$$-\alpha_K \frac{\partial P_K}{\partial x} + (P_{iK} - P_K)\frac{\partial \alpha_K}{\partial x} = -\alpha_K \frac{\partial P_{iK}}{\partial x} + \frac{\partial[\alpha_K(P_{iK} - P_K)]}{\partial x} \tag{3.7}$$

Furthermore, the seventh term in the RHS of Eq. (3.2) might be reformulated as done by Ishii & Hibiki (2011), i.e., through Eq. (3.8), where S_i is the interfacial perimeter.

$$\left(\overline{\boldsymbol{\nabla} A_K \cdot \tau_i^*}^{A}\right)_x = \tau_i^* \frac{S_i}{A} \tag{3.8}$$

By dropping the two operators defined in Eqs. (3.5) and (3.6) and by applying the aforementioned hypotheses in the mass conservation equations for the gas and liquid phases, Eqs. (3.1), they can be rewritten as formulated by Eqs. (3.9) and (3.10), respectively.

$$\frac{\partial(\alpha_G \rho_G)}{\partial t} + \frac{\partial(\alpha_G \rho_G U_G)}{\partial x} = 0 \tag{3.9}$$

$$\frac{\partial(\alpha_L \rho_L)}{\partial t} + \frac{\partial(\alpha_L \rho_L U_L)}{\partial x} = 0 \tag{3.10}$$

If once again the area-average and the volumetric-fraction-weighted-mean operators are dropped and the same previous hypotheses are considered, the momentum conservation equations for the gas and liquid are also reformulated as indicated by, respectively, Eqs. (3.11) and (3.12). In them, the definitions of Eqs. (3.7) and (3.8) were also employed.

$$\begin{aligned}\frac{\partial(\alpha_G \rho_G U_G)}{\partial t} &+ \frac{\partial\left(\mathcal{C}_{mG} \alpha_G \rho_G {U_G}^2\right)}{\partial x} \\ &= -\alpha_G \frac{\partial P_{iG}}{\partial x} + \frac{\partial[\alpha_G(P_{iG} - P_G)]}{\partial x} + \frac{\partial(\alpha_G \mathcal{J}_G)}{\partial x} \\ &- \alpha_G \rho_G g \sin\theta - \tau_{wG}\frac{S_G}{A} - \tau_i^* \frac{S_i}{A}\end{aligned} \tag{3.11}$$

$$\begin{aligned}\frac{\partial(\alpha_L\rho_L U_L)}{\partial t}+\frac{\partial\left(\mathcal{C}_{mL}\alpha_L\rho_L {U_L}^2\right)}{\partial x}\\ =-\alpha_L\frac{\partial P_{iL}}{\partial x}+\frac{\partial[\alpha_L(P_{iL}-P_L)]}{\partial x}+\frac{\partial(\alpha_L\mathcal{T}_L)}{\partial x}\\ -\alpha_L\rho_L g\sin\theta-\tau_{wL}\frac{S_L}{A}+\tau_i^*\frac{S_i}{A}\end{aligned} \tag{3.12}$$

By examining the momentum conservation equations, Eqs. (3.11) and (3.12), it is clear the necessity to develop a model and/or closure relations for several parameters, such as:

- The gas density ρ_G;
- The momentum distribution parameter $\mathcal{C}_{mK}$;
- The relation between the pressures P_{iK} at each side of the interface;
- The difference between the interfacial and bulk pressure $(P_{iK}-P_K)$;
- The axial momentum diffusion $\mathcal{T}_K$;
- Phase wall shear stress τ_{wK};
- The effective interfacial shear stress τ_i^*;

Two-phase flow in pipelines can be arranged in several patterns (Brennen, 2005; Hanratty, 2013). One key parameter for the 1D formulation is to define a basic flow pattern configuration, which will affect not only the cross section geometric parameters, like S_K and S_i, but also which approximation is more appropriated for the several parameters mentioned above. In the following topics, the modelling of the listed parameters, and others, are performed.

3.1.1. Base Flow Pattern

The pipeline configuration of interest in the present work is a horizontal or nearly horizontal pipeline, in the presence of both stratified and slug flows. Therefore, a possible base flow configuration is to consider the flow to be stratified (Issa & Kempf, 2003; Bonizzi *et al.*, 2009; Carneiro *et al.*, 2011; Nieckele *et al.*, 2013). Such configuration consists in a heavier phase, the liquid, in the cases of interest here, located at the bottom of the pipe and a lighter phase, the gas, at its upper part, as illustrated in Figure 3.1.

Besides illustrating the stratified flow configuration, Figure 3.1 also contains some of its key geometrical and dynamic parameters. Among them, h_L is the liquid phase height, δ is half of the liquid wetted angle and D is the pipe internal diameter.

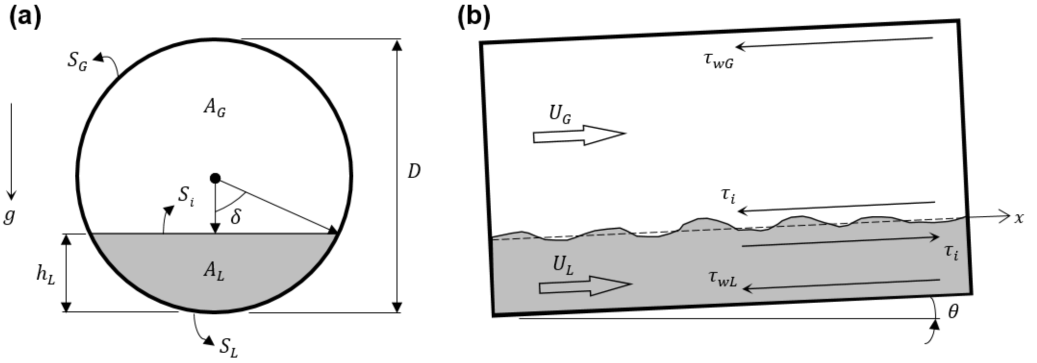

Figure 3.1 – Stratified flow configuration with a cross sectional flat interface: (a) cross sectional view; (b) lateral view.

The interface illustrated in Figure 3.1(a) is flat in the cross section. This may not always be true, especially for liquid-liquid flows (Rodriguez & Baldani, 2012) or for gas-liquid flows with a gas inertia much higher than the liquid inertia, such as stratified wavy flows near the transition to the annular pattern (Ullmann & Brauner, 2006; Zhang & Sarica, 2011). As in this work neither one of these scenarios have to be dealt with, assuming the interfacial flat in the cross section is a good approximation.

All key geometrical parameters (S_L, S_G, S_i and h_L) of the stratified configuration of a can be obtained based on the angle δ, as shown in Table 3.1.

Table 3.1 – Expressions for geometrical parameters as a function of $\boldsymbol{\delta}$.

Variable	Expression
S_L/D	δ
S_G/D	$\pi - \delta$
S_i/D	$\sin\delta$
h_L/D	${}^1\!/_2\,(1 - \cos\delta)$

The parameter δ in the schematic drawing of Figure 3.1(a) can be easily related to the liquid holdup α_L, by using simple trigonometry, as shown in Eq. (3.13).

$$\alpha_L = \frac{1}{\pi}\left(\delta - \frac{1}{2}\sin 2\delta\right) \tag{3.13}$$

However, the previous equation is implicit with relation to δ, which is an undesired aspect since a root-finding algorithm would have to be used in order to provide δ for a given α_L. With this in mind, Biberg (1999a) proposed an explicit approximation for δ in relation to α_L, which was successfully tested by Pasqualette *et al.* (2014) in the Regime Capturing Methodology. The referred expression, seen in Eq. (3.14), will be used throughout the present work.

$$\begin{aligned}\delta \approx \pi\alpha_L + \left(\frac{3\pi}{2}\right)^{1/3}\left[1 - 2\alpha_L + {\alpha_L}^{1/3} - (1-\alpha_L)^{1/3}\right] \\ - \frac{1}{200}\alpha_L(1-\alpha_L)(1-2\alpha_L)\{1 + 4[{\alpha_L}^2 + (1-\alpha_L)^2]\}\end{aligned} \tag{3.14}$$

3.1.2. Equation of State for the Gas Phase

As performed in several works (Issa & Kempf, 2003; Bonizzi *et al.*, 2009; Carneiro *et al.*, 2011; Han & Guo, 2015; Ferrari *et al.*, 2017), compressibility is only considered to the gas phase, i.e., the liquid is considered as incompressible. Further, as already mentioned, the gas compressibility factors of SF_6, the Eskerud Smith *et al.* (2011) database gas phase, are close to the unity. Thus, the gas density is calculated through the ideal gas law, shown in Eq. (3.15).

$$\rho_G = \frac{P_G}{\mathcal{R}_G T} \cong \frac{P_{iG}}{\mathcal{R}_G T} \tag{3.15}$$

In the referred equation, $\mathcal{R}_G$ is the gas constant (approximately 55 J/kg.K for the SF_6) and T is the flow temperature, which is constant due to the isothermal hypothesis of the present formulation. Finally, to determine the average density of the gas phase, the gas bulk pressure is approximated to the interfacial pressure at the side of the gas phase (P_{iG}).

3.1.3. The Momentum Distribution Parameter

The definition of the momentum distribution parameter $\mathcal{C}_{mK}$, $K \in \{G, L\}$, of phase K, present in the convective term of the momentum balance equations of the 1D Two-Fluid Model, Eqs. (3.11) and (3.12), is provided by Eq. (3.16) (Ishii & Hibiki, 2011).

$$\mathcal{C}_{mK} = \frac{\overline{\alpha_K {U_K}^2}^A}{\overline{\alpha_K}^A \overline{U_K}^A \overline{U_K}^A} \tag{3.16}$$

According to Eq. (3.16), the momentum distribution parameter represents the ratio between the average of the products and the product of the averages. It is evident that, for calculating such parameters, the velocity profiles in both gas and liquid are necessary. If only one phase is present, the momentum distribution parameter is well known for fully developed flow. For laminar flow, it is equal to 1.33 and for turbulent flow, it depends on empirical velocity profile, and it is near unity (Ishii & Hibiki, 2011).

For two-phase laminar flow, analytical expressions for $\mathcal{C}_{mK}$ can also be determined based on the solution of the axial steady-state fully developed momentum equation for phase K, for particular flow patterns. For turbulent flow, further approximations are needed, such as turbulence model, or empirical data. For turbulent stratified flow, Biberg (2007) determined this parameter based on the wall and interfacial shear stresses, which must be coupled through the velocity profile. Unfortunately, empirical data on three-dimensional velocity fields in stratified-wavy and slug flows is scarce. Hence, as the momentum distribution parameter is not the priority of this work and its modelling might be a source of uncertainties for the 1D Two-Fluid Model and the Regime Capturing Methodology, $\mathcal{C}_{mK}$ is considered to be unity, Eq. (3.17), as commonly found in several publications (Issa & Kempf, 2003; Bonizzi *et al.*, 2009; Carneiro *et al.*, 2011; Han & Guo, 2015; Ferrari *et al.*, 2017).

$$\mathcal{C}_K = 1 \tag{3.17}$$

3.1.4. Interfacial Pressure Jump

The interfacial pressure jump can be determined by applying the Young-Laplace formula, Eq. (3.18), where σ is the interfacial (or surface) tension, which is a properties of the phases in contact to each other, and κ is the curvature of the associated surface.

$$P_{iG} - P_{iL} = \sigma\kappa \tag{3.18}$$

Figure 3.2 illustrates the interface curvature κ through the curvature radius r_κ, together with the phasic interfacial pressures P_{iK}, $K \in \{G, L\}$.

Figure 3.2 – Curvature radius for the interface and phasic interfacial pressures.

In the case of a single important curvature radius, the curvature κ is expressed as indicated by Eq. (3.19) (Carneiro, 2006).

$$\kappa = \frac{1}{r_\kappa} \tag{3.19}$$

Through the infinitesimal geometric analysis of the curvature depicted in Figure 3.2, Ramshaw & Trapp (1978) and Carneiro (2006) determined that the curvature κ might be expressed as a function of the axial derivative of the liquid phase height $\partial h_L/\partial x$, as shown in Eq. (3.20).

$$\kappa = \frac{\frac{\partial^2 h_L}{\partial x^2}}{\left[1 + \left(\frac{\partial h_L}{\partial x}\right)^2\right]^{3/2}} \tag{3.20}$$

By considering that the local variations of $\partial h_L/\partial x$ are not significant, Ramshaw & Trapp (1978) and Carneiro (2006) simplified Eq. (3.20) to Eq. (3.21).

$$\kappa = \frac{\partial^2 h_L}{\partial x^2} \tag{3.21}$$

Then, by applying the definition of Eq. (3.21) into Eq. (3.18), the Young-Laplace formula becomes Eq. (3.22).

$$P_{iG} - P_{iL} = \sigma \frac{\partial^2 h_L}{\partial x^2} \tag{3.22}$$

With the Young-Laplace formula, Eq. (3.22), the interfacial pressure on the liquid side, P_{iL}, can be eliminated from the set of conservation equations.

3.1.5. Interfacial-Bulk Pressure Difference

The difference between the interfacial and bulk pressure for a phase K, $(P_{iK} - P_K)$, is one of the most difficult terms to be modelled, because it is affected by the pressure distribution around interfacial waves, which can result in very complex terms (Stuhmiller, 1977; Galimov *et al.*, 2005). However, such degree of complexity was avoided here.

Frequently, the interfacial-bulk pressure difference is considered to be originated from the cross sectional hydrostatic pressure distribution in each phase. This assumption is followed by several Regime Capturing Methodology works in literature, such as Issa & Kempf (2003), Carneiro *et al.* (2011), Han & Guo (2015) and Ferrari *et al.* (2017). The "hydrostatic pressure" approach is satisfactory and provides a valid physical interpretation to the pressure terms, when the vertical velocity is very small. In this context, the "dynamic pressure" seeks to take into consideration the effect on the interfacial-bulk pressure difference to distortions on the hydrostatic pressure distribution caused by the flow in the phases. This is the contribution to $(P_{iK} - P_K)$ that is influenced by the pressure distribution around interfacial waves (Stuhmiller, 1977; Galimov *et al.*, 2005) as well as by the axial velocity profile and cross sectional dynamic effects excluded from the 1D Two-Fluid Model by the area-averaging procedure (Renault, 2007). The dynamic pressure is often inappropriately, in the opinion of the author of this work, referred to as "interfacial pressure" in literature (Stuhmiller, 1977; Fullmer *et al.*, 2014).

With all of this in mind, the interfacial-bulk pressure difference for phase K can be written as a function of a hydrostatic pressure term, $\Delta P_{\mathcal{H},K}$, and a dynamic pressure term, $\Delta P_{\mathcal{D},K}$, as shown by Eq. (3.23).

$$P_{iK} - P_K = \Delta P_{\mathcal{H},K} + \Delta P_{\mathcal{D},K} \tag{3.23}$$

By applying the definition of Eq. (3.23) to the second term on the RHS of Eq. (3.7), the same can be written as formulated by Eq. (3.24).

$$\frac{\partial[\alpha_K(P_{iK} - P_K)]}{\partial x} = \frac{\partial\left(\alpha_K \Delta P_{\mathcal{H},K}\right)}{\partial x} + \frac{\partial\left(\alpha_K \Delta P_{\mathcal{D},K}\right)}{\partial x} \tag{3.24}$$

In the next topics, an expression for the hydrostatic pressure term is derived, according to literature procedures, followed by an equation for the dynamic pressure term.

3.1.5.1. Hydrostatic Pressure

To derive an expression for the hydrostatic pressure, it is convenient to refer to Figure 3.3, in which y is the cross sectional coordinate and $p_K(y)$ is the y-dependent local pressure in phase $K \in \{G, L\}$.

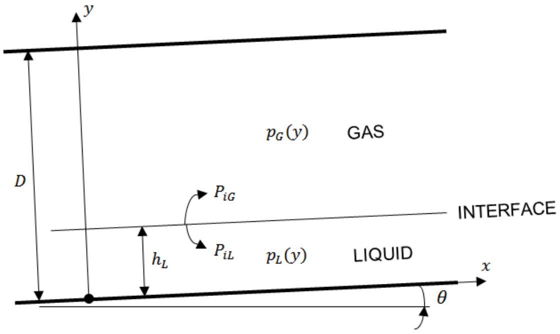

Figure 3.3 – Hydrostatic pressure distribution.

The relation between P_{iK} and p_K can be straightforwardly obtained by the hydrostatic relation: $P_{iK} - p_K(y) = -\rho_K\, g \cos\theta\, (h_L - y)$. Since the hydrostatic term on the RHS of Eq. (3.24) is actually an area-average (the operator has been dropped) and by applying the previous expression to it, it can be formulated as shown in Eq. (3.25) (Tomasello, 2009). In such equation, there is an implicit extra hypothesis that the inclination angle θ does not vary with x; and $y_{\min,K}$ and $y_{\max,K}$ are the y-axis integration limits related to each phase: 0 and h_L, for the liquid, and h_L and D, for the gas, respectively.

$$\frac{\partial\left(\alpha_K \Delta P_{\mathcal{H},K}\right)}{\partial x} = -\left(\frac{g\cos\theta}{A}\right)\frac{\partial}{\partial x}\left[\int_{y_{\min,K}}^{y_{\max,K}} \rho_K (h_L - y) D \sin\delta\, dy\right] \tag{3.25}$$

After some algebraic development of the RHS of Eq. (3.25), Eq. (3.26) was obtained, in which the parameters Ψ_K, $K \in \{G, L\}$, are expressed according to Eqs. (3.27) and (3.28) for the gas and the liquid, respectively (Tomasello, 2009).

$$\frac{\partial\left(\alpha_K \Delta P_{\mathcal{H},K}\right)}{\partial x} = -\rho_K \alpha_K g \cos\theta \frac{\partial h_L}{\partial x} - \left(\frac{g\cos\theta}{A}\right)\Psi_K \frac{\partial \rho_K}{\partial x} \tag{3.26}$$

$$\Psi_G = h_L A_G - \frac{D^3}{4}\left(\frac{\pi - \delta}{2} + \frac{\sin^3\delta}{3} + \frac{\sin 2\delta}{4}\right) \tag{3.27}$$

$$\Psi_L = h_L A_L - \frac{D^3}{4}\left(\frac{\delta}{2} - \frac{\sin^3\delta}{3} - \frac{\sin 2\delta}{4}\right) \tag{3.28}$$

While the first term on the RHS of Eq. (3.26) is, according to the literature, definitely important for the 1D Two-Fluid Model, the same statement cannot de made in relation to the second term (Issa & Kempf, 2003; Bonizzi *et al.*, 2009; Carneiro *et al.*, 2011; Han & Guo, 2015; Ferrari *et al.*, 2017). This is justified by the incompressibility assumption for the liquid, which makes the derivative $\partial\rho_L/\partial x$ become null. Although the gas is a compressible phase, the fact that the pressure variations along short laboratory-scale pipes, such as the one of the Eskerud Smith *et al.* (2011) database, not being significant makes the values of $\partial\rho_G/\partial x$ very modest. Nevertheless, the possibility that local pressure peaks (such as those found in the boundaries of a slug body) lead to significant values of $\partial\rho_G/\partial x$ and, consequently, make the two terms in the RHS of Eq. (3.26) become of the same order of magnitude is valid. This is a subject that needs to be investigated in the future, due to the uncertainties surrounding this term. However, this work follows the current practice of, for simplification, neglecting the second term of the RHS of Eq. (3.26), originating Eq. (3.29).

$$\frac{\partial\left(\alpha_K \Delta P_{\mathcal{H},K}\right)}{\partial x} = -\rho_K \alpha_K g \cos\theta \frac{\partial h_L}{\partial x} \tag{3.29}$$

3.1.5.2. Dynamic Pressure

As previously said, there are several complex methods for determining an expression for the dynamic pressure term $\Delta P_{\mathcal{D},K}$. These include those derived from a given interfacial wave characteristics and form, such as sinusoidal, from which the pressure distribution in the wave can be computed (Galimov *et al.*, 2005), or from the cross section momentum balance equation (Renault, 2007). Nevertheless, the most used expression is the one made by Bestion (1990), which is the one that guarantees that the standard 1D Two-Fluid Model is hyperbolic. The Regime

Capturing Methodology works, such as in Han & Guo (2015) and in Fontalvo (2017), successfully with the expression of Bestion (1990), providing satisfactory results. Such expression, for $\Delta P_{\mathcal{D},K}$, $K \in \{G, L\}$, is given by Eq. (3.30).

$$\Delta P_{\mathcal{D},K} = -\eta_{\mathcal{D}} \rho_{\mathcal{D}} (U_L - U_G)^2 \tag{3.30}$$

In the referred equation, the constant $\eta_{\mathcal{D}}$ is defined as 1.2 (Bestion, 1990; Han & Guo, 2015; Fontalvo, 2017), while the density $\rho_{\mathcal{D}}$ is formulated as shown in Eq. (3.31).

$$\rho_{\mathcal{D}} = \frac{\alpha_G \alpha_L \rho_G \rho_L}{\alpha_G \rho_L + \alpha_L \rho_G} \tag{3.31}$$

As it can be seen in the referred equation, $\rho_{\mathcal{D}}$ is a weighted average between the phasic densities ρ_G and ρ_L. The dynamic pressure contribution to the momentum equations can, thus, be expressed by Eq. (3.32).

$$\frac{\partial\left(\alpha_K \Delta P_{\mathcal{D},K}\right)}{\partial x} = -\frac{\partial\left[\alpha_K \eta_{\mathcal{D}} \rho_{\mathcal{D}} (U_L - U_G)^2\right]}{\partial x} \tag{3.32}$$

3.1.6. Molecular and Turbulent Axial Momentum Diffusion

The axial momentum diffusion term for phase K, $\mathcal{T}_K$, lumps up the two physical effects that promotes diffusion: molecular and turbulent effects. They are represented, as shown in Eq. (3.33), by a single effective phasic dynamic viscosity μ_K^{eff}, $K \in \{G, L\}$, defined in Eq. (3.34) (Fullmer *et al.*, 2011), as performed by Fullmer *et al.* (2014).

$$\mathcal{T}_K = \mu_K^{eff} \frac{\partial U_K}{\partial x} \tag{3.33}$$

$$\mu_K^{eff} = \eta_\mu (\mu_K + \mu_K^t) \tag{3.34}$$

In Eq. (3.34), μ_K is the molecular dynamic viscosity and μ_K^t is the turbulent dynamic viscosity for phase $K \in \{G, L\}$. $\eta_\mu \geq 1$ is a constant whose purpose is to increase μ_K^{eff} in order to compensate for the cross sectional diffusion effects that cannot be explicitly taken into account due to the area-averaging procedure performed for obtaining the 1D Two-Fluid Model (Fullmer *et al.*, 2014).

For modelling the turbulent viscosities, there are a huge number of options in literature, from enormously complex approaches to very simple ones (Pope, 2000). The complexity of the model used should be compatible with the 1D Two-Fluid Model, reason why a simple algebraic model is preferred here. The fact of the conventional derivation of the Reynolds-Average-Navier-Stokes (RANS) is not being followed, which is clear by the absence of the turbulent kinetic energy in Eq. (3.33) (Pope, 2000) also points to the use of a simple algebraic expression for computing μ_K^t. Based on the discussions and descriptions by Pope (2000) of this type of equation, a formulation, shown in Eq. (3.35), is proposed.

$$\mu_K^t = \eta_{\mu t} \rho_K D_{hK} |U_K| \tag{3.35}$$

In the proposed μ_K^t expression, Eq. (3.35), the characteristic velocity is the phase velocity and the characteristic length is proportional to the phase hydraulic diameter D_{hK}, $K \in \{G, L\}$. Such variable is not calculated by its classical definition, previously introduced, but for expressions, Eqs. (3.38) and (3.39), that contain assumptions on the gas and liquid flow and that will be properly presented in a next topic. In Eq. (3.35), the constant $\eta_{\mu t}$ is estimated as the ratio between the von Kármán constant 0.4 and an empirical Reynolds turbulent number approximately equal to 13 (Pope, 2000). The resulting value for $\eta_{\mu t}$ is, thus, 0.03

3.1.7. Phase Wall Shear Stress

The wall shear stresses for each phase $K \in \{G, L\}$, τ_{wK}, are expressed using a Fanning-like adimensionalization. This is depicted in Eq. (3.36), where f_K is the wall Fanning friction factor of phase K (henceforth referred to simply as “phase K friction factor”).

$$\tau_{wK} = \frac{1}{2} f_K \rho_K |U_K| U_K \tag{3.36}$$

The friction factor for each phase depends on the flow regime (laminar or turbulent) and it is defined based on the phase Reynolds number Re_K, formulated in Eq. (3.37), or the phase superficial Reynolds number Re_{sK}.

$$\mathrm{Re}_K = \frac{\rho_K |U_K| D_{hK}}{\mu_K} \tag{3.37}$$

A key point in the calculation of Re_K is the manner with which the hydraulic diameters D_{hK} of each phase are calculated. Primarily, it is important to remember that the hydraulic diameter is four times the ratio between the cross sectional area and the wetted perimeter, as previously shown. The basic assumption regarding the flow of the gas phase in gas-liquid horizontal stratified flows is that the gas flows as if the interface was considered a wall (Ng *et al.*, 2004; Hanratty, 2013). This corresponds to an analogy of single-phase gas flow, where the liquid was stationary, which can be a good hypothesis in many scenarios due to the gas bulk velocity being usually much higher than the liquid velocity. Following this reasoning, the wetted perimeter of the gas, when calculating its hydraulic diameter, is considered the sum of the actual gas wetted perimeter with the interfacial perimeter. The basic assumption of the flow in the liquid phase, on the other hand, is that the liquid flows as if the interface was a free surface, that is, as an open channel flow (Ng *et al.*, 2004; Hanratty, 2013). This way, the liquid wetted perimeter for the hydraulic diameter is, without any complications, equal to the actual liquid wetted perimeter. This entire discussion can be summarized in the two expressions, Eqs. (3.38) and (3.39), for the gas and liquid, respectively, with which D_{hK} can be calculated.

$$D_{hG} = \frac{4A_G}{S_G + S_i} \tag{3.38}$$

$$D_{hL} = \frac{4A_L}{S_L} \tag{3.39}$$

The superficial Reynolds number of phase $K \in \{G, L\}$, Re_{sK}, defined in Eq. (3.40), is based on the pipe diameter D and on the phasic superficial velocities U_{sK}, formulated in Eq. (3.41).

$$\mathrm{Re}_{sK} = \frac{\rho_K |U_{sK}| D}{\mu_K} \tag{3.40}$$

$$U_{sK} = \alpha_K U_K \tag{3.41}$$

These two Reynolds numbers, Re_{sK} and Re_K, can be related, for the stratified flow configuration of Figure 3.1, through Eqs. (3.42) and (3.43) for the gas and liquid, respectively.

$$\frac{\mathrm{Re}_{sG}}{\mathrm{Re}_G} = 1 - \frac{\delta}{\pi} + \frac{\sin\delta}{\pi} \tag{3.42}$$

$$\frac{\mathrm{Re}_{sL}}{\mathrm{Re}_L} = \frac{\delta}{\pi} \tag{3.43}$$

As different wall friction factors expressions are used for when the flow in the phase is laminar, $(f_K)_{\mathrm{lam}}$, or turbulent, $(f_K)_{\mathrm{turb}}$, the scheme in Eq. (3.44) is proposed for calculating f_K.

$$f_K = \begin{cases} (f_K)_{\mathrm{lam}} & ;\ \mathrm{Re}_K \leq \mathrm{Re}_{\mathrm{lam}} \\ w_t (f_K)_{\mathrm{turb}} + (1 - w_t)(f_K)_{\mathrm{lam}} & ;\ \mathrm{Re}_{\mathrm{lam}} < \mathrm{Re}_K < \mathrm{Re}_{\mathrm{turb}} \\ (f_K)_{\mathrm{turb}} & ;\ \mathrm{Re}_K \geq \mathrm{Re}_{\mathrm{turb}} \end{cases} \tag{3.44}$$

In the previous equation, w_t is an interpolation function that is commonly assumed linear in relation to the Reynolds number, as shown in Eq. (3.45) (Khaledi *et al.*, 2014). However, throughout this work a smoother form for the interpolation function based on the hyperbolic tangent, Eq. (3.46), is proposed and used.

$$w_t = \frac{\mathrm{Re}_K - \mathrm{Re}_{\mathrm{lam}}}{\mathrm{Re}_{\mathrm{turb}} - \mathrm{Re}_{\mathrm{lam}}} \tag{3.45}$$

$$w_t = \frac{1}{2} + \frac{1}{2}\tanh\left[\frac{3(2\ \mathrm{Re}_K - \mathrm{Re}_{\mathrm{turb}} - 3\ \mathrm{Re}_{\mathrm{lam}})}{\mathrm{Re}_{\mathrm{turb}} - \mathrm{Re}_{\mathrm{lam}}}\right] \tag{3.46}$$

In Figure 3.4, the two previously mentioned forms for the interpolation function are compared and it is possible to see the advantage of the form in Eq. in terms of smoothness.

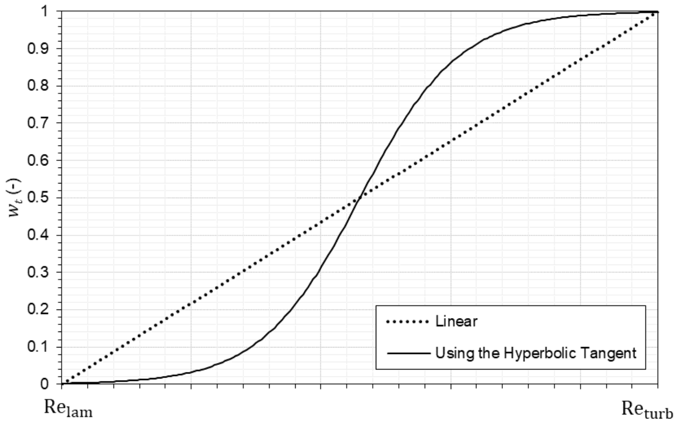

Figure 3.4 – Comparison of the forms for w_t.

There are several correlations to determine de phase friction factor as a function of the Reynolds number. A few of them are analyzed in the next chapter devoted to propose new correlations for the interfacial friction factor through an optimization technique.

3.1.8. Effective Interfacial Shear Stress

As previously mentioned in the literature review on the interfacial shear stress modelling, Brauner & Maron (1993; 1994) proposed an expression for the effective interfacial shear stress (nomenclature used for the 1D Two-Fluid Model), in which the effects of waves and of the smooth interface are separated. Their expression is given by Eq. (3.37).

$$\tau_i^* = \tau_i + \mathcal{J}_i \frac{\partial h_L}{\partial x} \tag{3.47}$$

The first term in the RHS of the previous equation is the usual interfacial shear stress (“pseudo-smooth” interfacial shear stress), which aims to represent the contribution of the smooth interface or of a wavy interface in which the instabilities are not being captured by the model (Brauner & Maron, 1993; 1994). The second term on the RHS of Eq. (3.47) is the explicit contribution of the interfacial waves to the effective interfacial shear stress τ_i^*. Although obvious, it is important to state that if such explicit contributions of the interface waviness are not taken into account, than the effective interfacial shear stress is equal to the “pseudo-smooth” one. According to Brauner & Maron (1993; 1994), due to the presence of the derivative $\partial h_L/\partial x$ in in the expression for τ_i^*, this model is labeled as “dynamic interfacial shear stress”.

3.1.8.1. Interfacial Shear Stress

The most common strategy to determine the interfacial shear stress τ_i is analogous to the phase wall shear stress, i.e., by relating the interfacial shear stress τ_i to f_i, which is the Fanning interfacial friction factor (henceforth only referred to as “interfacial friction factor”). For reasons of convenience, the expression of Eq. (2.2) is repeated in Eq. (3.48).

$$\tau_i = \frac{1}{2} f_i \rho_G |U_i| U_i \qquad (3.48)$$

The common definition of the reference interfacial velocity U_i as the difference between the gas and liquid bulk velocities (Hanratty, 2013) is used in this work, Eq. (3.49).

$$U_i = U_G - U_L \qquad (3.49)$$

As it will be seen in a more detailed way in the next Chapter, the interfacial friction factor f_i depends on the interfacial flow regime (laminar or turbulent) and also on the interfacial Reynolds number Re_i, defined by Eq. (3.50).

$$\mathrm{Re}_i = \frac{\rho_G |U_G - U_L| D_{hG}}{\mu_G} \qquad (3.50)$$

The definition of the interfacial friction factor is crucial for an accurate prediction of the gas-liquid flow. This is specifically critical for when the presence of waves is strong at the interface. With this in mind, the next chapter is devoted to the definition of the interfacial friction factor, where two new correlations are being proposed at the present work, based on an optimization procedure.

3.1.8.2. Dynamic Interfacial Shear Stress

The presence of the derivative $\partial h_L / \partial x$ in Eq. (3.47) is a sensible manner found by Brauner & Maron (1993; 1994) to represent the behavior of the effective interfacial shear stress around an interfacial wave. Using the gas phase as reference, they state that in the windward side of an interfacial wave, where $\partial h_L / \partial x > 0$, τ_i^* should increase and that in the leeward side, where $\partial h_L / \partial x < 0$, τ_i^* should decrease. The described behavior, for the gas phase, is summarized in Figure 3.5. The fact that the opposite behavior is valid for the liquid phase is automatically taken into account by the natural switch of the sign of τ_i^* in the gas and momentum balance equations, Eqs. (3.11) and (3.12).

The coefficient $\mathcal{J}_i$ that multiplies $\partial h_L / \partial x$ in Eq. (3.47) is expressed by Eq. (3.51) (Brauner & Maron, 1993; 1994).

$$\mathcal{J}_i = C_h \rho_G (U_G - U_L)^2 \qquad (3.51)$$

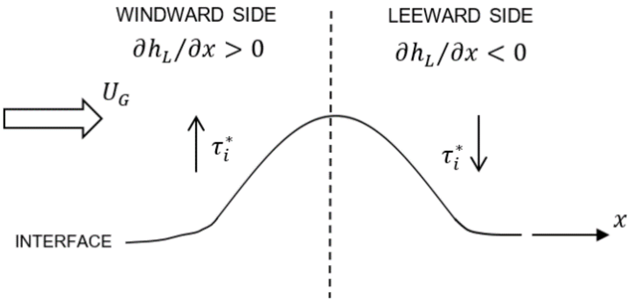

Figure 3.5 – Behavior if the effective interfacial shear around an interfacial wave, according to Brauner & Maron (1993; 1994).

Brauner & Maron (1993; 1994) created an equation for the memory coefficient C_h in Eq. (3.51). This equation was developed by assuming that the transition between stratified smooth and stratified wavy flow obtained with a linear stability analysis of the 1D Two-Fluid Model, including the dynamic term, should match experimental observations for a wide variety of conditions. The parameter C_h is evaluated in the equilibrium condition (steady-state and fully-development) and it is shown in Eq. (3.52), as a function of the Reynolds number $\mathrm{Re}_{L,\mathrm{pm}}$ and the liquid height Froude number $\mathrm{Fr}_{hL,\mathrm{pm}}$, which are calculated through Eqs. (3.53) and (3.54), respectively.

$$C_h = 2.45 \times 10^{-4} \left[\frac{\mathrm{Re}_{L,\mathrm{pm}}}{\left(\mathrm{Fr}_{hL,\mathrm{pm}}\right)^2} \right]^{m} \tag{3.52}$$

$$\mathrm{Re}_{L,\mathrm{pm}} = \frac{\rho_L U_{L,\mathrm{pm}} D_{hL,\mathrm{pm}}}{\mu_L} \tag{3.53}$$

$$\mathrm{Fr}_{hL,\mathrm{pm}} = \frac{U_{L,\mathrm{pm}}}{\sqrt{g h_{L,\mathrm{pm}} \cos\theta}} \tag{3.54}$$

The subscript "pm" present in so many terms in Eqs. (3.52)-(3.54) stands for "Point Model", which is the solution of an equilibrium version of the 1D Two-Fluid Model, as it will be more thoroughly detailed in the next chapter. All the terms containing such subscript were evaluated with the Point Model.

The exponent m in Eq. (3.52) depends on the phasic flow regime (if it is laminar, transitional or turbulent). Therefore, the same scheme of Eq. (3.44), used for calculating the wall friction factors f_K, $K \in \{G, L\}$, is proposed for evaluating

$\mathscr{m}$, as it can be seen in Eq. (3.55). This is not what was originally proposed by Brauner & Maron (1993; 1994), but it is what is adopted in this work for reasons of consistency with the procedures employed for evaluating f_K.

$$\mathscr{m} = \begin{cases} (\mathscr{m})_{\text{lam}} & ; \ \text{Re}_{L,\text{pm}} \le \text{Re}_{\text{lam}} \\ w_t(\mathscr{m})_{\text{turb}} + (1 - w_t)(\mathscr{m})_{\text{lam}} & ; \ \text{Re}_{\text{lam}} < \text{Re}_{L,\text{pm}} < \text{Re}_{\text{turb}} \\ (\mathscr{m})_{\text{turb}} & ; \ \text{Re}_{L,\text{pm}} \ge \text{Re}_{\text{turb}} \end{cases} \tag{3.55}$$

The expressions for the laminar, $(\mathscr{m})_{\text{lam}}$, and turbulent, $(\mathscr{m})_{\text{turb}}$, exponents $\mathscr{m}$ are written in Eqs. (3.56) and (3.57), respectively.

$$(\mathscr{m})_{\text{lam}} = 1 \tag{3.56}$$

$$(\mathscr{m})_{\text{turb}} = 1.565 - 0.072 \ln \text{Re}_{L,\text{pm}} \tag{3.57}$$

3.1.9. Final 1D Two-Fluid Model

By applying the closure relations, Eqs. (3.17), (3.22), (3.24), (3.29), (3.33) and (3.47), presented in the previous sections into Eqs. (3.9)-(3.12), the final form of the 1D Two-Fluid Model employed in the present work for horizontal and nearly horizontal pipelines can be shown. Those are: the gas mass conservation equation, Eq. (3.58), the liquid mass conservation equation, Eq. (3.59), the gas momentum conservation equation, Eq. (3.60), and the liquid momentum balance equation, Eq. (3.61).

$$\frac{\partial(\alpha_G \rho_G)}{\partial t} + \frac{\partial(\alpha_G \rho_G U_G)}{\partial x} = 0 \tag{3.58}$$

$$\frac{\partial(\alpha_L \rho_L)}{\partial t} + \frac{\partial(\alpha_L \rho_L U_L)}{\partial x} = 0 \tag{3.59}$$

$$\begin{aligned} \frac{\partial(\alpha_G \rho_G U_G)}{\partial t} + \frac{\partial\left(\alpha_G \rho_G {U_G}^2\right)}{\partial x} & \\ = -\alpha_G \frac{\partial P}{\partial x} - \left(\rho_G \alpha_G g \cos\theta + \mathcal{J}_i \frac{S_i}{A}\right) \frac{\partial h_L}{\partial x} - \frac{\partial\left(\alpha_G \Delta P_{\mathcal{D},G}\right)}{\partial x} & \\ + \frac{\partial}{\partial x}\left(\alpha_G \mu_G^{eff} \frac{\partial U_G}{\partial x}\right) - \alpha_G \rho_G g \sin\theta - \tau_{wG} \frac{S_G}{A} - \tau_i \frac{S_i}{A} & \end{aligned} \tag{3.60}$$

$$\begin{aligned}\frac{\partial(\alpha_L\rho_L U_L)}{\partial t}+\frac{\partial\left(\alpha_L\rho_L {U_L}^2\right)}{\partial x}
&=-\alpha_L\frac{\partial P}{\partial x}-\left(\rho_L\alpha_L g\cos\theta-\mathcal{J}_i\frac{S_i}{A}\right)\frac{\partial h_L}{\partial x}-\frac{\partial\left(\alpha_L\Delta P_{\mathcal{D},L}\right)}{\partial x}\\
&+\frac{\partial}{\partial x}\left(\alpha_L\mu_L^{eff}\frac{\partial U_L}{\partial x}\right)-\alpha_L\sigma\frac{\partial^3 h_L}{\partial x^3}-\alpha_L\rho_L g\sin\theta\\
&-\tau_{wL}\frac{S_L}{A}+\tau_i\frac{S_i}{A}\end{aligned}\tag{3.61}$$

The single pressure chosen for the model, is the gas interfacial pressure P_{iG}, whose subscripts are dropped in Eqs. (3.60) and (3.61), becoming the variable P. Therefore, the four unknown variables for the 1D Two-Fluid Model are one of the holdups, the bulk velocities and the gas interfacial pressure P.

3.1.9.1. Boundary and Initial Conditions

The 1D Two-Fluid Model comprises a boundary value problem (in space x) and an initial value problem (in time t). For the boundary value problem, as it has four basic unknown variables (one of the holdups, the bulk velocities and the pressure), four boundary conditions are needed. The ones used in the present work are:

- The inlet superficial gas velocity ($U_{sG,\mathrm{in}}$);
- The inlet superficial liquid velocity ($U_{sL,\mathrm{in}}$);
- The outlet pressure (P_{out});
- The gas holdup derivative at the outlet ($\partial\alpha_G/\partial x|_{\mathrm{out}}$).

The first three boundary conditions are Dirichlet-type and the last one is of the Neumann type. While the first three conditions are an input of the problem, that is, it depends on the flow case simulated, the gas holdup flux at the outlet is always considered null. Such boundary conditions are better displayed in Figure 3.6.

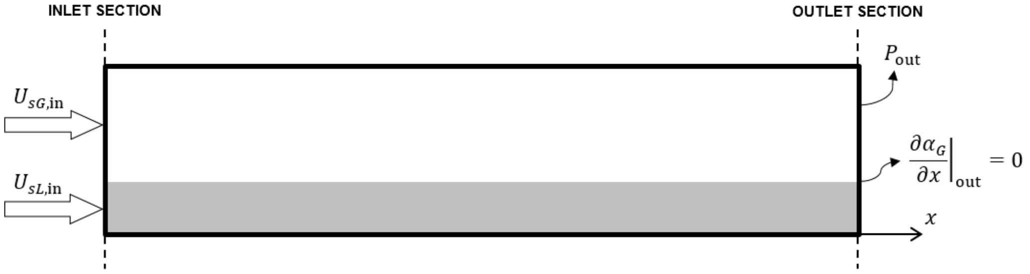

Figure 3.6 – Boundary conditions of the Regime Capturing Methodology.

A constant pressure field was considered as the initial pressure distribution, being equal to the outlet pressure P_{out}. The initial gas holdup field was determined assuming stratified flow in equilibrium, i.e., constant liquid level and velocities. The initial bulk velocities were also constant and determined from the ratio between the inlet phase superficial velocities and the equilibrium phase holdup, Eq. (3.41).

3.2. Numerical Method

To solve the system of conservation equations of the 1D Two-Fluid Model, the Finite Volumes Method (Patankar, 1980) is used. Here a brief presentation of the numerical solution methodology is made. Detailed information can be found in Carneiro (2006) and Fontalvo (2017).

The Finite Volume Method (Patankar, 1980) consists of dividing the domain of interest in control volumes and integrating the conservation equations in time and space in each control volume in order to guarantee global conservation of all variables of interest. Therefore, to present the method, first, the spatial mesh defined for the former are described, followed by the interpolation schemes used. Then, the discretized conservation equations used for evaluating the variables of interest (one of the holdups, the bulk phase velocities and the pressure) in the domain are presented and, afterwards, the numerical approach for handling local occurrences of single-phase flow is covered. At last, the numerical solution procedure as a whole is outlined.

3.2.1. Spatial Mesh

The spatial mesh used in the Finite Volume Method was defined using the Method A of Patankar (1980), in which first N_L nodal points are uniformly distributed throughout the spatial domain (coordinate x). Then, the faces of the finite volume elements are positioned in the middle of each pair of nodal points, equidistant to them. Besides, two additional faces are defined in the boundaries of the domain, coincident with the starting and final nodal points, providing a total of $(N_L + 1)$ faces. Figure 3.7 illustrates the resulting mesh and its key parameters. In the present work, a uniform mesh was employed.

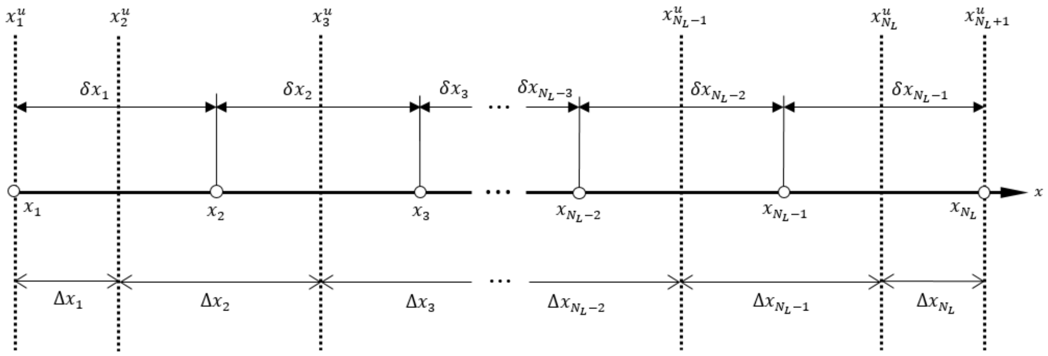

Figure 3.7 – Spatial mesh used in the Finite Volume Method.

In the referred figure, x_j, $j \in \{1, N_L\}$ is the j-th nodal point position; x_j^u, $j \in \{1, N_L + 1\}$, is the j-th face position; δx_j, $j \in \{1, N_L - 1\}$, is the distance between the j-th and $(j + 1)$-th nodal points; and Δx_j, $j \in \{1, N_L\}$, is the distance between the j-th and $(j + 1)$-th face. As characteristic of the Method A for mesh construction, the distance between the first two and last two faces is half of all the other distances Δx_j and δx_j of the mesh. This can be seen in Eqs. (3.62) and (3.63), which express the former and latter distances, respectively. In them, Δx (without the subscript j) is the most important distance of the mesh and it is defined by (3.64).

$$\Delta x_j = \begin{cases} \Delta x/2 \ ; & j = 1, N_L \\ \Delta x \ ; & j \neq 1, N_L \end{cases} \tag{3.62}$$

$$\delta x_j = \Delta x \ ; \ j \in \{1, \ldots, N_L - 1\} \tag{3.63}$$

$$\Delta x = \frac{L}{N_L - 1} \tag{3.64}$$

In accordance with recommendations of Patankar (1980), in order to avoid an oscillatory pressure field, a staggered mesh is used for the discretization of the conservation equations, i.e., at the nodal points, scale variables (e.g. holdups and pressure) are stored, while flow variables (e.g. bulk velocities) are stored at the control volumes faces. Figures 3.8(a) and 3.8(b) illustrates the main scalar control volume and the velocities (staggered) control volume, respectively, in which **P**, **W**, **WW**, **E** and **EE** allude, also respectively, the reference nodal point, and its neighbors from both sides, west and east. The faces w, ww, ee, e correspond to the face location at west and east side of the main central point.

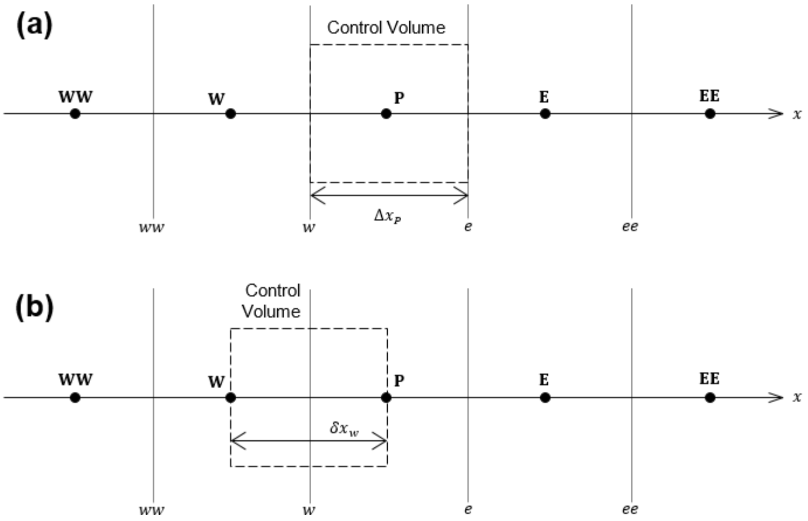

Figure 3.8 – Spatial meshes: (a) scalar variables; and (b) velocities.

3.2.2. Discretized Equations

To perform the time integration of the conservation equations, the fully implicit 1st order Euler scheme was applied, since it is unconditionally stable. The time steps are represented by the variable Δt and, during the procedure in time, the superscript “0” is used to refer to the previous time instant value of a variable.

To discretize the spatial convective terms, the first-order upwind scheme was employed. The operator $\tilde{\psi}$, of a general variable ψ, means that the upwind scheme was used for evaluating it. Thus, the values of scalar quantities at the control volume faces e and w were determined with Eqs. (3.65) and (3.66), respectively, and at the nodal points P and W with Eqs. and , respectively.

$$\tilde{\psi}_e = \llbracket \mathrm{sign}(U_e), 0 \rrbracket \psi_P - \llbracket -\mathrm{sign}(U_e), 0 \rrbracket \psi_E \tag{3.65}$$

$$\tilde{\psi}_w = \llbracket \mathrm{sign}(U_w), 0 \rrbracket \psi_W - \llbracket -\mathrm{sign}(U_w), 0 \rrbracket \psi_P \tag{3.66}$$

$$\tilde{\psi}_P = \llbracket \mathrm{sign}(U_P), 0 \rrbracket \psi_w - \llbracket -\mathrm{sign}(U_P), 0 \rrbracket \psi_e \tag{3.67}$$

$$\tilde{\psi}_W = \llbracket \mathrm{sign}(U_W), 0 \rrbracket \psi_{ww} - \llbracket -\mathrm{sign}(U_W), 0 \rrbracket \psi_w \tag{3.68}$$

For computing the values of the general variable ψ in nodal points **P** and **W** as a function of the face-stored variables, one might use simple arithmetic mean operations, as shown in Eqs. (3.69) and (3.70), respectively. Proceeding in an analogous way, an average of the scalar quantities at the faces e and w can be determined as shown by Eqs. (3.71) and (3.72), respectively. The operator $\breve{\psi}$, in the general variable ψ, represents such arithmetic mean.

$$\breve{\psi}_P = \frac{\psi_w + \psi_e}{2} \tag{3.69}$$

$$\breve{\psi}_W = \frac{\psi_{ww} + \psi_w}{2} \tag{3.70}$$

$$\breve{\psi}_e = \frac{\psi_P + \psi_E}{2} \tag{3.71}$$

$$\breve{\psi}_w = \frac{\psi_P + \psi_W}{2} \tag{3.72}$$

To facilitate the presentation of the discretized conservation equations, it is convenient to define the pseudo-fluxes F_K^*, $K \in \{G, L\}$, and the fluxes F_K, $K \in \{G, L\}$ at the faces $\not{f} \in \{ee, e, w, ww\}$. This is performed in Eqs. (3.73) and (3.74), respectively.

$$(F_K^*)_{\not{f}} = (\tilde{\rho}_K)_{\not{f}}(U_K)_{\not{f}}\, A \tag{3.73}$$

$$(F_K)_{\not{f}} = (\breve{\rho}_K)_{\not{f}}\, (\breve{\alpha}_K)_{\not{f}}(U_K)_{\not{f}}\, A \tag{3.74}$$

3.2.2.1. Gas Holdup

The holdup chosen as a basic variable of the 1D Two-Fluid Model was the gas holdup. Therefore, the conservation equation for α_G throughout the domain is the gas mass conservation equation, Eq. (3.58). The Finite Volume Method discretization of such equation in the standard spatial mesh of Figure 3.8(a) provides the discretized expression formulated in Eq. (3.75) for the nodal point **P** as a function of its neighbors **E** and **W**.

$$(a_{\alpha G})_P(\alpha_G)_P = (a_{\alpha G})_E(\alpha_G)_E + (a_{\alpha G})_W(\alpha_G)_W + (b_{\alpha G})_P \tag{3.75}$$

The coefficients $a_{\alpha G}$ at the nodal points **P**, **E** and **W** and at **P** for the previous time step are defined by Eqs. (3.76)-(3.79), respectively, and the discretized source term $b_{\alpha G}$ at **P** is given by Eq. (3.80).

$$(a_{\alpha G})_P = (a_{\alpha G})_E + (a_{\alpha G})_W + (\rho_G)_P \, A \frac{\Delta x_P}{\Delta t} + [(F_G^*)_e - (F_G^*)_w] \tag{3.76}$$

$$(a_{\alpha G})_E = [\![-(F_G^*)_e, 0]\!] \tag{3.77}$$

$$(a_{\alpha G})_W = [\![\, (F_G^*)_w, 0]\!] \tag{3.78}$$

$$(a_{\alpha G})_P^0 = (\rho_G)_P^0 \, A \frac{\Delta x_P}{\Delta t} \tag{3.79}$$

$$(b_{\alpha G})_P = (a_{\alpha G})_P^0 \, (\alpha_G)_P^0 \tag{3.80}$$

3.2.2.2. Liquid and Gas Bulk Velocities

For the evaluation of the bulk velocities of the gas and liquid phases, U_G and U_L, the momentum conservation equations of the 1D Two-Fluid Model, Eqs. (3.60) and (3.61), were discretized in the staggered mesh of Figure 3.8(b). After performing the Finite Volume discretization of these equations and using a sub-relaxation factor ς, fixed as 0.7 for facilitating the convergence, Eq. (3.81) is obtained. It expresses the bulk velocity U_K, $K \in \{G, L\}$, value at face w as a function of faces e and ww, of the pressure differences between the nodal points **W** and **P** and its values for the previous iteration (different from the previous time instant), represented by the superscript “pi”.

$$\begin{aligned}(a_{UK})_w (U_K)_w = (a_{UK})_e (U_K)_e + (a_{UK})_{ww} (U_K)_{ww} + (b_{UK})_w \\ + (\breve{\alpha}_K)_w \, A (P_W - P_P)\end{aligned} \tag{3.81}$$

The Eq. (3.81) can be reformulated as indicated by Eq. (3.82), using the variable d_K, which is expressed by Eq. (3.83) at the face w, and the concept of pseudo-velocity $\widehat{U}_K$, $K \in \{G, L\}$, which is defined in Eq. (3.84) for the face w.

$$(U_K)_w = \left(\widehat{U}_K\right)_w + (d_K)_w \, (P_W - P_P) \tag{3.82}$$

$$(d_K)_w = \frac{(\breve{\alpha}_K)_w A}{(a_{UK})_w} \tag{3.83}$$

$$\left(\widehat{U}_K\right)_w = \frac{1}{(a_{UK})_w}\left[(a_{UK})_e (U_K)_e + (a_{UK})_{ww}(U_K)_{ww} + (b_{UK})_w\right] \tag{3.84}$$

In Eqs. (3.85)-(3.88), the coefficients a_{UK}, $K \in \{G, L\}$, for faces w, e and ww and for w at the previous time step are respectively defined. The discretized source term b_{UK} at face w is formulated in Eq. (3.89).

$$(a_{UK})_w = \frac{1}{\varsigma}\left[(a_{UK})_e + (a_{UK})_{ww} + (a_{UK})_w^0 - \left(s_{\mathscr{p},UK}\right)_w \delta x_w A\right] \tag{3.85}$$

$$(a_{UK})_e = \left\llbracket -\left(\breve{F}_K\right)_P, 0 \right\rrbracket + \frac{(\alpha_K)_P \left(\mu_K^{eff}\right)_P A}{\Delta x_P} \tag{3.86}$$

$$(a_{UK})_{ww} = \left\llbracket \left(\breve{F}_K\right)_W, 0 \right\rrbracket + \frac{(\alpha_K)_W \left(\mu_K^{eff}\right)_W A}{\Delta x_W} \tag{3.87}$$

$$(a_{UK})_w^0 = (\breve{\rho}_K)_w^0 (\breve{\alpha}_K)_w^0 \, A \frac{\delta x_w}{\Delta t} \tag{3.88}$$

$$(b_{UK})_w = (a_{UK})_w^0 (U_K)_w^0 + \left(s_{c,UK}\right)_w \delta x_w \, A + (1 - \varsigma)(a_{UK})_w (U_K)_w^{\mathscr{p}i} \tag{3.89}$$

The source terms of the momentum conservation equations of the 1D Two-Fluid Model were approximated as linear functions of U_K. The linear and angular coefficients of these functions, $s_{c,UK}$ and $s_{\mathscr{p},UK}$, $K \in \{G, L\}$, are calculated by the expressions depicted for the face w in Eqs. (3.90) and (3.96), respectively. The hydrostatic pressure, dynamic pressure, surface tension, gravitational and interfacial contributions ($\mathcal{B}_{\mathcal{H},UK}$, $\mathcal{B}_{\mathcal{D},UK}$, $\mathcal{B}_{\sigma,UK}$, $\mathcal{B}_{\mathcal{G},UK}$ and $\mathcal{B}_{i,UK}$, respectively) to the linear coefficient $s_{c,UK}$ are calculated for face w through Eqs. (3.91)-(3.95), respectively. In Eq. (3.91), the upper sign of "∓" refers to the gas phase and the lower one to the liquid. The second order derivatives present in Eqs. (3.93) must be approximated by finite differences.

$$\begin{aligned}\left(s_{c,UK}\right)_w = \left(\mathcal{B}_{\mathcal{H},UK}\right)_w + \left(\mathcal{B}_{\mathcal{D},UK}\right)_w + \left(\mathcal{B}_{\sigma,UK}\right)_w + \left(\mathcal{B}_{\mathcal{G},UK}\right)_w \\ + \left(\mathcal{B}_{i,UK}\right)_w\end{aligned} \tag{3.90}$$

$$\left(\mathcal{B}_{\mathcal{H},UK}\right)_w = -\left[(\check{\rho}_K)_w(\check{\alpha}_K)_w g\cos\theta \mp (\mathcal{J}_i)_w\frac{(S_i)_w}{A}\right]\frac{(h_L)_P-(h_L)_W}{\delta x_w} \tag{3.91}$$

$$\left(\mathcal{B}_{\mathcal{D},UK}\right)_w = \frac{\left(\alpha_K\Delta P_{\mathcal{D},K}\right)_P - \left(\alpha_K\Delta P_{\mathcal{D},K}\right)_W}{\delta x_w} \tag{3.92}$$

$$\left(\mathcal{B}_{\sigma,UK}\right)_w = \begin{cases} 0 & ;K=G \\ (\check{\alpha}_L)_w\sigma\left[\left(\dfrac{\partial^2 h_L}{\partial x^2}\right)_P - \left(\dfrac{\partial^2 h_L}{\partial x^2}\right)_W\right]\dfrac{1}{\delta x_w} & ;K=L\end{cases} \tag{3.93}$$

$$\left(\mathcal{B}_{\mathcal{G},UK}\right)_w = -\,(\check{\alpha}_K)_w(\check{\rho}_K)_w g\sin\theta \tag{3.94}$$

$$\left(\mathcal{B}_{i,UK}\right)_w = \frac{1}{2}(f_i)_w\,(\check{\rho}_G)_w|(U_G)_w-(U_L)_w|(U_K)_w \tag{3.95}$$

$$\begin{aligned}\left(s_{\wp,UK}\right)_w = -\frac{1}{2}(f_K)_w(\check{\rho}_K)_w|(U_K)_w| \\ -\frac{1}{2}(f_i)_w(\check{\rho}_G)_w|(U_G)_w-(U_L)_w|\end{aligned} \tag{3.96}$$

3.2.2.3. Pressure

The evaluation of the pressure values in the domain is more complicated than it was for the gas holdup and for the bulk velocities, because the pressure is not present in the remaining conservation equation for the liquid mass. Indeed, the conservation equation used is a global mass balance, obtained after combining the phasic mass balance equations, Eqs. (3.58) and (3.59), normalized with their respective phasic densities (Issa & Kempf, 2003; Carneiro *et al.*, 2011). The normalization is performed since the order of magnitude of the liquid density is much larger than the gas density. This way, both mass conservation equations have similar order of magnitude, with the same weight to influence the determination of the pressure (Issa & Kempf, 2003; Carneiro *et al.*, 2011). Eq. (3.97) formulates such global mass balance equation, in which $\rho_{G,\mathrm{ref}}$ is a reference gas density evaluated with the ideal gas law, Eq. (3.15), for a reference pressure P_{ref} (defined as equal to P_{out}).

$$\frac{\partial \alpha_L}{\partial t} + \frac{\partial(\alpha_L U_L)}{\partial x} + \frac{1}{\rho_{G,\mathrm{ref}}}\left[\frac{\partial(\alpha_G \rho_G)}{\partial t} + \frac{\partial(\alpha_G \rho_G U_G)}{\partial x}\right] = 0 \tag{3.97}$$

The discretization of the global mass conservation equation, Eq. (3.97), in the scalar control volume of Figure 3.8(a) and its multiplication by A provides Eq. (3.98).

$$\begin{aligned}\left[(\alpha_L)_P - (\alpha_L)_P^0\right] A\mathit{\Delta} x_P &+ \left[(\alpha_L U_L)_e - (\alpha_L U_L)_w\right] A\Delta t \\ &+ \left[(\alpha_G \rho_G)_P - (\alpha_G \rho_G)_P^0\right] \frac{A\Delta x_P}{\rho_{G,\mathrm{ref}}} \\ &+ \left[(\alpha_G \rho_G U_G)_e - (\alpha_G \rho_G U_G)_w\right] \frac{A\Delta t}{\rho_{G,\mathrm{ref}}} = 0\end{aligned} \tag{3.98}$$

By applying the definition of Eq. (3.82) for the discretized phasic bulk velocities at faces e and w into Eq. (3.98) and by applying the ideal gas law of Eq. (3.15), $\rho_G = P/(\mathcal{R}_G T)$, the discretized pressure equation, Eq. (3.99), is obtained.

$$(a_P)_P P_P = (a_P)_E P_E + (a_P)_W P_W + (b_P)_P \tag{3.99}$$

The coefficients a_P of the discretized pressure equation at the nodal points **P**, **E** and **W** and the discretized source term b_P at the point **P** are given by Eqs. (3.100)-(3.103), respectively.

$$(a_P)_P = (a_P)_E + (a_P)_W + \frac{(\alpha_G)_P A}{P_{\mathrm{ref}}}\left(\frac{\Delta x_P}{\Delta t}\right) \tag{3.100}$$

$$(a_P)_E = (d_L)_e (\tilde{\alpha}_L)_e A + (d_G)_e (\tilde{\alpha}_G)_e A \frac{(\tilde{\rho}_G)_e}{\rho_{G,\mathrm{ref}}} \tag{3.101}$$

$$(a_P)_W = (d_L)_w (\tilde{\alpha}_L)_w A + (d_G)_w (\tilde{\alpha}_G)_w A \frac{(\tilde{\rho}_G)_w}{\rho_{G,\mathrm{ref}}} \tag{3.102}$$

$$\begin{aligned}(b_P)_P = &\left[(\alpha_L)_P^0 - (\alpha_L)_P + (\alpha_G)_P^0 \frac{(\rho_G)_P^0}{\rho_{G,\mathrm{ref}}}\right] \frac{A\Delta x_P}{\Delta t} + (\tilde{\alpha}_L)_w (\mathcal{U}_L)_w \\ &- (\tilde{\alpha}_L)_e \left(\widehat{U}_L\right)_e \\ &+ \left[(\tilde{\alpha}_G)_w \left(\widehat{U}_G\right)_w \frac{(\tilde{\rho}_G)_w}{\rho_{G,\mathrm{ref}}} - (\tilde{\alpha}_G)_e \left(\widehat{U}_G\right)_e \frac{(\tilde{\rho}_G)_e}{\rho_{G,\mathrm{ref}}}\right]\end{aligned} \tag{3.103}$$

3.2.3. Treatment of the Local Occurrence of Single-Phase Flow

Due to both physical and numerical reasons, local occurrences of single-phase might be a possibility, in spite of the flow being fundamentally two-phase. A liquid slug body free of gas is an example of local liquid single-phase flow in a macroscopic gas-liquid flow. When a phase vanishes, its corresponding discretized momentum (bulk velocity) equation becomes singular. To deal with this issue, a single-phase flow detector (flag), SF, is defined for the faces employing a harmonic mean between the gas holdups of the neighbor nodal points, as shown by Eq. (3.104) for face w (Ortega, 2004; Carneiro, 2006).

$$(SF)_w = \frac{2(\alpha_G)_W(\alpha_G)_P}{(\alpha_G)_W + (\alpha_G)_P} \tag{3.104}$$

When SF is lower than a critical value SF_{sp}, defined in this work as 0.02, the gas-liquid flow becomes liquid single-phase flow. On the other hand, when SF is higher than $(1 - SF_{sp})$, then the flow becomes gas single-phase flow. In terms of the numerical solution, when the two-phase flow becomes single-phase for a certain phase, the bulk velocities of the other phase is considered to be null. Besides, since theoretically there is no interface for this situation, the term $\mathcal{B}_{i,K}$ in Eq. (3.90) is neglected. For more information on the numerical consequences of this strategy for handling the occurrence of single-phase flow, the reader should refer to Ortega (2004), Carneiro (2006) and Fontalvo (2017).

3.2.4. Numerical Procedure

The numerical procedure to solve the set of discretized conservation equations consists in two levels: the transient one and the spatial one. The former is related to the initial value problem and the latter with the boundary value problem. Thus, for a given initial condition, a boundary value problem is solved and then the solution advances to the next time step with a time interval of Δt, calculated by Eq. (3.105). In it, CFL is the Courant-Friedrichs-Levy number, used for guaranteeing a proper distribution between the spatial and temporal meshes, in order to capture correctly the simulated phenomena in both space and time. The value chosen for CFL is of 0.05. Besides, $\Delta t_{\min}$ and $\Delta t_{\max}$ are, respectively the input minimum and maximum values of the Δt, and $U_{\max}$ is the maximum bulk velocity of the phases in the entire domain.

$$\Delta t = -\left[\!\left[-\left[\!\left[\frac{\mathrm{CFL}}{U_{\max}\Delta x}, \Delta t_{\min} \right]\!\right], -\Delta t_{\max} \right]\!\right] \tag{3.105}$$

The solution of the boundary value problem is iterative and the convergence is obtained after the maximum residue, $\mathrm{res}_{\max}$, in the domain for the four unknown variables (α_G, U_G, U_L and P) is lower than a tolerance tol of 10^{-6}. A maximum number $it_{\max}$ of iterations, it, was fixed as 20. The residue, res, for a variable $a \in \{\alpha_G, P\}$ at a nodal point **P** and the residue of a variable $\not{f} \in \{U_G, U_L\}$ at a face w are computed by, respectively, Eqs. (3.106) and (3.107), in which ψ is a general variable and a and b are a coefficient and a discretized source term, respectively.

$$(\mathrm{res}_a)_P = (a_a)_P \psi_P - [(a_a)_E \psi_E + (a_a)_W \psi_W + (b_a)_P] \tag{3.106}$$

$$\left(\mathrm{res}_{\not{f}}\right)_w = \left(a_{\not{f}}\right)_w \psi_w - \left[\left(a_{\not{f}}\right)_e \psi_e + \left(a_{\not{f}}\right)_{ww} \psi_{ww} + \left(b_{\not{f}}\right)_w\right] \tag{3.107}$$

Each linear system of equations composed by the discretization equation for all the domain composes a tridiagonal matrix, solved by the Thomas Algorithm (Patankar, 1980). The systems are solved sequentially in each iteration in which pressure-velocity coupling is handled with the Pressure Implicit Momentum Explicit (PRIME) algorithm (Maliska & Raithby, 1984) modified by Ortega & Nieckele (2005).

Assuming that the input parameters are already defined, the main algorithm can be outlined, excluding minor procedures and routines, as following:

- Step 1: Initialization of the unknown variables (initial conditions) and of the time: $t = 0$;
- Step 2: Solving the boundary-value problem for the time t: $it = 0$;
    - Step 2.1: Evaluation of the geometrical parameters and fluid properties for the entire domain;
    - Step 2.2: Evaluation of the U_K, $K \in \{G, L\}$, fields through the solution of the linear systems of equations originated from Eq. (3.81) for the entire domain;
    - Step 2.3: Evaluation of the P field through the solution of the linear

    system of equations originated from Eq. (3.99) for the entire domain;
    - Step 2.4: Correction of the U_K, $K \in \{G, L\}$, fields for the entire domain through Eq. (3.82);
    - Step 2.5: Evaluation of the α_G field through the solution of the linear system of equations originated from Eq. (3.75) for the entire domain;
    - Step 2.6: Evaluation of the residues field for each variable and for the entire domain through Eqs. (3.106) and (3.107);
    - Step 2.7: Check if $\text{res}_{\max} < tol$ or if $it = it_{\max}$:
        - Step 2.7.1: If yes, then go to Step 3;
        - Step 2.7.2: If no, then $it = it + 1$ and return to Step 2.1;
- Step 3: Check if $t = t_{\text{final}}$ (t_{final} is the total simulation time):
    - If yes, then terminate the numerical procedure;
    - If not, then calculate Δt through Eq. (3.105), update $t = t + \Delta t$ and return to Step 2.

3.3. The Stability-Hyperbolicity Problem of the 1D Two-Fluid Model

The stability-hyperbolicity of the 1D Two-Fluid Model can be analyzed in terms of the so called "characteristics" of the equation system, which will be defined below. In order to determine how the characteristics dictate the hyperbolicity of the mathematical problem, an explanation based in Drew & Passman (1999) is presented. Initially, a generalized first-order quasi-linear system of partial differential equations is considered in Eq. (3.108).

$$\mathbf{A}(\boldsymbol{\Phi})\frac{\partial \boldsymbol{\Phi}}{\partial t} + \mathbf{B}(\boldsymbol{\phi})\frac{\partial \boldsymbol{\Phi}}{\partial x} = \mathbf{c}(\boldsymbol{\Phi}) \tag{3.108}$$

In Eq. (3.108), $\boldsymbol{\Phi}(x,t) = [\Phi_1(x,t) \quad \Phi_2(x,t) \quad \cdots \quad \Phi_{N_\Phi}(x,t)]^{\mathrm{T}}$ is a vector that contains N_Φ variables $\Phi_j(x,t)$, $j \in \{1,2,\dots,N_\Phi\}$, dependent on time (t) and space (x). $\mathbf{A} = \mathbf{A}(\boldsymbol{\Phi})$ and $\mathbf{B} = \mathbf{B}(\boldsymbol{\Phi})$ are two coefficient matrices, $\mathbf{c} = \mathbf{c}(\boldsymbol{\Phi})$ is a source vector and the three of them depend on $\boldsymbol{\Phi}$.

Then, it is assumed that information regarding $\boldsymbol{\Phi}$ is available at all points (x,t) specified along a curve $\mathcal{C}_1$ defined as $x = x(t)$ and illustrated in Figure 3.9. Provided that the derivatives of $\boldsymbol{\Phi}$ can be calculated, Taylor series expansions might be used for obtaining the solution for $\boldsymbol{\Phi}$ in the neighborhood of $\mathcal{C}_1$. For facilitating the explanation, the variables $n = n(x,t)$ and $s = s(x,t)$, which represent the normal and tangential directions of C_1, are defined as it can be observed in Figure 3.9.

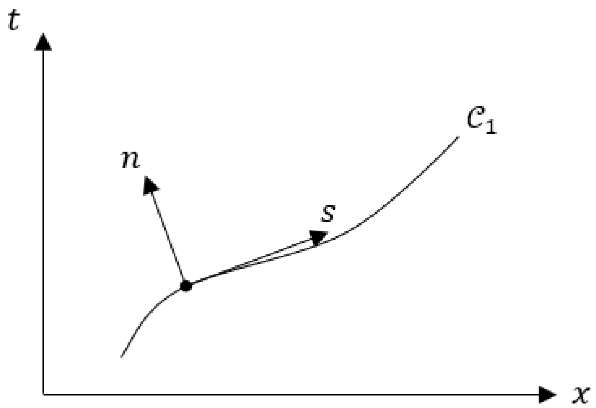

Figure 3.9 – The curve $\boldsymbol{C_1}$ and its associated variables $\boldsymbol{n}$ and $\boldsymbol{s}$.

By rewriting the quasi-linear system of Eq. (3.108) with the newly defined variables n and s, Eq. (3.109) is obtained.

$$\left[\mathbf{A}(\boldsymbol{\Phi})\frac{\partial n}{\partial t}+\mathbf{B}(\boldsymbol{\Phi})\frac{\partial n}{\partial x}\right]\frac{\partial \boldsymbol{\Phi}}{\partial n}=\mathbf{c}(\boldsymbol{\Phi})-\left[\mathbf{A}(\boldsymbol{\Phi})\frac{\partial s}{\partial t}+\mathbf{B}(\boldsymbol{\Phi})\frac{\partial s}{\partial x}\right]\frac{\partial \boldsymbol{\Phi}}{\partial s} \qquad (3.109)$$

As $\boldsymbol{\Phi}$ is given for all C_1 curve, which is equivalent to the statement that $\boldsymbol{\Phi}$ is known for all s values, the RHS of Eq. (3.109) is entirely known. Therefore, the analysis ends up in verifying if the coefficient matrix of $\partial\boldsymbol{\Phi}/\partial n$ is singular or not, which can be summarized as shown by Eq. (3.110). The parameter $\lambda = -\,(\partial n/\partial t)/(\partial n/\partial x)$ is the characteristic of the system of Eq. (3.108).

$$\det[\mathbf{B}(\boldsymbol{\phi}) - \lambda\,\mathbf{A}(\boldsymbol{\phi})] = 0 \qquad (3.110)$$

If the coefficient matrix of $\partial\boldsymbol{\Phi}/\partial n$ is singular, then the system of Eq. (3.108) is hyperbolic, otherwise it is elliptic (Drew & Passman, 1999). The system is hyperbolic and well-posed when all the characteristics λ's of the system of equations are real, and it is elliptic and ill-posed if one of them is complex. If all the characteristics are real and distinct, then the system is strongly hyperbolic and, if they are not, than it is weakly hyperbolic (Dinh *et al.*, 2003).

To determine the correspondence between the values of the characteristics and the hyperbolicity of the quasi-linear system, Prosperetti & Tryggvason (2007) presented a procedure based on introducing a perturbed solution $\boldsymbol{\Phi} = \boldsymbol{\Phi}_0 + \boldsymbol{\phi}$ ($\boldsymbol{\Phi}_0$

is a base state temporally and spatially steady and $\boldsymbol{\phi}$ is a small perturbation) is inserted in the system of conservation equations. Considering that products between $\boldsymbol{\phi}$ and its derivatives might be neglected, as well as that derivatives of $\boldsymbol{\Phi}_0$ are null, and using linear Taylor expansions, in a procedure detailed by Prosperetti & Tryggvason (2007), one obtains Eq. (3.111). In the referred equation, $\mathbf{D}_c = \mathbf{D}_c(\boldsymbol{\Phi}_0)$ is a matrix that contains the derivatives of each element of the vector $\mathbf{c}$ in relation to each variable $\Phi_j, j \in \{1, \dots, N_\Phi\}$.

$$\mathbf{A}(\boldsymbol{\Phi}_0)\frac{\partial \boldsymbol{\phi}}{\partial t} + \mathbf{B}(\boldsymbol{\Phi}_0)\frac{\partial \boldsymbol{\phi}}{\partial x} = \mathbf{D}_c(\boldsymbol{\Phi}_0) \cdot \boldsymbol{\phi} \tag{3.111}$$

The small perturbation is then classically defined as shown in Eq. (3.112), with the form of a travelling wave. There, $\mathbb{i} = \sqrt{-1}$ is the imaginary unit, k is the wave number, ω is its angular frequency and $\boldsymbol{\phi}_{\mathcal{A}}$ is the vector of amplitudes of the perturbations.

$$\boldsymbol{\phi} = \boldsymbol{\phi}_{\mathcal{A}} e^{\mathbb{i}(kx - \omega t)} \tag{3.112}$$

After applying the linear definition of $\boldsymbol{\phi}$ from Eq. (3.112) into Eq. (3.111) and performing some algebraic manipulations, one obtains a homogeneous linear system of equations in relation to $\boldsymbol{\phi}_{\mathcal{A}}$, which, for possessing a nontrivial solution should fulfill the condition present in Eq. (3.113).

$$\det\left[\mathbf{B}(\boldsymbol{\Phi}_0) - \lambda\,\mathbf{A}(\boldsymbol{\Phi}_0) + \frac{\mathbb{i}}{k}\mathbf{D}_c(\boldsymbol{\Phi}_0)\right] = 0 \tag{3.113}$$

In the dispersion relation formulated in Eq. (3.113), it is seen that the characteristic $\lambda = \omega/k$ appears in the expression. By maintaining the value λ constant and considering the limit of instabilities and perturbations with negligible wavelengths, $k \to \infty$, from Eq. (3.113) one obtains Eq. (3.110) (Ramshaw & Trapp, 1978). Thus, it has been shown that, through a linear stability analysis, which is required according to the third well-posedness condition of Hadamard, one can obtain the same rule of correspondence deduced in Drew & Passman (1999) between the characteristics and the hyperbolicity of the Eq. (3.108) system.

As previously stated, the 1D Two-Fluid Model, represented by Eqs. (3.58)-(3.61), often faces the problem of the ill-posedness (complex characteristics λ), which is overcome by the use of regularization methods. Since, at this point of the work, the 1D Two-Fluid Model has been thoroughly presented, it is possible to discuss such methods in an improved and more *ad hoc* manner and with the help of Eqs. (3.58)-(3.61).

Correctly modelling the interfacial-bulk pressure difference $(P_{iK} - P_K)$ for phase $K \in \{G, L\}$ is considered a regularizing method due to the known stabilizing features of both the hydrostatic (Chung & Song, 1996) and dynamic (Bestion, 1990; Han & Guo, 2015) pressure terms: the first term in the parentheses that multiplies the derivative $\partial h_L/\partial x$, in the RHS of the momentum balance equations, Eqs. (3.60)-(3.61), and the third term of the RHS of these equations, respectively. That is the reason why vertical flows $(\cos\theta = 0°)$ suffer from serious hyperbolicity issues, being in some cases even unconditionally ill-posed (Han & Guo, 2015). The dynamic pressure term is capable of completely hyperbolize the 1D Two-Fluid Model (Bestion, 1990; Han & Guo 2015), because linear stability analyses have shown that it limits the interfacial instabilities growth rate for all the wavelengths (Fullmer *et al.*, 2014). The second-order diffusion, induced by the axial momentum diffusion term of Eqs. (3.60)-(3.61) (fourth term on the RHS), also helps to regularize the model by controlling the growth rate of small wavelength interfacial instabilities (Fullmer *et al.*, 2014). The same is true for the third-order term due to the surface tension effect in Eq. (3.61) (fifth term on the RHS), although it acts mostly in very small wavelength interfacial instabilities (Fullmer *et al.*, 2014).

The methods and the effects of their associated terms and parameters in the 1D Two-Fluid Model previously mentioned are well known in literature. The same is not truth for the dynamic interfacial shear stress term, that is, the second term in the parentheses that multiplies the derivative $\partial h_L/\partial x$ in the RHS of the momentum balance equations, Eqs. (3.60)-(3.61). It was found by the author of this work solely one work (De Bertodano *et al.*, 2013) that addresses the effect of such term on the stability-hyperbolicity of the 1D Two-Fluid Model. With a simple Kelvin-Helmholtz stability analysis, De Bertodano *et al.* (2013) showed that the interfacial shear stress term destabilizes the model.

For checking the conclusion of the work of De Bertodano *et al.* (2013), simplified well-posedness (characteristics) analyses of the 1D Two-Fluid Model were performed through the solution of Eq. (3.110). For such investigation, not only the liquid phase, but also the gas was considered incompressible. Furthermore, the vector of unknown variables $\mathbf{\Phi}$ can be specified according to Eq. (3.114).

$$\mathbf{\Phi} = [\alpha_G \quad U_G \quad U_L \quad P]^{\mathrm{T}} \tag{3.114}$$

The 1D Two-Fluid Model, Eqs. (3.58)-(3.61), should be rewritten as a quasi-linear system, as in Eq. (3.108). First, the terms of second and third-order of the momentum balance equations were neglected (Montini, 2011). Then, the derivative $\partial h_L/\partial \alpha_L$ is formulated in Eq. (3.115) with the assistance of the geometrical definitions of Table 3.1 and Eq. (3.13).

$$\frac{\partial h_L}{\partial \alpha_L} = \pi D \left(\frac{\sin\delta}{2-\cos\delta}\right) \tag{3.115}$$

It is important as well to define the derivative of the dynamic pressure term $\Delta P_{\mathcal{D},K}$, $K \in \{G, L\}$, by taking into account the employment of the Bestion (1990) correlation, Eqs. (3.30) and (3.31). This is done in Eq. (3.116) and (3.117), where the auxiliary variable $\mathcal{H}_{\mathcal{D}}$ is expressed.

$$\frac{\partial\left(\Delta P_{\mathcal{D},K}\right)}{\partial x} = 2\eta_{\mathcal{D}}\rho_{\mathcal{D}}(U_L - U_G)\left(\frac{\partial U_G}{\partial x} - \frac{\partial U_L}{\partial x}\right) - \mathcal{H}_{\mathcal{D}}\frac{\partial \alpha_G}{\partial x} \tag{3.116}$$

$$\mathcal{H}_{\mathcal{D}} = [\alpha_L - \alpha_G - \alpha_G\alpha_L(\rho_L - \rho_G)]\left[\frac{\eta_{\mathcal{D}}\rho_G\rho_L(U_L - U_G)^2}{(\alpha_G\rho_L + \alpha_L\rho_G)^2}\right] \tag{3.117}$$

Afterwards, the gas and liquid mass conservation equations of the 1D Two-Fluid Model, Eqs. (3.58) and (3.59), are reformulated in Eqs. (3.118) and (3.119), respectively, in the same non-conservative form of the quasi-linear system of Eq. (3.108), using the unknown variables vector $\mathbf{\Phi}$**,** Eq. (3.114).

$$\rho_G\frac{\partial \alpha_G}{\partial t} + \rho_G U_G\frac{\partial \alpha_G}{\partial x} + \alpha_G\rho_G\frac{\partial U_G}{\partial x} = 0 \tag{3.118}$$

$$-\rho_L\frac{\partial \alpha_G}{\partial t} - \rho_L U_L\frac{\partial \alpha_G}{\partial x} + \alpha_L\rho_L\frac{\partial U_L}{\partial x} = 0 \tag{3.119}$$

A similar procedure is adopted for rewriting the momentum conservation equations, Eqs. (3.60) and (3.61), by additionally using the definitions of Eqs. (3.115)-(3.117). Such reshaped conservations equations are shown in Eqs. (3.120) and (3.121) for the gas and liquid, respectively.

$$\rho_G U_G \frac{\partial \alpha_G}{\partial t} + \alpha_G \rho_G \frac{\partial U_G}{\partial t} + \mathscr{b}_I \frac{\partial \alpha_G}{\partial x} + \mathscr{b}_{II} \frac{\partial U_G}{\partial x} + \mathscr{b}_{III} \frac{\partial U_L}{\partial x} + \alpha_G \frac{\partial P}{\partial x} = \Lambda_G \tag{3.120}$$

$$-\rho_L U_L \frac{\partial \alpha_G}{\partial t} + \alpha_L \rho_L \frac{\partial U_L}{\partial t} + \mathscr{b}_{IV} \frac{\partial \alpha_G}{\partial x} + \mathscr{b}_V \frac{\partial U_G}{\partial x} + \mathscr{b}_{VI} \frac{\partial U_L}{\partial x} + \alpha_L \frac{\partial P}{\partial x} = \mathit{\Lambda}_L \tag{3.121}$$

The coefficients $\mathscr{b}_j$, $j \in \{I, II, III, IV, V, VI\}$, present in the previous expressions are defined in Eqs. (3.122)-(3.127), respectively.

$$\mathscr{b}_I = \rho_G {U_G}^2 + \mathit{\Delta} P_{\mathcal{D},G} - \alpha_G \mathcal{H}_\mathcal{D} - \left(\alpha_G \rho_G g \cos\theta + \mathcal{J}_i \frac{S_i}{A}\right) \frac{\partial h_L}{\partial \alpha_L} \tag{3.122}$$

$$\mathscr{b}_{II} = 2\alpha_G [\rho_G U_G + \eta_\mathcal{D} \rho_\mathcal{D} (U_L - U_G)] \tag{3.123}$$

$$\mathscr{b}_{III} = -2\alpha_G \eta_\mathcal{D} \rho_\mathcal{D} (U_L - U_G) \tag{3.124}$$

$$\mathscr{b}_{IV} = -\rho_L {U_L}^2 - \mathit{\Delta} P_{\mathcal{D},L} - \alpha_L \mathcal{H}_\mathcal{D} - \left(\alpha_L \rho_L g \cos\theta - \mathcal{J}_i \frac{S_i}{A}\right) \frac{\partial h_L}{\partial \alpha_L} \tag{3.125}$$

$$\mathscr{b}_V = 2\alpha_L \eta_\mathcal{D} \rho_\mathcal{D} (U_L - U_G) \tag{3.126}$$

$$\mathscr{b}_{VI} = 2\alpha_L [\rho_L U_L - \eta_\mathcal{D} \rho_\mathcal{D} (U_L - U_G)] \tag{3.127}$$

The source term Λ_K, $K \in \{G, L\}$, in Eqs. (3.120) and (3.121) contemplate the gravitational and shear forces, as shown in Eq. (3.128), where the upper sign in “∓” refer to the gas phase and the lower sign to the liquid.

$$\Lambda_K = \alpha_K \rho_K g \sin\theta - \tau_{wK} \frac{S_K}{A} \mp \tau_i \frac{S_i}{A} \tag{3.128}$$

After rewriting the 1D Two-Fluid Model, one can determine the coefficient matrices $\mathbf{A}(\mathbf{\Phi})$ and $\mathbf{B}(\mathbf{\Phi})$ of the system, Eq. (3.108), as depicted in Eqs. (3.129) and (3.130), respectively.

$$\mathbf{A}(\mathbf{\Phi}) = \begin{bmatrix} \rho_G & 0 & 0 & 0 \\ -\rho_L & 0 & 0 & 0 \\ \rho_G U_G & \alpha_G \rho_G & 0 & 0 \\ -\rho_L U_L & 0 & \alpha_L \rho_L & 0 \end{bmatrix} \tag{3.129}$$

$$\mathbf{B}(\mathbf{\Phi}) = \begin{bmatrix} \rho_G U_G & \alpha_G \rho_G & 0 & 0 \\ -\rho_L U_L & 0 & \alpha_L \rho_L & 0 \\ \mathscr{b}_I & \mathscr{b}_{II} & \mathscr{b}_{III} & \alpha_G \\ \mathscr{b}_{IV} & \mathscr{b}_V & \mathscr{b}_{VI} & \alpha_L \end{bmatrix} \tag{3.130}$$

With the already defined matrices $\mathbf{A}(\mathbf{\Phi})$ and $\mathbf{B}(\mathbf{\Phi})$, it is possible to solve Eq. (3.110) for finding the characteristics λ's. Such equation might be developed into a easily solved quadratic polynomial, shown in Eq. (3.131). The variables ζ_j, $j \in \{0,1,2\}$ are expressed in Eqs. (3.132)-(3.134), respectively.

$$\zeta_0 + \zeta_1 \lambda + \zeta_2 \lambda^2 = 0 \tag{3.131}$$

$$\begin{aligned} \zeta_0 = {} & \alpha_G {\alpha_L}^2 \mathscr{b}_I - {\alpha_L}^2 U_G \mathscr{b}_{II} + \alpha_G \alpha_L U_L \mathscr{b}_{III} - {\alpha_G}^2 \alpha_L \mathscr{b}_{IV} \\ & + \alpha_G \alpha_L U_G \mathscr{b}_V - {\alpha_G}^2 U_L \mathscr{b}_{VI} \end{aligned} \tag{3.132}$$

$$\zeta_1 = {\alpha_L}^2 \mathscr{b}_{II} - \alpha_G \alpha_L (\mathscr{b}_{III} + \mathscr{b}_V) + {\alpha_G}^2 \mathscr{b}_{VI} \tag{3.133}$$

$$\zeta_2 = -\alpha_G \alpha_L (\alpha_G \rho_L + \alpha_L \rho_G) \tag{3.134}$$

Assuming that the holdups are equal to steady-state fully-developed equilibrium values for a given pair of superficial velocities, Eq. (3.131) is straightforwardly employed for evaluating the characteristics of the 1D Two-Fluid Model, subjected to the other previously mentioned hypotheses. In a following chapter, the results from this analysis, for the Eskerud Smith *et al.* (2011) database and for checking the findings of De Bertodano *et al.* (2013), are presented and discussed.

4. OPTIMIZATION OF THE INTERFACIAL SHEAR STRESS

In this chapter of the work, two new correlations for the interfacial friction factor are proposed to improve the predictions of stratified and slug flows. These correlations were developed based on the experimental database of Eskerud Smith *et al.* (2011), also used in Johansen *et al.* (2014) and in Khaledi *et al.* (2014), of viscous oil and gas flow in several regimes.

As clearly mentioned in the previous chapter, the accuracy of the numerical prediction depends strongly on the interfacial friction factor. However, it should be made clear that an appropriate interfacial friction factor is necessary not only for the Regime Capturing Methodology, described in the previous chapter, but also for so called “Point Models”. Point Models are based on simplified (steady-state and fully-developed) version of the 1D Two-Fluid Model for holdup and pressure gradient (henceforth labelled as “integral parameters”).

In the literature review regarding the modelling of the interfacial shear stress in horizontal stratified gas-liquid flows, a vast number of options was illustrated. However, most of the literature correlations for such parameter were made with experiments with low viscosity (i.e., close to the water viscosity at standard consitions, 1cp), while the Eskerud Smith *et al.* (2011) database is for a mineral, one hundred times more viscous than water. In fact, Pasqualette *et al.* (2015) have shown that correlations such as the ones found in the works of Andritsos & Hanratty (1987) and Andreussi & Persen (1987) may generate significantly disparate results, when employed in the Regime Capturing Methodology for simulating cases from the Eskerud Smith *et al.* (2011) database. It was shown how inefficient interfacial friction factor correlations commonly used in the literature are for simulating the Eskerud Smith *et al.* (2011) database within the referred framework. Therefore, at the presented work, needed new correlations based on such experimental data were developed.

This chapter begins by a thorough presentation of the viscous oil-gas horizontal flow cases of the Eskerud Smith *et al.* (2011) database, aiming to select the experimental cases from the database most appropriate to elaborate the new correlations. Afterwards, the Point model (steady-state fully-developed version of the 1D Two-Fluid Model) used for elaborating the correlations is explained. As the solution of this simplified 1D Two-Fluid Model might lead to multiple solutions (Ouyang & Aziz, 2002), an investigation was made in order to answer the question whether this is an issue (or not) for the cases selected from the database.

Before determining any interface friction factor expression, an optimization method implemented in the present work is described. This method was applied to determine an optimized interface friction factor, as well coefficients for new correlations for the interface friction factor.

Then, it is discussed which are the most often used methods for elaborating correlations for the interfacial friction factor and why they can be unsatisfactory. In the following topic, the wall shear stress correlations that were used in the simplified version of the 1D Two-Fluid Model and in the optimization framework are presented.

In the final topic, the elaborated correlations are introduced and the predictions for the integral parameters (pressure drop and holdup) obtained by the solution of the simplified 1D Two-Fluid Model are presented. Results obtained with other literature expressions for the interfacial friction factor are also compared and discussed.

4.1. The Eskerud Smith *et al*. (2011) Experimental Database and the Selected Cases

The Eskerud Smith *et al.* (2011) experimental database comprises of isothermal horizontal viscous oil-gas flows in a laboratory-scale pipe. Experimental measurements have been performed at the Tiller Laboratory of SINTEF in Norway (Eskerud Smith *et al.*, 2011). For each individual case, the complete description of flow and experimental conditions cannot be fully disclosed due to confidentiality reasons. For this reason, rather than using the superficial velocities for describing the flow conditions, the superficial Reynolds number is used. The superficial Reynolds number of phase K, Re_{sK}, is defined by Eq. (4.1)., where D is the pipe internal diameter, and ρ_K, U_{sK} and μ_K are, respectively, the density, superficial velocity and viscosity of phase $K \in \{G, L\}$ (G represents the gas and L the liquid).

$$\mathrm{Re}_{sK} = \frac{\rho_K |U_{sK}| D}{\mu_K} \tag{4.1}$$

Furthermore, the description done in this work is limited to the cases described by Eskerud Smith *et al.* (2011), Johansen *et al.* (2014) and Khaledi *et al.* (2014), who also used the same database.

The Eskerud Smith *et al.* (2011) database consists in two sets of experiments, both employing SF_6 as gas phase. The liquid phase of the first set is Exxsol, which is a de-aromatized aliphatic hydrocarbon oil commonly used in experiments for being non-flammable, nontoxic and transparent. The liquid phase of the second set is Nexbase 3080, a catalytically hydroisomerized and dewaxed base oil composed by hydrogenated and highly isoparaffinic hydrocarbons, and is also non-flammable and transparent. The main difference between these two mineral oils is that Exxsol D80 has a viscosity of the same order of magnitude than the viscosity of water, that is, 1cp, while the viscosity of Nexbase 3080 is approximately one hundred times this same value at pressures and temperatures close to standard conditions (1atm and 15°C). Since, the present work is concerned with viscous liquid, only the set of experiments that used Nexbase 3080 as the liquid was considered here.

The test section, or flow loop, used for performing the Nexbase 3080 and SF_6 experiments comprises of a horizontal pipe with an internal diameter of 6.86cm, i.e., 2.7 inches, and a length of 52.92m measured from the gas-liquid mixing point to the pipe outlet section, from where a large separator follows. From single-phase flow experiments, the internal wall absolute roughness of the pipe was evaluated as 7μm.

In the complete set of experiments, the absolute flow pressure and average temperature varied, respectively, between 7.0 and 7.6 bar and between 18.0 and 24.6°C. In such thermodynamic conditions, the key properties of the fluids used, varied within the range indicated in Table 4.1. Furthermore, both the gas viscosity and the interfacial tension were approximately constant in the experiments and had the values of, respectively, 0.0151cp and 0.2 N/m. From Table 4.1, the high viscosity of the mineral oil Nexbase 3080, at least much higher than the viscosity of the water, is very clear, as well as two particularities of the SF_6. First, it is the possibility of considering it as an ideal gas due to the values of its compressibility factor being so close to the unity. In addition, a gas constant about five times lower than the air gas constant, makes the SF_6 have a density five times higher than the density that air would have in the same conditions. Thus, it is clear the significant deviation of the properties of the present viscous oil-gas flow cases from air-water flows in standard conditions. It is important to mention that the methods and instruments used for measuring the fluid properties are not explored in this work and, for more information it is recommended referring to Eskerud Smith *et al.* (2011).

Table 4.1 – Minimum and maximum key fluid properties in the experiments.

Fluid Property	Minimum Value	Maximum Value
SF_6 compressibility factor	0.96	0.99
SF_6 density	43.3 kg/m³	47.0 kg/m³
Nexbase 3080 density	847.9 kg/m³	852.6 kg/m³
Nexbase 3080 viscosity	79.6cp	113.7cp

The pipe of the test section was equipped with six pressure cells, which provided an accurate measurement of the pressure gradient. The value measured by the first of these cells, located at 25.6m downstream from the mixing point, was considered the absolute pressure of the flow, whose values varied according to the limits previously mentioned. A broad-beam gamma densitometer was fixed at approximately 38.15m downstream from the mixing point and was used to acquire time traces of the liquid holdup α_L at a frequency of 10Hz. From such signals, the mean liquid holdup for each case could be determined. Only the broad-beam gamma densitometer measurements, the pressure gradient, the fluid properties and the flow conditions for each case were available to the author of this work. That is why, the other instruments present in the test section, e.g. narrow-beam gamma densitometer and high-speed videos, were not here described. Their detailing and the specification of the uncertainties of each instrument used can be found in Eskerud Smith *et al.* (2011).

Eighty flow cases of viscous oil (Nexbase 3080) and SF_6 (gas) had its main parameters and conditions measured in the previously described flow loop. In the database, the superficial Reynolds number of the gas phase, Re_{SG}, varied between 5.18×10^4 and 2.30×10^6 and the liquid superficial Reynolds number, Re_{SL}, ranged from 60 to 2.06×10^3. Although it is not exactly Re_{SK} that determines if a phase is laminar, transitional or turbulent, from them it can be seen that, while the gas should always be turbulent, the liquid probably will be either laminar or transitional.

It should be emphasized here that one of the purposes of developing a new correlation for the interfacial shear stress is to include it in methodologies that use the 1D Two-Fluid Model, such as the Regime Capture Methodology, but also similar formulations, as well as in Point Model formulations.

Considering the Regime Capture Methodology presented in the previous chapter, its base configuration for horizontal or slightly horizontal pipelines is a stratified flow, therefore, these flow patterns should be identified from the Eskerud Smith *et al.* (2011) database for the correlations development. Further, within the framework of the Regime Capturing Methodology in fine meshes, large-scale waves are naturally captured and only small-scale interfacial effects must be included in the interfacial shear stress. Thus, the stratified wavy flows must also be subdivided depending on the wave's amplitude.

If it is assumed that only small-scale interfacial effects must be included in the interfacial shear stress, since those of large-scale should theoretically be captured, the new correlations for the interfacial shear stress should be developed employing only cases with small-amplitude interfacial waves. Therefore, the stratified wavy flow with large-amplitude waves are excluded from the elaboration of the correlations and solely those with small-amplitude waves are used.

In order to identify the flow pattern of the eighty cases selected from Eskerud Smith *et al.* (2011) database, the signal of the broad-beam gamma densitometer liquid holdup α_L was employed. At the present work, the Eskerud Smith *et al.* (2011) database was examined and the following classification was considered:

- Slug flow;
- Bubbly flow;
- Stratified wavy flow with small amplitude waves;
- Stratified wavy flow with large amplitude waves;
- High gas flow rate flow patterns.

No stratified smooth flow was observed in the present database due to the viscosity of the oil. Very high gas flow rate cases, with flow patterns such as annular, misty and stratified low-liquid loading flows were lumped into the single label “high gas flow rate flow patterns”, because it is not possible to differentiate between them only using the gamma densitometer signals. Further, these patterns were not the focus of the present work.

The procedure used for determining the flow pattern of each case with the broad-beam gamma densitometer liquid holdup time traces is summarized in Figure 4.1.

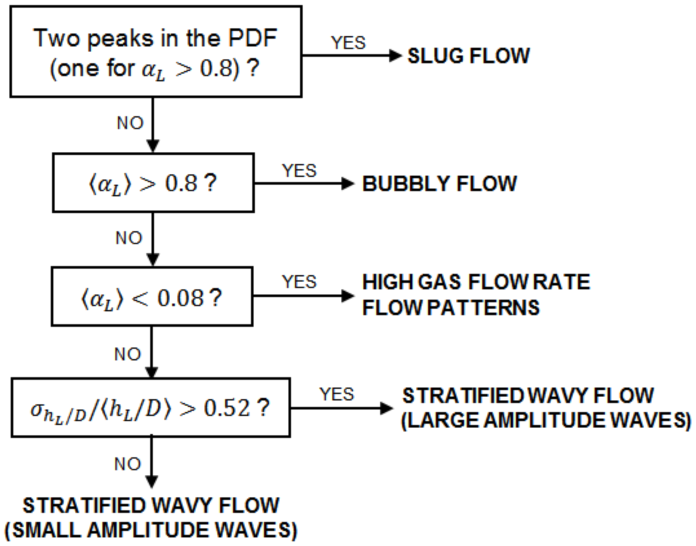

Figure 4.1 – Procedure for the flow pattern classification of the Eskerud Smith *et al.* (2011) database.

Beginning in the upper box in Figure 4.1, the procedure starts by analyzing the histogram of the liquid holdup signal. If the histogram has two peaks, being one of them for a value of α_L higher than 0.8, the flow is classified as slug flow. The value of 0.8 was selected in order to avoid that slug aeration leads the procedure to a fallacious classification. After checking if the flow has slugs, it should be verified if the mean liquid holdup value, $\langle \alpha_L \rangle$ is higher than 0.8. If it is, than the case is bubbly flow, otherwise, it is verified if $\langle \alpha_L \rangle$ is lower than 0.08. If yes, than the flow gains the previous mentioned label of "high gas flow rate flow patterns" and, if not, than it is already known that the flow regime consists in stratified wavy flow. For determining if its waves have a small or large amplitude, one must convert the liquid holdup α_L signals of the gamma densitometer to dimensionless liquid height h_L/D signals, by using the geometrical relations of the stratified flow configuration (Figure 3.1). If the ratio between the standard deviation of the liquid height $\sigma_{h_L/D}$ and the mean dimensionless liquid height value $\langle h_L/D \rangle$ is superior to 0.52, it indicates that the stratified flow has large-amplitude waves. Otherwise, the stratified flow has small-amplitude waves and it is adequate to be used in the elaboration of the new correlations for the interfacial friction factor. It is important to mention that the values in Figure 4.1 were especially chosen for the Eskerud

Smith *et al.* (2011) database, with the aid of available video footages of the flows, as a manner for systematizing the flow pattern classification

To identify the type of wave of a stratified wavy flow, one can examine the absolute wave amplitude. However, in order to classify the type of wave in a rigorous way, one must employ the ratio of dimensionless standard deviation and liquid height $\sigma_{h_L/D}/\langle h_L/D\rangle$, with the threshold value of 0.52 to separate the small and large amplitude waves. Figure 4.2 shows the liquid holdup time traces of the two cases, with the same superficial Reynolds number, Figure 4.2(a) is a case with $\sigma_{h_L/D}/\langle h_L/D\rangle = 0.519$, and contains the liquid holdup signal of a stratified wavy flow with small-amplitude waves while Figure 4.2(b) corresponds to large-amplitude waves case ($\sigma_{h_L/D}/\langle h_L/D\rangle = 0.549$).

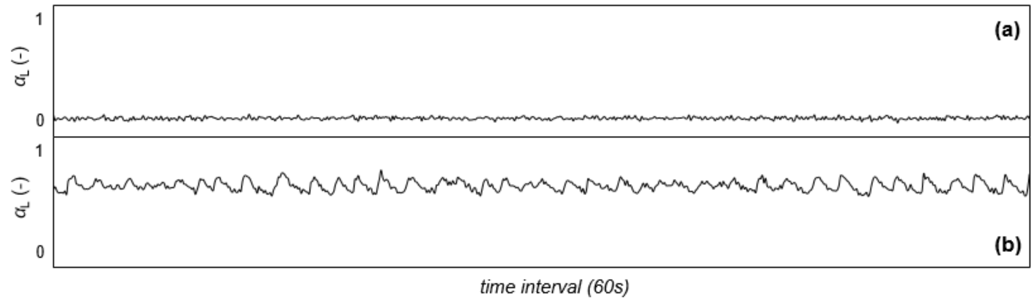

Figure 4.2 – Stratified wavy flow cases in the threshold of $\sigma_{h_L/D}/\langle h_L/D\rangle = 0.52$: (a) small-amplitude waves; (b) large-amplitude waves.

In Figure 4.3, the experimental liquid holdup α_L time traces, obtained with the broad-beam gamma densitometer, of one example-case is depicted for each type of flow pattern from the previously defined classification. An example of a bubbly flow case is clearly seen in Figure 4.3(a) due to its high liquid holdup. In Figure 4.3(b), the liquid holdup signal of a slug flow case, characterized by the intermittency between separated flow and liquid slug bodies, is visible. The two peaks in slug flow holdup histograms represent those two intermittent features. Both the liquid holdup time traces of Figures 4.3(c) and 4.3(d) belong to stratified wavy flows. In them, small-amplitude interfacial waves are present, resembling almost a type of roughness, but only in Figure 4.3(c) there are also large-amplitude waves. Lastly, in Figure 4.3(e), the very low displayed liquid holdup signal points to a high gas flow rate case. It is clear how challenging it would be to confirm if, in the latter figure, a misty flow, an annular flow or a stratified wavy flow with a much curved interface (low-liquid loading condition) is present.

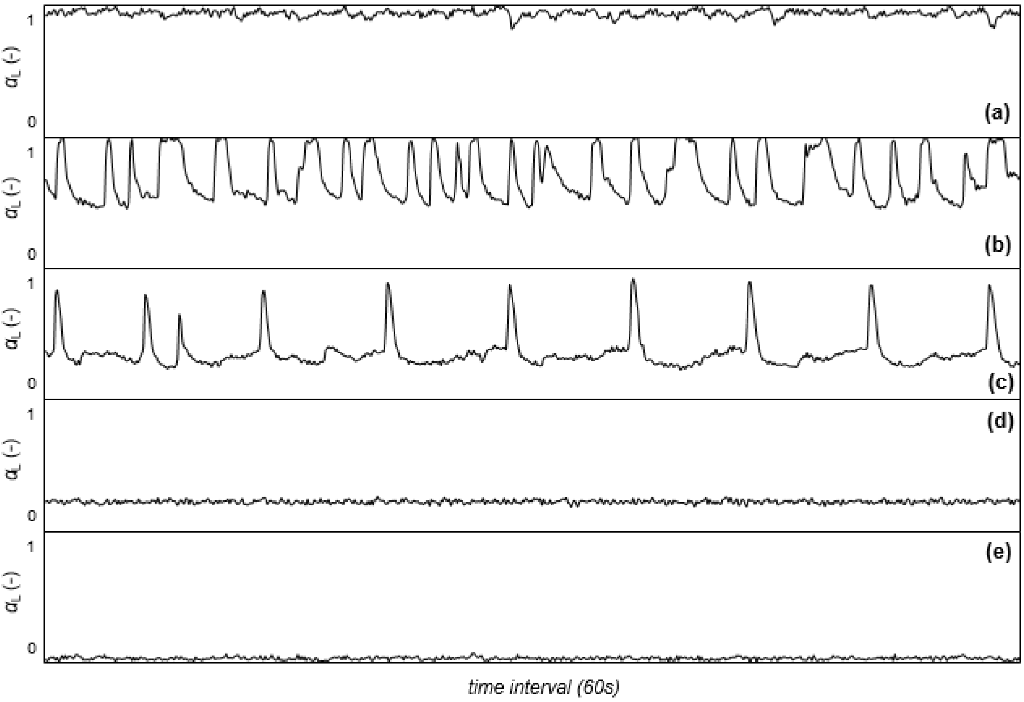

Figure 4.3 – Liquid holdup time traces measured by the broad-beam gamma densitometer: (a) bubbly flow case; (b) slug flow case; (c) stratified wavy flow case with large amplitude waves case; (d) stratified wavy flow case with small amplitude waves case; (e) high gas flow rate case.

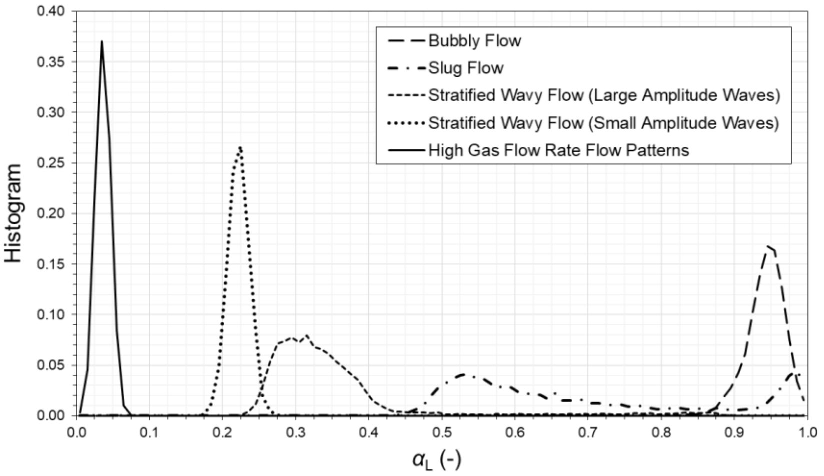

Figure 4.4 – Liquid holdup histograms of one case for each flow pattern from the classification.

The liquid holdup histograms of the same cases, whose broad-beam gamma densitometer measurements were plotted in Figure 4.3, are displayed in Figure 4.4. The histograms were plotted in the style of a Probability Density Function for reasons of aesthetic. It is interesting to observe in the referred figure that, excluding the slug flow case, the "width" of the histogram peaks represent the degree of intermittency of the flow. Some of the same observations made with Figure 4.3 can also be made with Figure 4.4.

The previous paragraphs have shown that Eskerud Smith *et al.* (2011) database is quite large, with a variety of flow patterns. To develop the new interfacial friction factor correlations, a sub-set of cases was selected as described. To summarize, the gas-liquid considered were SF_6-Nexbase 3080. Further, only the stratified wavy flow with small amplitude waves were considered.

4.2. The Point Model

To develop the new interfacial friction factor, the Point Model was applied, which corresponds to a steady state and fully developed flow. The same base flow configuration employed in the previous chapter was considered here, i.e., a stratified flow, with a flat interface in the cross section as shown in Figure 3.1(a) and with geometrical variables expressed by Table 3.1 and Eq. (3.14).

To obtain the Point Model, the conservation equations for the Regime Capturing Model presented in the previous chapter, Eqs. (3.60) and (3.61), were simplified, considering steady state and fully developed flow, resulting in the gas and liquid momentum balances of Eqs. (4.2) and (4.3).

$$\frac{\partial P_G}{\partial x} = -\rho_G g \sin\theta - \tau_{wG}\frac{S_G}{A_G} - \tau_i\frac{S_i}{A_G} \tag{4.2}$$

$$\frac{\partial P_L}{\partial x} = -\rho_L g \sin\theta - \tau_{wL}\frac{S_L}{A_L} + \tau_i\frac{S_i}{A_L} \tag{4.3}$$

In the referred equations, the interfacial pressure gradient was rewritten employing the phasic pressure gradient, using Eq. (3.7), and the phase holdup was written as $\alpha_K = A_K/A$.

The two algebraic momentum balance equations, Eqs. (4.2) and (4.3), are the core of the simplified 1D Two-Fluid Model. Its solution is plainly defined as finding a value of liquid holdup α_L for which the pressure gradient in both phases are equal (Andritsos & Hanratty, 1987b). This is mathematically represented in Eq. (4.4) by the necessity of finding the zero of the function $\mathcal{G}(\alpha_L)$.

$$\mathcal{G}(\alpha_L) = \left.\frac{\partial P_G}{\partial x}\right|_{\alpha_L} - \left.\frac{\partial P_L}{\partial x}\right|_{\alpha_L} \tag{4.4}$$

The function $\mathcal{G}(\alpha_L)$ can be rewritten, by substituting, Eqs. (4.2) and (4.3) in Eq. (4.4), resulting in Eq. (4.5).

$$\mathcal{G}(\alpha_L) = \tau_{wL}\frac{S_L}{A_L} - \tau_{wG}\frac{S_G}{A_G} - \tau_i\left(\frac{S_i}{A_L} + \frac{S_i}{A_G}\right) + (\rho_L - \rho_G)g\sin\theta \tag{4.5}$$

In this way, the solution of the simplified 1D Two-Fluid Model is able to provide estimates for the pressure gradient and the liquid holdup of the flow. Finding the zero of $\mathcal{G}(\alpha_L)$ is a task that can be executed through several algorithms. However, in this work, a simple and standard secant method was found to be sufficient. It is interesting to see that, as a contrast to the complete 1D Two-Fluid Model, there is no need for spatial grid resolution in its simplified version. That is why the solution of the simplified 1D Two-Fluid Model for obtaining values for the integral parameters of the flow is labelled in this work as “Point Model”.

The shear stresses for each phase $K \in \{G, L\}$, τ_{wK}, and interface shear stress τ_i (here equal to the effective interface shear stress τ_i^*) are expressed using Eqs. (3.36) and (3.48), which are repeated here as Eqs. (4.6) and (4.7), with the definition of Eq. (3.49).

$$\tau_{wK} = \frac{1}{2}f_K\rho_K|U_K|U_K \tag{4.6}$$

$$\tau_i = \frac{1}{2}f_i\rho_G|U_G - U_L|(U_G - U_L) \tag{4.7}$$

Thus, to complete the problem formulation, it remains to determine the phase K friction factor f_K and interface friction factor f_i. As already mentioned, the former depend on the phase Reynolds number Re_K or superficial phase Reynolds number Re_{sK}, and the latter on the interface Reynolds number Re_i. Further, it is important to determine the regime of each phase, i.e., if it is laminar, transitional or turbulent. In the Point-Model and in the Regime Capturing Methodology, the threshold for transition of laminar and turbulent regime were defined based on the recommendations of Khaledi *et al.* (2014). In other words, for $\mathrm{Re} \le \mathrm{Re}_{\mathrm{lam}} = 1400$ the flow is laminar, for $\mathrm{Re} > \mathrm{Re}_{\mathrm{turb}} = 4000$ it is turbulent, otherwise, there is a transition. To obtain a smooth transition of friction factor between regimes, it was handled as explained in the previous chapter, employing Eq. (3.44).

4.3. Multiple Solutions Problem

As pointed out in the literature, the Point Models might possess multiple solutions. In other words, there are situations in which there is more than one α_L root of the function $\mathcal{G}(\alpha_L)$ in Eq. (4.4). Landman (1991) analytically solved the model for a scenario in which both phases were laminar, and verified the non-uniqueness of the solution. The same work also uncovered that, when there are multiple solutions, the lowest root of $\mathcal{G}(\alpha_L)$ is the most stable one, while the highest α_L root is surely unstable and the intermediate values might be stable or not. Nevertheless, for this work the main question is if the occurrence of multiple solutions is a problem for the isothermal horizontal stratified gas-liquid flows cases with small-amplitude waves selected from the database. Ouyang & Aziz (2002) stated that the existence of multiple solutions depends on several flow parameters (e.g. pipe diameter, fluid properties, pipe inclination angle and flow rates), but is more commonly found in upward (positive angle θ) inclined flows. Since the present work is concerned with horizontal flows, the possibility of multiple solutions being an issue is small, however, the uncertainty persists.

To verify the possibility of occurrence of multiple solutions the following procedure often employed in the literature (Landman, 1991; Ouyang & Aziz, 2002) can be applied. Let's assume that $\partial P_G/\partial x = \partial P_L/\partial x$, i.e., equating Eqs. (4.2) to (4.3), and by dividing the resulting equation by τ_{wG}, one obtains Eq. (4.8).

$$X_L \frac{S_L}{\alpha_L} - X_i S_i \left(\frac{1}{\alpha_G} + \frac{1}{\alpha_L}\right) + X_{\mathcal{W}} - \frac{S_G}{\alpha_G} = 0 \tag{4.8}$$

The dimensionless parameters X_L, X_i and $X_{\mathcal{W}}$ are defined according to Eqs. (4.9)-(4.11), respectively. The parameter X_L is analogous to the widely known parameter of Lockhart & Martinelli (1949).

$$X_L = \frac{\tau_{wL}}{\tau_{wG}} \tag{4.9}$$

$$X_i = \frac{\tau_i}{\tau_{wG}} \tag{4.10}$$

$$X_{\mathcal{W}} = \frac{(\rho_L - \rho_G) g \sin\theta}{\tau_{wG}} \tag{4.11}$$

As the stratified gas-liquid flows with small-amplitude waves selected from the Eskerud Smith *et al.* (2011) database refer to a totally horizontal pipe, the parameter $X_{\mathcal{W}}$, defined by Eq. (4.11), is null. Therefore, Eq. (4.8) can be rewritten as Eq. (4.12).

$$X_i = \left(X_L \frac{\delta}{\alpha_L} - \frac{\pi - \delta}{\alpha_G} \right) \left(\frac{\alpha_G \alpha_L}{\sin\delta} \right) \tag{4.12}$$

By examining Eq. (4.12), it can be seen that for a horizontal flow, only three variables control de behavior of the Point Model: X_i, X_L and the liquid holdup α_L. Then, a multiple solution scenario would occur when for the same values of X_i and X_L there were two or more values of α_L that satisfy Eq. (4.12). For checking this, the variable X_i was computed for $\alpha_L \in]0.0,1.0[$ and for six very disparate values of X_L. The results were plotted in the diagram shown in Figure 4.5, where it is evident that for all values of X_L, except 0.01, and for low liquid holdups, one value of X_i can be associated with two values of α_L. Therefore, there is a non-uniqueness of the Point Model for situations in which α_L is lower than approximately 0.08. However, cases of the Eskerud Smith *et al.* (2011) database with such values of mean liquid holdup $\langle \alpha_L \rangle$ were classified as “high gas flow rate flow patterns” and were not used in the elaboration of the new interfacial friction factor correlations. As a result, it can be considered that for stratified wavy flow with small-amplitude waves cases there is no multiple solutions problem when using the Point Model.

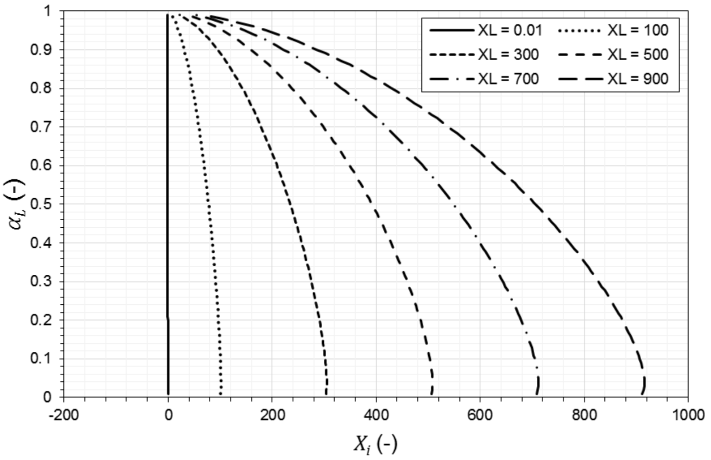

Figure 4.5 – Diagram for analyzing Point Model multiple solutions for horizontal flows.

4.4. Optimization Method

The optimization procedure implement in this work, is based on two objective function formulations. Both objective function formulations depend on a root-mean-squared error, e, that combines the relative (to the measurements) errors of the Point Model results for pressure gradient and liquid holdup: $e_{dP/dx}$ and $e_{\alpha L}$, respectively. Such variables are formulated in Eqs. (4.13) and (4.14), for a Eskerud Smith *et al.* (2011) database stratified wavy flow with small-amplitude waves case jc, where the subscript “pm” represents what was calculated by the Point Model, and Eq. (4.15) shows the expression for the aforementioned error e. One should recall that the Point Model is valid when $\mathcal{G}(\alpha_L) = 0$, Eq. (4.4).

$$e_{dP/dx}\Big|_{jc} = \frac{dP/dx|_{\mathrm{pm},jc} - dP/dx|_{\mathrm{exp},jc}}{dP/dx|_{\mathrm{exp},jc}} \tag{4.13}$$

$$e_{\alpha L}|_{jc} = \frac{\alpha_L|_{\mathrm{pm},jc} - \alpha_L|_{\mathrm{exp},jc}}{\alpha_L|_{\mathrm{exp},jc}} \tag{4.14}$$

$$e|_{jc} = \sqrt{\left(e_{\alpha L}|_{jc}\right)^2 + \left(e_{dP/dx}\Big|_{jc}\right)^2} \tag{4.15}$$

The optimization procedure proposed in this work has the purpose of minimizing the errors of the calculations of the Point Model, i.e., to obtain values for liquid holdup and pressure gradient closest to the measurements as possible. Two optimization problems were considered here. The first optimization problem was applied aiming to determine an optimized interface friction factor. This is performed by considering f_i as the optimization variable of the procedure and by solving the optimization problem for each flow case. The objective function formulation $\mathcal{F}_{\mathrm{obj}}^{I}$ that should be used in this framework is the one shown in Eq. (4.16) for case $jc \in \{1, \ldots, N_c\}$ (N_c is the number of cases used in the optimization).

$$\mathcal{F}_{\mathrm{obj}}^{I}\Big|_{jc} = e|_{jc} \tag{4.16}$$

The second optimization problem was applied to determine the new correlations for the interface friction factor, and its application will be presented in another topic. In the second optimization problem, the optimization procedure has the coefficients $\eta_j, j \in \{1, \ldots, N_v\}$ (N_v is the total number of coefficients) as variables, contained in the vector $\boldsymbol{\eta}$, of a pre-proposed expression for f_i, rather than the values of f_i themselves. Besides that, the coefficients in $\boldsymbol{\eta}$ are optimized for all selected flow cases, that is, are not case-specific anymore, such as the first optimization problem described. In this way, the new expressions for the interfacial friction factor are elaborated. With these remarks in mind, the objective function of Eq. (4.17) shall be used in this optimization problem.

$$\mathcal{F}_{\mathrm{obj}}^{II} = \frac{1}{N_C} \sum_{jc=1}^{N_C} e|_{jc} \tag{4.17}$$

In terms of best possible values (optimized) of pressure gradient, $dP/dx|_{\mathrm{opt},jc}$, and liquid holdup, $\alpha_L|_{\mathrm{opt},jc}$, for each case jc, it is worth mentioning that the first optimization problem provides better results than the second one, since, in the latter, the interfacial friction factor is constrained by a pre-proposed expression and the procedure is not case-specific. The two optimization problems just described, originated from the same optimization procedure, are outlined in Figure 4.6, by the depiction of its optimization variables, objective functions used and main outputs.

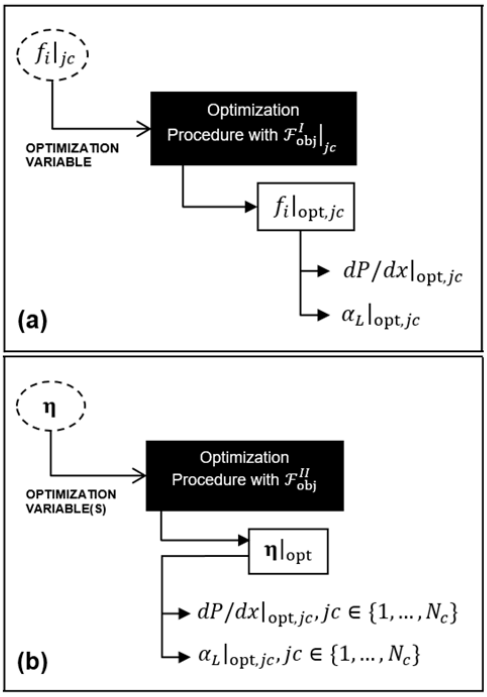

Figure 4.6 – The two optimization problem formulations: (a) for evaluating the best possible results of the Point Model (applied to each specific case jc); (b) for elaborating new correlations for the interfacial friction factor.

For solving the optimization procedure in both optimization problems, outlined in Figure 4.6, the Particle Swarm Optimization (PSO) algorithm (Kennedy & Eberhart, 1995) was chosen. In this evolutionary algorithm, a population of samples (or particles), each one represented by the vector $\mathbf{p}$ which contains all the optimization variables, is initialized and then recursively updated as shown by Eqs. (4.18) and (4.19).

$$\mathbf{v}_{js}^{it+1} = \beta_\omega \mathbf{v}_{js}^{it} + \beta_1 \mathbf{r}_{1js}\left(\mathbf{ib}_{js}^{it} - \mathbf{p}_{js}^{it}\right) + \beta_2 \mathbf{r}_{2js}\left(\mathbf{gb}^{it} - \mathbf{p}_{js}^{it}\right) \tag{4.18}$$

$$\mathbf{p}_{js}^{it+1} = \mathbf{p}_{js}^{it} + \mathbf{v}_{js}^{it+1} \tag{4.19}$$

In the referred equations, the subscript js is the index of the sample in the population and the superscript it is the number of the update or iteration in the algorithm. In addition, $\mathbf{v}$ is the update vector, defined by Eq. (4.18) and β_ω, β_1, β_2 are constants that control, respectively, the inertia, the individuality and the sociability of each sample. The elements of the vectors $\mathbf{r}_{1js}$ and $\mathbf{r}_{2js}$ are taken from a uniform distribution between 0 and 1. The vector $\mathbf{ib}$ is the individual best of a sample, that is, the best values that the sample has had since the beginning of the iterations of the optimization algorithm, while $\mathbf{gb}$ is the global best, i.e., a vector with the globally best values obtained so far in the procedure. The term “best values” means the values of the sample that provided the minimum value for the objective function. All the vectors present in Eqs. (4.18) and (4.19) have a number of elements equal to the number of optimization variables.

The PSO algorithm implemented in the present work, is based on the one originally elaborated by Kennedy & Eberhart (1995), and it is outlined in Table 4.2, where it is the iteration number. Here, the following values for the constants in Eq. (4.18) were used: $\beta_\omega = 0$, $\beta_1 = 2$ and $\beta_2 = 2$.

Table 4.2 – Outline of the PSO (Kennedy and Eberhart, 1995) algorithm used in this work.

Step 1 (initialization and definition of the initial population): • Define $it = 0$; • For initializing the population, each variable of each sample is taken from a Gaussian distribution.
Step 2 (calculation of the objective function): • For each sample, the objective function is evaluated.

Step 3 (bests): - Check which are the individual bests $\mathbf{ib}_{js}^{it}$ for each sample; - Check which is the global best $\mathbf{gb}^{it}$.
Step 4 (is it over?) - If it is superior to a maximum number of iterations, finish the algorithm; - Otherwise, proceed to Step 5.
Step 5 (updating the samples): - Update $it = it + 1$; - Perform the update of each sample through Eqs. (4.18) and (4.19); - Return to Step 2.

4.5. The “Experimental” Interfacial Friction Factor

The most common approach to determine the interfacial friction factors is through calibration of its value employing estimated “experimental” values of the interfacial shear stress. “Experimental” is used in quotes, because the interfacial shear stress is never directly measured, but calculated from other measurements.

The “experimental” interfacial friction factor can be determined by using accurate measurements of axial velocity profile and liquid height variation by the Particle Image Velocimetry (PIV) technique, as done by André & Bardet (2017). Another option would be to use Reynolds shear stress measurements, as performed by Kowalski (1987). However, such non-standard measurements are not available for the Eskerud Smith *et al.* (2011) database, which provides only integral parameters (mean liquid holdup and the pressure gradient). In this case, as anticipated, the use of the momentum balance equations, Eqs. (4.2) and (4.3), of the Point Model is the most adopted path. The experimental integral parameters are then applied directly to one of the two momentum balance equations and the interfacial shear stress (and consequently the interfacial friction factor) is obtained. The term “directly applied” means to assume $\partial P_K/\partial x$ and α_K, $K \in \{G, L\}$, equal to their experimental values, respectively, $\partial P/\partial x|_{\text{exp}}$ and $\alpha_K|_{\text{exp}}$. Such calculation is easily seen in the rearranged momentum balance equation for phase $K \in \{G, L\}$, shown in Eq. (4.20), where, once again, the upper sign in “∓” refers to the gas phase and the lower to the liquid.

$$\tau_i = \mp \frac{A_K}{S_i}\left(\frac{\partial P_K}{\partial x} + \rho_K g \sin\theta + \tau_{wK}\frac{S_K}{A_K}\right) \tag{4.20}$$

In the previously mentioned framework, the gas phase momentum balance is the one most used in literature for calculating the experimental interfacial friction factor (Andritsos & Hanratty, 1987b; Spedding & Hand, 1997; Newton & Behnia, 1998). The presence of the gas wall shear stress τ_{wG} poses a problem, because experimental values for it are not always available, as in Newton & Behnia (1998). When such issue is present, a correlation is used for the gas friction factor and the gas wall shear stress is then computed (Andritsos & Hanratty, 1987b; Spedding & Hand, 1997).

An alternative option for evaluating the "experimental" interfacial friction factor would be to use Eq. (4.21), a combination of the gas and liquid momentum balance equations, as well as a correlation for the gas and liquid friction factors.

$$\tau_i = \alpha_G \alpha_L \frac{A}{S_i}\left[(\rho_L - \rho_G) g \sin\theta + \tau_{wL}\frac{S_L}{A_L} - \tau_{wG}\frac{S_G}{A_G}\right] \tag{4.21}$$

For the three different approaches to indirectly determine the interface friction factor, information about the phase friction factor is need. Thus, first, a model for the wall friction factors f_K, $K \in \{G, L\}$, is necessary. In this topic of the chapter, little discussion is dedicated to the modelling of such parameter, since in the following topic the subject will be developed and more thoroughly treated.

In this first analysis, the laminar wall friction factor, $(f_K)_{\text{lam}}$, for both phases were calculated with Eq. (4.22), adapted from the single-phase Poiseuille flow analytical solution in a circular pipe is used (Hanratty, 2013). For the turbulent wall friction factor, $(f_K)_{\text{turb}}$, the explicit approximation of the Colebrook (1939) expression performed by Haaland (1983), shown in Eq. (4.23) (ε is the internal pipe wall absolute roughness) is used at this moment. These correlations will be referred here as classical wall friction factor correlations. Again, further discussions on these and other correlations will be made later in this work, because those correlations are not the ones that were ultimately used in the other topics and analyses.

$$(f_K)_{\text{lam}} = \frac{16}{\text{Re}_K} \tag{4.22}$$

$$(f_K)_{\text{turb}} = \left\{-3.6 \log_{10}\left[\frac{6.9}{\text{Re}_K} + \left(\frac{1}{3.7}\frac{\varepsilon}{D_{hK}}\right)^{1.11}\right]\right\}^{-2} \tag{4.23}$$

The transition between the regimes was handled as explained in the previous chapter, employing Eq. (3.44).

Theoretically, whether using the gas momentum balance equation, the liquid momentum balance equation or Eq. (4.21) should not make any difference in the evaluated values of the “experimental” interfacial friction factor. However, due to lack of accuracy of the correlations used for the gas friction factor and/or the liquid friction factor, the three options for computing the referred parameter provide different results. Nevertheless, even if ideal correlations for the wall friction factors are used, more fundamental and implicit issues would maintain this consistency problem between the three approaches. When the measured values of the integral parameters, $\alpha_L|_{\text{exp}}$ and $\partial P/\partial x|_{\text{exp}}$, are used directly in the momentum balance equations, for the three approaches to provide the same values of “experimental” interfacial friction factor, the answers for the three following Questions must be positive:

- Question 1: Is there a value of α_L that would make $\partial P_G/\partial x$ equal to $\partial P_L/\partial x$?
- Question 2: If the answer to Question 1 is “yes”, is this value of α_L equal to $\alpha_L|_{\text{exp}}$?
- Question 3: If the answer to Question 1 is “yes”, is the value of pressure gradient equal to $\partial P/\partial x|_{\text{exp}}$?

For the stratified wavy flow cases with small-amplitude waves selected from the Eskerud Smith *et al.* (2011) database, it is very unlikely that the answers to Questions 1-3 will be “yes”, due to the hypotheses inherent to the Point Model (steady-state, fully hydrodynamic development, among others). Consequently, the direct use of the experimental integral parameters will always lead to this just described consistency problem between the three approaches.

4.5.1. Comparison of the “Experimental” and Optimized Interfacial Friction Factor

Rather than choosing one of the approaches described to evaluate the “experimental” values of the interfacial friction factor, it can be determined through the optimization procedure presented in section 4.4. In it, the experimental integral parameters are not used directly in momentum balance equations, but in an indirect way through an optimization methodology. To appreciate the results of the optimization procedure of Figure 4.6(a), the optimized pressure gradient and liquid holdup are compared with the experimental data in Figures 4.7-4.8.

The average relative errors obtained for the liquid holdup and pressure gradient were equal to 6.9% and 10.5%, respectively. Besides, it can be seen in the referred figures that for the majority of cases from the Eskerud Smith *et al.* (2011) database selected (stratified wavy flow with small-amplitude waves), the liquid holdup deviation from the experimental data does not surpass 15% and the pressure gradient errors also do not overcome 15%. Therefore, it can be concluded that the best possible values for the integral parameters are reasonably good.

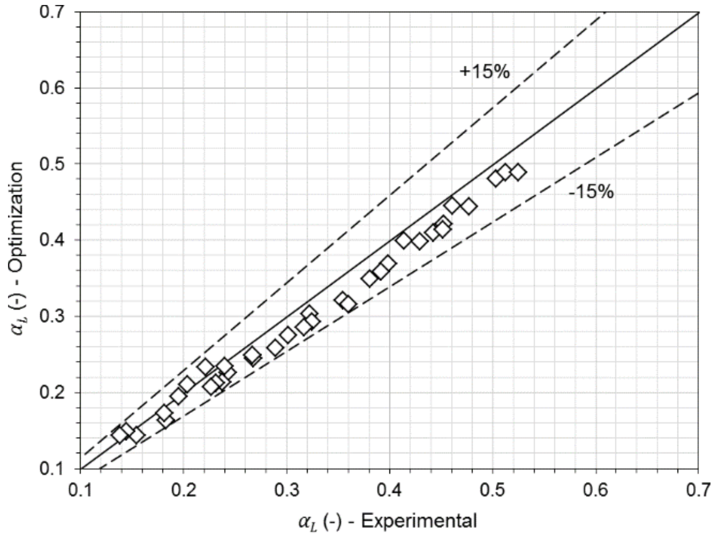

Figure 4.7 – Comparison of optimized, in the framework of Figure 4.6(a), liquid holdup values against the measurements for the classical set of wall friction factor correlations.

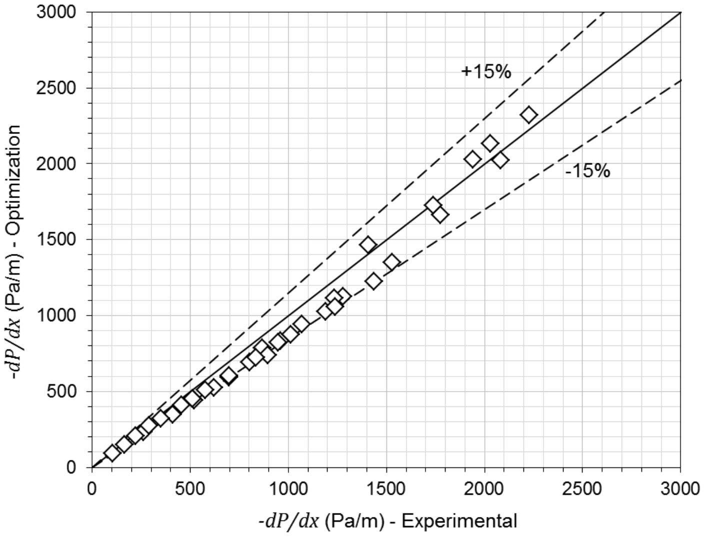

Figure 4.8 - Comparison of optimized, in the framework of Figure 4.6(b), pressure gradient values against the measurements for the classical of wall friction factor correlations.

A deeper insight is needed on the difference between the three previously described approaches that evaluate the “experimental” interfacial friction factors by the direct use of the experimental integral parameters. To this end, a comparison is performed with the optimized values of f_i resulting from the solution of the first optimization problem, outlined in Figure 4.6(a). The three “direct” approaches considered are, respectively: the one that uses the gas momentum balance equation, the one that uses the liquid momentum balance equation, and the one that uses a combination of them, as shown in Eq. (4.21).

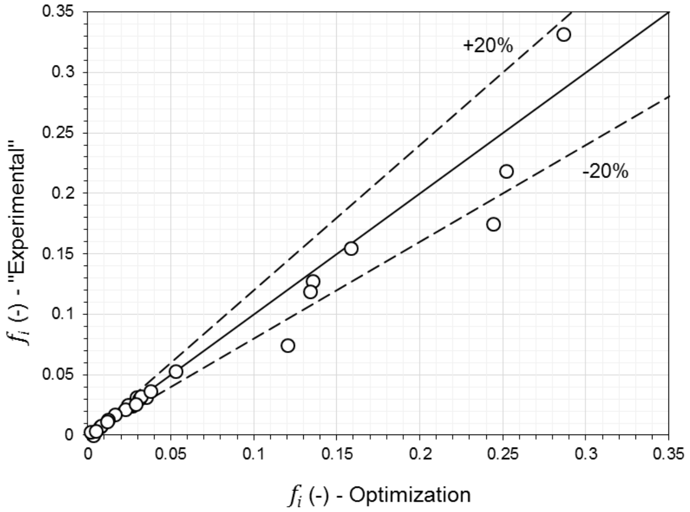

Figure 4.9 – Comparison between the optimized interfacial friction factors, through the optimization problem of Figure 4.6(a), and their “experimental” values obtained with the gas momentum balance equation.

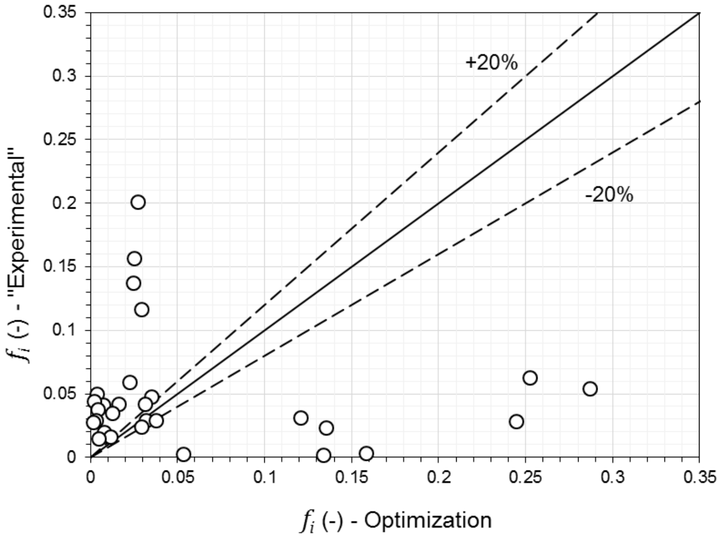

Figure 4.10 - Comparison between the optimized interfacial friction factors, through the optimization problem of Figure 4.6(a), and their “experimental” values obtained with the liquid momentum balance equation.

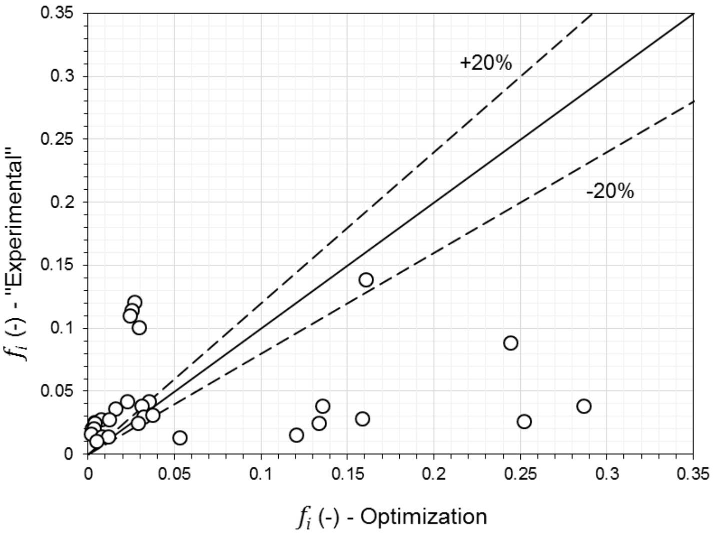

Figure 4.11 – Comparison between the optimized interfacial friction factors, through the optimization problem of Figure 4.6(a), and their "experimental" values obtained with the total momentum balance equation of Eq. (4.21).

Figures 4.90-4.11 show a comparison between the "experimental" values of the interfacial friction factor of the Eskerud Smith *et al.* (2011) database stratified wavy flow with small-amplitude waves cases with the optimized values.

In Figures 4.90-4.11, the "experimental" values are compared to the optimized ones with the help of equivalence lines (mark the equivalence between the values from each graph axis) and of lines that represent deviations of 20%. As aforementioned, the main purpose of this initial analysis is just to show the differences between these approaches and how they compare to the optimization.

Primarily, by observing Figures 4.90-4.11, the difference between the results of any of the direct approaches and the optimized values is very clear. This is actually not surprising, because the distinctions between the methodologies are very significant. The exceptions for these large differences are some cases shown in Figure 4.9, based on the gas momentum balance equation, which is the mostly adopted in literature. This shows that, among the three direct approaches, using the gas momentum balance equation is indeed more valid than using the liquid momentum balance equation or Eq. (4.21). However, the arguments for the use of optimization in this work remain valid. By analyzing Figures 4.90-4.11, the consistency problem of the direct approaches is evident, since the calculated "experimental" interfacial friction factors of each case differ between approaches.

After this preliminary analysis, it is wise to perform a complete discussion of the wall friction factor correlations used and the possibility of using improved ones not only in the elaboration of new correlations for the interfacial friction factor, but in the Regime Capturing Methodology.

4.6. Analysis of the Wall Friction Factor Expressions

When presenting the features of the first optimization problem, the one outlined in Figure 4.6(a), it was mentioned that one of the possibilities in using the interfacial friction factor as an optimization variable was that the wall friction factor correlations could be analyzed and different ones compared. Such analysis is performed in this topic not just aiming the elaboration of satisfactory new correlations for the interfacial friction factor, but also for improving the predictions of the Regime Capturing Methodology in the upcoming chapters of this work.

To improve the quality of the gas wall friction factor for very viscous oil-gas flow, it is important to perform a correction in the pipe wall internal roughness in the gas phase. Due to the high viscosity of Nexbase 3080 oil, oil filaments stay trapped in the gas wall perimeter, increasing its apparent roughness. The expression of Eq. (4.24) for the corrected gas wall roughness, ε_G, was proposed by Khaledi *et al.* (2014).

$$\varepsilon_G = \varepsilon \left\{ 1 + 9 \exp \left[-100 \left(\frac{0.00175}{\mu_L} \right)^2 \right] \right\} \tag{4.24}$$

Also due to the significant viscosity of the liquid, for the range of superficial Reynolds number observed in **Erro! Fonte de referência não encontrada.**, probably the liquid flow is laminar, and an improved laminar liquid friction factor $(f_L)_{\text{lam}}$ must be seeked. The most commonly used expression in literature is actually the one previously defined in Eq. (4.22). Nevertheless, the value of 16 present in the referred equation is valid solely for a flow in a circular pipe (Çengel, 2006), and not for a stratified flow, as seen in Figure 3.1(a). Accounting for the cross sectional geometry in the evaluation of Re_K through D_{hK} is not sufficient. Therefore, other constant values are found in the literature, such as 24, taken from channel flow (Spedding & Hand, 1997; Çengel, 2006), and 20.76, obtained by fitting a mechanistic model (Zhao *et al.*, 2015). However, this value should also change with the liquid holdup, due to variations of the cross sectional geometry. Biberg (1999c), who analytically solved the steady-state fully developed laminar flow in the liquid phase of a gas-liquid stratified flow, settled this issue and obtained an analytical expression for the laminar liquid wall shear stress $(\tau_{wL})_{\mathrm{lam}}$, as shown in Eq. (4.25).

$$(\tau_{wL})_{\mathrm{lam}} = \frac{8\mu_L U_L}{D_{hL}^*} - c_i^* \tau_{i0} \tag{4.25}$$

In the referred equation, D_{hL}^* is a modified hydraulic diameter, which takes into account the actual liquid phase geometry and its variations with the holdup; and c_i^* is the influence function, responsible for representing the influence of the holdup in $(\tau_{wL})_{\mathrm{lam}}$. τ_{i0} is the interfacial shear stress for a smooth interface, determined with Eq. (4.7), based on the smooth interfacial friction factor, f_{i0}, which is determined employing empirical correlations. By examining Eq. (4.25), it is clear that depending on the value of $c_i^* \tau_{i0}$, the liquid wall shear stress $(\tau_{wL})_{\mathrm{lam}}$, and consequently $(f_L)_{\mathrm{lam}}$, can become negative, what is undesired. However, Pasqualette *et al.* (2017) examined the second term in the RHS of Eq. (3.36), and verified that it is much smaller than the first one. Thus, Biberg (1999c) expression was modified by eliminating the second term, resulting in the expression of Eq. (4.26) for the laminar liquid wall friction factor.

$$(f_L)_{\mathrm{lam}} = \frac{16}{\mathrm{Re}_L}\left(\frac{D_{hL}}{D_{hL}^*}\right) \tag{4.26}$$

For evaluating D_{hL}^*, Biberg (1999c) proposed an approximated rational polynomial expression, whose form is given by Eq. (4.27) for a generic parameter $\mathcal{V}$ and generic variable ξ.

$$\mathcal{V} = \frac{\sum_{j=0}^{13} \mathcal{n}_j \xi^j}{\sum_{j=0}^{6} \mathcal{d}_j \xi^j} \tag{4.27}$$

The values of the coefficients $\mathcal{n}_j, j \in \{0, \ldots, 13\}$, and $\mathcal{d}_j$, $j \in \{0, \ldots, 6\}$, which depend on the parameter $\mathcal{V}$, as the choice of variable ξ does, are listed in Table 4.3 not just for D_{hL}^*, but for other parameters that will appear throughout this work. Such parameters, thus, shall be properly described later.

In Figure 4.12, the laminar wall liquid friction factor, given by Eq. (4.26) is plotted versus the liquid holdup. It can be seen that the modified Biberg (1999c) expression, Eq. (4.26), ranges from 15.5 to almost 18.0, showing the 16 constant parameter is not adequate, unless for α_L values between 0.15 and 0.6.

Table 4.3 – Coefficients and variables of Eq. (4.27) (Biberg 1999b; 1999c).

Parameter ($\mathcal{V}$)	ϵ_G^*	ϵ_L^*	γ_G^*	γ_L^*	D_{hL}^*/D
Variable (ξ)	$\pi - \delta$	δ	$\pi - \delta$	δ	δ/π
n_0	0	0	3.819×10^{-6}	1.500×10^{-6}	-1.000×10^{-6}
n_1	2.991×10^{-5}	-8.129×10^{-6}	1.204×10^{-1}	1.325×10^{-1}	3.550×10^{-4}
n_2	-7.338×10^{-4}	1.424×10^{-6}	-1.220×10^{-1}	-1.005×10^{-1}	6.748
n_3	6.591×10^{-3}	1.849×10^{-3}	4.794×10^{-2}	4.024×10^{-2}	-7.093
n_4	5.731×10^{-1}	8.964×10^{-1}	-8.646×10^{-3}	-9.401×10^{-3}	-11.96
n_5	1.798×10^{-1}	7.751×10^{-2}	6.054×10^{-4}	9.797×10^{-4}	19.60
n_6	-4.049×10^{-1}	-7.077×10^{-2}	0	0	-7.028
n_7	1.524×10^{-1}	2.734×10^{-1}	0	0	0
n_8	-1.107×10^{-1}	1.728×10^{-2}	0	0	0
n_9	9.604×10^{-2}	-1.894×10^{-2}	0	0	0
n_{10}	-4.063×10^{-2}	-3.185×10^{-3}	0	0	0
n_{11}	8.653×10^{-3}	2.820×10^{-3}	0	0	0
n_{12}	-9.172×10^{-4}	-5.190×10^{-4}	0	0	0
n_{13}	3.881×10^{-5}	3.228×10^{-5}	0	0	0
d_0	1	1	1	1	1
d_1	0	0	-8.628×10^{-1}	-4.684×10^{-1}	-1.113
d_2	0	0	1.881×10^{-1}	8.701×10^{-2}	1.584
d_3	0	0	3.023×10^{-2}	-6.701×10^{-2}	-4.451
d_4	0	0	-1.607×10^{-2}	2.867×10^{-2}	5.941
d_5	0	0	1.588×10^{-3}	-3.417×10^{-3}	-3.631
d_6	0	0	0	0	0.9412

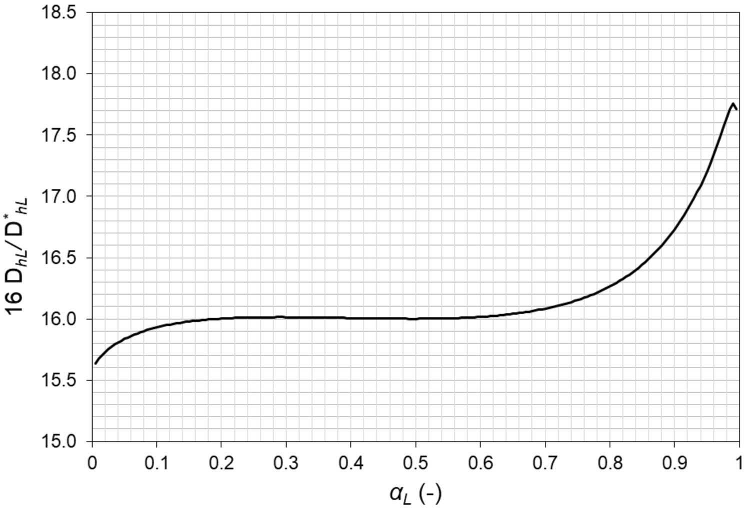

Figure 4.12 – Variation of the term $16(D_{hL}/D_{hL}^*)$ of Eq. (4.26) with the liquid holdup.

For the gas phase, which is predominantly turbulent, the laminar wall friction factor is not as important as it is for the liquid phase. So, the previous expression, Eq. (4.22) is maintained here and repeated in Eq. (4.28).

$$(f_G)_{\mathrm{lam}} = \frac{16}{\mathrm{Re}_G} \tag{4.28}$$

For evaluating the turbulent wall friction factor of the gas and the liquid, the most adopted approach in literature is the one used in the last topic, Eq. (4.23), that is, to use an explicit approximation for the Colebrook (1939) equation. This equation is coupled with the definition of hydraulic diameters, Eqs. (3.38) and (3.39), which contain the hypotheses that the gas flows as if the interface was “part of the pipe wall” and that the liquid flows as if the interface was a free surface. Although this approach is very useful and practical, since it does not involve implicit and complex expressions, such as in the Biberg (2007) framework, it lacks accuracy in several situations. One of the reasons of the failure of this correlation is due to the fact that it does not account for the influence of the interface dynamics on the wall friction factors. Another explanation why the Colebrook (1939) expression may not be adequate is directly related to its derivation. Colebrook (1939) equation is a combination of the Prandtl (Pope, 2000) and von Kármán (Pope, 2000) expressions for smooth and rough pipes, respectively. They are obtained after a pre-integration of the axial velocity profiles based on the corresponding logarithmic law of the wall of each situation, which use the wall friction velocity (based on the wall shear stress) and the wall roughness (Pope, 2000). Standard logarithmic law of the wall (Pope, 2000) is often unable to represent the velocity profile near the interface when it is wavy (Belcher & Hunt, 1993). Another reason is associated with the coupling of the hydraulic diameters expressions with Colebrook (1939) equation for evaluating $(f_K)_{\mathrm{turb}}$, $K \in \{G, L\}$. The gas hydraulic diameter assumes that the wall shear stress acts on the interface, and for the liquid hydraulic diameter, there is no shear stress at the interface. Further, it is assumed that the interface has a surface roughness equal to the pipe wall internal roughness. It is clear from the aforementioned facts that it is also necessary to improve the phase wall friction factors.

Biberg (1998) attacked the problem by deducing a new expression for $(f_G)_{\mathrm{turb}}$. This was done by the pre-integration of a double-logarithm velocity profile, originated from two laws of the walls (one for the interface and another for the actual wall), of the gas stream of a turbulent gas-liquid flow in a horizontal channel. By using two different laws of the walls, it was possible for Biberg (1998) to use the interfacial shear stress in the law applied to the interface and the wall shear stress for the law applied to the actual wall. After some simplifications and several algebraic manipulations, the expression in Eq. (4.29) was obtained.

$$(f_G)_{\mathrm{turb}} = \left\{ \frac{-3.6 \log_{10}\left[\frac{6.9}{\mathrm{Re}_G} + \left(\frac{1}{3.7}\frac{\varepsilon_G}{D_{hG}}\right)^{1.11}\right]}{1 + 4\sqrt{f_{i0}}\frac{|U_G - U_L|}{|U_G|}\log_{10}\left(1 + \frac{S_i}{S_G}\right)} \right\}^{-2} \tag{4.29}$$

In the case of the liquid, Nossen *et al.* (2000) elaborated an expression for computing $(f_L)_{\mathrm{turb}}$ seeking to represent the effects of the interface dynamics and to improve the results when the basic hypothesis involved in the liquid hydraulic diameter expression fails. The correlation proposed, Eq. (4.30), is an interpolation of the Hand (1991) empirical correlation and the explicit approximation for the Colebrook (1939) expression of Haaland (1983). With the interpolation term z_t, Eq. (4.31), the correlation can approach Haaland (1983) expression when the free surface flow hypothesis is more valid, otherwise it can approach the Hand (1991) expression. The effect of the interface dynamics can be seen in the presence of the smooth interfacial Froude number Fr_{i0}, Eq. (4.32), in the expression for z_t in Eq. (4.31).

$$(f_L)_{\mathrm{turb}} = \left\{ 6.178 z_t (\alpha_L \mathrm{Re}_{sL})^{0.0695} - 3.6(1 - z_t)\log_{10}\left[\frac{6.9}{\mathrm{Re}_L} + \left(\frac{1}{3.7}\frac{\varepsilon}{D_{hL}}\right)^{1.11}\right] \right\}^{-2} \tag{4.30}$$

$$z_t = \tanh(2000\,\mathrm{Fr}_{i0})\frac{S_i}{S_L} \tag{4.31}$$

$$\mathrm{Fr}_{i0} = \frac{\tau_{i0}}{(\rho_L - \rho_G) g D \cos\theta} \tag{4.32}$$

The previous friction factor expressions, show that the turbulent friction factors of both phases depend directly on the smooth interfacial friction factor f_{i0}. It can determined employing Issa & Kempf (2003) recommendation: the laminar smooth interfacial friction factor, $(f_{i0})_{\mathrm{lam}}$, Eq. (4.33), is analogous to the laminar gas friction factor, and the turbulent smooth interfacial friction factor, $(f_{i0})_{\mathrm{turb}}$, is determined with the Blasius-like expression of Taitel & Dukler (1976), seen in Eq. (4.34).

$$(f_{i0})_{\mathrm{lam}} = \frac{16}{\mathrm{Re}_i} \tag{4.33}$$

$$(f_{i0})_{\mathrm{turb}} = 0.046\ \mathrm{Re}_i{}^{-0.2} \tag{4.34}$$

The same previously defined expression, Eq. (3.50), for Re_i should be used for Eqs. (4.33) and (4.34), and it is here repeated for convenience as Eq. (4.35).

$$\mathrm{Re}_i = \frac{\rho_G |U_G - U_L| D_{hG}}{\mu_G} \tag{4.35}$$

Once again, a smooth transition between the regimes was handled by employing a scheme similar to the one of Eq. (3.44) for interpolating between the smooth interfacial friction factors of each regime.

For evaluating the effectiveness of these new set of wall friction factor correlations presented in this topic, with the ones used in the analysis of the previous topic, Eqs. (4.22) and (4.23), the optimization problem of Figure 4.6(a) is solved for both cases. The resulting optimized integral parameters (liquid holdup and pressure gradient) are compared to the experimental values in Figures 4.13 and 4.14, for the classical set of wall friction factor correlations, and in Figures 4.15 and 4.16, for the new set. Both in the classical and in the new sets of wall friction factor, the gas roughness correction of Eq. (4.24) was used.

Examining Figures 4.15 and 4.16, it can be seen that an improvement on the results obtained with the new correlations was obtained: the average relative errors are 5.5%, for the liquid holdup, and 8.5%, for the pressure gradient. Furthermore, in Figures 4.15 and 4.16, neither the results for the liquid holdup nor the ones for the pressure gradient, in their majority, have a deviation much greater than 10%.

The improvements obtained were modest, because for the majority of the cases selected, the regime of the liquid phase is laminar, and the liquid holdup α_L varies in the range from 0.15 to 0.6, when there is no practical difference between the Biberg (1999c) expression for $(f_L)_{\mathrm{lam}}$, Eq. (4.26), and the expression of the old set of wall friction factors, Eq. (4.22), as shown in Figure 4.12. Therefore, the change of expressions for evaluating $(f_L)_{\mathrm{lam}}$ indeed should not make difference for such cases, nevertheless, it will for cases with lower and higher liquid holdups.

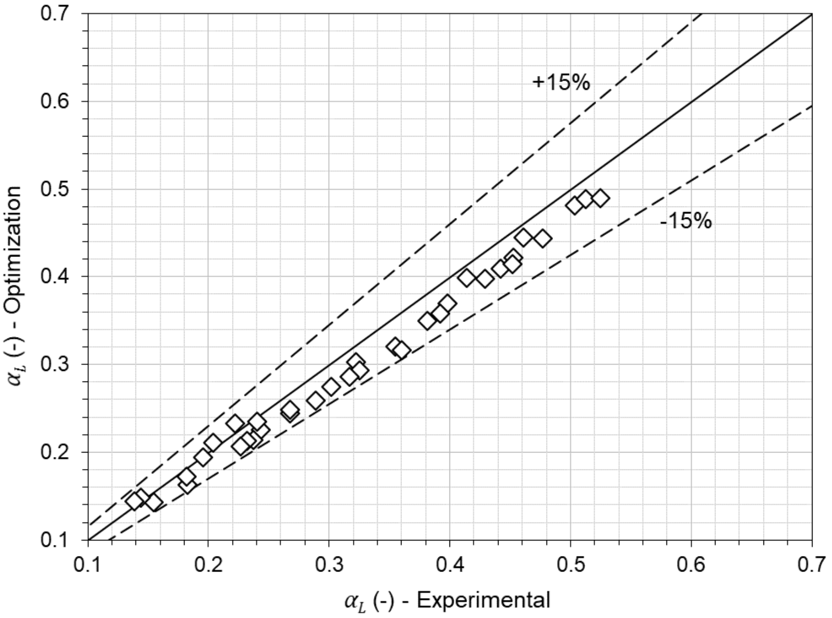

Figure 4.13 - Comparison of optimized, through the optimization problem of Figure 4.6(a), liquid holdup values against the measurements for the classical set of wall friction factor correlations.

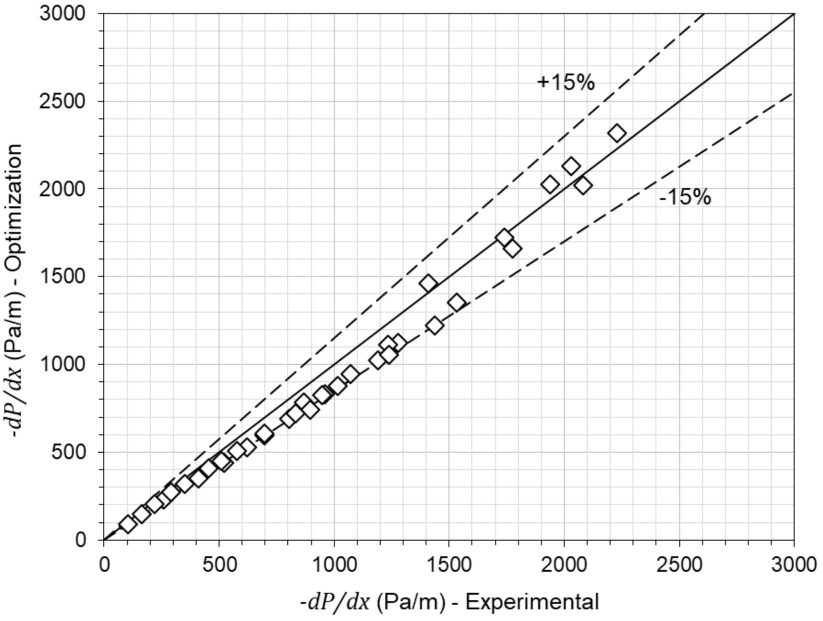

Figure 4.14 - Comparison of optimized, through the optimization problem of Figure 4.6(a), liquid holdup values against the measurements for the classical set of wall friction factor correlations.

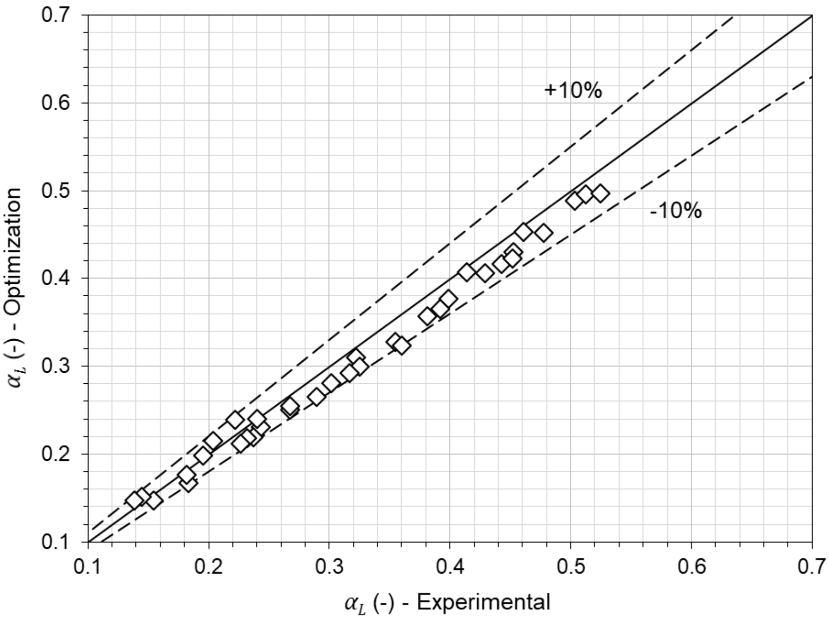

Figure 4.15 - Comparison of optimized, through the optimization problem of Figure 4.6(a), liquid holdup values against the measurements for the new set of wall friction factor correlations.

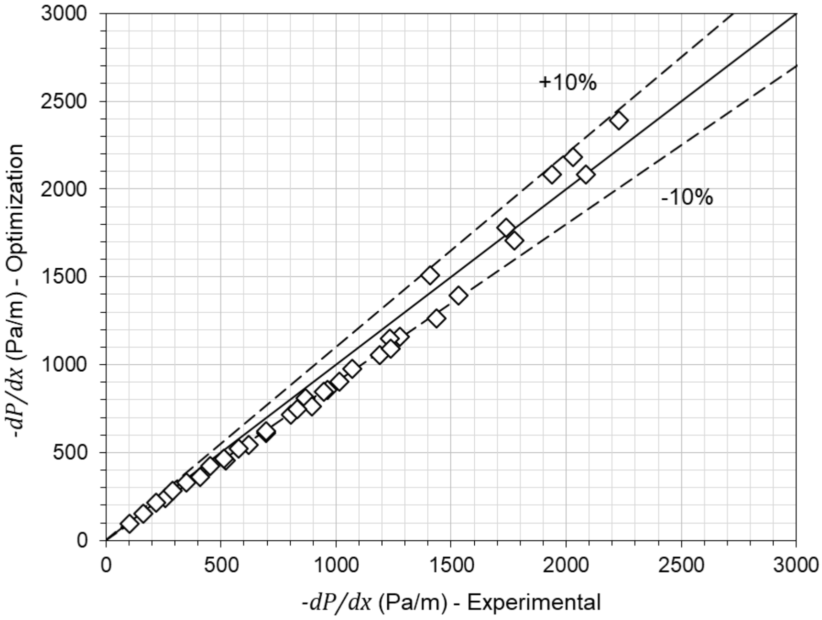

Figure 4.16 - Comparison of optimized, through the optimization problem of Figure 4.6(a), pressure gradient values against the measurements for the new set of wall friction factor correlations.

Although, the improvement in the results with the new set of wall friction factor correlations was not significant, the major advantages of the new wall friction factor correlations must actually appear in hydrodynamic conditions outside the range of the stratified wavy flow cases with small-amplitude waves flow. Thus, it is expected to lead to more accurate results when applying the Regime Capturing Methodology to simulate slug and stratified flow cases from the Eskerud Smith *et al.* (2011) database. Thus, this new set of wall friction factor correlations was used throughout this entire work.

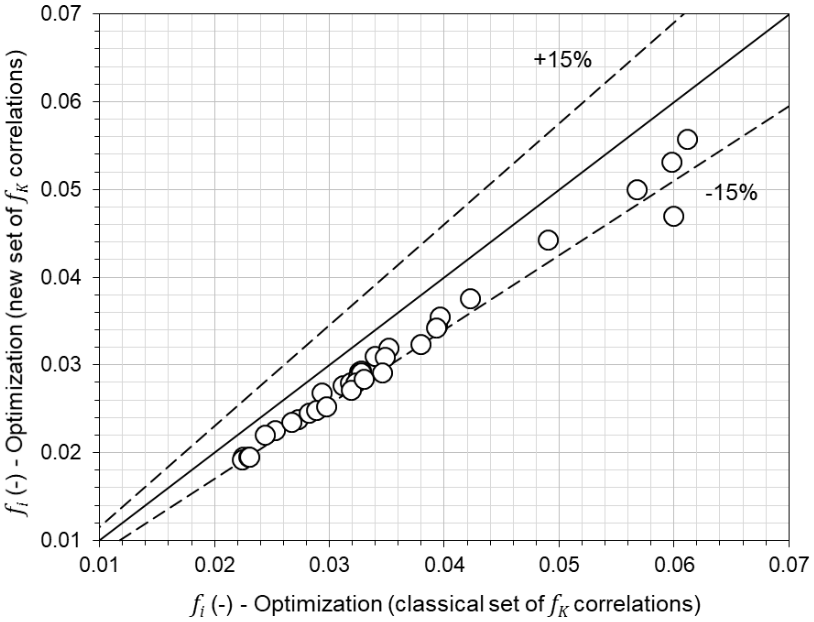

Figure 4.17 – Comparison of the optimized interfacial friction factors with the alternative wall friction factor correlations and the common ones.

For a deeper insight on the difference between the new and the classical sets of wall shear stress correlations, Figure 4.17 compares the optimized, Figure 4.6(a), interfacial friction factors obtained for these two sets. It is interesting to observe that the deviation between such values does not surpass 15%, for most cases.

4.7. Proposed Expressions for the Interfacial Friction Factor

In this topic, the new correlations for the interfacial friction factor, elaborated in this work, will finally be presented. The correlations should be explicit and simple, features that drew the attention of this work to expressions of the type that calculates the ratio between the interfacial friction factor and a reference friction factor, such as the correlations of Andritsos & Hanratty (1987b), Andreussi & Persen (1987) and Spedding & Hand (1997). It is important to compare the Point Models results for liquid holdup and pressure gradient obtained with the new interfacial friction factor correlations against the ones provided with literature correlations, which are the ones here firstly presented.

One of these literature correlations for the interfacial friction factor is the one of Andreussi & Persen (1987) modified by Calgaro (2012), formulated in Eq. (4.36), in which, f_{G0} is the gas wall friction factor for a null pipe wall roughness.

$$\frac{f_i}{f_{G0}} = \begin{cases} 1 & ; \ \mathrm{Fr}_G \leq \mathrm{Fr}_{G,\mathrm{crit}} \\ 1 + 29\left(\mathrm{Fr}_G - \mathrm{Fr}_{G,\mathrm{crit}}\right)^{0.7} \left(\dfrac{h_L}{D}\right)^{0.2} & ; \ \mathrm{Fr}_G > \mathrm{Fr}_{G,\mathrm{crit}} \end{cases} \tag{4.36}$$

Also in Eq. (4.36), Fr_G is the gas Froude number, evaluated with Eq. (4.37), in which the derivative dA_L/dh_L is expressed by Eq. (4.38), obtained with the geometrical relations of the stratified configuration of Figure 3.1.

$$\mathrm{Fr}_G = U_G \sqrt{\left(\frac{\rho_G}{\rho_L - \rho_G}\right) \frac{dA_L}{dh_L} \left(\frac{1}{g A_G \cos\theta}\right)} \tag{4.37}$$

$$\frac{dA_L}{dh_L} = \sqrt{1 - \left(\frac{2h_L}{D} - 1\right)^2} \tag{4.38}$$

In Eq. (4.36), $\mathrm{Fr}_{G,\mathrm{crit}}$ is the critical gas Froude number, which marks the appearance of waves at the gas-liquid interface and, as a consequence, the increase in the interfacial friction factor. Rather than using the constant value of 0.36, originally proposed by Andreussi & Persen (1987), $\mathrm{Fr}_{G,\mathrm{crit}}$ is calculated with Eq. (4.39), as suggested by Calgaro (2012). The critical gas superficial velocity $U_{G,\mathrm{crit}}$, which appears in Eq. (4.39), is evaluated with Eq. (4.40), in which the critical wavenumber k_{crit} should be computed with Eq. (4.41).

$$\mathrm{Fr}_{G,\mathrm{crit}} = U_{G,\mathrm{crit}} \sqrt{\left(\frac{\rho_G}{\rho_L - \rho_G}\right) \frac{1}{g D \cos\theta}} \tag{4.39}$$

$$U_{G,\mathrm{crit}} = U_L + \sqrt{\frac{2\rho_L g}{\rho_G k_{\mathrm{crit}}}} \tag{4.40}$$

$$k_{\mathrm{crit}} = \sqrt{\frac{\rho_L g \cos\theta}{\sigma}} \tag{4.41}$$

The other literature correlation for the interfacial friction factor to be compared with the newly elaborated correlations is the one of Tzotzi & Andritsos (2013), depicted in Eq. (4.42).

$$\frac{f_i}{f_{G0}} = \begin{cases} 1 & ; U_{sG} \leq U_{sG,t\mathrm{2D}} \\ 1 + 0.35\left(U_{sG} - U_{sG,t\mathrm{2D}}\right)\sqrt{\dfrac{2h_L}{D}} & ; U_{sG,t\mathrm{2D}} < U_{sG} < U_{sG,t\mathrm{KH}} \\ 2\left(\dfrac{\mu_L}{\mu_{L,\mathrm{ref}}}\right)^{0.1}\left(\dfrac{h_L}{D}\right)^{0.1} + 4\left(U_{sG} - U_{sG,t\mathrm{KH}}\right)\sqrt{\dfrac{h_L}{D}} & ; U_{sG} > U_{sG,t\mathrm{KH}} \end{cases} \quad (4.42)$$

In the referred equation, $U_{sG,t\mathrm{2D}}$ is the gas superficial velocity that marks the transition from a smooth interface to one with 2D waves and $U_{sG,t\mathrm{KH}}$ represents the appearance of Kelvin-Helmholtz irregular waves. These superficial gas velocities are evaluated with Eqs. (4.43) and (4.44), respectively.

$$U_{sG,t\mathrm{2D}} = \frac{1}{1.95}\left(\frac{\rho_L}{\rho_{L,\mathcal{S}}}\right)^{0.1}\left(\frac{\rho_{G,\mathcal{S}}}{\rho_G}\right)^{0.5}\left(\frac{\mu_L}{\mu_{L,\mathcal{S}}}\right)^{0.35}\ln\left[\frac{0.8}{U_{sL}}\left(\frac{\mu_L}{\mu_{L,\mathcal{S}}}\right)^{0.2}\right] \quad (4.43)$$

$$U_{sG,t\mathrm{KH}} = \frac{1}{0.65}\left(\frac{\rho_L}{\rho_{L,\mathcal{S}}}\right)^{0.5}\left(\frac{\rho_{G,\mathcal{S}}}{\rho_G}\right)^{0.5}\left(\frac{\sigma_{\mathcal{S}}}{\sigma}\right)^{0.35}\ln\left[\frac{1.39}{U_{sL}}\left(\frac{\mu_{L,\mathcal{S}}}{\mu_L}\right)^{0.15}\right] \quad (4.44)$$

In Eqs. (4.42)-(4.44), all the variables with the subscript "$\mathcal{S}$" are evaluated for an air-water system at 1 atm and 20°C.

In the new interfacial friction factor correlations to be constructed, instead of using the gas friction factor with null wall roughness as reference of friction factor, as in Andreussi & Persen (1987) and Tzotzi & Andritsos (2013), it is proposed to use the smooth interfacial friction factor. This physically makes more sense, since in the interfacial friction factor correlations the ratio between it and the reference friction factor deviates from unity when waves appear at the interface. Therefore, the new correlations are written for f_i/f_{i0}. However, considering such ratio to be unity can be a valid approach, since in literature, when the increase in the interfacial friction factor due to waves is not taken into account, it is taken to be equal to the reference friction factor. It is defined, then, the "Standard Expression" for the interfacial friction factor, shown in Eq. (4.45).

$$\frac{f_i}{f_{i0}} = 1 \quad (4.45)$$

To illustrate the need to develop a new correlation for the interface friction factor, Point Model results were computed for the previously selected Eskerud Smith *et al.* (2011) cases, with the Standard Correlation, the Andreussi & Persen (1987) correlation modified by Calgaro (2012) and the correlation of Tzotzi & Andritsos (2013).

In Figure 4.18, the calculated Point Model results of liquid holdup and pressure gradient, respectively, for the three referred literature correlations are shown and compared against the experimental data.

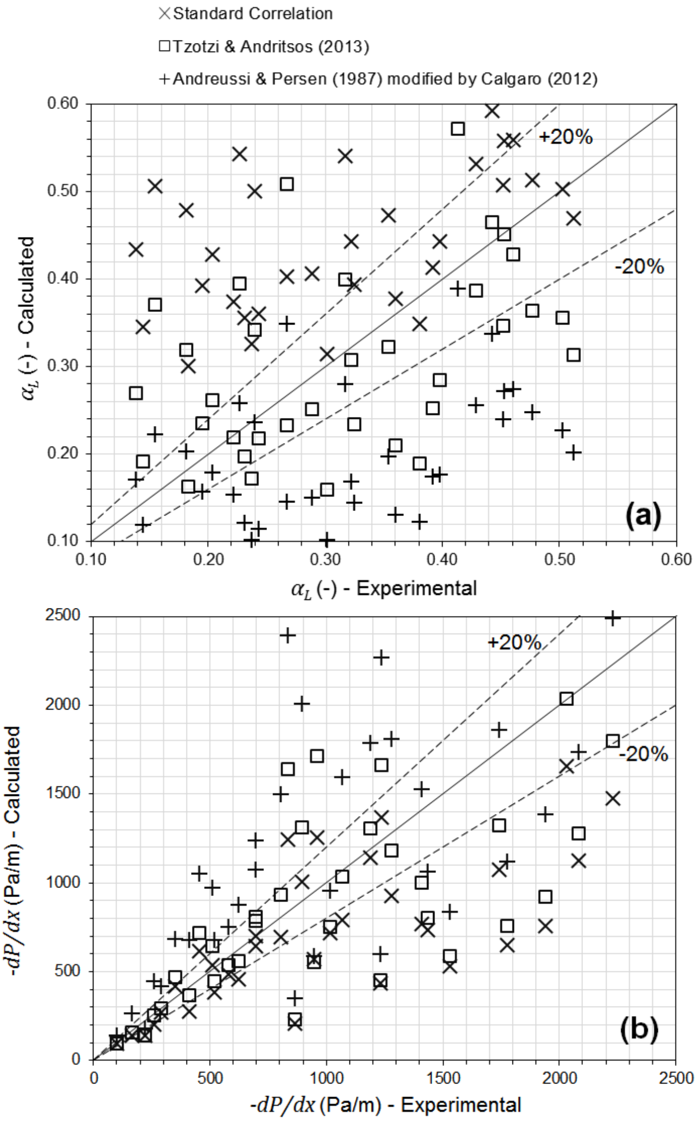

Figure 4.18 - Point Model calculations with literature correlations for the interfacial friction factor for: (a) liquid holdup; and (b) pressure gradient.

In the referred figure, the degree of scattering of the plots, in which few results appear close to the equivalence line, is astonishing. In the results shown for the liquid holdup Point Model, in Figure 4.18(a), almost all the values presented a deviation in relation to the measurements significantly larger than 20%, for the three correlations of f_i. The average relative liquid holdup error is of 61.0%, for the Standard Correlation, 33.7%, for the Tzotzi & Andritsos (2013) correlation, and 57.0%, for the Andreussi & Persen (1987) modified by Calgaro (2012). Respectively, the pressure gradient average relative errors from these same correlations are 31.1%, 30.9% and 38.9%. With few exceptions, such as the group of cases with smaller values of pressure gradient, the results for such parameter, in Figure 4.18(b), have a relative error that surpasses 20%.

Those very negative results obtained with the Point Model and the three previously mentioned correlations for f_i confirm that the current literature correlations are not satisfactory for the Eskerud Smith *et al.* (2011) database, and new correlations must be developed.

Along this chapter, it has been mentioned, several times, that two new correlations for the interfacial friction factor were elaborated in this work. Before the explanation advances, it is important to tackle the question of why elaborating two new correlations and not just one. Several proposed expressions for such parameter can be satisfactorily adjusted via the solution of the optimization problem of Figure 4.6(b) with the experimental data of the stratified wavy flow cases with small-amplitude waves from the Eskerud Smith *et al.* (2011) database. The greater issue is to come up with a correlation that behaves adequately outside the range of flow parameters of the cases used for elaborating it. That is why two qualitatively different correlations, rather than solely one, were elaborated here. When the Regime Capturing Methodology is used in this work, it will be analyzed which one of the two provides the best results.

As in the new interfacial friction factor correlations, it is desired to take into account the increase in the latter due to a roughened interface, it is important to know at which conditions this should take place. Instead of using a critical gas Froude number as criterion, as in Andreussi & Persen (1987), it was chosen to use the superficial gas velocity U_{sG} to monitor the formation of waves and when f_i/f_{i0} should not be unity anymore. Thus, the correlation of Tzotzi & Andritsos (2013), with its complete and accurate expressions for the transition gas superficial velocities $U_{sG,t\mathrm{2D}}$ and $U_{sG,t\mathrm{KH}}$, comes to mind. According to the calculated values of $U_{sG,t\mathrm{2D}}$ and $U_{sG,t\mathrm{KH}}$ for the stratified wavy flow cases with small-amplitude waves from the Eskerud Smith *et al.* (2011) database, they all possess Kelvin-Helmholtz irregular waves, which is in consonance with the remarks of Tzotzi & Andritsos (2013) on viscous oil-gas flows. Thus, $U_{sG,t\mathrm{KH}}$ is used as transition gas superficial velocity and indicator of when f_i should increase in relation to f_{i0} in the two new correlations.

Since the liquid viscosity is a key parameter for this work, it is an interesting idea to insert it directly in the new correlations, which is performed through the mixture viscosity μ_M of Biberg (1999b), defined by Eq. (4.46). In it, it is possible to see that μ_M is a type of weighted harmonic mean between the viscosities of each phase (μ_L and μ_G), whose weights are γ_L^* and γ_G^* and given by Eq. (4.27) together with Table 4.3.

$$\mu_M = \frac{\mu_G \mu_L}{\gamma_L^* \mu_G + \gamma_G^* \mu_L} \tag{4.46}$$

As the balance between viscous and surface tension effects is important for small-scale phenomena (Biberg, 1999b), such as the small-amplitude waves of the Eskerud Smith *et al.* (2011) database cases selected, the Capillary number should be used in the new correlations. Two formulations are used, one for each correlation, for this non-dimensional number: the one proposed by Biberg (1999b), seen in Eq. (4.47), and a new one, formulated in Eq. (4.48).

$$\mathrm{Ca}_i = \frac{\mu_M}{\sigma}\left|\frac{U_{sG}}{\epsilon_G^*} - \frac{U_{sL}}{\epsilon_L^*}\right| \tag{4.47}$$

$$\mathrm{Ca}_{sG} = \frac{\mu_M}{\sigma}\left|U_{sG} - U_{sG,t\mathrm{KH}}\right| \tag{4.48}$$

The Capillary numbers of the referred equations are the interfacial Capillary number Ca_i, for Eq. (4.47), and the superficial gas Capillary number Ca_{sG}, for Eq. (4.48). The label of the former originates from the use, in Eq. (4.47), of a relative velocity between a modified gas and liquid velocities, calculated as the ratio between the respective superficial velocity of each phase and a modified holdup ϵ_K^*, $K \in \{G, L\}$, calculated with Eq. (4.27) and the definitions in Table 4.3. Similarly, the label of Ca_{sG} comes from the use of the gas superficial velocity in Eq. (4.48).

The first correlation for the interfacial friction factor in the condition of irregular Kelvin-Helmholtz waves ($U_{sG} > U_{sGt,\mathrm{KH}}$), according to Tzotzi & Andritsos (2013) is given by Eq. (4.49). Henceforth, it is labeled as “Proposed Expression 1” (PE1).

$$\frac{f_i}{f_{i0}} = 1 + \eta_1 \mathrm{Ca}_i^{\eta_2} \left(U_{sG} - U_{sG,t\mathrm{KH}}\right)^{\eta_3} \tag{4.49}$$

In PE1, η_j, $j \in \{1,2,3\}$, are the coefficients to be determined through the solution of the optimization problem outlined in Figure 4.6(b). Furthermore, in PE1, it can be seen the interfacial Capillary number Ca_i, defined in Eq. (4.47), and the important term $\left(U_{sG} - U_{sG,t\mathrm{KH}}\right)$ that provides the degree of dynamics in the interface in relation to the condition of appearance of waves in $U_{sG} = U_{sG,t\mathrm{KH}}$. The known effect of the liquid height in f_i is implicit in Ca_i.

The second new correlation for the interfacial friction factor, also for $U_{sG} > U_{sG,t\mathrm{KH}}$, shall be labeled as “Proposed Expression 2” (PE2) and it is formulated in Eq. (4.50). In it, the gas superficial Capillary number Ca_{sG} contains the significant parameter $\left(U_{sG} - U_{sG,t\mathrm{KH}}\right)$. The exponential term in PE2, which represents the influence of the liquid height, was inspired by the work of Spedding & Hand (1997) and the reasonable results provided by its correlation for f_i in the Regime Capturing Methodology of Pasqualette *et al.* (2015). That is why the original value for $\eta_3 = 3.1$ from Spedding & Hand (1997) was maintained in this work and solely η_j, $j \in \{1,2\}$, are to be evaluated through optimization.

$$\frac{f_i}{f_{i0}} = 1 + \eta_1 \mathrm{Ca}_{sG}^{\eta_2} \exp\left(\eta_3 \frac{h_L}{D}\right) \tag{4.50}$$

Through the solution of the optimization problem in Figure 4.6(b) and the experimental data of viscous oil-gas stratified wavy flow with small-amplitude waves selected, the coefficients $\boldsymbol{\eta} = [\eta_1 \quad \eta_2 \quad \eta_3]^{\mathrm{T}}$, for PE1, and $\boldsymbol{\eta} = [\eta_1 \quad \eta_2]^{\mathrm{T}}$, for PE2, were determined. The final values of all the coefficients for PE1 and PE2 are registered in Table 4.4.

Table 4.4 – Coefficients of PE1 and PE2.

Proposed Expression	η_1	η_2	η_3
1, Eq. (4.49)	150	0.65	0.38
2, Eq. (4.50)	993	1.29	3.10

With the two solutions of the referred optimization problem, the optimized values of liquid holdup and pressure gradient, for each Proposed Expression, are depicted and compared against experimental data in Figures 4.19 and 4.20.

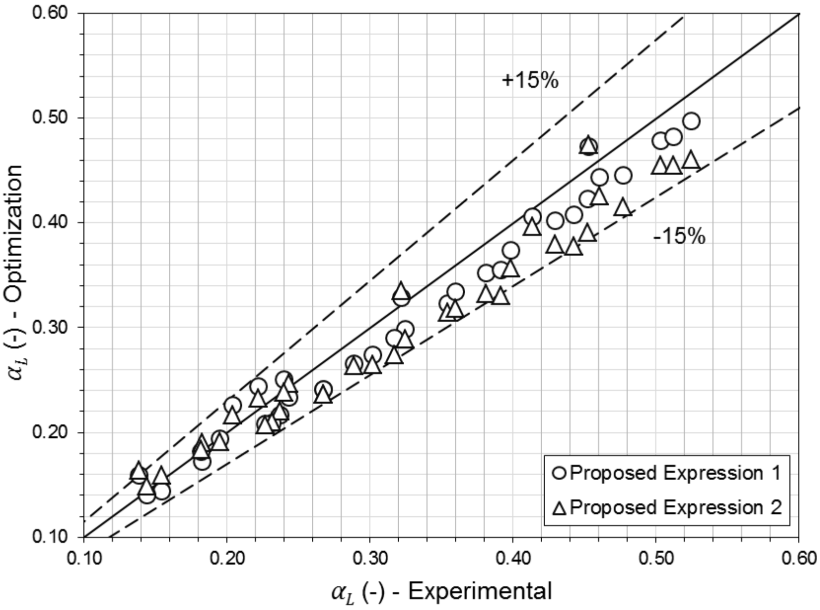

Figure 4.19 – Optimized liquid holdup values of PE1 and PE2 compared against experimental data.

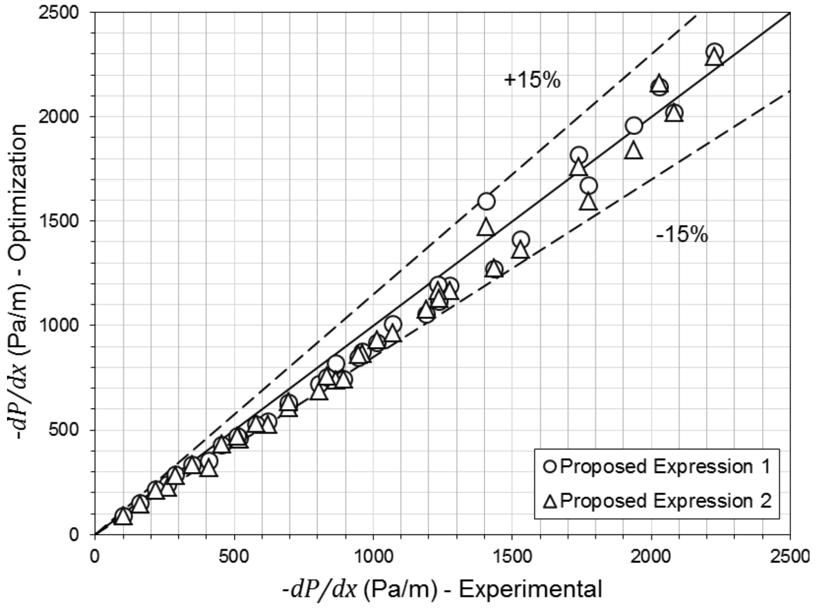

Figure 4.20 – Optimized pressure gradient values of PE1 and PE2 compared against experimental data.

In Figure 4.19, it can be seen that the liquid holdup optimized values, in their majority, does not deviate from the experimental data in more than 15%. Their average relative errors are, for PE1, 6.7% and, for PE2, 8.8%. For the pressure gradient (Figure 4.20), the average relative errors for PE1 and PE2 are, respectively, 8.2% and 9.3%. The deviation of the pressure gradient results in relation to the measurements does not exceed 15%, similarly to the values of liquid holdup. With these results, it can be concluded that the optimization procedure performed for obtaining two qualitatively different correlations, PE1 and PE2, was successful.

The optimized values of f_i obtained through the solution of the problem in Figure 4.6(a) and the ones provided by the newly created PE1 and PE2 are compared in Figure 4.21. In it, it is possible to see that the calculated values from PE1 are closer to the optimized values (most deviations are inside the 15% limit) than those provided by the PE2. This justifies the better results for the former, in comparison with the latter, for the optimized liquid holdup (Figure 4.19) and pressure gradient (Figure 4.20) values.

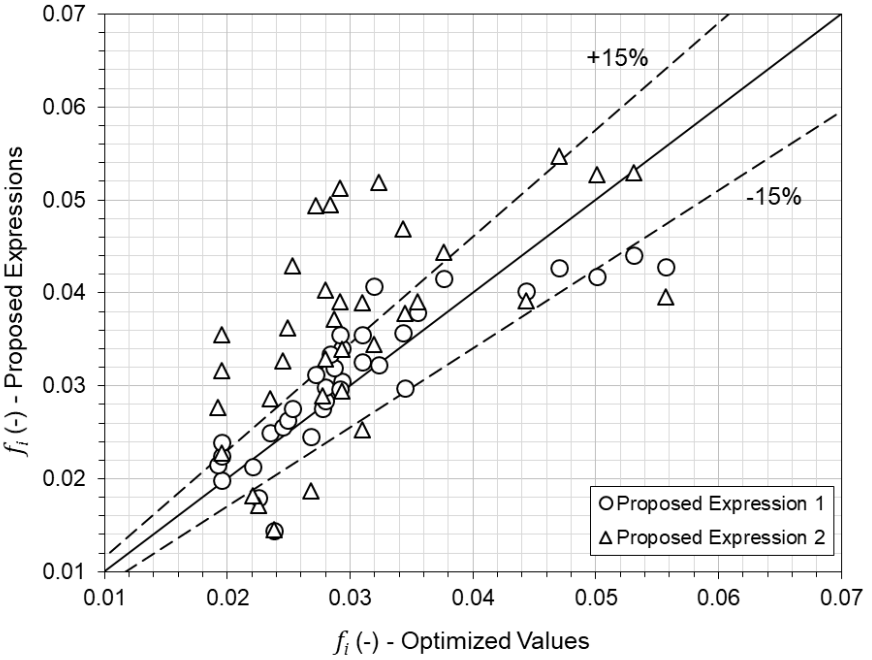

Figure 4.21 – Comparison of the optimized interfacial friction factors with the alternative wall friction factor correlations and the common ones.

As previously mentioned, both PE1 and PE2 assume that $U_{sG} > U_{sG,t\mathrm{KH}}$, which is a valid condition for all the cases selected from the Eskerud Smith *et al.* (2011) database, due to the high viscosity of the Nexbase 3080 oil. However, how to apply these new correlations for flows which are not in the previously described condition? The framework shown in Eqs. (4.51) and (4.52), for PE1 and PE2, respectively, is then employed.

$$\frac{f_i}{f_{i0}} = \begin{cases} 1 & ; \; U_{sG} \leq U_{sG,t\mathrm{2D}} \\ 1 + 150\ \mathrm{Ca}_i^{\;0.65} \left(U_{sG} - U_{sG,t\mathrm{KH}}\right)^{0.38} & ; \; U_{sG} > U_{sG,t\mathrm{KH}} \end{cases} \tag{4.51}$$

$$\frac{f_i}{f_{i0}} = \begin{cases} 1 & ; \; U_{sG} \leq U_{sG,t\mathrm{2D}} \\ 1 + 993\ \mathrm{Ca}_{sG}^{\;1.29} \exp\left(3.1 \dfrac{h_L}{D}\right) & ; \; U_{sG} > U_{sG,t\mathrm{KH}} \end{cases} \tag{4.52}$$

5. SIMULATIONS AND RESULTS

In this chapter, the results from the Regime Capturing Methodology applied to some cases from the Eskerud Smith *et al.* (2011) database are shown and discussed. To this end, three cases were selected from the Eskerud Smith *et al.* (2011) database to be simulated: one corresponds to a slug flow and two of a wavy stratified flow pattern. Those cases are explained and detailed below. Then, the numerical results are presented and compared to measurements.

The strategy employed in the present work to investigate the performance of the Regime Capturing Methodology to predict viscous oil/gas flow is to begin by analyzing the classical 1D Two-Fluid Model, mostly used in literature (Issa & Kempf, 2003; Bonizzi *et al.*, 2009; Nieckele *et al.*, 2013). As presented, the classical model does not consider the dynamic pressure contribution ($\boldsymbol{\Delta P_{\mathcal{D},K} = 0}$) nor the axial momentum diffusion ($\boldsymbol{\mu_K^{eff} = 0}$) and dynamic interfacial shear stress ($\boldsymbol{\mathcal{J}_i = 0}$). However, those effects must be contemplated to evaluate their impact in the 1D Two-Fluid Model predictions.

Based on the simplified incompressible characteristics analysis of the 1D Two Fluid Model, without its high-order derivative terms (shown in chapter 3), it was verified that the dynamic pressure contribution acts to increase the region in which the pair of superficial velocities of gas and liquid are well-posed. The same analyses showed that the dynamic interfacial shear stress acts in the opposite direction, however, the combined effect, might render the solution well-posed and also improve the quality of the predictions. Therefore, a map delimitating the well/ill posed region of superficial velocities for the fluids considered in the present work is created to verify the result. Finally, as discussed in chapter 3, since the axial momentum diffusion is a second order term, it does not appear in the simplified characteristics analysis. However, it is well know that diffusion is has a stabilizing effect in the flow. Therefore, the set of simulations outlined in Table 5.1 was performed, together with the first one which does not consider any of the new terms ($\boldsymbol{\Delta P_{\mathcal{D},K}}$, $\boldsymbol{\mu_K^{eff}}$ and $\boldsymbol{\mathcal{J}_i}$). Table 5.1 shows that the second set solely takes into account the dynamic pressure, the third set considers only the axial momentum diffusion and the fourth set regards both dynamic pressure and dynamic interfacial shear stress.

Table 5.1 – Modelling setup for each set of simulations.

Set	$\Delta P_{\mathcal{D},K}, K \in \{G,L\}$	$\mu_K^{eff}, K \in \{G,L\}$	$\mathcal{J}_i$
1st	0	0	0
2nd	Eq. (3.30)	0	0
3rd	0	Eq. (3.34)	0
4th	Eq. (3.30)	0	Eq. (3.51)

Coupled with the set of simulations listed in Table 5.1, simulations were also performed to evaluate the impact in the solution of the new proposed correlations for the interfacial friction factor, Proposed Expressions 1 and 2, Eqs. (4.60) and (4.61), respectively, when compared with the Standard Expression, Eq. (4.56). The main purpose of these tests was to assess if the new correlations managed to improve the predictions of the Regime Capturing Methodology in the same manner they did for the Point Model of Eq. (4.6).

In all tests performed here, the wall-shear stresses, τ_{wK}, $K \in \{G,L\}$, are modelled precisely as presented in the optimization procedure that led to the elaboration of the Proposed Expressions 1 and 2 (sections 4.6 and 4.7).

5.1. The Selected Cases

Three cases were selected from the isothermal horizontal viscous oil-SF_6 flows (in a laboratory-scale pipeline) Eskerud Smith *et al.* (2011) database. Key features of the cases are registered in Table 5.2, which includes the gas and liquid superficial Reynolds numbers and the flow patterns. All the data on these cases shown in this work is also present in Johansen *et al.* (2014).

Cases 1, 2 and 3, as seen in Table 5.2, consist in one slug flow (Case 1) and two stratified wavy flow with small-amplitude waves (Cases 2 and 3). It should be noted that Cases 2 and 3 were also used in the optimization procedure for elaborating the Proposed Expressions 1 and 2 for the interfacial friction factor f_i.

Table 5.2 – Key features of the selected cases from the Eskerud Smith *et al*. (2011) database.

Case	Re_{sG}	Re_{sL}	Flow Pattern	Used in the optimization?
1	1.03×10^5	615	Slug	No
2	6.47×10^5	492	Stratified Wavy (Small-Amplitude Waves)	Yes
3	1.08×10^6	583	Stratified Wavy (Small-Amplitude Waves)	Yes

Cases 2 and 3 were selected to allow a comparison of the optimized Point Model results, for such expressions, with the numerical results from the Regime Capturing Methodology. Such comparison can act as a verification tool for the Regime Capturing Methodology, because, for very coarse meshes, its results must coincide with the predictions of the Point Model. It also makes possible the desired evaluation of whether or not the new Proposed Expressions for f_i improve the methodology predictions in relation to the Standard Expression, in the same manner as they do in the Point Model.

Including a slug flow in the simulations, Case 1, is of paramount importance for analyzing how the Proposed Expressions for f_i, elaborated with small-amplitude interfacial waves data, behave when a large intermittency (small and large waves together with slugging) takes place.

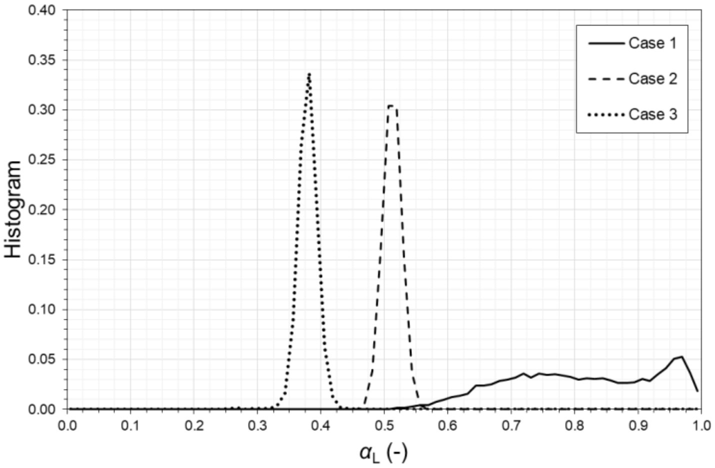

Figure 5.1 – Histograms of the liquid holdup signals (x = 38.15m) for Cases 1, 2 and 3.

As is was previously detailed, experimental time traces for the *in situ* liquid holdup α_L for each case are available due to the measurements of a broad beam-gamma densitometer, located 38.15m downstream the pipe inlet section (Eskerud Smith *et al.*, 2011). The histograms of these α_L signals for Cases 1, 2 and 3 are plotted in Figure 5.1, which confirms their listed flow patterns.

It can be seen a high probability of the liquid holdup with a constant value for Cases 2 and 3, confirming that these cases correspond to stratified flow pattern. On the other hand, for Case 1, the highest probability is related to liquid holdup equal to 1, indicating the presence of slug flow, and there is a wide range of liquid holdups from 0.7 to 0.9 with also a high probability of occurrence.

Figure 5.2 shows the time evolution of the experimental liquid holdup for Cases 1, 2 and 3, for a 30s interval. The slug flow pattern of Case 1, Figure 5.2(a), and the stratified wavy (with small-amplitude waves) flow pattern of Cases 1 and 2, Figures 5.2(b) and 5.2(c), can be clearly noticed.

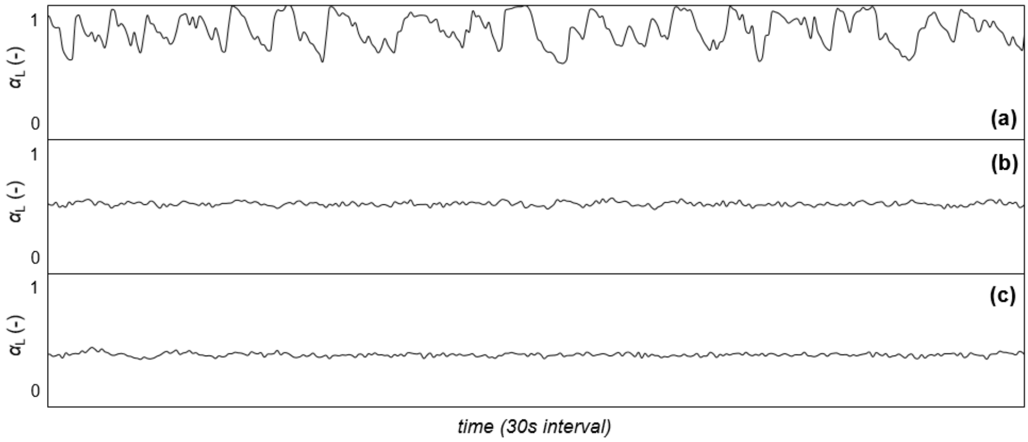

Figure 5.2 – Experimental liquid holdup profiles in time at x = 38.15m for: (a) Case 1; (b) Case 2; and (c) Case 3.

The numerical results of the Regime Capturing Methodology simulations for liquid holdup histograms and transient profiles will be compared against the experimental data shown in Figures 5.1 and 5.2. Besides, the mean (in time and at the same position of 38.15m) liquid holdup α_L, obtained with the gamma densitometer data, and the pressure gradients dP/dx, provided by pressure cells measurements, are also used for comparing with the predictions of the methodology for Cases 1, 2 and 3. Table 5.3 lists the experimental values for these mean parameters for the three Cases.

For a joint comparison of the numerical results for the mean liquid holdup and for the pressure gradient against experimental data, a root-mean-squared error, e_{RMS}, is defined by Eq. (5.1), inspired by Eqs. (4.14)-(4.15). The subscript “num” refers to the simulation results.

Table 5.3 – Some features of the selected cases from the Eskerud Smith *et al*. (2011) database.

Case	Measurements (gamma densitometer and pressure cells)	
	α_L $(-)$	$-dP/dx$ (Pa/m)
1	0.823	507.8
2	0.525	945.9
3	0.392	1236.9

$$e_{RMS} = \sqrt{\left(\frac{\alpha_L|_{\text{num}} - \alpha_L|_{\text{exp}}}{\alpha_L|_{\text{exp}}}\right)^2 + \left(\frac{dP/dx|_{\text{num}} - dP/dx|_{\text{exp}}}{dP/dx|_{\text{exp}}}\right)^2} \tag{5.1}$$

As Cases 2 and 3 were used in the Point Model optimization procedure that resulted in two new Proposed Expressions for f_i, it is important to list not just the optimized mean liquid holdup and pressure gradient values for these expressions, but also the Point Model predictions with the Standard Expression of Eq. (4.45). Those values are all shown in Table 5.4. It is important to mention that these values do not have a meaning for Case 1, since the Point Model cannot be applied to slug flows.

Table 5.4 – Integral parameters Point Model predictions for the selected cases from the Eskerud Smith *et al*. (2011) database.

Case	Predicted Values (Standard Expression)		Optimized Values (Proposed Expression 1)		Optimized Values (Proposed Expression 2)	
	α_L $(-)$	$-dP/dx$ (Pa/m)	α_L $(-)$	$-dP/dx$ (Pa/m)	α_L $(-)$	$-dP/dx$ (Pa/m)
2	0.638	735.8	0.497	848.3	0.460	862.2
3	0.518	863.1	0.355	1113.4	0.330	1128.1

5.2. Stability-Hyperbolicity Analysis

Due to the known stability-hyperbolicity problem of the isothermal 1D Two-Fluid Model, a mesh convergence test is performed for each Case for every different simulation setup. During these tests, the mean liquid holdup, pressure gradient and liquid holdup histograms are monitored as the spatial mesh is refined, that is, as the mesh aspect ratio $(\Delta x/D)$ is decreased. If these results stabilizes after a certain value of $\Delta x/D$, the simulation is considered to be well-posed and the stabilized results are considered the valid Regime Capturing Methodology predictions. On the other hand, if the results do not stop varying with $\Delta x/D$, then the simulation is considered ill-posed.

Assuming that the Regime Capturing Methodology is ideally well-posed and mesh-convergent, when Cases 2 and 3 are simulated with the Proposed Expressions 1 and 2, the provided liquid holdup profile should be completely flat. This is because the effects of small-amplitude waves are already included in these correlations for the interfacial friction factor. Nevertheless, in Case 1 the large-amplitude waves and the liquid pipe section bridging (slugging) should be captured. When, the Standard Expression for f_i is used, the small-amplitude interfacial waves should be predicted in Cases 1, 2 and 3.

5.2.1. Well/ill-posedness Maps

As previously said (in section 3.3), although the effects on the stability-hyperbolicity problem of the dynamic pressure and of the axial momentum diffusion terms are known (Fullmer *et al.*, 2014; Han & Guo, 2015), the influence of considering the dynamic interfacial shear stress of Brauner & Maron (1993; 1994) has not been much explored in literature. The only exception, recapitulating, is the work of De Bertodano *et al.* (2013), which verified that such term destabilizes the flow, which tends to enhance the stability-hyperbolicity problem.

As described in section 3.3, for checking if the finding of De Bertodano *et al.* (2013) is valid for the Eskerud Smith *et al.* (2011) database, well-posedness analyzes were performed by the evaluation of the 1D Two-Fluid Model quasi-linear system, Eq. (3.108), characteristics. This task was accomplished in a previous chapter in Eqs. (3.131)-(3.134) with their intrinsic and previously provided hypotheses. Both symbolic and numerical operations were performed with the Wolfram Mathematica software. Besides, the effect of the dynamic interfacial shear stress of Brauner & Maron (1993; 1994), the influence of the dynamic pressure of Bestion (1990) was also verified. The effects of the axial momentum diffusion was obviously not verified here, because the second and third-order derivatives terms cannot be accounted in the such well-posedness analysis. Therefore, μ_K^{eff} is considered null in this topic.

Through this methodology, the U_{sL} vs. U_{sG} well-posedness maps for the Eskerud Smith *et al.* (2011) database of Figures 5.3 and 5.4 were obtained. In them, the red color region corresponds to the region where the system of equations are ill-posed. Figure 5.3(a) corresponds to the classical case, i.e., without dynamic pressure contribution ($\Delta P_{\mathcal{D},K} = 0$) nor the dynamic interfacial shear stress ($\mathcal{J}_i = 0$). It can be seen that for a wide range of liquid superficial velocities, when the gas superficial velocities is high, the system is ill-posed. The map presented in Figure 5.3(b) corresponds to the solution, when only the dynamic pressure difference is added to the model. Note that, according to this simplified analysis, for all superficial velocities the system is well-posed. This result is expected, since Bestion (1990) designed the dynamic pressure distribution to render the system well-posed.

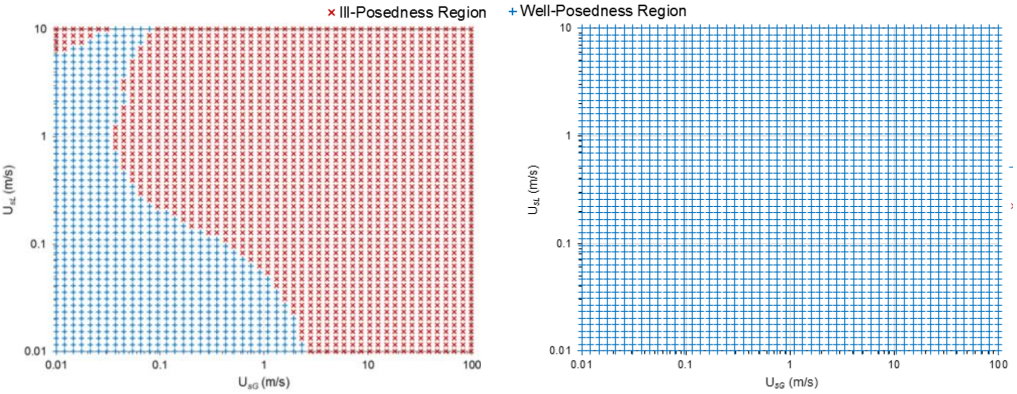

(a) $\Delta P_{\mathcal{D},K} = 0;\ \mu_K^{eff} = 0;\ \mathcal{J}_i = 0.$ (b) $\Delta P_{\mathcal{D},K} \neq 0;\ \mu_K^{eff} = 0;\ \mathcal{J}_i = 0.$

Figure 5.3 – Well-posedness for the Eskerud Smith *et al.* (2011) database, without the dynamic interfacial shear stress.

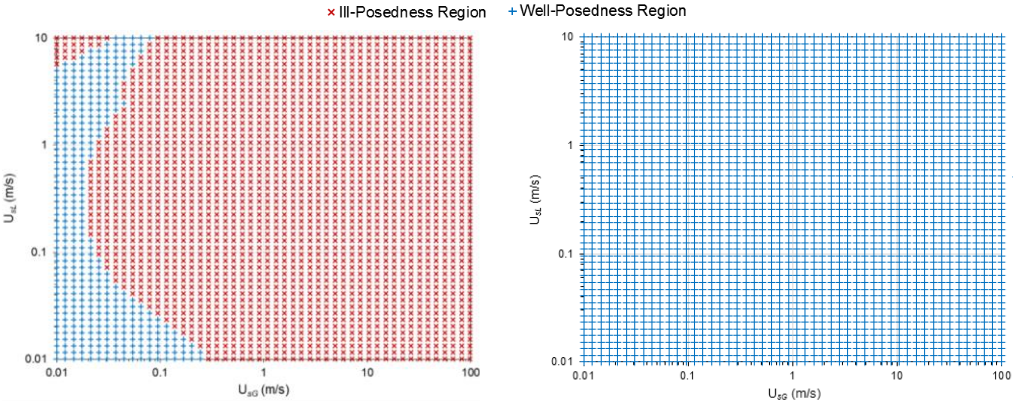

(a) $\Delta P_{\mathcal{D},K} = 0;\ \mu_K^{eff} = 0;\ \mathcal{J}_i \neq 0.$ (b) $\Delta P_{\mathcal{D},K} \neq 0;\ \mu_K^{eff} = 0;\ \mathcal{J}_i \neq 0.$

Figure 5.4 – Well-posedness for the Eskerud Smith *et al.* (2011) database considering the dynamic interfacial shear stress.

The maps presented in Figure 5.4 were constructed with the dynamic interfacial shear stress of Brauner & Maron (1993; 1994). In Figure 5.4(a), there is no dynamic pressure contribution. Comparing this map, with the map of Figure 5.3(a), one can clearly see that the dynamic interfacial shear stress reduced the size of the well-posed region. This result agrees with De Bertodano *et al.* (2013) observation, that the dynamic interfacial shear stress of Brauner & Maron (1993; 1994) destabilizes the flow. On the other hand, the map obtained with the simplified analysis, showed that the presence of the dynamic pressure contribution guarantees a well-posed solution, even in the presence of the dynamic interfacial shear stress.

The present map results indicates that the dynamic pressure contribution is a positive factor to render the system of equations well-posed, even in the presence of the dynamic shear stress term, what is an encouragement, to investigate, the performance of the Regime Capturing Methodology, for these situations.

5.3. First Set of Simulations

In the first set of simulations, as aforementioned, the dynamic pressure, the axial diffusion and the dynamic interfacial shear stress terms are not considered in the 1D Two-Fluid Model of Eqs. (3.58)-(3.61) (Table 5.1). In the presentation of the results, first the predictions for Case 1 (slug flow) are shown, followed by the results of Cases 2 and 3 of wavy stratified flow.

5.3.1. Case 1: Standard Expression

The first results obtained for Case 1, based on the classical 1D Two-Fluid Model, employed the Standard Expression for the interfacial friction factor. The simulations were performed with several spatial meshes with the aspect ratios $\Delta x/D$ of 0.5, 0.75, 1.0, 1.5, 2, 5, and 10. Figure 5.6 depicts the results for the mean liquid holdup α_L (at the position of 38.15m) and pressure gradient dP/dx, while Figure 5.6 presents the combined error, e_{RMS}, Eq. (5.1).

In Figure 5.5(a), it can be seen that α_L starts with a numerical value higher than the experimental one, which decreases as the mesh is refined until it stabilizes for $\Delta x/D$ values lower than 2.5. The α_L value for which the results stabilized is lower than the measurement and has a larger deviation than the starting α_L value for $\Delta x/D = 10$. In an analogous manner, in Figure 5.5(b), the pressure gradient prediction for $\Delta x/D = 10$ is lower than experimental value and, as the aspect ratio decreases, $|dP/dx|$ increases until stabilizing for aspect ratios lower than 2.5 in a value very close to the experimental one.

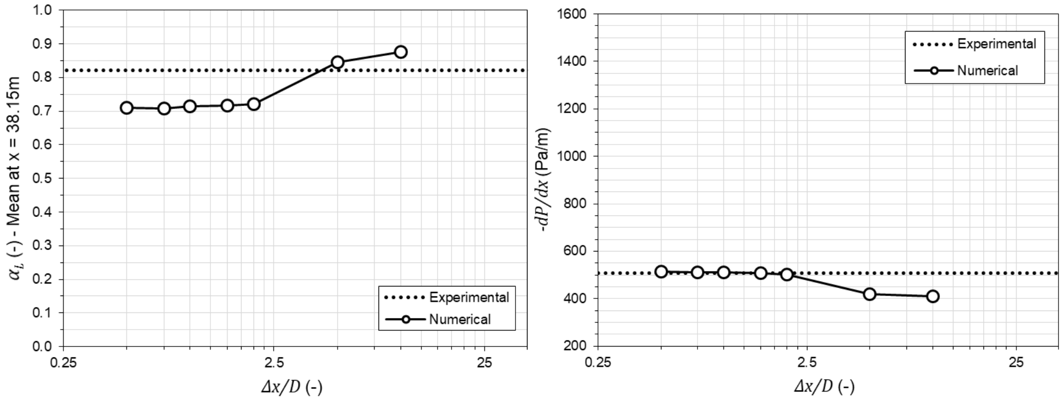

(a) Mean liquid holdup (b) Pressure gradient

Figure 5.5 – Grid test for Case 1 with the Standard Expression in the first set of simulations.

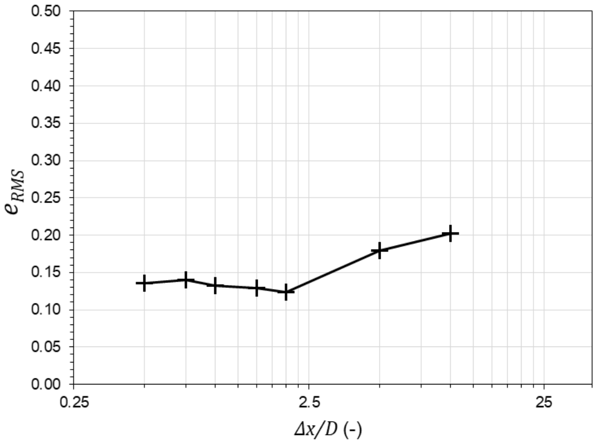

Figure 5.6 – Values of the root-mean-squared error of Eq. (5.1) for Case 1 with the Standard Expression in the first set of simulations.

By combining the observations of Figures 5.5(a) and 5.5(b), one comes to the conclusion that the Regime Capturing Methodology for Case 1, with the Standard Expression for f_i in the first set of simulations is well-posed and mesh-convergent for values of $\Delta x/D$ lower than 2.5. It is interesting to see, in Figure 5.6, the evolution of e_{RMS} with the refinement of the spatial mesh and how it barely changes for $\Delta x/D$ lower than 2.5.

From the three previous figures, it is easily identified three groups of results: for the mesh aspect ratio of 10, 5 and for values lower than 2.5, when the former stabilizes. This is a consequence of three different interfacial dynamic behaviors, observed in Figure 5.7 through the transient profiles of the numerical liquid holdup for Case 1, relative to the aspect ratios 10, 5 and 0.5. The pipe position (38.15m) from which the values of α_L were taken is the same position of the gamma densitometer, whose measurements are also plotted in Figure 5.2.

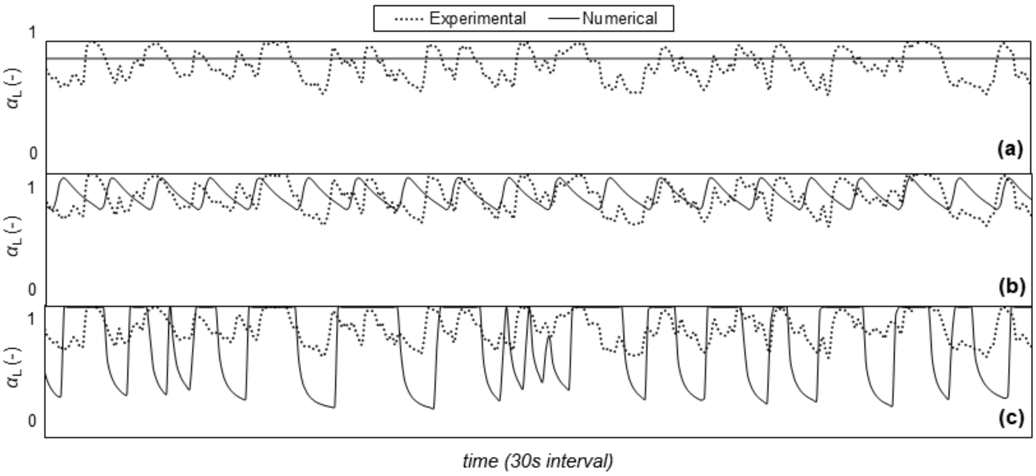

Figure 5.7 – Case 1 numerical liquid holdup profiles at 38.15m for the Standard Expression in the first set of simulations and for: (a) mesh aspect ratio of 10; (b) mesh aspect ratio of 5; and (c) mesh aspect ratio of 0.5.

In Figure 5.7(a), due to the small number of nodal points, the mesh is not fine enough to capture the appearance of interfacial instabilities, growth and development into slugs. Therefore, the interface remains axially flat and very different from the data obtained by the gamma densitometer. For the aspect ratio of 5, in Figure 5.7(b), waves arise originating a very regular interfacial behavior. However the mesh is still not fine enough for predicting the slug flow of Case 1, although the values of numerical α_L slightly resemble the measured ones in Figure 5.7(b). A slug flow is only obtained for aspect ratios lower than 2.5, the value for which the results stabilize, as it can be seen in Figure 5.7(c). Figure 5.7 shows, therefore, that the ability of capturing interfacial dynamics, for Case 1 (slug flow), is improved as the mesh is refined, until it converges to a well-posed solution. The higher amplitudes of the liquid holdups, when compared to the ones of the experimental signals, represent how the numerical interfacial behavior is still different from the experimental one, although the predictions of mean α_L, Figure 5.5(a), and pressure gradient, Figure 5.5(b), are satisfactory, Figure 5.6.

Similar observations can be drawn from Figure 5.8, which shows the numerical and experimental histograms at 38.15m, for the same results obtained for

Case 1, from the first set of simulations obtained with the Standard Expression.

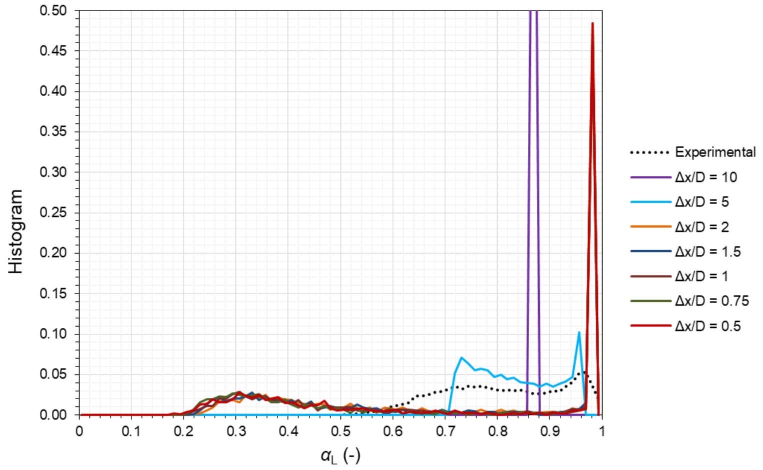

Figure 5.8 – Liquid holdup histograms for Case 1 with the Standard Expression in the first set of simulations.

Besides the same aspect ratios of Figure 5.7, Figure 5.8 also includes the histograms of the other $\Delta x/D$ values registered in Figures 5.5 and 5.6. The previously mentioned three distinct interfacial behaviors (for the aspect ratios 10, 5 and the ones lower than 2.5) can be identified in Figure 5.8. As Case 1 consists in a slug flow, two peaks can be observed in the histograms: one related to the slugs (α_L close to unity) and another regarding the liquid films (intermediate α_L). Comparing the numerical histograms for aspect ratios lower than 2.5 and the gamma densitometer histogram, in Figure 5.8, it can be seen that the numerical liquid film peaks correspond to liquid holdups lower than it does for the measurements. This is a consequence of the greater α_L amplitudes aforementioned regarding Figure 5.7(c). Furthermore, the numerical slug histogram peak is much higher than the experimental one. This fact alone could imply either longer slugs or higher slug frequencies, than the measured ones. However, it is also possible that this discrepancy occurs due to entrainment of gas bubbles into the slugs in the experiments. As mentioned before, gas entrainment is not taken into account in the current model.

5.3.2. Case 1: Proposed Expressions 1 and 2

With the intention of improving the numerical predictions for the integral parameters (mean liquid holdup and pressure gradient) and the transient liquid holdup behavior, depicted in Figure 5.7, the new interfacial friction factor expressions (Proposed Expressions 1 and 2), created in the optimization procedure previously described, are used. Starting with the Proposed Expression 1, Figures 5.9(a), 5.9(b) and 5.10 show, respectively, the variation of the mean liquid holdup, the pressure gradient and of e_{RMS} with the spatial mesh aspect ratio $\Delta x/D$ for the Case 1 simulation results in the first set of simulations.

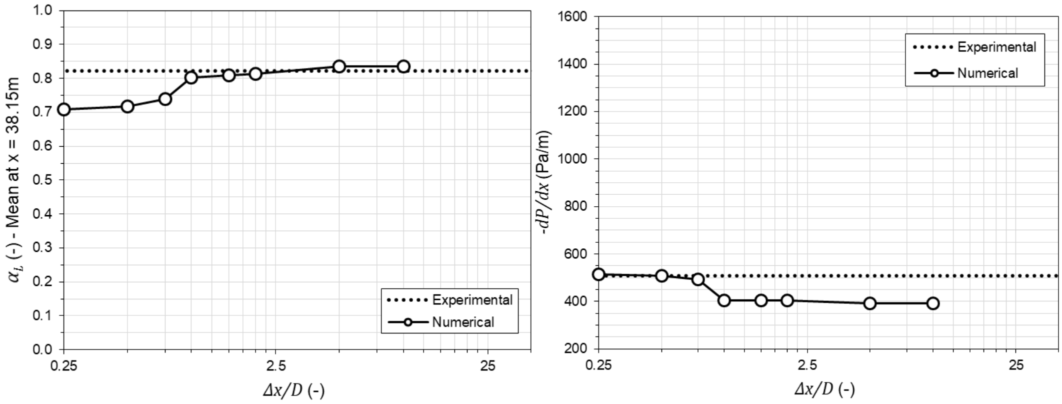

(a) Mean liquid holdup (b) Pressure gradient

Figure 5.9 – Grid test for Case 1 with the Proposed Expression 1 in the first set of simulations.

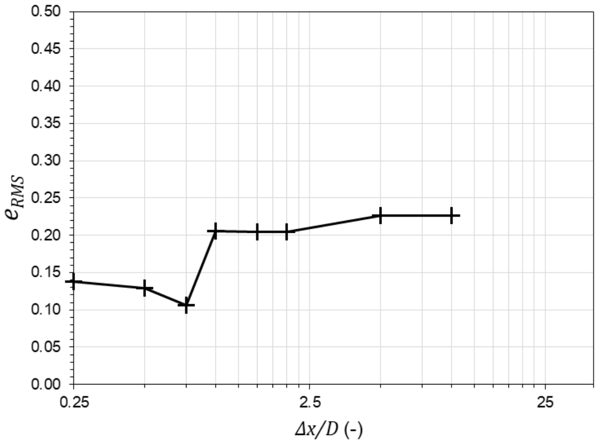

Figure 5.10 – Values of the root-mean-squared error of Eq. (5.1) for Case 1 with the Proposed Expression 1 in the first set of simulations.

In Figures 5.9 and 5.10, the behavior with the mesh aspect ratio is very similar to what was obtained when the Standard Expression was used (Figures 5.5 and 5.6). The main difference lies in the necessity, for the Proposed Expression 1, of smaller grid spacing for obtaining mesh convergence when compared to the Standard Expression simulations. This is actually not a surprise, since higher interfacial shear stresses tend to suppress the formation of interfacial instabilities, although it does not affect the classical well-posedness analysis (Issa & Kempf, 2003; Liao *et al.*, 2008; Fullmer *et al.*, 2014; Pasqualette *et al.*, 2017). This is more clearly seen in Figure 5.11, where the predicted liquid holdup histograms (at 38.15m) for the Proposed Expression 1 are plotted together with the experimental one.

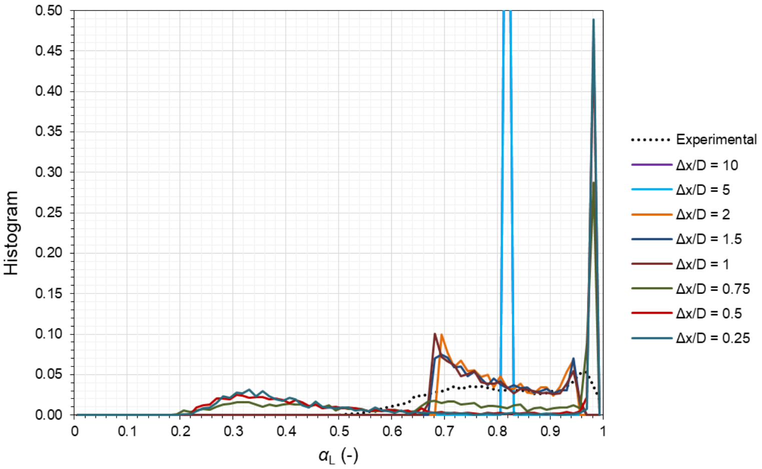

Figure 5.11 – Liquid holdup histograms for Case 1 with the Proposed Expression 1 in the first set of simulations.

In the referred figure, it can be seen that slugs only start to appear for an aspect ratio of 0.75, in which, besides the liquid film and slug holdup peaks, there is an evident occurrence of α_L values between 0.7 and 0.9, which is not the case neither for $\Delta x/D = 0.5$ nor for $\Delta x/D = 0.25$. For these aspect ratios, the results can be considered mesh convergent and well-posed, if one observes Figures 5.9 and 5.10. By analyzing the converged numerical histogram results for Proposed Expression 1, it can be seen that the same disparities verified for Standard Expression when compared against the experimental data, are again obtained for Proposed Expression 1. Those are the high probability of liquid holdups close to unity (slugs) and the low holdups in the liquid film region .

The same results of Figures 5.9 and 5.10 are now shown in Figures 5.12 and 5.13, respectively, , but now for Case 1, in the first set of simulations, with the Proposed Expression 2 for the interfacial friction factor.

The behavior of the numerical mean liquid holdup, pressure gradient and e_{RMS} results for Case 1, using the Proposed Expression 2, with the mesh aspect ratio is, again, very similar to the one obtained for the Standard Expression (Figures 5.5 and 5.6) and for the Proposed Expression 1 (Figures 5.9 and 5.10).

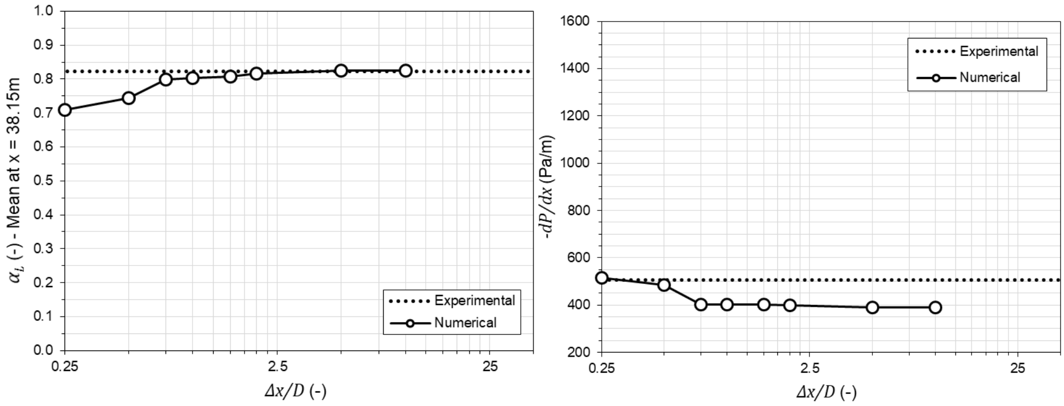

(a) Mean liquid holdup (b) Pressure gradient

Figure 5.12 – Grid test for Case 1 with the Proposed Expression 2 in the first set of simulations.

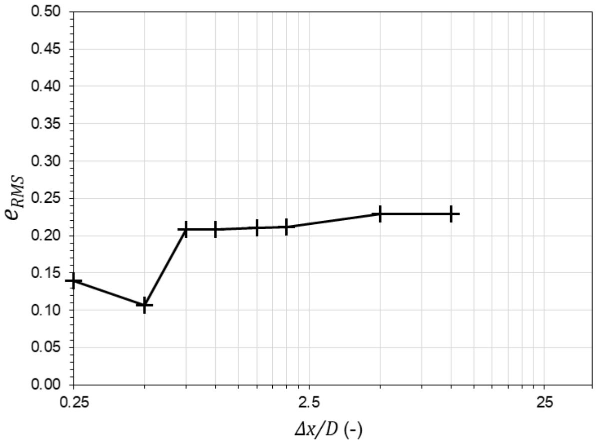

Figure 5.13 – Values of the root-mean-squared error of Eq. (5.1) for Case 1 with the Proposed Expression 2 in the first set of simulations.

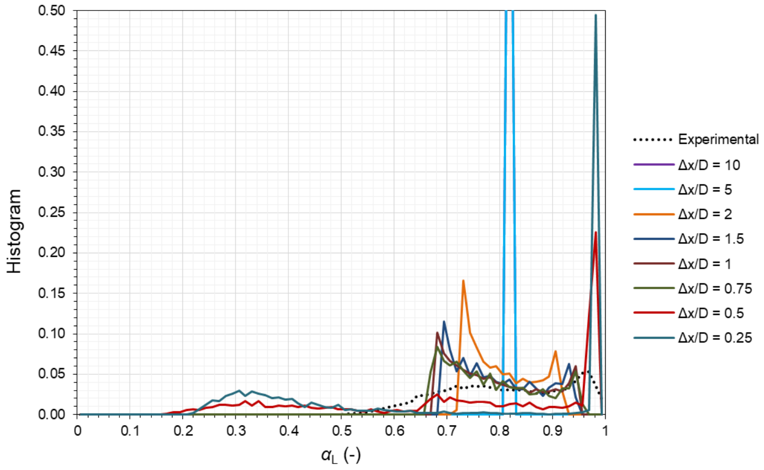

Figure 5.14 – Liquid holdup histograms for Case 1 with the Proposed Expression 2 in the first set of simulations.

What separates the Proposed Expression 2 results from the others is that a stabilization of the results is only roughly obtained. This is also evident in Figure 5.14, where the numerical liquid holdup histograms are plotted, for the Proposed Expression 2, the same way as they were in Figures 5.7 and 5.11 for the Standard Expression and Proposed Expression 1, respectively.

The similarity between the slug flow histograms obtained with Proposed Expression 2, in Figure 5.14, with the ones in Figures 5.7 and 5.11, is evident. This is especially true when histogram results for the mesh aspect ratios of 0.75 (Figure 5.14) and 0.5 (Figure 5.11) are compared. The histogram of the Proposed Expression 2 liquid holdup results for $\Delta x/D = 0.5$ is extremely similar to the histogram correspondent to mesh convergent conditions for the Standard Expression and for the Proposed Expression. That is the reason why it is safe to state that, although a clear convergence of the results does not take place in Figures 5.12 and 5.13, the Proposed Expression 2 results are well-posed for aspect ratios equal or lower to 0.25.

For directly comparing the converged numerical liquid holdup values at 38.15m for Case 1 (first set of simulations), obtained with the Standard Expression ($\Delta x/D = 0.50$), Proposed Expressions 1 ($\Delta x/D = 0.50$) and 2 ($\Delta x/D = 0.25$), such time traces are plotted in Figure 5.15 for a 30s time interval together with the gamma densitometer measurements.

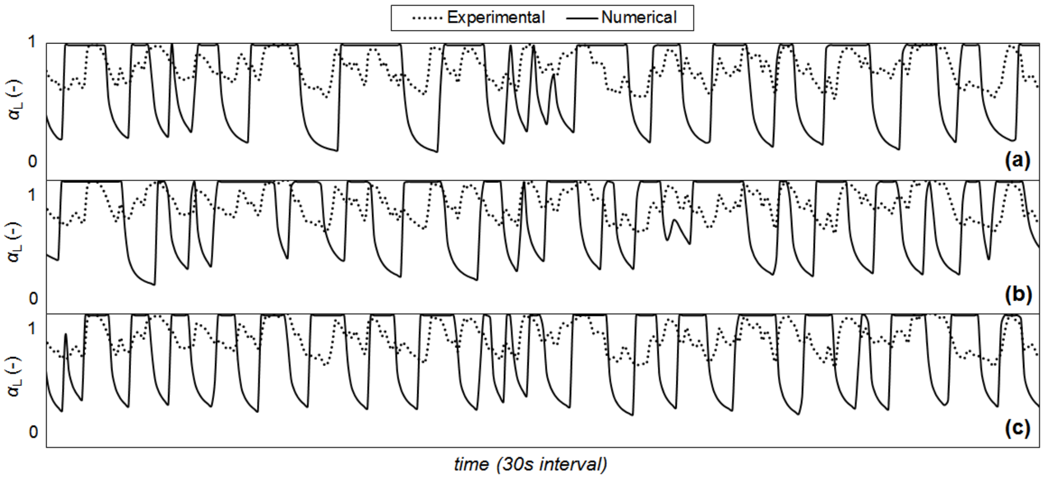

Figure 5.15 – Case 1 numerical liquid holdup profiles for aspect ratio of 0.5 in the first set of simulations and for: (a) Standard Expression (aspect ratio of 0.5); (b) Proposed Expression 1 (aspect ratio of 0.5); and (c) Proposed Expression 2 (aspect ratio of 0.25).

By observing the transient liquid holdup results in Figure 5.15, it can be seen that the converged Case 1 simulations in the first set of simulations tend to similar interfacial behavior. The same high intermittency amplitudes and the low holdup of the liquid film region, when compared to the measured α_L signals, were obtained with $\Delta x/D = 0.5$ for the Standard Expression, Figure 5.15(a), for the Proposed Expression 1, Figure 5.15(b), and for the Proposed Expression 2, Figure 5.15(c). What also draws attention are the similar α_L and dP/dx results for these converged simulations, which are outlined in Table 5.5. Nevertheless, the results for such integral parameters are satisfactory: relative errors of about 13% for the liquid holdup and 1% for the pressure gradient.

Table 5.5 – Case 1 integral parameter results for converged results in the first set of simulations.

	$\Delta x/D$	α_L (−)	$-dP/dx$ (Pa/m)	Relative Error (α_L)	Relative Error (dP/dx)	e_{RMS}
Standard Expression	0.50	0.711	513.0	-13.56%	1.01%	0.14
Proposed Expression 1	0.50	0.716	509.9	-12.95%	0.40%	0.13
Proposed Expression 2	0.25	0.709	514.1	-13.87%	1.23%	0.14

5.3.3. Case 1: Slug Statistics

This analysis, so far, has revealed that the use of more precise interfacial friction factor expression that increase its values has no significant impact on the qualitative interfacial behavior or on the predictions of integral parameters. In other words, the switch from the Standard Expression to the Proposed Expressions 1 and 2 did not improve the already satisfactory integral parameters, nor did it make the predicted interfacial dynamics physically consistent with the measurements. For advancing the analysis, it is important to assess the slug statistics for just comparing the converged results from each interfacial friction factor expression for Case 1 in the first set of simulations. With this in mind, for such simulations, the average and standard deviation of the Taylor bubbles velocities (U_b) and lengths (L_b) and of slugs translational velocities (U_t) and lengths (L_S), together with the slug frequency (ν_S), are shown in Table 5.6. It is important to highlight that the absolute values of the slug statistics do not receive attention, that is, it is not evaluated if they are close to experiments or to correlations predictions or not, since the analysis is only for comparing the different aspects of numerical predictions.

Once again, the similarity between the numerical slug statistics from each interfacial friction factor expression is remarkable in Table 5.6. The only exceptions are the standard deviation of L_S/D and the average value of L_b/D, for the Proposed Expression 1. This confirms that, for Case 1 and for the first set of simulations, the use of the newly obtained Proposed Expression 1 and 2 did not affect any significant parameter of the results, when compared to the Standard Expression, neither qualitatively nor quantitatively, once the simulations are converged and well-posed. The sole aspect affected is the aspect ratio necessary for obtaining mesh convergence, due to the values of f_i from the Proposed Expressions 1 and 2 being higher than the ones from the Standard Expression. Furthermore, one cannot help to notice that the ratio between $\langle U_b \rangle$ (or U_t, nearly equal to U_b when the flow reaches steady-state) and U_M is approximately 1.45. For laminar flow, the case of the present liquid phase due to the oil viscosity, such ratio is the C_0 parameter of Eq. (2.1), whose experimental value, as observed in literature, is about 2.0 (Gokcal, 2008; Foletti *et al.*, 2011), very different from the 1.45 obtained. It is important mentioning that for such laminar flows, the U_d velocity in Eq. (2.1) is approximetely null (Foletti *et al.*, 2011).

Table 5.6 – Case 1 slug statistics for the converged results in the first set of simulations.

	$\Delta x/D$	U_b (m/s)		L_b/D (−)		U_t (m/s)		L_S/D (−)		ν_S (Hz)
		$\langle U_b \rangle$	σ_{U_b}	$\langle L_b/D \rangle$	$\sigma_{L_b/D}$	$\langle U_t \rangle$	σ_{U_t}	$\langle L_S/D \rangle$	$\sigma_{L_S/D}$	
Standard Expression	0.50	2.03	1.00	21.50	5.95	1.93	0.16	18.60	12.48	0.80
Proposed Expression 1	0.50	1.94	1.10	31.16	5.57	1.99	0.20	18.74	16.36	0.80
Proposed Expression 2	0.25	1.98	0.97	19.52	5.13	1.90	0.16	19.49	12.34	0.82

5.3.4. Cases 2 and 3: Standard Expression

After presenting and discussing the Case 1 simulation results with the three expressions for the interfacial friction factor, the integral parameters obtained by simulating the stratified wavy Cases 2 and 3, with the Standard Expression for f_i, are presented. In Figures 5.16 and 5.17, the numerically obtained mean liquid holdup and pressure gradient, respectively, are plotted as a function of the mesh aspect ratio $\Delta x/D$ together with the experimental values and the Point Model, Eq.

(4.4), predictions, registered in Tables 5.3 and 5.4. Figure 5.18, the e_{RMS} values of such results of Cases 2 and 3 are depicted.

The first observation to be made regarding Figures 5.16 and 5.17 is that, for both Cases 2 and 3, the Regime Capturing Methodology results for the very coarse mesh of $\Delta x/D = 40$ coincide with the Point Model predictions. This is exactly what was to be expected, since a mesh of a single finite volume (in the limiting case) becomes the Point Model. In Figures 5.16-5.18, as the mesh is refined, the mean liquid holdup decreases, the pressure gradient augments and the e_{RMS} values first decreases and then increases. However, it can be noticed that neither the α_L results nor the dP/dx values stabilize: the former keeps decreasing and the latter increasing, as the mesh aspect ratios diminishes. Therefore, the Case 2 and 3 results (in the first set of simulations) for the Standard Expression are not mesh convergent and are ill-posed.

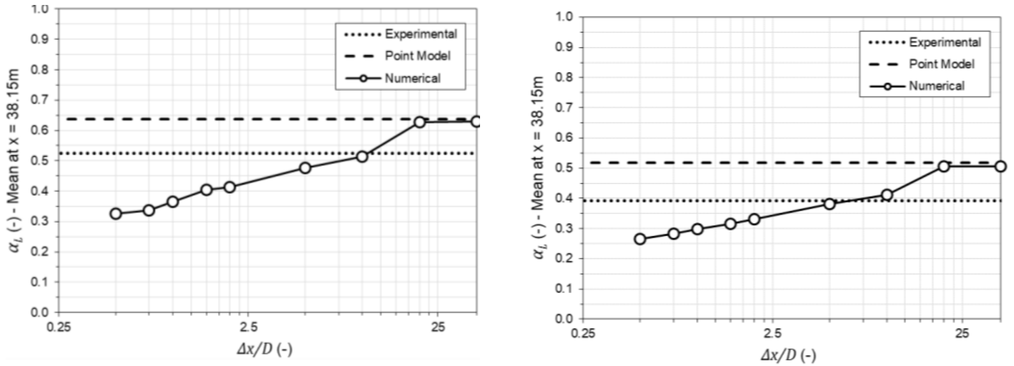

(a) Case 2. (b) Case 3.

Figure 5.16 – Mean liquid holdup numerical results for Cases 2 and 3 with the Standard Expression in the first set of simulations.

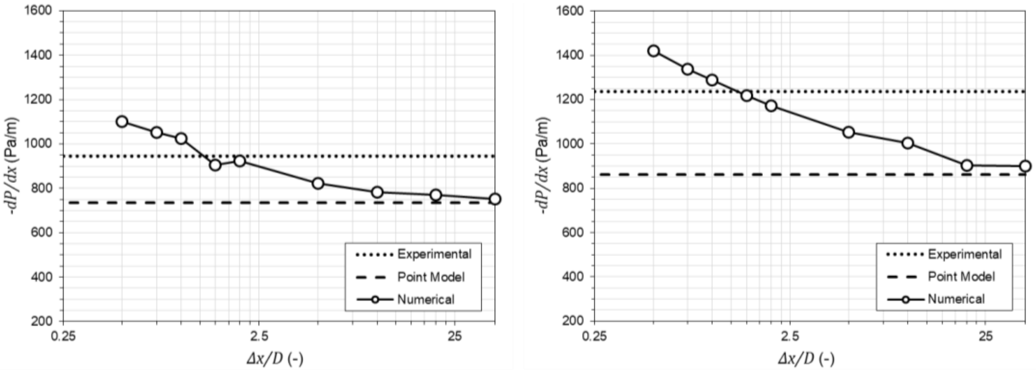

(a) Case 2. (b) Case 3.

Figure 5.17 – Pressure gradient numerical results for Cases 2 and 3 with the Standard Expression in the first set of simulations.

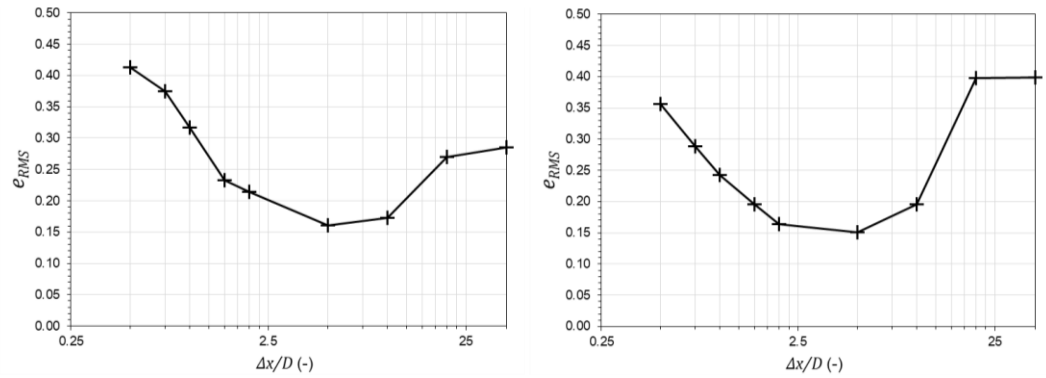

(a) Case 2. (b) Case 3.

Figure 5.18 – Values of the root-mean-squared error of Eq. (5.1) for Cases 2 and 3 with the Standard Expression in the first set of simulations.

Such loss of hyperbolicity of Cases 2 and 3 is more clearly seen in Figure 5.19, where the experimental and numerical liquid holdup histograms (aspect ratios of 40, 20, 10, 5, 2, 1.5, 1, 0.75 and 0.5) at 38.15m are depicted. In Figure 5.19(a), it is remarkable how, for the aspect ratio of 20, interfacial instabilities already appear. The amplitudes of such spurious waves grow indefinitely, forming slugs for $\Delta x/D \leq 1.5$, making the histogram format never become steady. The same is observed, with less intensity, in Figure 5.19(b) for Case 3. Besides being inconsistent to compare the numerical histogram with the experimental ones in such strongly ill-posed simulations, one cannot avoid noticing how the former are different from the latter.

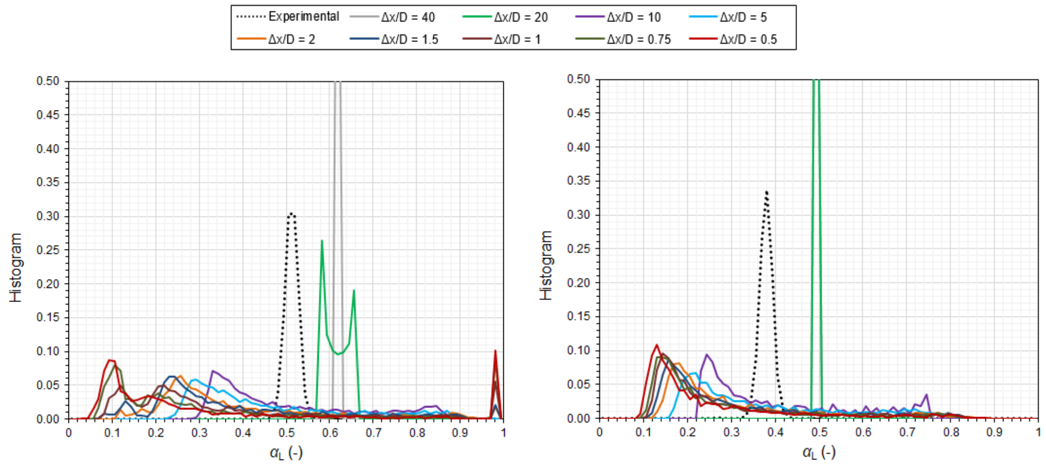

(a) Case 2. (b) Case 3.

Figure 5.19 – Liquid holdup histograms for Cases 2 and 3 with the Standard Expression in the first set of simulations.

For correctly simulating Cases 2 and 3 and for comparing the efficiency of the newly developed expressions for the interfacial friction factor against the Standard Expression on such stratified flows, it is of utmost importance to make the simulations well-posed and mesh convergent. Due to the strong ill-posedness of Cases 2 and 3 with the Standard Expression (observed in Figures 5.16-5.19), it is very improbable that the increase in f_i due to using either Proposed Expression 1 or 2 would control the growth of the spurious interfacial instabilities enough for making the simulations mesh convergent. Besides, as aforementioned, although an augment of the interfacial shear stress makes more difficult the appearance and growth of interfacial waves, as seen in Figures 5.8, 5.11 and 5.14 and in literature (Fullmer *et al.*, 2014; Pasqualette *et al.*, 2017), it does not affect the well-posedness (hyperbolicity) analysis (Liao *et al.*, 2008). Therefore, there is no point in repeating Case 2 and 3 simulations of this first set for Proposed Expressions 1 and 2. Therefore, for trying to obtain the desired hyperbolicity for such cases, one should consider in the 1D Two-Fluid Model of the Regime Capturing Methodology the terms initially neglected in the first set of simulations (Table 5.1). This work starts by taking into account the dynamic pressure terms in the second set of simulations.

5.4. Analysis of the Dynamic Pressure Term (Second Set of Simulations)

As seen in Table 5.1, in the second set of simulations, the dynamic pressure term ($\Delta P_{\mathcal{D},K}$) is considered in momentum conservation equations, Eqs. (3.60) and (3.61), of the 1D Two-Fluid Model, while both the axial diffusion (μ_K^{eff}) and the dynamic interfacial shear stress ($\mathcal{J}_i$) remain null. As aforementioned, the primary purpose of considering the dynamic pressure is to make the simulations of Cases 2 and 3 mesh-convergent and well-posed in order to compare the efficiency of the Standard Expression and the Proposed Expressions 1 and 2. Nevertheless, the results for Case 1 for this three interfacial friction factor expression should also be presented, since one might obtain improvements for Cases 2 and 3 (stratified wavy), but, at the same time, worsen the results for Case 1 (slugs).

5.4.1. Case 1 ($\Delta P_{\mathcal{D},K} \neq 0$)

Following the same presentation order of the first set of simulations, the mean liquid holdup (at 38.15m) and pressure gradient results for Case 1 with the Standard Expression for f_i are shown in Figure 5.20 as a function of the mesh aspect ratios, together with the measured values of Table 5.3. In Figure 5.21, the e_{RMS} values relative to those variables are plotted.

In Figure 5.20, the same behavior, previously observed for the mean α_L and pressure gradient numerical values regarding the mesh refinement, is verified: the former starts decreasing for a certain aspect ratio, in which the latter begins to augments. As seen before, this is a consequence of the appearance of interfacial instabilities that start to be captured, for Case 1, with the Standard Expression with $\Delta P_{\mathcal{D},K} \neq 0$, for $\Delta x/D = 2$, as the mesh is refined.

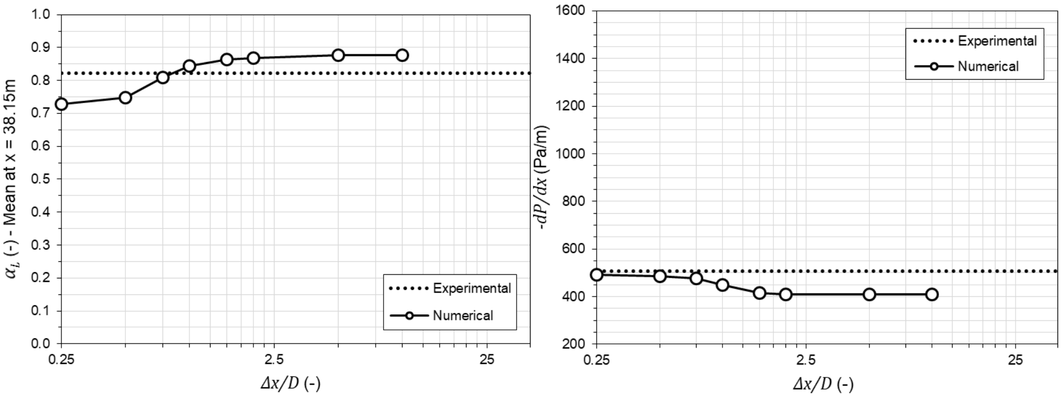

(a) Mean liquid holdup (b) Pressure gradient

Figure 5.20 – Grid test for Case 1 with the Standard Expression in the second set of simulations.

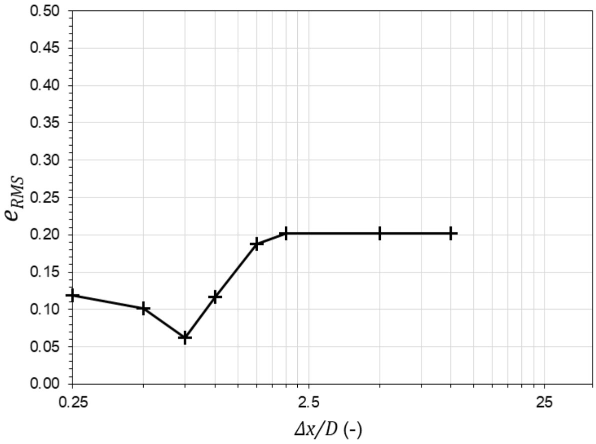

Figure 5.21 – Values of the root-mean-squared error of Eq. (5.1) for Case 1 with the Standard Expression in the second set of simulations.

This is also observed in Figure 5.22, where the numerical liquid holdup histograms of the present simulations for several aspect ratios (10, 5, 2, 1.5, 1, 0.75, 0.5 and 0.25) and the correspondent experimental data are plotted. The results in Figures 5.20 and 5.21 resemble in several aspects the predictions of Case 1 with the Proposed Expression 2 (Figures 5.12 and 5.13), , in the first set of simulations, including their almost non-convergence with the mesh. The reason for this behavior, is that both augmenting the interfacial shear stress and adding a pressure dynamic term suppress the growth rate of interfacial instabilities (Fullmer *et al.*, 2014). By examining Figure 5.22, the presence of slugs can be seen in the histograms for aspect ratios smaller than they were for Figure 5.8 (Case 1, with the Standard Expression, in the first set of simulations, $\Delta P_{\mathcal{D},K} = 0$).

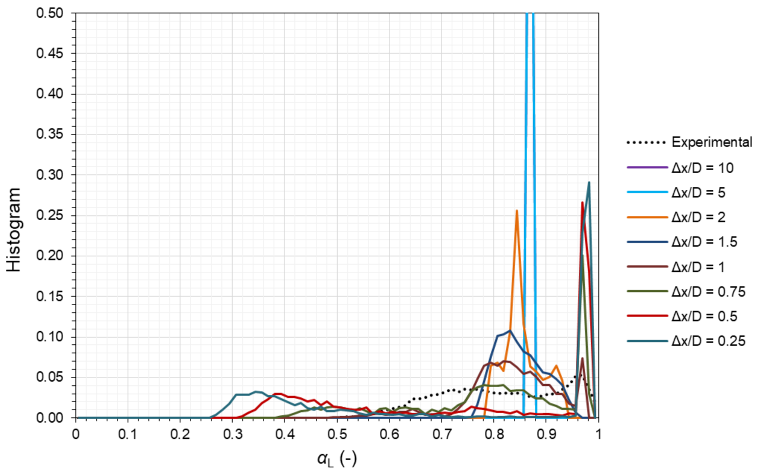

Figure 5.22 – Liquid holdup histograms for Case 1 with the Standard Expression in the second set of simulations.

The same numerical parameters (liquid holdup, pressure gradient and error) for Case 1, plotted in Figures 5.20 and 5.21, as a function of the mesh aspect ratios, are depicted in Figures 5.23 and 5.24 with the Proposed Expression 1 in the second set of simulations ($\Delta P_{\mathcal{D},K} \neq 0$).

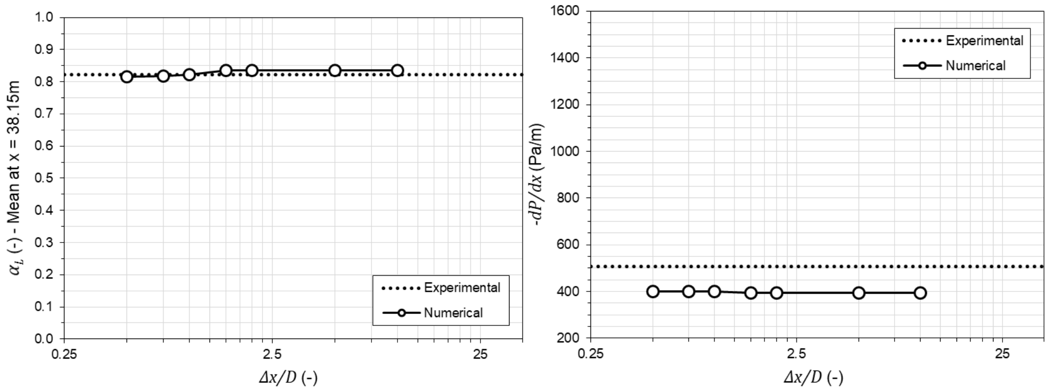

(a) Mean liquid holdup (b) pressure gradient

Figure 5.23 – Grid test for Case 1 with the Proposed Expression 1 in the second set of simulations.

It is promptly noticed in Figures 5.23 and 5.24 that the Case 1 results for the Proposed Expression 1 barely change with the $\Delta x/D$ values, the range of which varies from 0.5 to 10. This might indicate that no significant interfacial instability was captured by the simulations, which is confirmed by the liquid holdup histograms of these simulations, for each aspect ratio, in Figure 5.25.

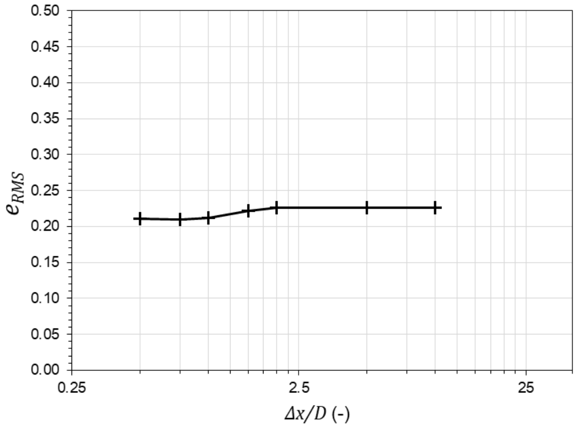

Figure 5.24 – Values of the root-mean-squared error of Eq. (5.1) for Case 1 with the Proposed Expression 1 in the second set of simulations.

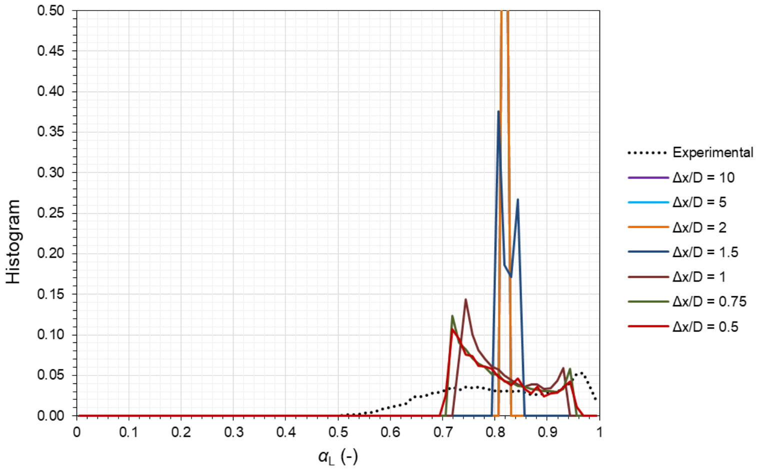

Figure 5.25 – Liquid holdup histograms for Case 1 with the Proposed Expression 1 in the second set of simulations.

By looking at the histograms regarding the aspect ratios 0.75 and 0.5 (Figure 5.25) it can be seen that a mesh convergence was obtained. Nevertheless, the instabilities are small and do not grow enough for developing into slugs. This suppression of the interfacial waves is a product of the combined effects of the dynamic pressure term and of the greater f_i values of the Proposed Expression 1, when compared to the Standard Expression. Therefore, although slugs were obtained for the Proposed Expression 1 in the Case 1 results of first set of simulations (Figures 5.9-5.11), the addition of the dynamic pressure term was excessive. One could argue that, if the mesh was refined even more, in Figures 5.23-

5.25, large-amplitude waves and possibly slugs could have been represented by the Regime Capturing Methodology. However, such meshes would have to possess a very small aspect ratio, which would increase computational costs significantly. Besides, as aforementioned, a mesh-convergence was obtained for a liquid holdup histogram shape that does not indicate the existence of any slugs (Figure 5.25).

Moving on to Proposed Expression 2, such correlation for the interfacial friction factor was used in the Case 1 simulations that led to the liquid holdup, pressure gradient and e_{RMS} numerical values plotted, respectively, in Figures 5.26 and 5.27, as a function of $\Delta x/D$ and together with the measurements.

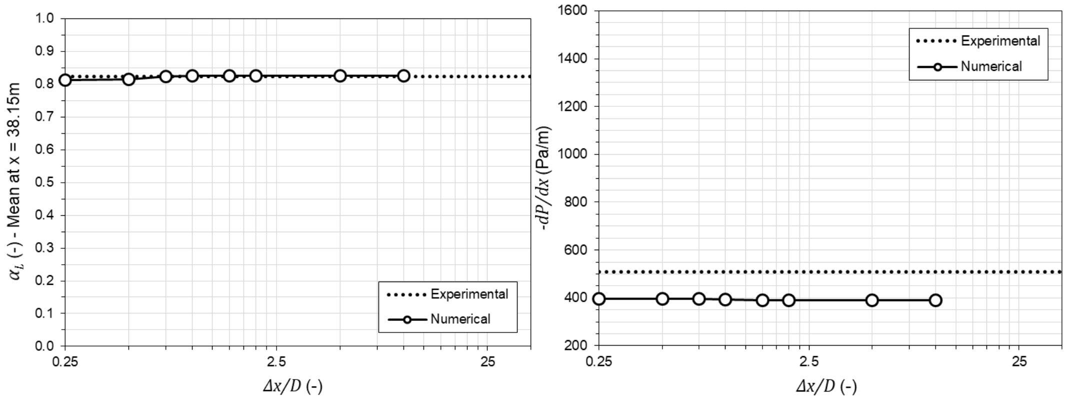

Figure 5.26 – Grid test for Case 1 with the Proposed Expression 2 in the second set of simulations.

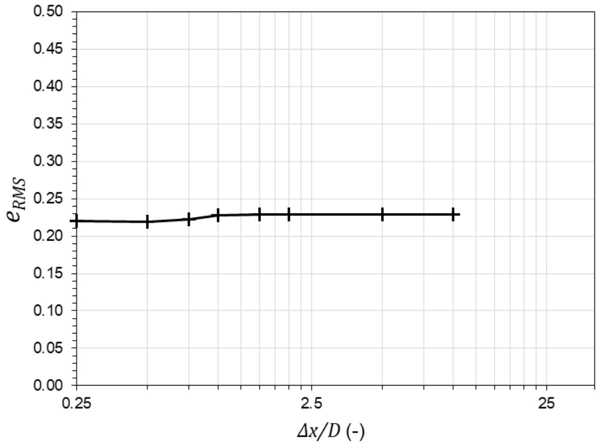

Figure 5.27 – Values of the root-mean-squared error of Eq. (5.1) for Case 1 with the Proposed Expression 2 in the second set of simulations.

Similarly to what has been verified for Proposed Expression 1 in Figures 5.23 and 5.24, the joint stabilizing effects of the dynamic pressure term and of the high f_i/f_{i0} values from Proposed Expression 2, have rendered the results for these simulations almost not sensitive to the mesh refinement (see Figures 5.26 and 5.27). The clear lack of large-amplitude waves observed in the numerical liquid holdup histograms plotted in Figure 5.28 (resembles significantly Figure 5.25) proves the previous statement.

From the Case 1 results presented for the second set of simulations with the Standard Expression and with the Proposed Expressions 1 and 2, it can be concluded that the dynamic pressure term used stabilizes excessively the flow. This either suppresses completely the appearance of slugs or creates the need of using meshes so refined that would make the Regime Capturing Methodology simulations unfeasible computationally. The physical background of the dynamic pressure term was described in a previous chapter of this work, therefore, rather than revealing an inconsistency in considering a dynamic pressure, the present observation asserts the inadequacy of the Bestion (1990) formulation for such parameter. As already described, the Bestion (1990) expression for $\Delta P_{\mathcal{D},K}$, $K \in \{G, L\}$, was made for hyperbolizing a 1D Two-Fluid Model different from the one used in this work. Eqs. (3.58)-(3.61) aim, especially, to make well-posed simulations for vertical pipes, in which hydrostatic term $\Delta P_{\mathcal{H},K}$ (with its stabilizing effect) is not present. As a consequence, it is not exactly a surprise that the Bestion (1990) dynamic pressure might suppress the growth rates instabilities for certain horizontal flows, particularly, when a greater (than usual) interfacial shear stress is present and for a flow which is already well-posed and mesh-convergent even when $\Delta P_{\mathcal{H},K}$ is neglected. Therefore, independently from the effects of the dynamic pressure on Case 2 and 3 simulations, the Bestion (1990) formulation is unfit for Case 1 simulations for harming the satisfactory results obtained for this case in the first set of simulations.

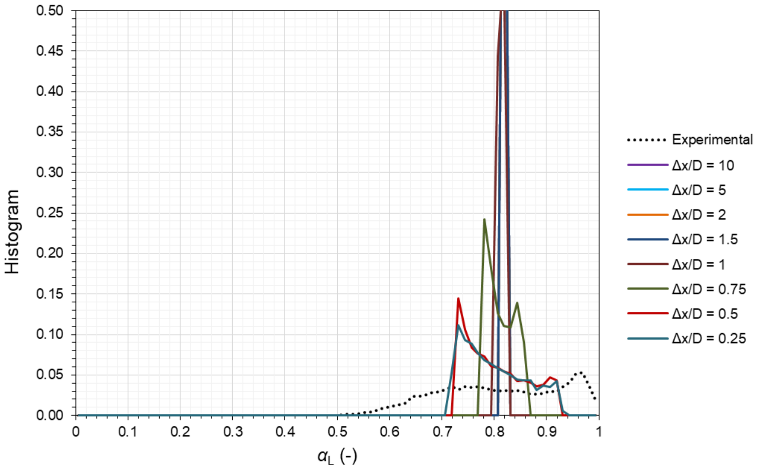

Figure 5.28 – Liquid holdup histograms for Case 1 with the Proposed Expression 2 in the second set of simulations.

5.4.2. Cases 2 and 3: ($\mathit{\Delta P}_{\mathcal{D},K} \neq 0$)

The results of Cases 2 and 3, in this second set of simulations, are presented, starting by the ones obtained with the Standard Expression for the interfacial friction factor. Figures 5.29-5.31 depict the behavior, with the mesh aspect ratios, respectively, of the numerical liquid holdup, pressure gradient and e_{RMS} values, for Cases 2 and 3 with such correlation for f_i. In the referred figures, together with the experimental data, the predictions of the Point Model of Eq. (4.4) (Table 5.4) are also illustrated.

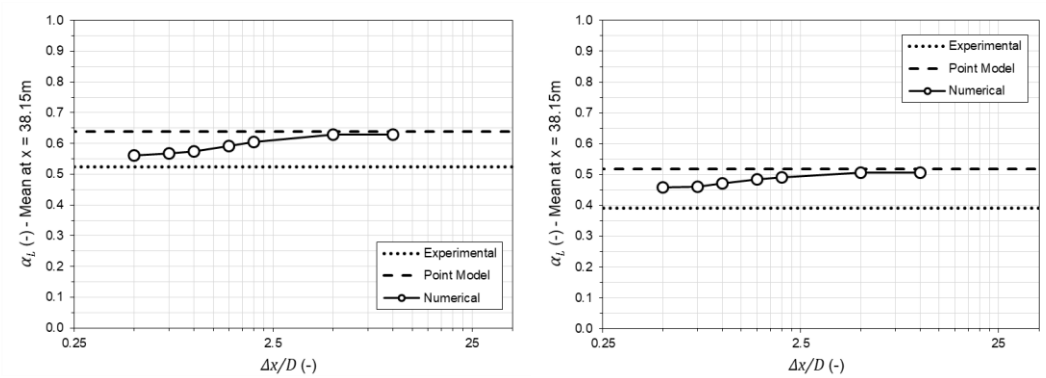

(a) Case 2. (b) Case 3.

Figure 5.29 – Mean liquid holdup numerical results for Cases 2 and 3 with the Standard Expression in the second set of simulations.

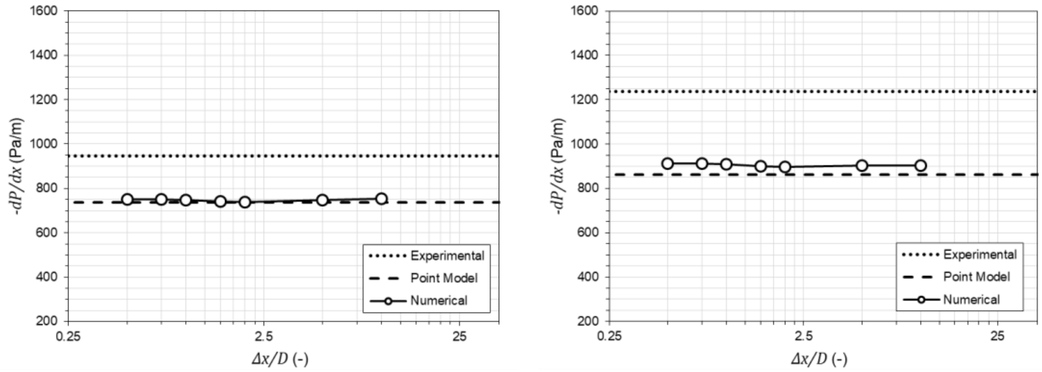

(a) Case 2. (b) Case 3.

Figure 5.30 – Pressure gradient numerical results for Cases 2 and 3 with the Standard Expression in the second set of simulations.

Neither in Figure 5.29, for the liquid holdup, nor in Figure 5.30, for the pressure gradient, significant variations on the integral parameters were observed, in contrast to the results presented in Figures 5.16 and 5.17 also for Cases 2 and 3 with the Standard Expression, with $\mathit{\Delta P}_{\mathcal{D},K} = 0$. On the contrary: the decrease in α_L and the increase in the pressure gradient, Figures 5.29 and 5.30, with the refinement of the mesh take place smoothly. For the smaller aspect ratios of 0.75 and 0.50, these integral parameters barely change, which indicates that the mesh converged and that the simulation setup is well-posed.

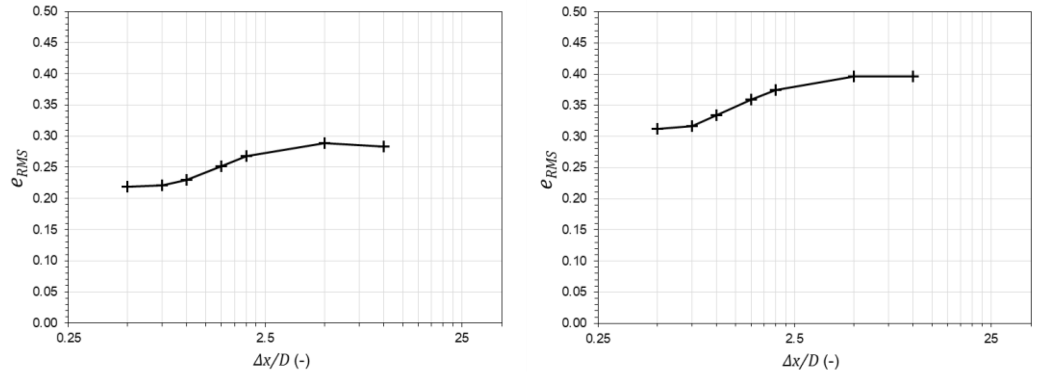

(a) Case 2. (b) Case 3.

Figure 5.31 – Values of the root-mean-squared error of Eq. (5.1) for Cases 2 and 3 with the Standard Expression in the second set of simulations.

The consistency between the Point Model and the Regime Capturing Methodology is obtained in the referred results, since the predicted integral parameters for the different approaches coincide for high values of $\Delta x/D$. It is interesting to observe that the e_{RMS} values, in Figure 5.31, decrease (improve) as the mesh becomes finer, until it almost stabilizes for the aspect ratios 0.75 and 0.5. The reason for such behavior of the results with $\Delta x/D$ is the same that was explored before, especially in Figure 5.7, and it is verified again in Figure 5.32, in which the numerical and experimental liquid holdup time traces for Case 2 are plotted for a 30s interval, at 38.15m, for three different mesh aspect ratios: 10, 1.5 and 0.5.

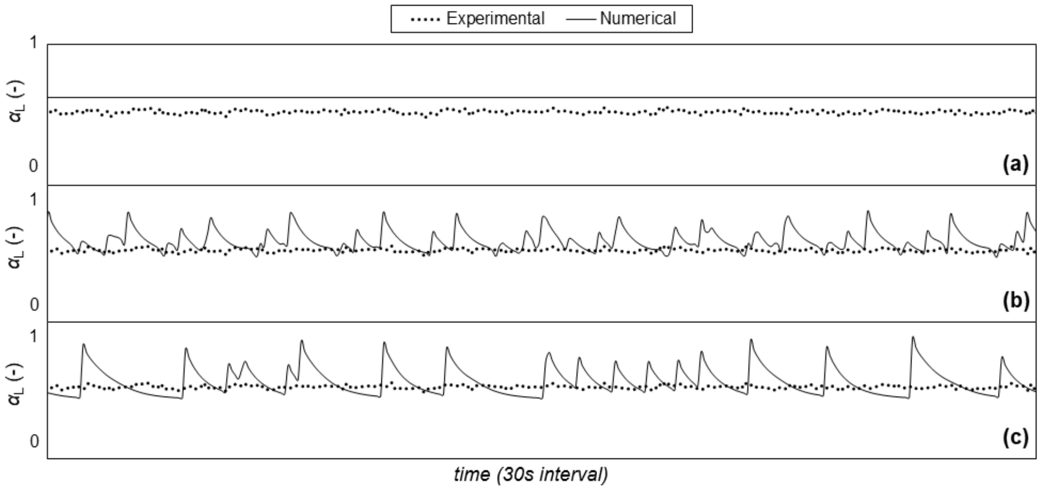

Figure 5.32 – Case 2 numerical liquid holdup profiles (at 38.15m) for the Standard Expression in the second set of simulations and for: (a) aspect ratio of 10; (b) aspect ratio of 1.5; and (c) aspect ratio of 0.5.

Similarly to the previous analysis for slug flow in Figure 5.7, Figure 5.32

illustrates for the stratified wavy Case 2 that, as the mesh is refined, more interfacial instabilities are captured by the solution of the 1D Two-Fluid Model. It begins with a completely flat transient profile, in Figure 5.32(a), reason why the corresponding predictions are equivalent to the ones of the Point Model. Then, irregular interfacial waves appear for $\Delta x/D = 1.5$, Figure 5.32(b), which increase in regularity and amplitude in Figure 5.32(c), for $\Delta x/D = 0.5$. Therefore, according to the e_{RMS} values, the capturing of waves for mesh-convergent simulations leads to improved predictions in comparison to the Point Model. This remark is consistent with the fact that the Regime Capturing Methodology has potentially more predictability than the Point Model.

More detailed information on the Case 2 (Standard Expression with $\Delta P_{\mathcal{D},K} \neq 0$) regarding the numerical liquid holdup profiles can be extracted from their respective histograms, depicted in Figure 5.33 for several mesh aspect ratios and with the gamma densitometer signal histogram. Once again, it can be seen in the referred figure that the mesh refinement causes the appearance of interfacial waves and that for the aspect ratios of 0.75 and 0.5 a mesh-convergence was obtained. It is remarkable how different such histograms are from the ones of the simulations without the dynamic pressure term, Figure 5.19, demonstrating the efficiency of the Bestion (1990) expression in controlling the instabilities growth rate for Cases 2 and 3. Nevertheless, the numerical mesh-convergent liquid holdup time traces are qualitatively different from the experimental ones, which can be seen both in the transient profile of Figure 5.32(c), for Case 2, and on the histograms of Figure 5.33.

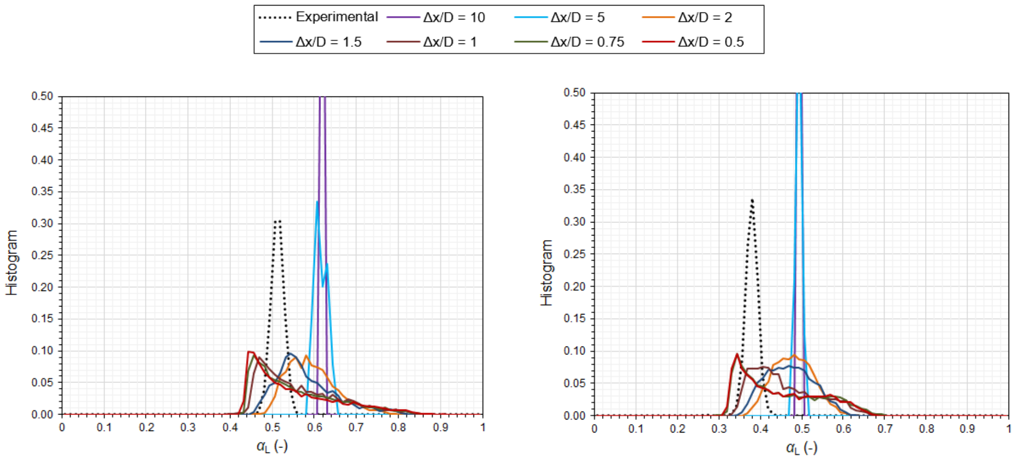

(a) Case 2.

(b) Case 3.

Figure 5.33 – Liquid holdup histograms for Cases 2 and 3 with the Standard Expression in the second set of simulations.

It should be highlighted that small-amplitude instabilities, for Cases 2 and 3, do have to be obtained by the Regime Captured Methodology when the Standard Expression is used, as a consequence of the lack of modelling of such instabilities in the interfacial friction factor, which happens solely for the Proposed Expressions 1 and 2.

Aiming to improve the qualitative interfacial dynamics of the numerical results, so that they are closer to the measurements and to reduce the e_{RMS} values, the Proposed Expression 1 is firstly used in Cases 2 and 3. The respective mean liquid holdup, pressure gradient and e_{RMS} values for these simulations from the second set (with $\Delta P_{\mathcal{D},K} \neq 0$) are plotted in Figures 5.34-5.36, together with the experimental data and the Point Model predictions (Table 5.4).

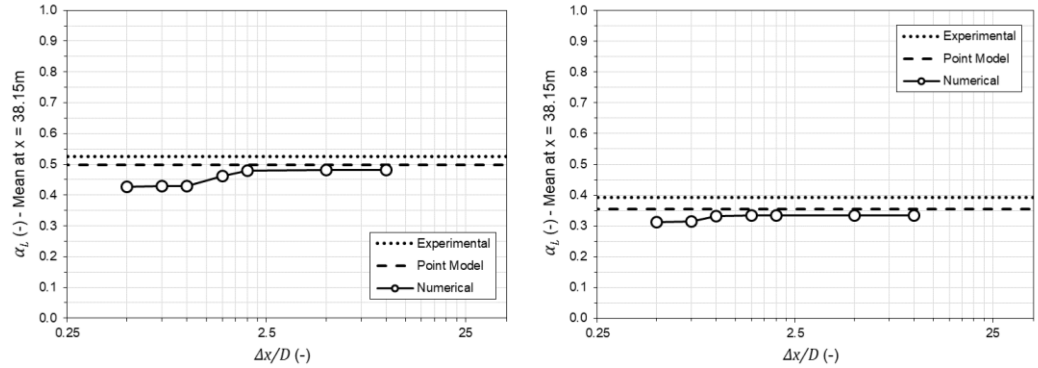

(a) Case 2. (b) Case 3.

Figure 5.34 – Mean liquid holdup numerical results for Cases 2 and 3 with the Proposed Expression 1 in the second set of simulations.

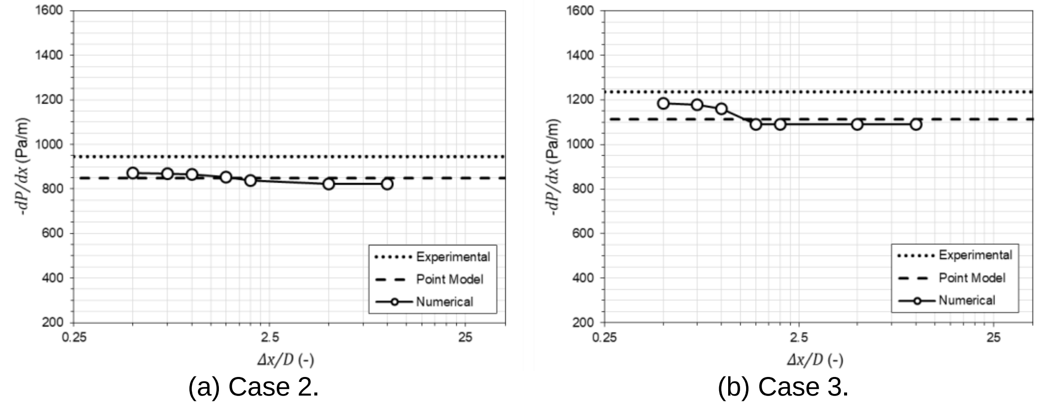

(a) Case 2. (b) Case 3.

Figure 5.35 – Pressure gradient numerical results for Cases 2 and 3 with the Proposed Expression 1 in the second set of simulations.

Primarily, in Figures 5.34 and 5.35, it can be seen that the Regime Capturing Methodology results for very high aspect ratios and the Proposed Expression 1 results of the Point Model coincide, which is valid and consistent. The same behavior previously observed is once again verified for the liquid holdup, Figure 5.34, and for the pressure gradient, Figure 5.35: the former decreases with the $\Delta x/D$ values and the latter increases. For both Cases 2 and 3, the results of Figures 5.34-5.36, show that a mesh convergence of the results was obtained for the mesh aspect ratios equal to or lower than 0.75, which indicates the ability of the dynamic pressure of Bestion (1990) for making such stratified wavy flow simulations well-posed. This is more clearly seen in Figure 5.37, where the numerical and experimental liquid holdup histograms of the Case 2 and 3 simulations of the second set of the Proposed Expression 1 are plotted. The formats of the α_L histograms related to the aspect ratios of 0.75 and 0.5 are practically equal, which enhances the mesh convergence of the predictions. Furthermore, it illustrates the appearance of interfacial intermittencies with the mesh refinement and that the Proposed Expression 1 did not manage to improve the consonance between the converged numerical histograms and the one from the measurements.

Lastly, the behavior of the e_{RMS} values, in Figure 5.36, draws attention for being opposed to the one of Figure 5.31. In other words, when the Proposed Expression 1 is used in Cases 2 and 3, the e_{RMS} tends to increase with the lowering of the $\Delta x/D$, while, for the Standard Expression, it decreased. This shows that the relation between the Point Model predictions and the ones of the Regime Capturing Methodology (when fine meshes are used) is not so straightforward, that is, not necessarily the numerical integral parameters of the latter are better than the former.

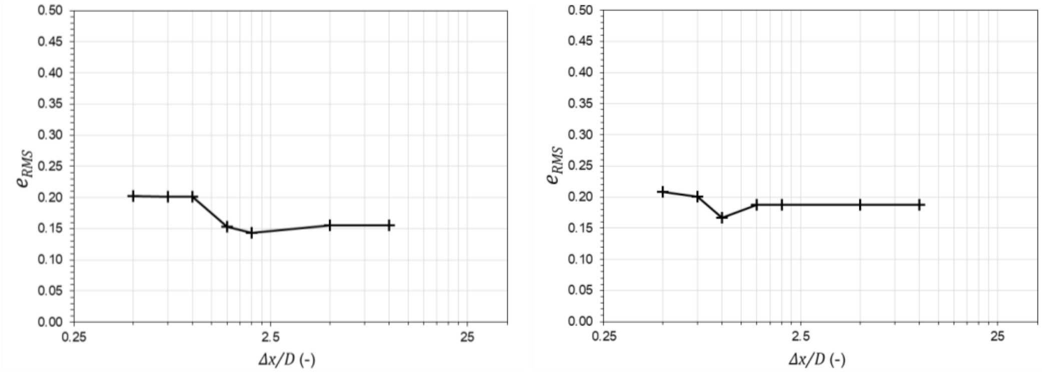

(a) Case 2. (b) Case 3.

Figure 5.36 – Values of the root-mean-squared error of Eq. (5.1) for Cases 2 and 3 with the Proposed Expression 1 in the second set of simulations.

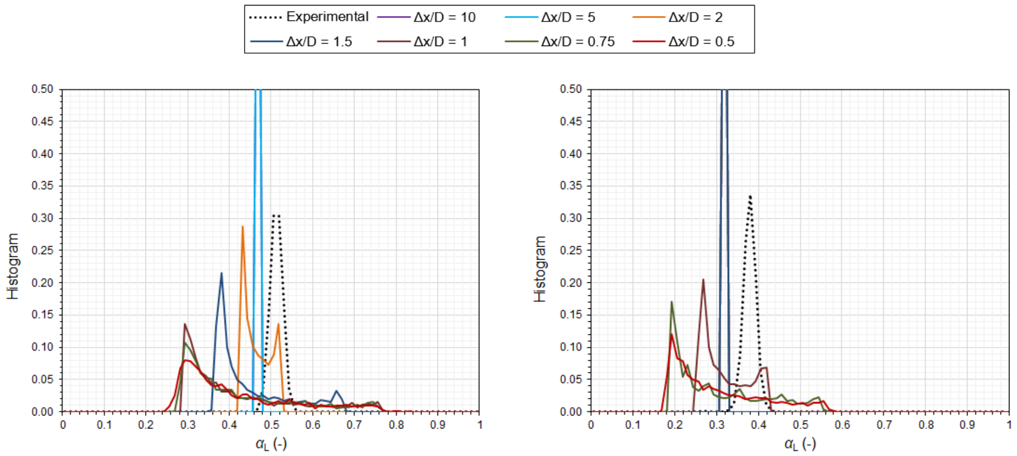

(a) Case 2. (b) Case 3.

Figure 5.37 – Liquid holdup histograms for Cases 2 and 3 with the Proposed Expression 1 in the second set of simulations.

As previously stated, Proposed Expression 2 was also employed in the Cases 2 and 3 simulations of this second set aiming an improvement in the results obtained in relation to the Standard Expression. Figures 5.38-5.40 depict the behavior of liquid holdup, pressure gradient and e_{RMS} values for such simulations, with the mesh refinement, together with the measurements and the Point Model predictions (Table 5.4).

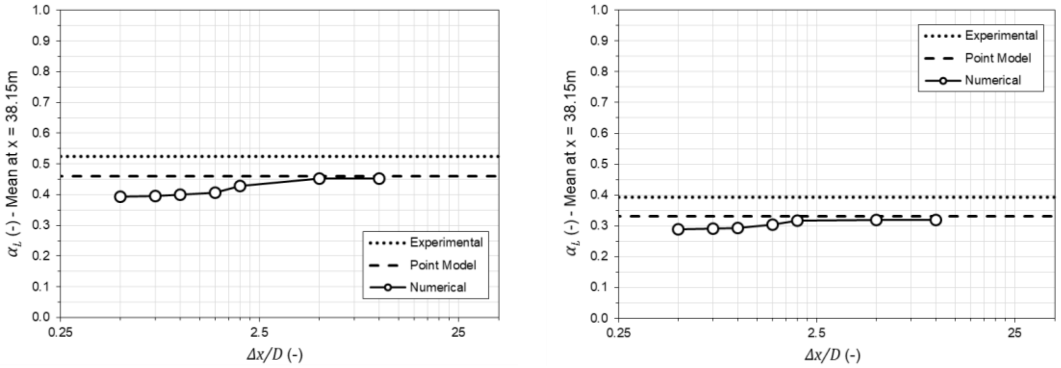

(a) Case 2. (b) Case 3.

Figure 5.38 – Mean liquid holdup numerical results for Cases 2 and 3 with the Proposed Expression 2 in the second set of simulations.

Most of the observations made for the results of Cases 2 and 3 employing Proposed Expression 1, shown in Figures 5.34-5.36, can be verified in Figures 5.38-5.40, corresponding to the use of the Proposed Expression 2. Among them, are the consistency between the Point Model and the Regime Capturing Methodology, the "classical" integral parameters behavior with the mesh refinement and the augment of the e_{RMS} values with the decrease in $\Delta x/D$.

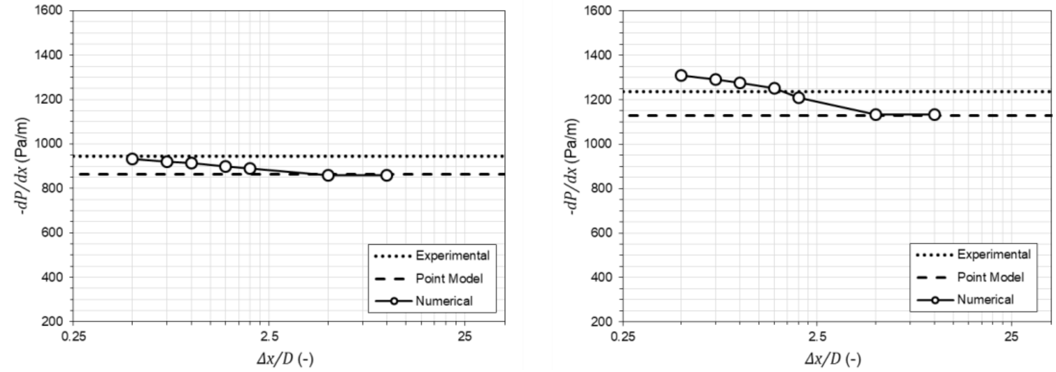

(a) Case 2. (b) Case 3.

Figure 5.39 – Pressure gradient numerical results for Cases 2 and 3 with the Proposed Expression 2 in the second set of simulations.

A particular feature of the Proposed Expression 2 results is that a complete mesh convergence was not obtained, since the pressure gradient still has a non-null derivative in relation to the mesh aspect ratio for $\Delta x/D = 0.5$ in Figure 5.39. Nevertheless, combining the stabilization of the liquid holdup results for the lower mesh aspect ratios in Figure 5.38 and the fact that the pressure gradient values are clearly on the verge of stabilizing, in Figure 5.39, it is safe to state that a mesh convergence was obtained for these simulations with the use of the dynamic pressure term.

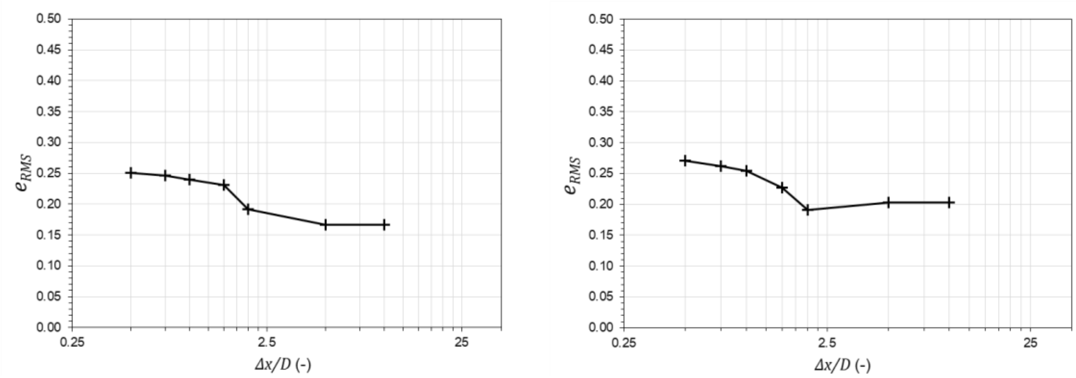

(a) Case 2. (b) Case 3.

Figure 5.40 – Values of the root-mean-squared error of Eq. (5.1) for Cases 2 and 3 with the Proposed Expression 2 in the second set of simulations.

Figure 5.41 shows the numerical liquid holdup histograms for the same Cases 2 and 3 simulations with the Proposed Expression 2, together with the respective experimental ones. As in Figure 5.37, the mesh convergence for the lowest $\Delta x/D$ value can be observed in Figure 5.41, besides the persistent difference between the numerically converged liquid holdup histograms and the ones obtained by the gamma densitometer.

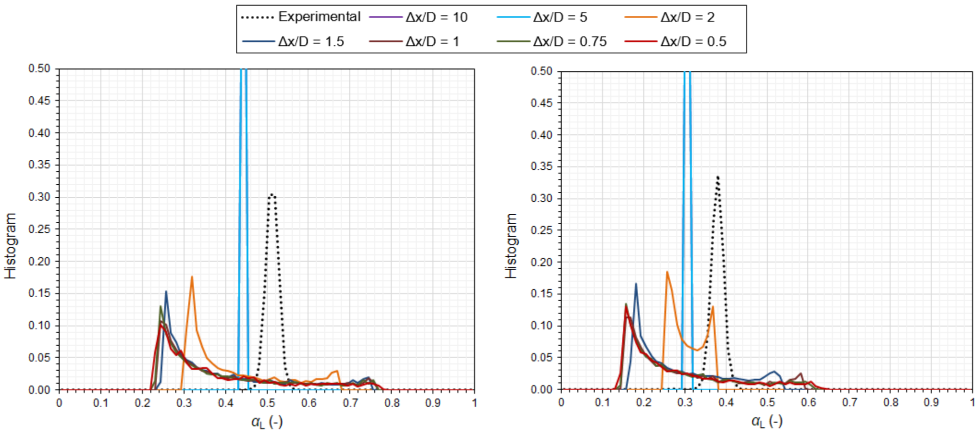

(a) Case 2. (b) Case 2.

Figure 5.41 – Liquid holdup histograms for Cases 2 and 3 with the Proposed Expression 2 in the second set of simulations.

After obtaining mesh convergence for the Cases 2 and 3 employing the three interfacial friction factor correlations (Standard Expression and Proposed Expressions 1 and 2) with the dynamic pressure term, it is possible to compare their respective results. First, for a qualitative evaluation of interfacial dynamics related to each expression for f_i, Figures 5.42 and 5.43 show for, respectively, Cases 2 and 3, the numerical and experimental transient liquid holdup profiles at 38.15m and in a 30s time interval for the aforementioned expressions and for a value of 0.5 for $\Delta x/D$.

It is primarily noticed in Figures 5.42 and 5.43 the major difference in the interfacial behavior between each expression for the interfacial friction factor. For both Cases 2 and 3, it is observed that the frequency of instabilities appears to be lower for the Standard Expression results. Furthermore, it increases for the Proposed Expression 1 and that it has its greater value for the proposed Expression 2. Concerning the amplitude of such instabilities, it seems, especially for Case 3 (Figure 5.43), that this variable is slightly higher for the Proposed Expression 2 when compared to both Standard Expression and Proposed Expression 1. These differences are related to the qualitative differences in the form of the expressions for interfacial friction factor, which, unsurprisingly, lead to distinct behaviors of the growth rate of instabilities with their scale (Fullmer *et al.*, 2014).

When comparing the transient liquid holdup profiles in Figures 5.42 and 5.43 with the measured signals from the gamma densitometer for the stratified wavy flows (with small-amplitude waves) of Cases 2 and 3, several facts stand out. The first is that, for both Cases, employing the Standard Expression leads to unphysical large-amplitude interfacial waves, since the experimental α_L profile solely shows small-amplitude waves. Another fact is that such large-amplitude waves are still present even when the Proposed Expression 1 and 2 are used. This is inconsistent, because, as previously explained, the interface should have presented a fully stabilized (flat) numerical behavior since the effects of the only type of waves, the small-amplitude ones, are already implicit in the newly created correlations for the interfacial friction factor. Therefore, although the dynamic pressure term of Bestion (1990) managed to produce a well-posed solution (mesh convergent results) for Cases 2 and 3, a correct qualitative prediction of the interfacial dynamic of such stratified wavy (small-amplitude) flows is still a challenge for the Regime Capturing Methodology.

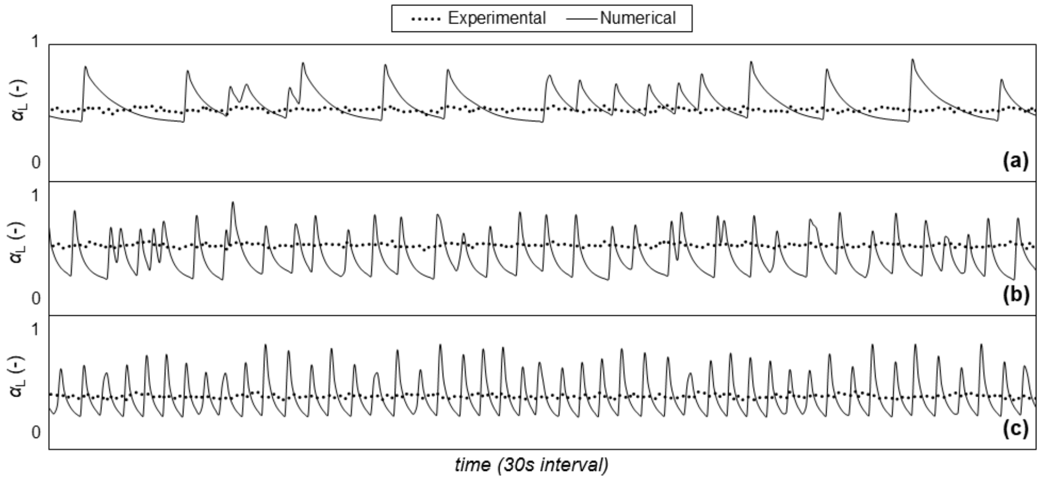

Figure 5.42 – Case 2 numerical liquid holdup profiles for aspect ratio of 0.5 in the second set of simulations and for: (a) Standard Expression; (b) Proposed Expression 1; and (c) Proposed Expression 2.

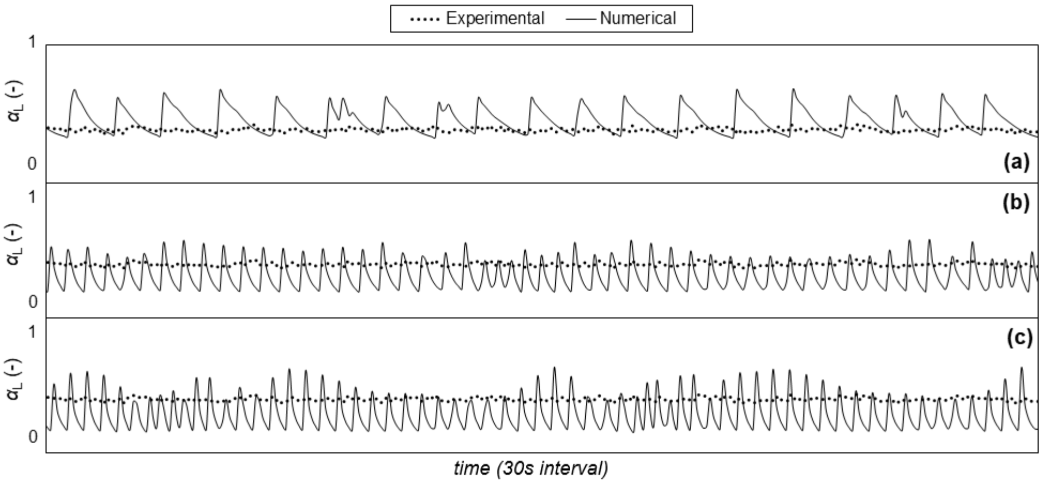

Figure 5.43 – Case 3 numerical liquid holdup profiles for aspect ratio of 0.5 in the second set of simulations and for: (a) Standard Expression; (b) Proposed Expression 1; and (c) Proposed Expression 2.

After the former qualitative comparison between the Cases 2 and 3 transient α_L profile for each expression for the interfacial friction factor, it is of paramount importance comparing in a clear quantitative manner the resulting integral parameters of the simulations. With this purpose, Tables 5.7 and 5.8 outline for, respectively, Cases 2 and 3, the α_L and dP/dx results for the converged ($\Delta x/D = 0.5$) simulations of this second set and their respective relative errors (in relation to the experiments) and e_{RMS} values.

In Table 5.7 (Case 2), it can be seen that, for the Standard Expression, a good relative error was obtained for the liquid holdup, while a significant one was observed for the pressure gradient. When using the Proposed Expression 1 or 2, the latter error improves considerably, which is compensated by the worsening of the relative errors of the liquid holdup. This provides similar e_{RMS} values for the three interfacial friction factor expressions. Nevertheless, it can be verified that the Proposed Expression 2 slightly increased e_{RMS}, when compared to the Standard Expression, and that Proposed Expression 1 made such value better.

Table 5.7 – Case 2 integral parameter results for the mesh aspect ratio of 0.5 in the second set of simulations.

	α_L (−)	$-dP/dx$ (Pa/m)	Relative Error (α_L)	Relative Error (dP/dx)	e_{RMS}
Standard Expression	0.562	749.8	7.07%	-20.73%	0.22
Proposed Expression 1	0.427	872.7	-18.66%	-7.74%	0.20
Proposed Expression 2	0.394	932.8	-25.00%	-1.39%	0.25

Table 5.8 – Case 3 integral parameter results for the mesh aspect ratio of 0.5 in the second set of simulations.

	α_L (−)	$-dP/dx$ (Pa/m)	Relative Error (α_L)	Relative Error (dP/dx)	e_{RMS}
Standard Expression	0.459	913.4	17.13%	-26.15%	0.31
Proposed Expression 1	0.312	1185.0	-20.35%	-4.20%	0.21
Proposed Expression 2	0.288	1309.7	-26.38%	5.89%	0.27

While the liquid holdup relative errors, in

Table **5.8** (Case 3), of the three f_i expressions are high, employing the Proposed Expressions 1 and 2 managed to improve the pressure gradient relative error of the Standard Expression. Consequently, the resulting e_{RMS} values of Proposed Expressions 1 and 2 are both lower than the one from the Standard Expression. Between the two, Proposed Expression 1 provided a better e_{RMS} value.

A key feature of the currently analyzed results, as previously mentioned, is that those from the Regime Capturing Methodology (converged simulations) are not always better than those of the Point Model. This is not expected, since the predictability of the former is greater than of the latter. To illustrate this more clearly, Table 5.9 lists the e_{RMS} values for Cases 2 and 3 from the Regime Capturing Methodology (converged simulations) and the Point Model.

Table 5.9 – Comparison of the root-mean-squared error of Eq. (5.1) for the Regime Capturing Methodology converged simulations (second set) results and the predictions of the Point Model.

Interfacial friction factor expression	Regime Capturing Methodology ($\Delta x/D = 0.5$) - e_{RMS}		Point Model - e_{RMS}	
	Case 2	Case 3	Case 2	Case 3
Standard Expression	0.22	0.31	0.31	0.44
Proposed Expression 1	0.20	0.21	0.12	0.14
Proposed Expression 2	0.25	0.27	0.15	0.18

In the referred table, it is evident that, while the Standard Expression with the Regime Capturing Methodology provides better e_{RMS} values than the Point Model, the opposite is true for the Proposed Expressions 1 and 2 in both Cases. In the Regime Capturing Methodology, simulations in high resolution meshes are in theory able to capture more interfacial instabilities, which make the pressure gradient increase and the liquid holdup decrease. For both Cases 2 and 3, the three expressions for the interfacial friction factor, applied in the Point Model, result in an underpredicted pressure gradient. Such model should coincide with the Regime Capturing Methodology with very coarse meshes. Therefore, mesh refinement would lead to an increase in pressure gradient and, therefore, decrease its relative error (Figures 5.35 and 5.36). On the other hand, while the Point Model with the

Standard Expression overpredicts the liquid holdup, when the Proposed Expression 1 or 2 are applied in the Point Model, the liquid holdup is underpredicted (Figures 5.34 and 5.38). Therefore, when the mesh is refined, the α_L results for the Standard Expression improve and the ones for the Proposed Expressions 1 and 2 worsen. Therefore, for a refined and converged mesh for Cases 2 and 3 employing the Regime Capturing Methodology lead to e_{RMS} values for the Standard Expression that are better than the ones of the Point Model, while, for the Proposed Expressions 1 and 2, the former values are worse than the latter.

5.4.3. Summary

In this second set of simulations, in which the dynamic pressure term was considered in the 1D Two-Fluid Model (Table 5.1), it was observed that it excessively stabilizes the flow in Case 1, avoiding the formation of slugs. However, it managed to make the Case 2 and 3 simulations mesh convergent and well-posed and made it possible for comparing the Proposed Expressions 1 and 2 with the Standard Expression. By comparing the integral parameters predictions for the converged Cases 2 and 3 simulations, it can be verified in Tables 5.7 and 5.8 that the Proposed Expression 1 provided the best results for both Cases. For this reasons, henceforth, in the third and fourth sets of simulations (Table 5.1), only such correlation for the interfacial friction factor is used in the Regime Capturing Methodology.

However, it was verified that the dynamic pressure term of Bestion (1990) was not capable of controlling the growth rate of interfacial instabilities with the intensity enough for avoiding the existence of large-amplitude waves for Cases 2 and 3 (Figures 5.42 and 5.43). This might be caused by the incapacity of the dynamic pressure term to dissipate the large-scale instabilities, as diffusive terms in the 1D Two-Fluid Model are capable of doing (Fullmer *et al.*, 2014). In other words, according to the linear stability analysis of Fullmer *et al.* (2014), the dynamic pressure leads to smaller (or even null) growth rate of waves or , but never negative. Combining such remarks with the fact that the Bestion (1990) expression is more physically valid for vertical flows (Han & Guo, 2015), it can be understood that it is important to search for alternative solutions to improve the model´s result. One should test alternative ways for acquiring mesh convergence, and at the same time improve the quality of the results, that the dynamic pressure could not. Further, it is important that the alternative modeling does not harm the predictions that were already satisfactory in the first set of simulations. With this in mind, the third set of simulations neglects the dynamic pressure term for testing the axial momentum diffusion term (Table 5.1).

5.5. Analysis of the Axial Momentum Diffusion Term (Third Set of Simulations)

In the third set of simulations, the axial momentum diffusion term is considered in the 1D Two-Fluid Model momentum conservation equations, Eqs. (3.60) and (3.61), while the dynamic pressure and dynamic interfacial shear stress terms are neglected (Table 5.1). As previously said, the main purpose of this topic is to test an improved alternative to the employment of the dynamic pressure for obtaining satisfactory and mesh-convergent results for Cases 1, 2 and 3 with the Regime Capturing Methodology.

The main parameter of the axial diffusion term, Eq. (3.33), is the effective dynamic viscosity μ_K^{eff} of phase K, $K \in \{G, L\}$, which is calculated by Eq. (3.34). The coefficient η_μ of such expression is primarily considered to be equal to 1.0 and the turbulent viscosity μ_K^t is calculated precisely as formulated in Eq. (3.35). As aforementioned, due to the good performance of the Proposed Expression 1 in the second set of simulations, especially for Cases 2 and 3, it is the only correlation for the interfacial friction factor used in the third set of simulations.

5.5.1. Case 1 ($\mu_K^{eff} \neq 0$)

The first numerical integral parameter results shown for the present set of simulations are plotted in Figures 5.44 and 5.45 as a function of the mesh aspect ratio $\Delta x/D$. Such figures illustrate for Case 1 simulations, respectively, the mean liquid holdup (at 38.15m), the pressure gradient and the e_{RMS} values together with the measurements.

Several observations can be made regarding the results present in Figures 5.44 and 5.45, but the most important one is that such results are similar in every aspect to those of Case 1 with the Proposed Expression 1, in the first set of simulations

(Figures 5.9 and 5.10). Therefore, the same remarks valid for the latter are also true for the present results (Figures 5.44 and 5.45).

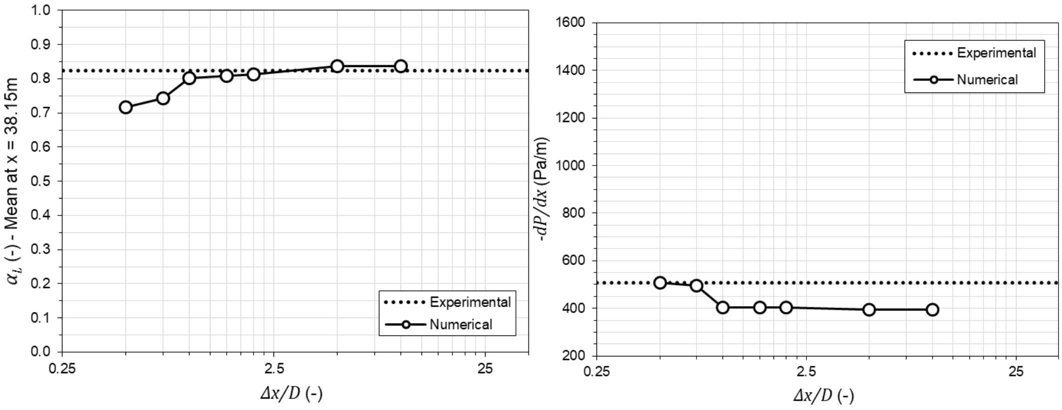

(a) Mean liquid holdup (b) Pressure gradient

Figure 5.44 – Grid test for Case 1 with the Proposed Expression 1 in the third set of simulations ($\boldsymbol{\eta_\mu = 1}$).

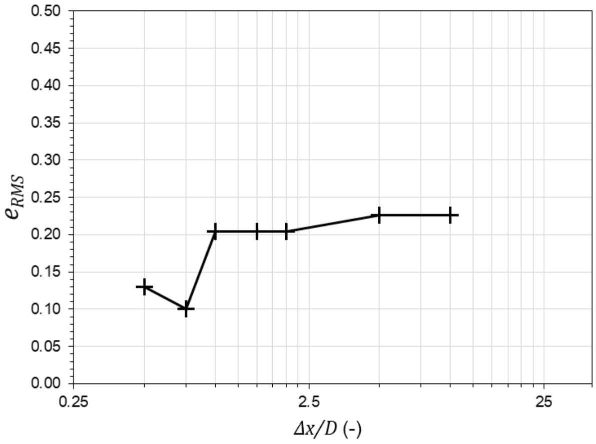

Figure 5.45 – Values of the root-mean-squared error of Eq. (5.1) for Case 1 with the Proposed Expression 1 in the third set of simulations ($\boldsymbol{\eta_\mu = 1}$).

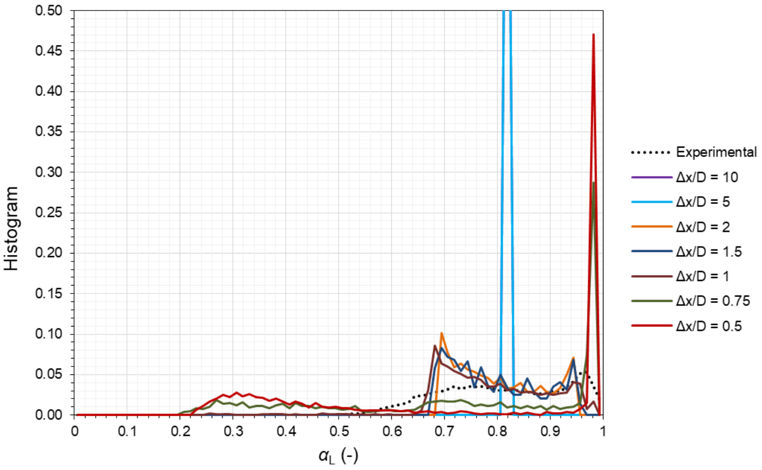

Figure 5.46 – Liquid holdup histograms for Case 1 with the Proposed Expression 1 in the third set of simulations ($\boldsymbol{\eta_\mu = 1}$).

The similarity between numerical α_L histograms of Case 1, in the third set of simulations, plotted in Figure 5.46 for various mesh aspect ratios, and the histograms for the previously referred results from the first set of simulations (Figure 5.11) is also noteworthy. This equivalence between such results might indicate that considering the axial momentum diffusion term has no impact on the slug flow simulated and its integral parameters, at least when modelling μ_K^{eff} as described ($\eta_\mu = 1$).

5.5.2. Cases 2 and 3 ($\mu_K^{eff} \neq 0$)

For extending the analysis for Cases 2 and 3, with the Proposed Expression 1 and for $\eta_\mu = 1$, Figures 5.47-5.49 depict the liquid holdup, pressure gradient and e_{RMS} values as a function of the mesh refinement, the same way as Figures 5.44 and 5.45.

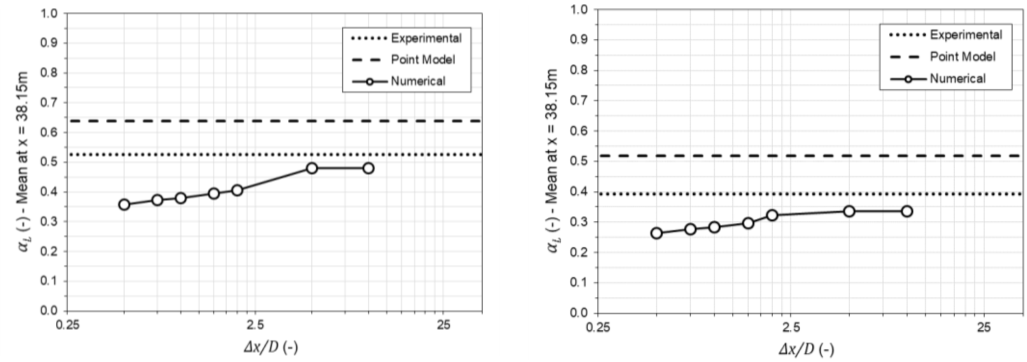

(a) Case 2.

(b) Case 3.

Figure 5.47 – Mean liquid holdup numerical results for Cases 2 and 3 with the Proposed Expression 1 in the third set of simulations ($\boldsymbol{\eta_\mu = 1}$).

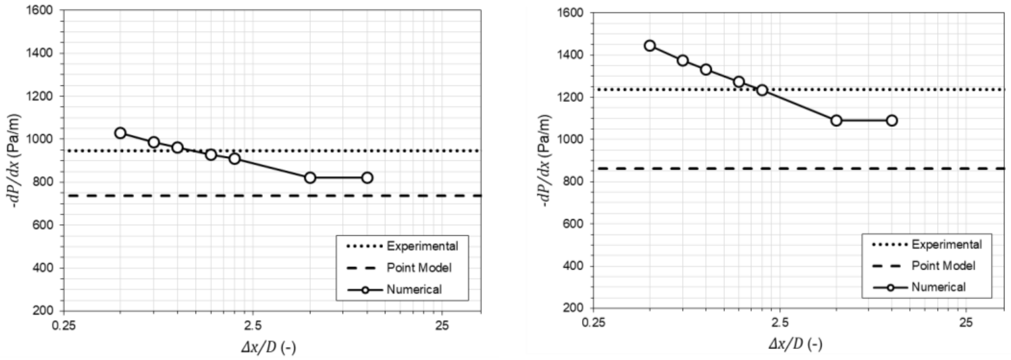

(a) Case 2.

(b) Case 3.

Figure 5.48 – Pressure gradient numerical results for Cases 2 and 3 with the Proposed Expression 1 in the second set of simulations ($\boldsymbol{\eta_\mu = 1}$).

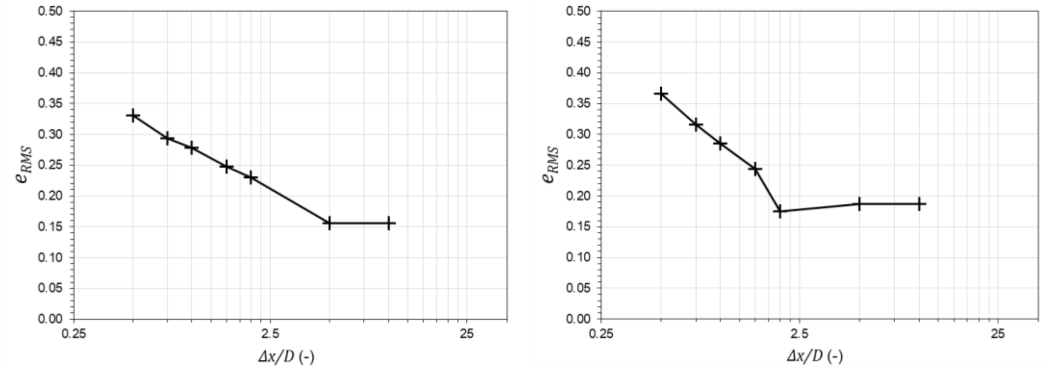

(a) Case 2. (b) Case 3.

Figure 5.49 – Values of the root-mean-squared error of Eq. (5.1) for Cases 2 and 3 with the Proposed Expression 1 in the second set of simulations ($\boldsymbol{\eta_\mu = 1}$).

A clear ill-posedness of the simulations is observed in Figures 5.47-5.49 as a consequence of the lack of stabilization of the α_L and dP/dx values for the refined meshes. As already extensively assessed in this work, this is due to the appearance and uncontrolled growth of interfacial instabilities as the mesh aspect ratio diminishes, which is more clearly observed in the liquid holdup histogram plots of Figure 5.50 for the same simulations of Cases 2 and 3.

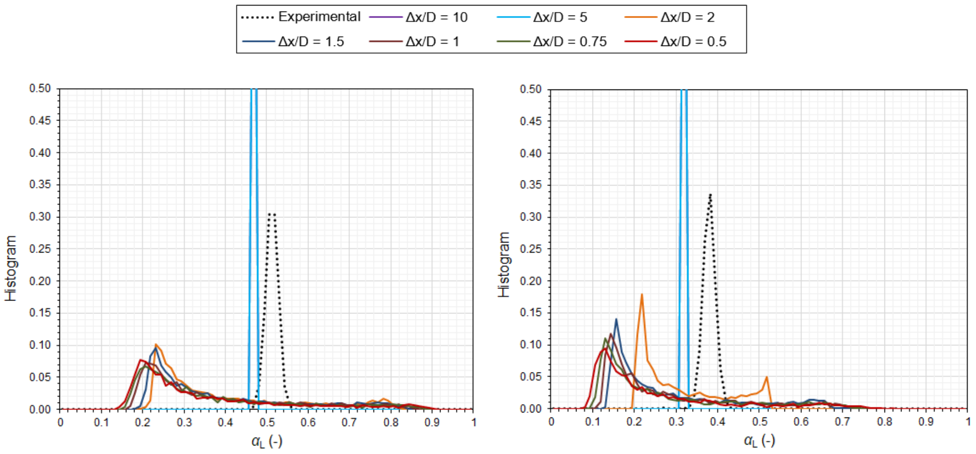

(a) Case 2. (b) Case 3

Figure 5.50 – Liquid holdup histograms for Cases 2 and 3 with the Proposed Expression 1 in the third set of simulations ($\eta_\mu = 1$).

Considering the axial diffusion term, as previously described ($\eta_\mu = 1$), it could be observed that it was not enough for making the simulations of such Cases mesh convergent, even when a correlation for f_i that provides high values for it (Proposed Expression 1), when compared to the Standard Expression, is employed. This is evidenced by the fact that the results of Figures 5.47-5.50 generally resemble more those of the same Cases with the Standard Expression in the first set of simulations (Figures 5.16-5.19), than those with the Proposed Expression 1 in the second set of simulations (Figures 5.34-5.37).

5.5.3. Increased Diffusion

From the previously analyzed results for Cases 1, 2 and 3, it is very clear that the axial diffusion term made no significant difference in the hyperbolicity and mesh convergence of the simulations. A possible reason for this is that the effective dynamic viscosity μ_K^{eff} should possess higher values than the ones provided by the current model. This is represented by the possible low value chosen for the coefficient η_μ of Eq. (3.34) fixed as unity for the simulations of Figures 5.44-5.50. Fullmer *et al.* (2014), for example, considered η_μ equal to 8.1, in contrast to η_μ = 1.0, which might not be enough for the current objectives (i.e., introducing a dissipative effect). It is important to state that a very large value for η_μ should also not be considered, because the physical meaning of the coefficient would be lost. Therefore, for exploring this possibility, the simulations of this third set for Cases 1, 2 and 3 with the Proposed Expression 1 were remade, but equating η_μ to 10.

For $\eta_\mu = 10$ and the Proposed Expression 1, Figures 5.51 and 5.52 illustrate the mean liquid holdup, pressure gradient and e_{RMS} values, respectively, as a function of $\Delta x/D$ for Case 1 together with its experimental data.

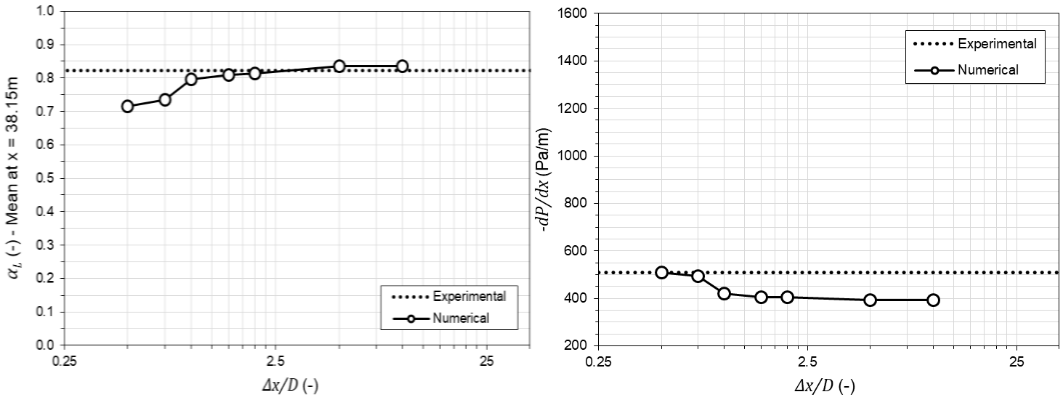

(a) Mean liquid holdup (b) pressure gradient

Figure 5.51 – Grid test for Case 1 with the Proposed Expression 1 in the third set of simulations ($\boldsymbol{\eta_\mu = 10}$).

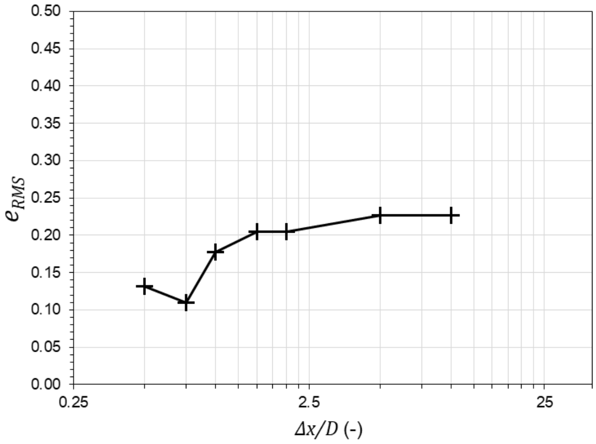

Figure 5.52 – Values of the root-mean-squared error of Eq. (5.1) for Case 1 with the Proposed Expression 1 in the third set of simulations ($\boldsymbol{\eta_\mu = 10}$).

By looking at the plots in the referred Figures 5.51 and 5.52 and comparing them with the ones obtained for $\eta_\mu = 1$ (Figures 5.44 and 5.45), it is clear that increasing it to 10 did not impact significantly on the integral parameters of Case 1. In other words, these new results for such Case still considerably resemble the values plotted in Figures 5.9 and 5.10 for the first set of simulations. A similar conclusion can be reached when the liquid holdup histograms for each $\Delta x/D$ value, depicted in Figure 5.53, are compared against the ones obtained for $\eta_\mu = 1$ (Figure 5.46). Therefore, increasing the η_μ value from 1 to 10 was not enough for reasonably influencing the dynamics of the flow in this case.

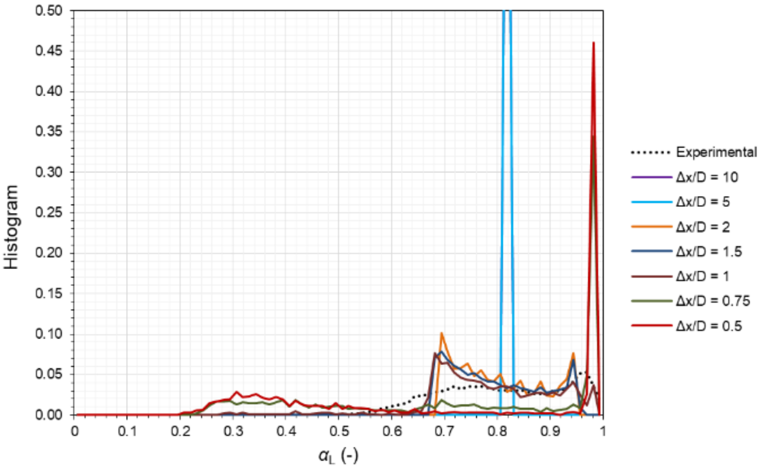

Figure 5.53 – Liquid holdup histograms for Case 1 with the Proposed Expression 1 in the third set of simulations ($\boldsymbol{\eta_\mu = 10}$).

For the stratified wavy flow (with small-amplitude interfacial waves) Cases 2 and 3, simulated again in this third set with $\eta_\mu = 10$, Figures 5.54-5.56 plot as a function of the mesh aspect ratios, respectively, the α_L values, pressure gradient and e_{RMS} values, together with the measurements and Point Model predictions (Table 5.4).

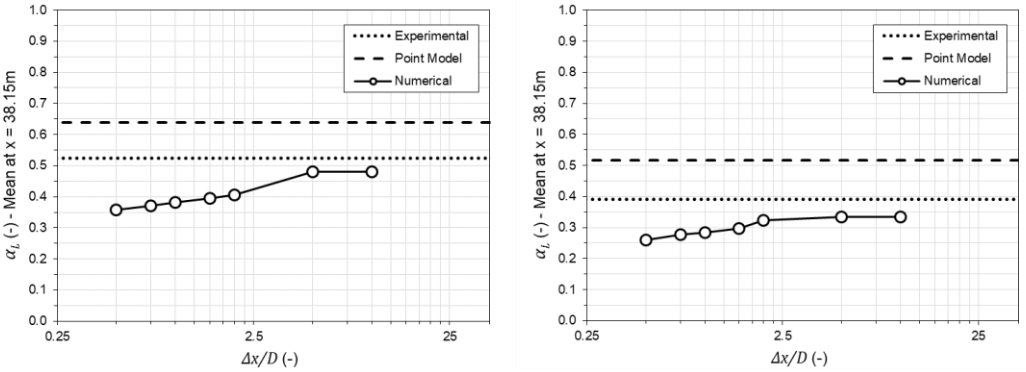

(a) Case 2. (b) Case 3.

Figure 5.54 – Mean liquid holdup numerical results for Cases 2 and 3 with the Proposed Expression 1 in the third set of simulations ($\boldsymbol{\eta_\mu = 10}$).

Regarding mesh dependency, the same behavior is again verified for $\eta_\mu = 10$ in Figures 5.54-5.56, when compared to the results for $\eta_\mu = 1$. The same can be verified in Figure 5.57 in which the numerical liquid holdup histograms are depicted together with the ones acquired by the gamma densitometer. Therefore, the increase in the value of coefficient η_μ, Eq. (3.34), from 1 to 10 was not sufficient for making the Cases 2 and 3 simulations mesh-convergent. It is important to comment that the Regime Capturing Methodology results in Figures 5.54 and 5.55 for coarse meshes would probably only coincide with the Point Model predictions for aspect ratios higher than 25, as in Figures 5.16 and 5.17.

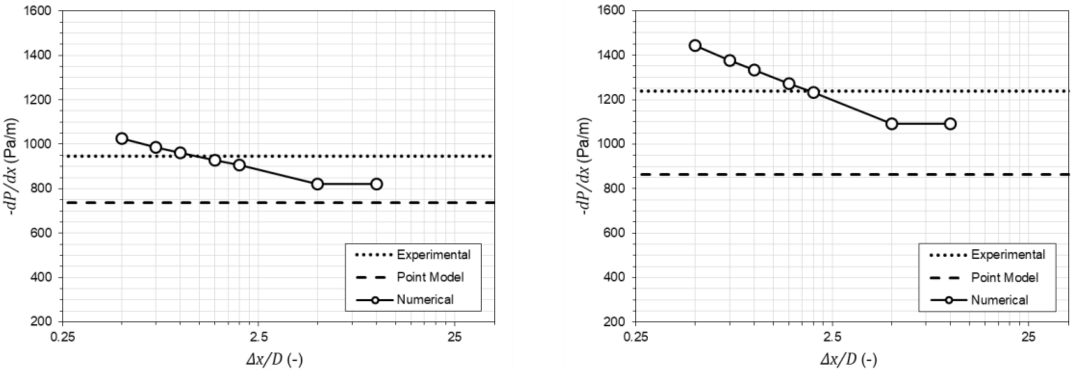

(a) Case 2. (b) Case 3.

Figure 5.55 – Pressure gradient numerical results for Cases 2 and 3 with the Proposed Expression 1 in the second set of simulations ($\boldsymbol{\eta_\mu = 10}$).

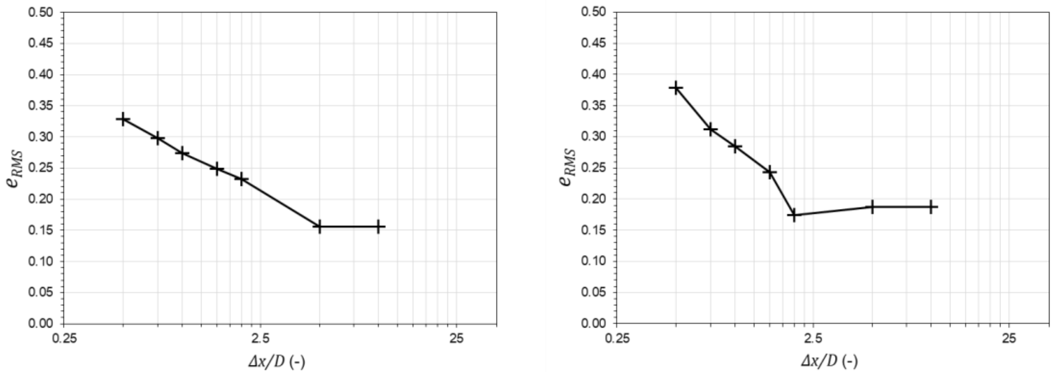

(a) Case 2. (b) Case 3.

Figure 5.56 – Values of the root-mean-squared error of Eq. (5.1) for Cases 2 and 3 with the Proposed Expression 1 in the second set of simulations ($\boldsymbol{\eta_\mu = 10}$).

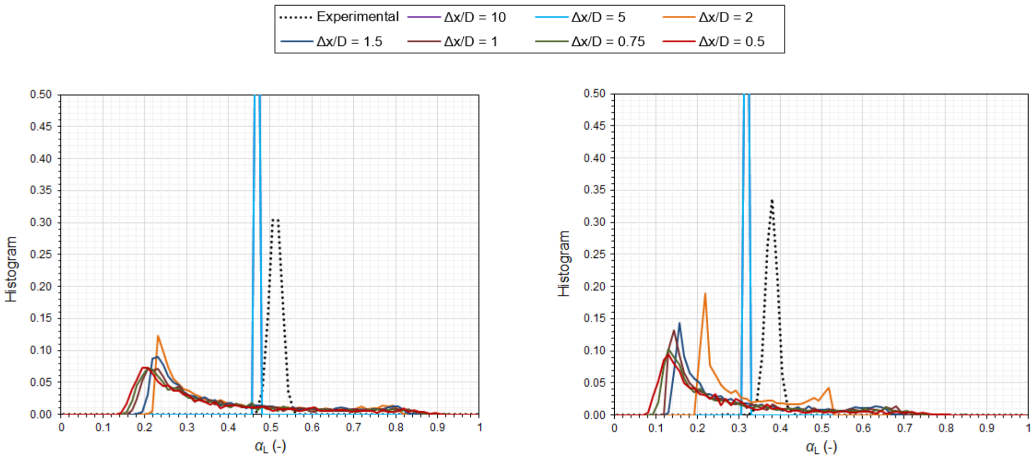

(a) Case 2. (b) Case 3.

Figure 5.57 – Liquid holdup histograms for Cases 2 and 3 with the Proposed Expression 1 in the third set of simulations ($\boldsymbol{\eta_\mu = 10}$).

In this third set of simulations, it was seen that taking into account the axial momentum diffusion term in the 1D Two-Fluid Model does not lead to improved results, for Case 1, nor to mesh-convergence, for Cases 2 and 3. Actually, it has little impact on the results, which is true for both η_μ values tested: 1 and 10, even with the significant molecular viscosity of the mineral oil of the Eskerud Smith *et al.* (2011) database. It should be stated that such remarks are only valid for the specific model for the axial diffusion term chosen for this work. In other words, a more extensive analysis on several approaches for modelling $\mathcal{T}_K$, Eqs. (3.11) and (3.12), is necessary, as well as an assessment of the minimum order of magnitude for μ_K^{eff} required for the axial diffusion to really influence the simulations. This should be performed even knowing that, for most flows, as previously mentioned, a further increase in η_μ would be unphysical and purely artificial. In spite of this approach being considered equally artificial in literature, an alternative could be the addition of diffusion on the mass conservation equations of the 1D Two-Fluid Model, Eqs. (3.58) and (3.59), (Fullmer *et al.*, 2014).

5.5.4. Summary

For Case 1, the simulations of the first set are preferable over the ones of the third set for being similar in results, but for having one less term in the 1D Two-Fluid Model momentum equations (Table 5.1). For Cases 2 and 3, the simulations of the second set were the most satisfactory due to the ability of the Bestion (1990) dynamic pressure to render mesh convergence and well-posedness. Nevertheless, the previously commented problems of the dynamic pressure term still persist and it is desirable to overcome them, especially the excessive stabilization of Case 1 and the appearance of large-amplitude instabilities. With this purpose, in the fourth set of simulations, the dynamic interfacial shear stress expression of Brauner & Maron (1993; 1994) is taken into account together with the dynamic pressure term (Table 5.1).

5.6. Analysis of the Dynamic Interfacial Shear Stress Term (Fourth Set of Simulations)

In this topic, the results of the fourth set of simulations, in which the dynamic pressure and the dynamic interfacial shear stress terms are considered in the momentum conservation equations of the 1D Two-Fluid Model, are presented. As in the third set of simulations, only the Proposed Expression 1 is employed for modelling the interfacial friction factor.

5.6.1. Case 1 ($\Delta P_{\mathcal{D},K} \neq 0$; $\mathcal{J}_i \neq 0$)

Starting with Case 1, Figures 5.58 and 5.59 show the plots, as a function of the mesh aspect ratio, of the liquid holdup, the pressure gradient and the e_{RMS} values from the simulations and the measurements.

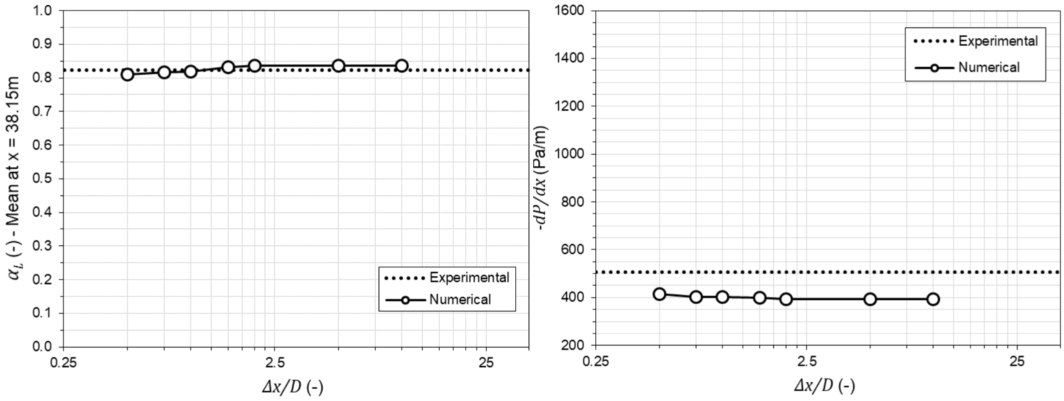

(a) Mean liquid holdup (b) Pressure gradient

Figure 5.58 – Grid test for Case 1 with the Proposed Expression 1 in the fourth set of simulations.

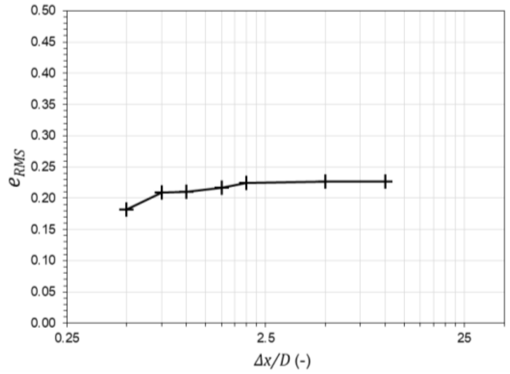

Figure 5.59 – Values of the root-mean-squared error of Eq. (5.1) for Case 1 with the Proposed Expression 1 in the fourth set of simulations.

Comparing the results of the referred figures with the ones for the same Case 1, with the Proposed Expression 1, of the second set of simulations (Figures 5.23 and 5.24) it can be seen how remarkably similar they are. The same can be stated about the numerical liquid holdup histograms of the current simulations, located in Figure 5.60, and those from the previously mentioned simulations of the second set (Figure 5.25). Nevertheless, by comparing the histograms for $\Delta x/D = 0.5$ in Figures 5.25 and 5.60, one can see that the dynamic interfacial shear stress of Brauner & Maron (1993; 1994) did manage to slightly destabilize the flow, and a few slugs could be captured. However, the numerical liquid holdup histogram for this mesh aspect ratio in Figure 5.60 is still very different from the experimental one. Besides, the results behavior in Figures 5.58 and 5.59 indicate the mesh convergence was not obtained. Despite all of this, the Case 1 results for the fourth set of simulations indicate that using the dynamic interfacial shear stress combined with the dynamic pressure might be the right way for improving the second set of simulations predictions.

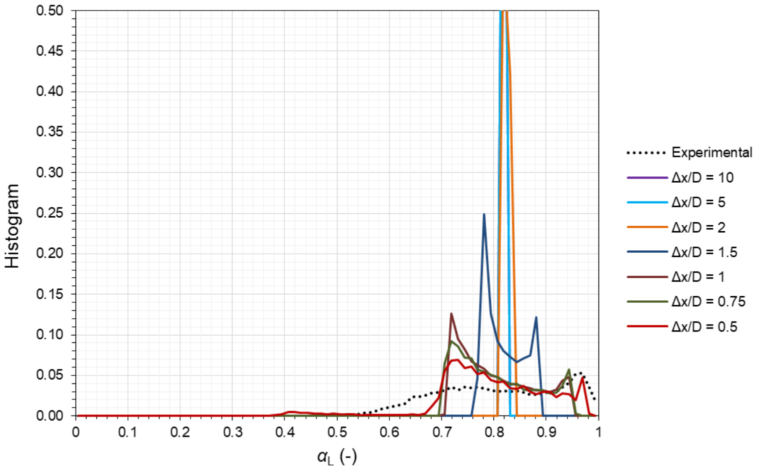

Figure 5.60 – Liquid holdup histograms for Case 1 with the Proposed Expression 1 in the fourth set of simulations.

5.6.2. Cases 2 and 3 ($\Delta P_{\mathcal{D},K} \neq 0\,; \mathcal{J}_i \neq 0$)

For the originally stratified wavy (with small-amplitude waves) flows of Cases 2 and 3, the integral parameter results for the fourth set of simulations are shown in Figures 5.61-5.63. They depict the plots of, respectively, the liquid holdup, the pressure gradient and the e_{RMS} values together with the corresponding measurements and Point Model predictions (Table 5.4).

It is interesting to observe that the results in Figures 5.61-5.63 are almost identical to those from Cases 2 and 3 of the second set of simulations, with the Proposed Expression 1, in Figures 5.34-5.36. The same can be said regarding the liquid holdup histogram results of the Cases 2 and 3 fourth-set simulations, plotted in Figure 5.64 and of those plotted in Figure 5.37.

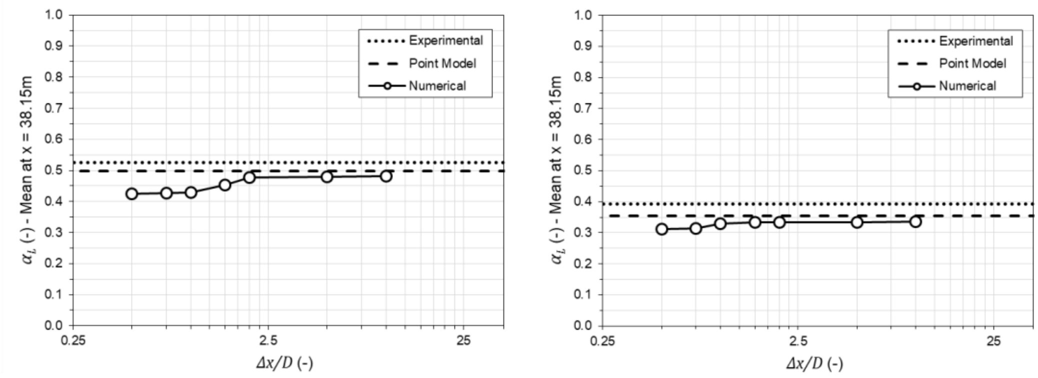

(a) Case 2.

(b) Case 3.

Figure 5.61 – Mean liquid holdup numerical results for Cases 2 and 3 with the Proposed Expression 1 in the fourth set of simulations.

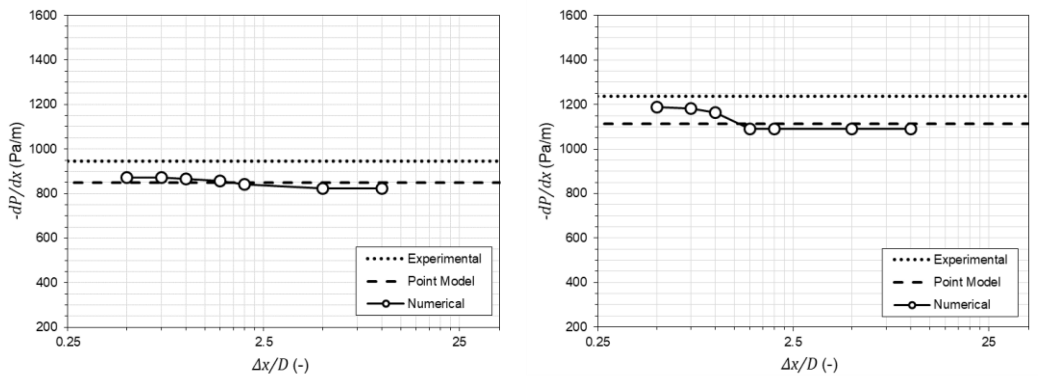

(a) Case 2. (b) Case 3.

Figure 5.62 – Pressure gradient numerical results for Cases 2 and 3 with the Proposed Expression 1 in the fourth set of simulations.

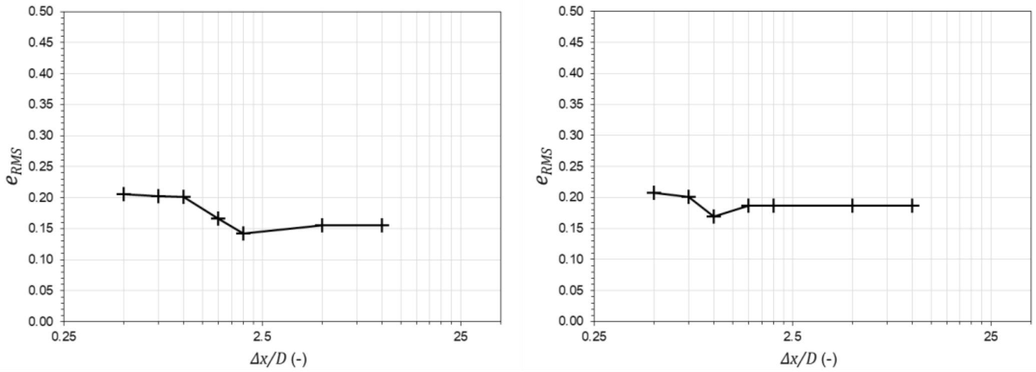

(a) Case 2. (b) Case 3.

Figure 5.63 – Values of the root-mean-squared error of Eq. (5.1) for Cases 2 and 3 with the Proposed Expression 1 in the fourth set of simulations.

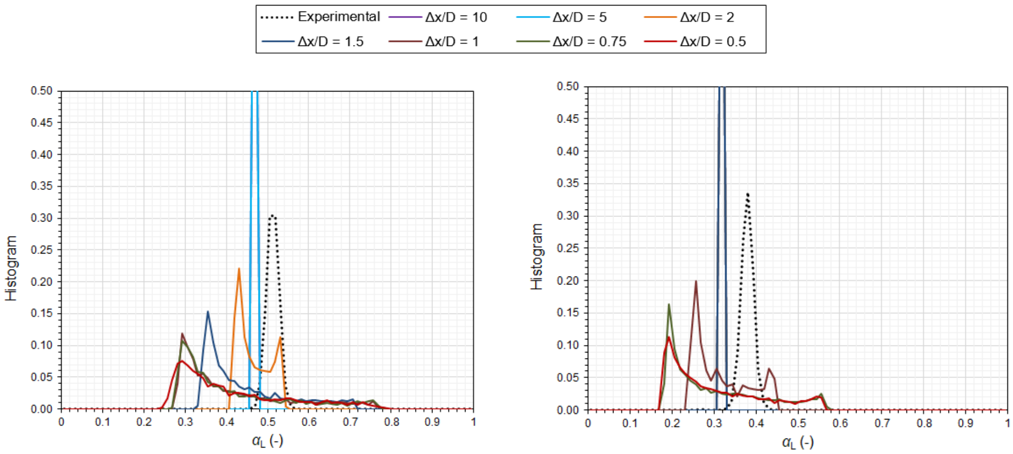

(a) Case 2. (b) Case 3.

Figure 5.64 – Liquid holdup histograms for Cases 2 and 3 with the Proposed Expression 1 in the fourth set of simulations.

After the presentation of the results from this forth set of simulations, it can be concluded that the inclusion of the dynamic interfacial shear stress term (together with the dynamic pressure) did not destabilize the flow sufficiently in order to compensate the overly stabilizing effect of $\Delta P_{\mathcal{D},K}$. The reason might be that the Brauner & Maron (1993; 1994) modelling for $\mathcal{J}_i$ provides low values, which do not play a significant role in the 1D Two-Fluid Model. Therefore, a more thorough investigation on this term is needed, due to its solid physical background and destabilizing effect evidenced in the well-posedness analysis and present simulations. Hence, potential improvement in the Regime Capturing Methodology may be possible with this term.

6. CONCLUSIONS

In this work, an attempt was made for extending the Regime Capturing Methodology, extensively validated for air-water flows (Issa & Kempf, 2003; Nieckele *et al.*, 2013; Ferrari *et al.*, 2017), to viscous oil-gas flows, through simulations of isothermal horizontal stratified wavy and slug cases from the Eskerud Smith *et al.* (2011) database. With this purpose, two new expressions for the interfacial friction factor were generated using the stratified wavy flow (small-amplitude waves) data and a new framework based on an optimization procedure, solved with the PSO algorithm (Kennedy & Eberhert, 1995). These new expressions (Proposed Expressions 1 and 2) provided liquid holdup and pressure gradient values, with the Point Model, much closer to the measurements than more common literature formulations. Besides, through a different formulation for the optimization problem, it was also possible to evaluate the most efficient wall friction factor correlations. It was seen that the Biberg (1999) expression, modified by Pasqualette *et al.* (2017), for $(f_L)_{\mathrm{lam}}$, the Nossen *et al.* (2002) correlation for $(f_L)_{\mathrm{turb}}$ and the Biberg (1998) equation for $(f_G)_{\mathrm{turb}}$ were more efficient, in terms of objective function, than standard literature approaches.

Well-posedness (characteristics) analyzes of the 1D Two-Fluid for the Eskerud Smith *et al.* (2011) database were performed, considering the gas as incompressible and neglecting second-order and higher order derivative terms. From the analysis, it became clear that the dynamic pressure term, as expected, contributes to the well-posedness and that the dynamic interfacial shear stress makes the model more unstable and ill-posed.

Four sets of Regime Capturing Methodology simulations (Table 5.1) were performed and their results were presented for three Eskerud Smith *et al.* (2011) database cases: one slug flow (Case 1) and two stratified-wavy flows (Cases 2 and 3). In the first set of simulations, the slug flow case was mesh convergent and well-posed and the analysis of integral parameters, liquid holdup histograms and their transient profiles revealed that the use of Proposed Expressions 1 and 2 only slightly changes the results, when compared to the Standard Expression. Such comparison was not possible to be made for Cases 2 and 3, because those cases were ill-posed. In the second set of simulations, i.e., using the dynamic pressure of Bestion (1990), Case 1 become overly stabilized, which harmed the prediction of slugs, while Cases 2 and 3 become mesh-convergent and the analysis of their results showed a superiority of the Proposed Expression 1, when compared to the Standard Expression and to the Proposed Expression 2. The simulations of the third set were aimed to replace the excessive stabilizing effects due to the dynamic pressure by the axial momentum diffusion. However, it did not manage to guarantee that Cases 2 and 3 were well-posed. It was suggested that only an artificial augmentation of the diffusion would cause the desired effect. Finally, the four set of simulations tested the impact of the model of Brauner & Maron (1993; 1994) for the dynamic interfacial shear stress in the simulations. However, it was observed that such term does have little impact, probably due to low values of adjusting parameters provided by the model of Brauner & Maron (1993; 1994).

As seen, this work managed to make several interesting remarks, new knowledge and observations on the use of the Regime Capturing Methodology for viscous oil-gas flows. Furthermore, it contains an optimization-based new method for creating interfacial friction factor expressions and for analyzing wall friction factor correlations. Several analyzes, approaches and descriptions of topics were made in manners different and better than what is currently found in the literature. Therefore, this work had several contributions to the development of the technology studied: the Regime Capturing Methodology. Nevertheless, much more can still be performed as it can be grasped from the following suggestions for future works.

6.1. Suggestions for Future Work

In the optimization of the interfacial shear stress, a suggestion for a future work would be to generalize the Proposed Expressions 1 and 2 by using extra experimental database for different fluids. In addition, one should look for even better wall shear stress correlations than the ones used in this work. The consideration in the Point Model of the term of Liné & Lopez (1997), which explicitly takes into account the effects of the interfacial waves on the interface would also be a novel task to be performed.

Regarding the stability-hyperbolicity problem, rather than only using well-posedness (characteristics) analyses, it is recommendable to use also a linear stability analysis and/or the von Neumann analysis. The former would make possible to assess the effects of the higher-order terms and to have a more complete mapping of the model stability for all wavelengths. The von Neumann analysis would go even further and provide as well the influence of the discretization schemes in the stability-hyperbolicity problem.

For the Regime Capturing Methodology, it is interesting to explore more wall and interfacial shear stress closure relations for the viscous-oil gas flows. Besides, the analysis of the axial momentum diffusion and of the dynamic interfacial shear stress should advance, because part of what was performed in this work on such topics was inconclusive. Testing the effects of the artificial diffusion on the mass equations is also significantly important, for being an effect that may significantly dampen the growth rate of spurious instabilities (Fullmer *et al.*, 2014) and for being a strong candidate for improving qualitatively the transient liquid holdup profiles and their histograms. Using Power-Spectrum-Density (PSD) plots, as in Fontalvo (2017), is recommendable in the future for being a resource that provides deep information on the numerical results.

Lastly, for slug flows, the incorporation of gas entrainment effects is important, especially at higher mixture velocities. This effect is not taken into account in the current version of the model and may help to improve hold-up predictions, as evidenced by numerical results shown here. Excessively high peaks in the histograms of the hold-up signals were obtained for α_L values close to one, which were not observed in the experiments.

REFERENCES

ALVES, M.V.C., WALTRICH, P.J., GESSNER, T.R., *et al.*, 2016. Modeling transient churn-annular flows in a long vertical tube. International Journal of Multiphase Flow, vol. 89, p. 399-412.

ANDRÉ, M.A., BARDET, P.M., 2017. Viscous stress distribution over a wavy gas-liquid interface. International Journal of Multiphase Flow, vol. 88, p. 1-10.

ANDREUSSI, P., PERSEN, L.N., 1987. Stratified gas-liquid flow in downwardly inclined pipes. International Journal of Multiphase Flow, v. 13, n. 4, p. 565-575.

ANDRITSOS, N., HANRATTY, T.J., 1987a. Interfacial instabilities for horizontal gas-liquid flows in pipelines. International Journal of Multiphase Flow, vol. 13, n. 5, p. 583-603.

ANDRITSOS, N., HANRATTY, T.J., 1987b. Influence of interfacial waves in stratified gas-liquid flows. AIChE Journal, vol. 33, n. 3, p. 444-454.

ANDRITSOS, N., 1989. Effect of liquid viscosity on the stratified-slug transition in horizontal pipe flow. International Journal of Multiphase Flow, vol. 15, n. 6, p. 877-892.

AYATI, A.A., KOLAAS, J., JENSEN, A., *et al.*, 2016. The effect of interfacial waves on the turbulence structure of stratified air/water pipe flow. International Journal of Multiphase Flow, vol. 78, p. 104-116.

BAER, M.R., NUNZIATO, J.W., 1986. A two-phase mixture theory for the deflagration-to-detonation transition (DDT) in reactive granular materials. International Journal of Multiphase Flow, vol. 12, n. 6, p. 861-889.

BELCHER, S.E., HUNT, J.C.R., 1993. Turbulent shear flow over slowly moving waves. Journal of Fluid Mechanics, vol. 251, p. 109-148.

BENDIKSEN, K.H., MALNES, D., MOE, R., *et al.*, 1991. The dynamic two-fluid model OLGA: theory and application. SPE Production Engineering, vol. 6, n. 2, p. 171-180.

BENDIKSEN, K.H., MALNES, D., NYDAL, O.J., 1996. On the modelling of slug flow. Chemical Engineering Communications, vol. 141-142, n. 1, p. 71-102.

BESTION, D., 1990. The physical closure laws in the CATHARE code. Nuclear Engineering and Design, vol. 124, n. 3, p. 229-245.

BIBERG, D., 1998. A simple friction model for two-phase stratified pipe flow. In: 3rd International Conference on Multiphase Flow, Lyon, France, 8-12 June.

BIBERG, D., 1999a. An explicit approximation for the wetted angle in two-phase stratified pipe flow. The Canadian Journal of Chemical Engineering, vol. 77, n. 6, p. 1221-1224.

BIBERG, D., 1999b. Two-phase stratified pipe flow modelling: a new expression for the interfacial shear stress. In: 2nd International Symposium on Two-Phase Flow Modelling and Experimentation, Pisa, Italy, 22-25 Sept.

BIBERG, D., 1999c. Liquid wall friction factor in two-phase turbulent gas laminar liquid stratified pipe flow. The Canadian Journal of Chemical Engineering, vol. 77, n. 6, p. 1073-1082.

BIBERG, D., 2007. A mathematical model for two-phase stratified turbulent duct flow. Multiphase Science and Technology, vol. 19, n. 1, p. 1-48.

BONIZZI, M., ISSA, R.I., 2003. A model for simulating gas bubble entrainment in two-phase horizontal slug flow. International Journal of Multiphase Flow, vol. 29, n. 11, p. 1685-1717.

BONIZZI, M., ANDREUSSI, P., BANERJEE, S., 2009. Flow regime independent, high resolution multi-field modelling of near-horizontal gas-liquid flows in pipelines. International Journal of Multiphase Flow, vol. 35, n. 1, p. 34-46.

BRAUNER, N., MARON, D.M., 1993. The role of interfacial shear modelling in predicting the stability of stratified two-phase flow. Chemical Engineering Science, vol. 48, n. 16, p. 2867-2879.

BRAUNER, N., MARON, D.M., 1994. Dynamic model for the interfacial shear as a closure law in two-fluid models. Nuclear Engineering and Design, vol. 149, n. 1-3, p. 67-79.

BRENNEN, C.E., 2005. Fundamentals of multiphase flows. 1st ed., Cambridge University Press, USA.

CALGARO, B., 2012. Development of closure relationships for advanced two-phase flow analysis. Ph.D. Thesis, Università di Pisa, Italy.

CAZAREZ-CANDIA, O., BENÍTEZ-CENTENO, O.C., ESPINOSA-PAREDES, G., 2011. Two-fluid model for transient analysis of slug flow in oil wells. International Journal of Heat and Fluid Flow, vol. 32, n. 3, p. 762-770.

CARNEIRO, J.N.E., 2006. Numerical simulation of two-phase slug flow in horizontal and nearly horizontal pipes. M.Sc. Dissertation, PUC-Rio, Brazil. (in Portuguese)

CARNEIRO, J.N.E., FONSECA Jr., R., ORTEGA, A.J., *et al.*, 2011. Statistical characterization of two-phase slug flow in a horizontal pipe. Journal of the Brazilian Society of Mechanical Sciences and Engineering, vol. 33, p. 251-258.

ÇENGEL, Y.A., 2006. Heat and mass transfer. 3rd ed., McGraw-Hill, USA.

CHUNG, M.-H., SUNG, C.-K., 1996. Onset of slugging criterion based on characteristics and stability analyses of transient one-dimensional two-phase flow equations of two-fluid model. International Communications of Hear and Mass Transfer, vol. 23, n. 4, p. 473-484.

COELHO, F.M.C., NIECKELE, A.O., CARNEIRO, J.N.E., 2016. Evaluation of blowdown time of a two-phase flow gas pipeline. In: 9th Congresso Nacional de Engenharia Mecânica, Fortaleza, Brazil, 21-25 August.

COLEBROOK, C.F., 1939. Turbulent flow in pipes, with particular reference to the transition region between the smooth and rough pipe laws. Journal of the Institution of Civil Engineers, vol. 11, n. 4, p. 133-156.

DANIELSON, T.J., BANSAL, K.M., HANSEN, R., *et al.*, 2005. LEDA: the next multiphase flow performance simulator. In: 12th International Conference on Multiphase Production Technology, Barcelona, Spain, 25-27 May.

DE BERTODANO, M.L., FULLMER, W., VAIDHEESWARAN, A., 2013. One-dimensional two-equation two-fluid model stability. Multiphase Science and Technology, vol. 25, n. 2-4, p. 133-167.

DE LEEBEECK, A., NYDAL, O.J., 2010. Simulation of large amplitude waves in a slug tracking scheme compared to roll wave experiments at high pressure. International Journal of Multiphase Flow, vol. 36, p. 40-50.

DINH, T.N., NOURGALIEV, R.R., THEOFANUS, T.G., 2003. Understanding the ill-posed two-fluid model. In: 10th International Topical Meeting in Nuclear Reactor Thermal Hydraulics, Seoul, South Korea, 5-9 Oct.

DREW, D.A., PASSMAN, S.L., 1999. Theory of multicomponent fluids. 1st ed., Springer, USA.

DUKLER, A.E., HUBBARD, M.G., 1975. A model for gas-liquid slug flow in horizontal and near horizontal tubes. Industrial & Engineering Chemistry Fundamentals, vol. 14, n. 4, p. 337-347.

EMAMZADEH, M., ISSA, R.I., 2013a. One-dimensional model for numerical simulation of annular flow in horizontal and vertical pipes. Multiphase Science and Technology, vol. 25, n. 1, p. 25-56.

EMAMZADEH, M., ISSA, R.I., 2013b. A model for predicting the transition between stratified and annular flow in horizontal pipes. Multiphase Science and Technology, vol. 25, n. 1, p. 79-100.

ESKERUD SMITH, I., KRAMPA, F.N., FOSSEN, M., *et al.*, 2011. Investigation of horizontal two-phase gas-liquid pipe flow using high viscosity oil: comparison with experiments using low viscosity oil and simulations. In: 15th International Conference on Multiphase Production, Cannes, France, 15-17 June.

ESKERUD SMITH, I., NYDAL, O.J., 2016. The effect of boundary conditions and droplet entrainment on severe slugging using a Lagragian slug tracking model. International Journal of Multiphase Flow, vol. 85, p. 245-257.

FARSETTI, S., FARISÈ, S., POESIO, P., 2014. Experimental investigation of high viscosity oil-air intermittent flow. Experimental Thermal and Fluid Sciences, vol. 57, p. 285-292.

FERRARI, M., BONZANINI, A., POESIO, P., 2016. A slug capturing method applied to unconventional scenarios: high viscous oils and actual pipeline geometries. In: 9th International Conference on Multiphase Flow, Firenze, Italy, 22-27 May.

FERRARI, M., BONZANINI, A., POESIO, P., 2017. A five-equation, transient, hyperbolic, one-dimensional model for slug capturing in pipes. International Journal for Numerical Methods in Fluids, accepted for publication.

FIGUEIREDO, A.B., BAPTISTA, R.M., RACHID, F.B.F., *et al.*, 2016. Numerical simulation of stratified-pattern two-phase flow in gas pipelines using a two-fluid model. International Journal of Multiphase Flow, vol. 88, p. 30-49.

FLÅTTEN, T., LUND, H., 2011. Relaxation two-phase flow models and subcharateristic condition. Mathematical Models and Methods in Applied Sciences, vol. 21, n. 12, p. 2379-2407.

FOLETTI, C., FARISÉ, S., GRASSI, B., *et al.*, 2011. Experimental investigation on two-phase air/high-viscosity-oil flow in horizontal pipe. Chemical Engineering Science, vol. 66, n. 23, p. 5968-5975.

FONTALVO, E.M.G., 2017. Assessment of the dynamic pressure closure in 1D Two-Fluid Model for vertical annular flow. M.Sc. Dissertation, PUC-Rio, Brazil. (in Portuguese)

FONTALVO, E.M.G., NIECKELE, A.O., CARNEIRO, J.N.E., 2016. Assessment of the dynamic pressure effect in 1D Two-Fluid Model for a vertical annular gas-liquid flow. In: 16th Brazilian Congress of Thermal Sciences and Engineering, Vitória, Brazil, 7-10 Nov.

FULLMER, W.D., DE BERTODANO, M.A.L., RANSOM, V.H., 2011. The Kelvin-Helmholtz instability: comparisons of one- and two-dimensional simulations. In: 14th International Topical Meeting on Nuclear Reactor Thermal Hydraulics, Toronto, Canada, 25-30 Sep.

FULLMER, W.D., RANSOM, V.H., DE BERTODANO, M.A.L., 2014. Linear and nonlinear analysis of an unstable, but well-posed, one-dimensional two-fluid model for two-phase flow based on the inviscid Kelvin-Helmholtz instability. Nuclear Engineering and Design, vol. 268, p. 173-184.

GALIMOV, A.Y., DREW, D.A., LAHEY, R.T., *et al.*, 2005. The analysis of interfacial waves. Nuclear Engineering and Design, vol. 235, n. 10-12, p. 1283-1292.

GOKCAL, B., 2008. An experimental and theoretical investigation of slug flow for high oil viscosity in horizontal pipes. Ph.D. Thesis, University of Tulsa, USA.

HAALAND, S.E., 1983. Simple and explicit formulas for the friction factor in turbulent pipe flow. ASME Journal of Fluids Engineering, vol. 105, n. 1, p. 89-90.

HADAMARD, J., 1902. On the problem of partial derivatives and their physical significance. Princeton University Bulletin, vol. 13, n. 4, p. 49-52 (in French).

HAN, P., GUO, L., 2015. Numerical simulation of terrain-induced severe slugging coupled by hydrodynamic slugs in a pipeline-riser system. International Journal of Heat and Fluid Flow, vol. 56, p. 355-366.

HAND, N.P., 1991. Gas-liquid cocurrent flow in a horizontal pipe. Ph.D. Thesis, Queen’s University of Belfast, Northern Ireland.

HOLMAS, H., 2010. Numerical simulation of transient roll-waves in two-phase pipe flow. Chemical Engineering Science, vol. 65, n. 5, p. 1811-1825.

HANRATTY, T.J., 2013. Physics of gas-liquid flows. 1st ed.. Cambridge University Press, USA.

INTERNATIONAL ENERGY AGENCY (I.E.A.), 2015. World Energy Outlook. 1st ed., Organization for Economic Co-operation and Development, France.

ISHII, M., 1975. Thermo-fluid dynamic theory of two-phase flow. 1st ed., Eyrolles, France.

ISHII, M., GROLMES, M.A., 1975. Inception criteria for droplet entrainment in two-phase cocurrent film flow. AIChE Journal, vol. 21, n. 2, p. 308-318.

ISHII, M., HIBIKI, T., 2011. Thermo-fluid dynamics of two-phase flow. 2nd ed., Springer, USA.

ISSA, R.I., KEMPF, M.H.W., 2003. Simulation of slug flow in horizontal and nearly horizontal pipes with the two-fluid model. International Journal of Multiphase Flow, vol. 29, n. 1, p. 69-95.

ISSA, R., GALLENI, F., 2015. Mechanistic simulation of slug flow in vertical pipes using the one-dimensional two-fluid model. Multiphase Science and Technology, vol. 27, n. 2-4, p. 229-245.

JOHANSEN, S.T., MO, S., KJØLAAS, J., *et al.*, 2014. Simulation of two-phase viscous oil flow. In: 10th International Conference on CFD in Oil & Gas, Metallurgical and Process Industries, Trondheim, Norway, 17-19 June.

KENNEDY, J., EBERHART, R., 1995. Particle swarm optimization. In: IEEE 4th International Conference on Neural Networks, Perth, Australia, 27 Nov. - 01 Dec.

KHALEDI, H.A., ESKERUD SMITH, I., UNANDER, T.E., *et al.*, 2014. Investigation of two-phase flow pattern, liquid holdup and pressure drop in viscous oil-gas flow. International Journal of Multiphase Flow, vol. 67, p. 37-51.

KOWALSKI, J.E., 1987. Wall and interfacial shear stress in stratified flow in a horizontal pipe. AIChE Journal, vol. 33, n. 2, p. 274-281.

LANDMAN, M.J., 1991. Non-unique holdup and pressure drop in two-phase stratified inclined pipe flow. International Journal of Multiphase Flow, vol. 17, n. 3, p. 377-394.

LIAO, J., MEI, R., KLAUSNER, J.F., 2008. A study on the numerical stability of the two-fluid model near ill-posedness. International Journal of Multiphase Flow, vol. 34, n. 11, p. 1067-1087.

LIN, P.Y., HANRATTY, T.J., 1986. Prediction of the initiation of slugs with linear stability theory. International Journal of Multiphase Flow, vol. 12, n. 1, p. 79-98.

LINÉ, A., LOPEZ, D., 1997. Two-fluid model of wavy separated two-phase flow. International Journal of Multiphase Flow, vol. 23, n. 6, p. 1131-1146.

LOCKHART, R.W., MARTINELLI, R.C., 1949. Proposed correlation of data for isothermal two-phase, two-component flow in pipes. Chemical Engineering Progress, vol. 45, p. 38-48.

LYCZKOWSKI, R.W., GIDASPOW, D., SOLBRIG, C.W., *et al.*, 1975. Characteristics and stability analyses of transient one-dimensional two-phase flow equations and their finite difference approximations. In: Winter Annual ASME Meeting, Houston, USA, 30 Nov. – 4 Dec.

MALEKZADEH, R., BELFROID, S.P.C., MUDDE, R.F., 2012. Transient drift flux modelling of severe slugging in pipeline-riser systems. International Journal of Multiphase Flow, vol. 46, p. 32-37.

MALISKA, C.R., RAITHBY, G.D., 1984. A method for computing three dimensional flows using a non-orthogonal boundary-fitted co-ordinates. International Journal for Numerical Methods in Fluids, vol. 4, n. 6, p. 519-537.

MANDHANE, J.M., GREGORY, G.A., AZIZ, K., 1974. A flow pattern map for gas-liquid flow in horizonal pipes. International Journal of Multiphase Flow, vol. 1, n. 4, p. 537-553.

MARON, D.M., BRAUNER, N., 1987. The role of interfacial mobility in determining the interfacial shear factor in two-phase wavy film flow. International Communications in Heat and Mass Transfer, vol. 14, n. 1, p. 45-55.

MATSUBARA, H., NAITO, K., 2011. Effect of liquid viscosity on flow patterns of gas-liquid two-phase flow in a horizontal pipe. International Journal of Multiphase Flow, vol. 37, n. 10, p. 1277-1281.

MITO, Y., HANRATTY, T.J., 2007. Trajectory mechanism for particle deposition in annular flows. International Journal of Multiphase Flow, vol. 33, p. 101-107.

MONTINI, M., 2011. Closure relations of the one-dimensional two-fluid model for the simulation of slug flows. Ph.D. Thesis, Imperial College, England.

NÄDLER, M., MEWES, D., 1995. Effects of the liquid viscosity on the phase distributions in horizontal gas-liquid slug flow. International Journal of Multiphase Flow, vol. 21, n. 2, p. 253-266.

NÁRAIGH, L.Ó., SPELT, P.D.M., MATAR, O.K., *et al.*, 2011. Interfacial instability in turbulent flow over a liquid film in a channel. International Journal of Multiphase Flow, vol. 37, n. 7, p. 812-830.

NASDAQ, 2017. Crude Oil. Available at: http://www.nasdaq.com/markets/crude-oil-brent.aspx (accessed on 31/07/2017).

NEWTON, C.H., BEHNIA, M., 1998. On the use of the stratified momentum balance for the deduction of shear stress in horizontal gas-liquid pipe flow. International Journal of Multiphase Flow, vol. 24, n. 8, p. 1407-1423.

NEWTON, C.H., BEHNIA, M., REIZES, J.A., 1999. The effect of liquid viscosity on gas wall and interfacial shear stress in horizontal two-phase pipe flow. Chemical Engineering Science, vol. 54, n. 8, p. 1071-1079.

NG, T.S., LAWRENCE, C.J., HEWITT, G.F., 2004. Friction factors in stratified two-phase flows. Chemical Engineering Research and Design, vol. 82, n. 3, p. 309-320.

NIECKELE, A.O., CARNEIRO, J.N.E., CHUCUYA, R.C., *et al*, 2013. Initiation and statistical evolution of horizontal slug flow with a Two-Fluid Model. ASME Journal of Fluids Engineering, vol. 135, n. 12, 121302.

NIECKELE, A.O., CARNEIRO, J.N.E., 2017. On the numerical modeling of slug and intermittent flows in oil and gas production. In: ASME 36th International Conference on Ocean, Offshore and Arctic Engineering, Trondheim, Norway, 25-30 June.

NORSK PETROLEUM, 2017. Annual production from fields in the Norwegian Sea. Available at: http://www.norskpetroleum.no/en/facts/production/ (accessed on

27/08/2017).

NOSSEN, J., SHEA, R.H., RASMUSSEN, J., 2000. New developments in flow modelling and field data verification. In: 2nd North American Conference Multiphase Technology, Banff, Canada, 21-23 June.

NYDAL, O.J., BANERJEE, S., 1996. Dynamic slug tracking simulations for gas-liquid flow in pipelines. Chemical Engineering Communications, vol. 141-142, n. 1, p. 13-39.

NYDAL, O.J., 2012. Dynamic models in multiphase flow. Energy & Fuels, vol. 26, n. 7, p. 4117-4123.

ORELL, A., 2005. Experimental validation of a simple model for gas-liquid slug flow in horizontal pipes. Chemical Engineering Science, vol. 60, n. 5, p. 1371-1381.

ORTEGA, A.J.M., 2004. Analysis of slug flow in horizontal pipelines by the Two Fluid Model. M.Sc. Dissertation, PUC-Rio, Rio de Janeiro, Brazil. (in Portuguese)

ORTEGA, A.J.M., NIECKELE, A.O., 2005. Simulation of horizontal two-phase slug flows using the Two-Fluid Model with a conservative and non-conservative formulation. In: 18th International Congress of Mechanical Engineering, Ouro Preto, Brazil, 6-11 Nov.

OTTENS, M., HOEFSLOOT, H.C.J., HAMERSMA, P.J., 2001. Correlations predicting liquid hold-up and pressure gradient in steady-state (nearly) horizontal co-current gas-liquid pipe flow. Chemical Engineering Research and Design, vol. 79, n. 5, p. 581-592.

OUYANG, L.-B., AZIZ, K., 2002. Solution nonuniqueness for separated gas-liquid flow in pipes and wells. I. occurrence. Petroleum Science and Technology, vol. 20, n. 1-2, p. 143-171.

PASQUALETTE, M.A., CARNEIRO, J.N.E., NIECKELE, A.O., 2014. Numerical simulation of horizontal slug flows with the Two-Fluid Model using explicit geometrical approximations. In: 15th Brazilian Congress of Thermal Sciences and Engineering, Belém, Brazil, 10-13 Nov.

PASQUALETTE, M.A., CARNEIRO, J.N.E., NIECKELE, A.O., *et al.*, 2015. Numerical simulation of horizontal viscous oil-gas flows in the stratified and slug regimes with the Two-Fluid Model. In: 3rd Journeys in Multiphase Flow, Campinas, Brazil, 23-27 March.

PASQUALETTE, M.A., CARNEIRO, J.N.E., NIECKELE, A.O., *et al.*, 2017. Optimization of the interfacial shear stress for the simulation of horizontal viscous oil-gas flows with the 1D Two-Fluid Model. In: 4th Journeys in Multiphase Flow, São Paulo, Brazil, 27-31 March.

PATANKAR, S.V., 1980. Numerical Heat Transfer and Fluid Flow. 1st ed., McGraw-Hill, USA.

PENG, D.Y., ROBINSON, D.B., 1976. A new two-constant equation of state. Industrial & Engineering Chemistry Fundamentals, vol. 15, n. 1, p. 59-64.

POPE, S.B., 2000. Turbulent flows. 1st ed., Cambridge University Press, USA.

PROSPERETTI, A., TRYGGVASON, G., 2007. Computational methods for multiphase flow. 1st ed., Cambridge University Press, USA.

RAMSHAW, J.D., TRAPP, J.A., 1978. Characteristics, stability and short-wavelength phenomena in two-phase flow equation systems. Nuclear Science and Engineering, vol. 66, n. 1, p. 93-102.

RENAULT, F., 2007. A Lagrangian slug capturing scheme for gas-liquid flows in pipes. Ph.D. Thesis, Norwegian University of Science and Technology, Norway.

RODRIGUEZ, O.M.H., BALDANI, L.S., 2012. Prediction of pressure gradient and holdup in wavy stratified liquid-liquid inclined pipe flow. Journal of Petroleum Science and Engineering, vol. 96-97, p. 140-151.

SANDERSE, B., ESKERUD SMITH, I., HENDRIX, M.H.W., 2017. Analysis of time integration methods for the compressible two-fluid model for pipe flow simulations. International Journal of Multiphase Flow, vol. 95, p. 155-174.

SANTIM, C.G.S., GASPARI, E.F., PATERNOST, G.M., 2017. A transient analysis of gas-liquid slug flow inside a horizontal pipe using different models.

Journal of Petroleum Science and Engineering, vol. 151, p. 62-76.

SAUREL, R., ABGRALL, R., 1999. A multiphase Godunov method for compressible multifluid and multiphase flows. Journal of Computational Physics, vol. 150, n. 2, p. 425-467.

SILVA, I.S.F., NIECKELE, A.O., 2016. Numerical simulation of annular flow in horizontal pipes using the two fluid model. In: 9th International Conference on Multiphase Flow, Firenze, Italy, 22-27 May.

SIMÕES, E.F., CARNEIRO, J.N.E., NIECKELE, A.O., 2014. Numerical prediction of non-boiling heat transfer in horizontal stratified and slug flow by the Two-Fluid Model. International Journal of Heat and Fluid Flow, vol. 47, p. 135-145.

SCHLUMBERGER, 2017. Oilfield Glossary. Available at: http://www.glossary.oilfield.slb.com/ (accessed on 27/07/17).

SONG, J.H., 2003. A remedy for the ill-posedness of the one-dimensional two-fluid model. Nuclear Engineering and Design, vol. 222, n. 1, p. 40-53.

SPEDDING, P.L., HAND, N.P., 1997. Prediction in stratified gas-liquid co-current flow in horizontal pipelines. International Journal of Heat and Mass Transfer, vol. 40, n. 8, p. 1923-1935.

STUHMILLER, J.H., 1977. The influence of interfacial pressure on the character of two-phase flow model equations. International Journal of Multiphase Flow, vol. 3, n. 6, p. 551-560.

TAITEL, Y., DUKLER, A.E., 1976. A model for predicting flow regime transitions in horizontal and near horizontal gas-liquid flow. AIChE Journal, vol. 22, n. 1, p. 47-55.

TOMASELLO, A., 2009. One-dimensional modelling of mixing, dispersion and segregation of multiphase fluids flowing in pipelines. Ph.D. Thesis, Imperial College of London, England.

TZOTZI, C., ANDRITSOS, N., 2013. Interfacial shear stress in wavy stratified gas-liquid flow in horizontal pipes. International Journal of Multiphase Flow, vol. 54, p. 43-54.

ULLMANN, A., BRAUNER, N., 2006. Closure relations for two-fluid models for two-phase stratified smooth and stratified wavy flows. International Journal of Multiphase Flow, vol. 32, n. 1, p. 82-105.

WALLIS, G.B., 1969. One-dimensional two-phase flow. 1st ed., McGraw-Hill, USA.

WEISMAN, J., DUNCAN, D., GIBSON, J., *et al.*, 1979. Effects of fluid properties and pipe diameter on two-phase flow patterns in horizontal lines. International Journal of Multiphase Flow, vol. 5, n. 6, p. 437-462.

ZEE MA, Y., HOLDITCH, S.A., 2016. Unconventional oil and gas resources handbook: evaluation and development. 1st ed., Gulf Professional Publishing, United Kingdom.

ZHANG, H.-Q., SARICA, C., 2011. A model for wetted-wall fraction and gravity center of liquid film in gas/liquid pipe flow. SPE Journal, vol. 16, n. 3, p. 692-697.

ZHAO, Y., YEUNG, H., ZORGANI, E.E., *et al.*, 2013. High viscosity effects on characteristics of oil and gas two-phase flow in horizontal pipes. Chemical Engineering Science, vol. 95, p. 343-352.

ZHAO, Y., LAO, L., YEUNG, H., 2015. Investigation and prediction of slug flow characteristics in highly viscous liquid and gas flows in horizontal pipes. Chemical Engineering Research and Design, vol. 102, p. 124-137.

ZUBER, N., FINDLAY, J.A., 1965. Average volumetric concentration in two-phase flow systems. ASME Journal of Heat Transfer, vol. 87, n. 4, p. 453-468.